PREFACE

This dissertation is submitted for the degree of Doctor of Philosophy at the University of Cambridge. The research described herein was conducted under the supervision of Professor H. K. D. H. Bhadeshia in the Department of Materials Science and Metallurgy, University of Cambridge, between October 1998 and October 2001.

This work is to the best of my knowledge original, except where acknowledgements and references are made to previous work. Neither this, nor any substantially similar dissertation has been or is being submitted for any other degree, diploma or other qualification at any other university. This dissertation contains less than 60,000 words.

Part of this work has been presented in the following publications:

T. Sourmail, *Precipitation in creep resistant austenitic stainless steels.*, Mat. Sci. Tech., 17:1, 1-14.
This was a highly commended entry of the Institute of Materials Literature Survey Competition 2001.

T. Sourmail, H. K. D. H. Bhadeshia and D. J. C. MacKay, *A neural network model of the creep strength of austenitic stainless steels.*, Mat. Sci. Tech., *in press.*

Thomas Sourmail

January 2002

ACKNOWLEDGEMENTS

I would like to thank Professors D. J. Fray and A. H. Windle for the provision of the laboratory facilities in the Department of Materials Science and Metallurgy at the University of Cambridge. I am extremely grateful to my supervisor Professor H. K. D. H. Bhadeshia for his endless support, enthusiasm, knowledge and friendship.

I am indebted to Innogy Plc. and EPSRC for co-funding this project, and in particular to Dr David Gooch for his valuable comments and input throughout the project.

I would like to thank Hugh Davies and John Gisby from the National Physical Laboratory for their constant support with MT-DATA, together with the past and present members of the Phase Transformations and Complex Properties Research Group for their help and friendship, in particular to Harsha Sree Lalam, Miguel-Yescas Gonzales, Marimuthu Murugananth, Shingo Yamasaki, Catherine Neal, Gareth Hopkin, Hiroshi Matsuda, Pedro Rivera, Toshihiro Tsuchiyama, Franck Tancret, Pascal Jacques, Carlos Garcia, Daniel Gaude-Fugarolas.

Thanks also to my friends and to the people I met both at Darwin College and other Colleges during my time in Cambridge.

Finally, I take this opportunity to express my gratitude to my family for their love, unfailing encouragement and support.

ABSTRACT

Despite their apparent simplicity due to their fully austenitic structure, modern Cr-Ni stainless steels are complex systems often containing more than 10 alloying elements. Offering excellent corrosion and creep resistance at elevated temperatures, they are choice materials for applications such as superheater tubes in steam power plants. Over the past 30 years, considerable improvement has been made to the strength of austenitic stainless steels, through careful chemical composition control and sometimes purposely designed heat-treatment.

The present work is concerned with the experimental study of the recently designed NF709, the best austenitic steel currently available on the market, and with the development of models to predict the microstructural evolution and mechanical properties of such steels. The experimental study of the precipitation state as a function of ageing time, which involves an array of complementary techniques, reveals precipitation sequences with no documented equivalent.

Physical modelling based on the theory for simultaneous transformations is used to attempt to predict the precipitation as a function of time. Full use of modern thermodynamic tools is made, avoiding previously necessary approximations. Once multicomponent effects are correctly accounted for, good agreement is obtained with published results. However, serious limitations are highlighted both in the absence of reliable quantitative experimental information, and in the lack of thermodynamic data on phases commonly found in modern austenitic steels.

A neural network in a Bayesian framework is used to estimate the creep strength and creep life of austenitic stainless steels. Models built with this technique not only reproduce correctly known influence of composition, but also grasp the interactions between different parameters. It is further shown to be a superior method of extrapolation when compared to conventional methods.

A new finding, that of σ-phase in a chromium-enriched NF709, is shown to be of no consequence to the long-term creep properties of the alloy.

Contents

Nomenclature and Abbreviations

R	the gas constant.
P	the pressure of the system.
T	the temperature of the system.
t	the time.
G^0	contribution of the pure components to the molar Gibbs energy of a phase indicated in subscript if necessary.
G^{id}_{mix}	ideal mixing contribution to the molar Gibbs energy of a phase indicated in subscript if necessary.
G^{xs}_{mix}	excess Gibbs energy change for mixing of a phase indicated in subscript if necessary.
ε_{AB}	the energy of a pair A-B.
G^*_θ	the activation energy for homogeneous nucleation of phase θ.
$G^*_{d,\theta}$	the activation energy for nucleation on a dislocation.
$G^*_{B,\theta}$	the activation energy for nucleation on a grain boundary.
G^*_t	the activation energy for the transfer of an atom across the interface.
x^γ_i	the mole fraction of component i in phase γ.
$x^{\gamma\theta}_i$	the mole fraction of component i in phase γ in equilibrium with θ.
$\overline{x^\gamma_i}$	the average mole fraction of i in phase γ.
y^k_i	the site fraction occupancy of component i on sublattice k in a sublattice phase.
ω^v_{ij}	the binary interaction parameter (i and j) in the Redlich-Kister development, depending on the value of v.
$L_{A,B:C}$	the parameter for interactions between A and B on the first sublattice when C occupies the second.
G_θ	the molar Gibbs energy of phase θ.
ΔG_v	the driving force for nucleation per unit volume of precipitate phase.
ΔG_n	the driving force for nucleation per mole of precipitate phase.
ΔG_m	the driving force for nucleation as defined by the parallel tangent construction.
V^θ_m	the molar volume of phase θ.

N_θ	the number density of nucleation sites for phase θ.
N_v	the number of atoms per unit volume.
L_d	the length of dislocation per unit volume.
$\sigma_{\gamma\gamma}$	the energy per unit area for an interface between the phases indicated in subscript.
D_i^γ	the volume diffusion coefficient of element i in γ.
I_θ	the nucleation rate for phase θ.
ψ_θ	the growth rate for phase θ.
c_i^γ	the concentration of component i in phase γ.
$c_i^{\theta\gamma}$	the concentration of component i in phase θ in equilibrium with γ.
$\overline{c_i^\gamma}$	the average concentration of component i in phase γ.
Ω_i	the supersaturation of component i.
J_i	the flux of component i.
$\mu_{i,\theta}$	the chemical potential of component i in phase θ.
C	shape factor relating the volume of a particle to the cube of its radius.
V^e	the extended volume of a phase indicated in subscript.
V_p	the volume of a particle at a given time.
$V_f(phase)$	the volume fraction of a phase.
V	the total volume in which the transformation occurs.
C_{Pi}	the heat capacity for the temperature range i.
d_{hkl}	the interplanar spacing for plans (hkl).
λ	the wavelength associated with electrons.
σ	the stress during a creep test.
$\sigma_{f,10^4h}$	the stress to obtain creep rupture after 10^4 h.
t_R	the time to rupture.

TEM	Transmission Electron Microscopy.
SEM	Scanning Electron Microscopy.
EDX	Energy Dispersive X-ray analysis.
TTP	Time Temperature Precipitation.
MT-DATA	Metallurgical and Thermochemical Databank.
SGTE	Scientific Group Thermodata Europe.
JCPDS	Joint Committee of Power Diffraction Standard.
bcc	body-centred cubic.
fcc	face-centred cubic.
hcp	hexagonal close-packed.

Chapter 1

Introduction

The purpose of this chapter is to present the motivation for the research activities on creep-resistant austenitic stainless steels, and to provide a general background about these materials.

1.1 Materials requirements in the power generation industry

Over the last decade, considerable research has been devoted to the improvement of power plant efficiency. This is both for economical and environmental reasons: operating at higher temperatures improves the thermodynamic efficiency, and hence reduces the CO_2 emissions per unit of energy. In this context, materials-related issues are the limiting factor. Most of the steam-turbine plant now in service operate with a maximum steam temperature of 568 °C and pressure of 160 MPa, with the current state-of-the-art plant operating at 300 MPa, 600 °C [1]. When exposed for many years to such conditions, the tubes in which steam circulates have to offer suitable corrosion and creep resistance. Cost considerations imply that ferritic steels are used as much as possible, and considerable work is being devoted to design stronger ferritic alloys for use at operating temperatures of 650 °C. They also have a lower thermal expansion coefficient which makes them less prone to thermal fatigue.

However, the lower parts of the superheater tubes on a conventional boiler (figure 1.1), encounter temperatures at which ferritic steels cannot be used, and are therefore

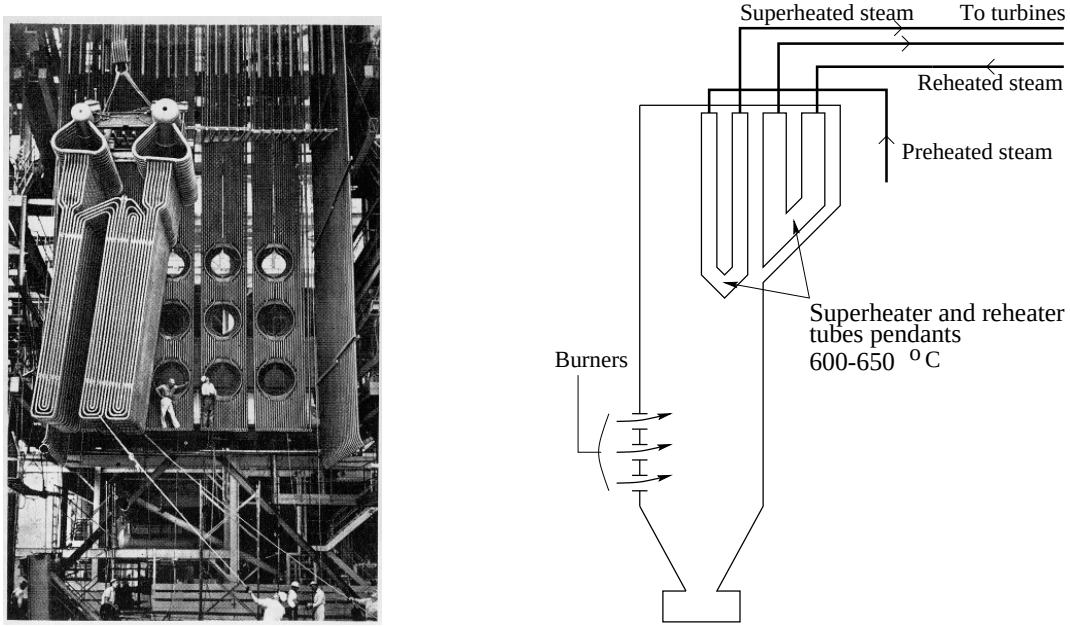

Figure 1.1: Superheater tubing (left) and scheme of a simplified boiler, after [2]

conventionally made out of austenitic stainless steels. As a part of the effort to improve the efficiency of power plants, much research focuses on improving the creep strength of these alloys, and consequently to raise their operating temperature.

The following gives a short introduction to the different austenitic stainless steels used in industry, and the latest compositions.

1.2 Austenitic stainless steels

1.2.a Composition and constituents

Austenitic stainless steels are essentially alloys of Fe-Cr-Ni, which owe their name to their room temperature austenitic structure. The addition of chromium has long been known to improve corrosion resistance. Chromium is also a 'ferrite stabiliser' and Fe-Cr stainless steels have a ferritic structure, possibly martensitic depending on the heat-treatment and exact chemical composition. The addition of austenite stabilising elements in sufficient quantities can allow an austenitic structure to be stable at all temperatures.

Nickel is the basic substitutional element used to stabilise austenite. The equilibrium phases depend on the proportion of the three elements, as well illustrated in an isothermal section of the ternary diagram for Fe-Cr-Ni (fig. 1.2) calculated using MT-DATA [3].

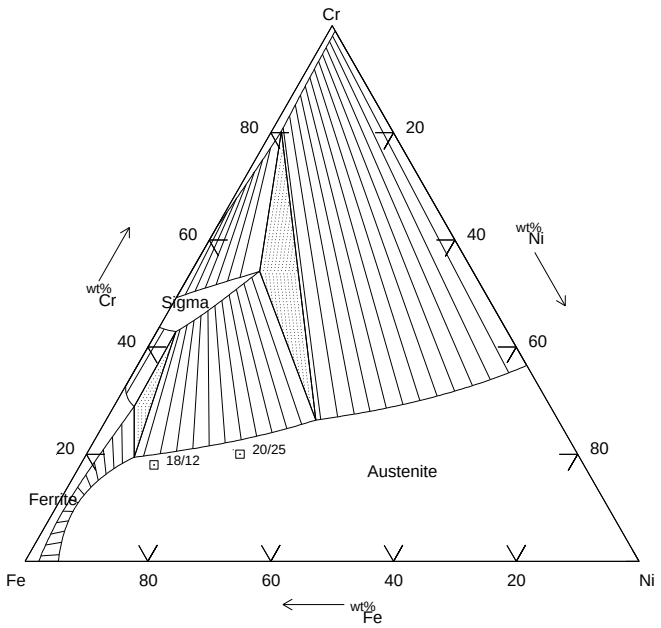

Figure 1.2: Isothermal section of the Fe-Cr-Ni diagram at 750 °C: a typical 18Cr-12Ni wt% lies in the austenitic field. Calculated using MT-DATA and the SGTE database.

Often, alloying elements, either interstitial such as C or N, or substitutional such as Mo, Mn, Ti, Nb, V, W, Cu, Al,... are also used to obtain the required properties. They can be classified as ferrite-stabilisers or austenite-stabilisers and their effect in this respect is often approximated using the notion of chromium and nickel equivalents, calculated by formulae like [4]:

$$\mathrm{Ni_{eq}} = \mathrm{Ni} + \mathrm{Co} + 0.5(\mathrm{Mn}) + 30(\mathrm{C}) + 0.3(\mathrm{Cu}) + 25(\mathrm{N})$$

$$\mathrm{Cr_{eq}} = \mathrm{Cr} + 2.0(\mathrm{Si}) + 1.5(\mathrm{Mo}) + 5.5(\mathrm{Al}) + 1.75(\mathrm{Nb}) + 1.5(\mathrm{Ti}) + 0.75(\mathrm{W})\ \mathrm{wt\%}$$

In this example, the composition has to be given in weight%. The use of such formulae is not always straightforward, as they rely on the austenite content, which can be modified by various precipitation reactions involving these elements.

Whether the austenitic structure is retained at room temperature depends on the M_S (martensite-start) temperature. Several empirical formulae have been derived to describe the effect of chemical composition on M_S, an example is [5]:

$$M_S(^\circ\mathrm{C}) = 502 - 810(\mathrm{C}) - 1230(\mathrm{N}) - 13(\mathrm{Mn}) - 30(\mathrm{Ni}) - 12(\mathrm{Cr}) - 54(\mathrm{Cu}) - 6(\mathrm{Mo})\ \mathrm{wt}\%$$

A typical type 304 steel (table 1.2) has its M_S well below room temperature. However, it should be borne in mind that deformation-induced martensite formation can occur well above M_S. M_{d30} is the temperature at which 50% of martensite has formed for a true strain of 30%. Again, formulae like:

$$M_{d30}(^\circ\mathrm{C}) = 497 - 462(\mathrm{C}+\mathrm{N}) - 9.2(\mathrm{Si}) - 8.1(\mathrm{Mn}) - 20(\mathrm{Ni}) - 13.7(\mathrm{Cr}) - 18.5(\mathrm{Mo})\ \mathrm{wt}\%$$

have been derived to describe the effect of alloying elements [5].
At high temperatures, a steel containing 18Cr, 12Ni wt% should be fully austenitic. However, the addition of other alloying elements often results in the formation of carbides, nitrides and intermetallics. These phases are not always desirable and a good knowledge of precipitation reactions is required to avoid loss of mechanical or chemical properties. A good example is the sensitisation of non-stabilised austenitic stainless steels: sensitisation occurs when the precipitate $M_{23}C_6$ forms at grain boundaries, depleting the chromium content in the vicinity, which eventually results in intergranular corrosion. This can be avoided by tying up the carbon with strong carbide formers like Ti and Nb. The steel is then said to be stabilised. These precipitate phases will be described in detail in a later section.

1.2.b Grades of austenitic stainless steels

From a simple type 304 to the recent NF709, austenitic stainless steel compositions cover a large range. The two main alloying elements are chromium and nickel, so the steels will often be referred to by their content of Cr and Ni. For example, 18/10 refers to an austenitic stainless steels with 18Cr, 10Ni wt% .

The AISI 300 series and other variants The AISI 300 specifications for the compositions of different austenitic stainless steels (wt%) are shown in table 1.2 (after [6]).

wt%	C	Mn	P	Ni	Cr	
Type 304 [6]	≤ 0.07	≤ 2.00	0.04	8-10	17-19	
NF-709 [7]	0.06	1.00	0.006	25	20	
wt%	Mo	Nb	Ti	B	N	Si
Type 304	~ 0	~ 0	~ 0	~ 0	~ 0	~ 0
NF-709	1.5	0.26	0.05	0.005	0.167	0.40

Table 1.1: Compositions of two austenitic stainless steels

	C max.	Si max.	Mn max.	Cr	Ni	Mo	Ti	Nb	Al	V
301	0.15	1.00	2.00	16-18	6-8					
302	0.15	1.00	2.00	17-19	8-10					
304	0.08	1.00	2.00	18-20	8-12					
310	0.25	1.50	2.00	24-26	19-22					
316	0.08	1.00	2.00	16-18	10-14	2.0-3.0				
321	0.08	1.00	2.00	17-19	9-12		5×%C min.			
347	0.08	1.00	2.00	17-19	9-13			10×%C min.		
E 1250	0.1	0.5	6.0	15.0	10.0					0.25
20/25-Nb	0.05	1.0	1.0	20.0	25.0			0.7		
A 286	0.05	1.0	1.0	15.0	26.0	1.2	∼1.9		∼0.18	∼0.25

Table 1.2: The AISI 300 series and other examples of heat resistant austenitic stainless steels; E1250 is Esshete 1250. All compositions given in wt%.

Grades denoted L contain low carbon (< 0.03 wt%) and 'N' contain nitrogen (eg: 316LN). Most often used as creep-resistant steels are types 316, 321 and 347, or alloys containing all of Mo, Nb and Ti. There are many other variants of these compositions, like the Japanese SUS300 series which mirrors the AISI 300 series, but sometimes with addition of both Ti and Nb. For convenience, as is sometimes done in the literature, the AISI 300 series will be used even for steels not strictly belonging to it, like a 316 with a Ti addition.

In fact, it is not the intention to describe, in the next chapter, the precipitation sequences in all different grades of creep-resistant austenitic stainless steels, but rather to examine the occurrence of the various precipitates in such a way that the precipitation behaviour of undocumented grades can be inferred from the conclusions reached.

There is a large amount of material on the precipitation phenomena in the 300 series of alloys, which have been used widely as creep-resistant steels. The same is true for 20Cr-25Ni steels. However, it appears that the long-term behaviour of Ti, Al alloyed austenitic stainless steels (type A286) is little documented [8]. This is possibly because production difficulties have restricted the application of such steels to parts requiring relatively small ingot sizes (aeroengine turbine discs), the design life of which is much shorter than the

few 100000 h required for steam plants [9].

Role of alloying elements

- Mn has been introduced in austenitic stainless steels as a substitute for Ni during shortages in the international market or for economical reasons. The nickel content can be halved to 4 wt% by the addition of 2-6 Mn wt%. Although the austenitic structure is achieved, such steels do not exhibit the same corrosion resistance as an 18/8 steel. Mn is also used to increase the solubility of nitrogen in austenite.

- Mo is, on the contrary, a ferrite stabiliser. It improves the creep properties of stainless steels by solid solution hardening and also improves the resistance to pitting corrosion. It also facilitates carbides precipitation. However, it promotes σ-phase and Laves phase formation on long term ageing.

- Stabilising elements like niobium, titanium and vanadium greatly improve the creep strength of austenitic stainless steels mainly by precipitating fine carbides intragranularly. On the other hand, they reduce the creep ductility. The ratio in which they are added to carbon is important to maximise the strengthening effect and avoid precipitation of detrimental phases. They can also have a solid-solution strengthening effect.

- Carbon acts principally by solid-solution strengthening in non-stabilised grades, but mainly by precipitation strengthening when Nb, Ti or V are present.

- Nitrogen is a strong austenite stabiliser. It has also a role in increasing the creep life of austenitic stainless steels: it can act like carbon in stabilised stainless steels by precipitating in the form of titanium or niobium nitrides, but the nitrogen remaining in solid solution has also a much greater strengthening effect than carbon. It has been believed to lower the diffusivity of chromium and carbon in the matrix, therefore delaying the coarsening of precipitates [5, 6]. However, more recent results indicate that nitrogen enhances chromium diffusion, but retards the nucleation of $M_{23}C_6$ because of its low solubility in this carbide [10].

1.2.c Modern grades for high-temperature applications

Steels from the AISI 300 series have been used for long in power plant, where strong corrosion resistance and creep strength are required. Modern austenitic grades have however significantly improved over these by the use of new combinations of chemical elements, such as SUPER304H which, in addition to the required composition of a 304 steel, contains Nb, N and Cu; SAVE25 which contains W, Nb, Cu and N, or NF709, presented previously.

Figure 1.3 illustrates the development progress of austenitic steels for boilers, and on the far right, the most advanced austenitic stainless steels, which all contain several other elements in addition to Cr and Ni. In practice, the compositions are controlled much more accurately than suggested by the intervals of compositions and include controlled additions of B which has been shown to have beneficial effects on the creep strength.

Figures 1.4 and 1.5, adapted from [11], compare the allowable stresses as a function of temperature, for some of these steels, and give a clear idea of the progress that has been made from the H-Grade AISI 300 series. The definition of 'allowable stress' is not given in this reference; the value of the stress probably refers to a particular service life.

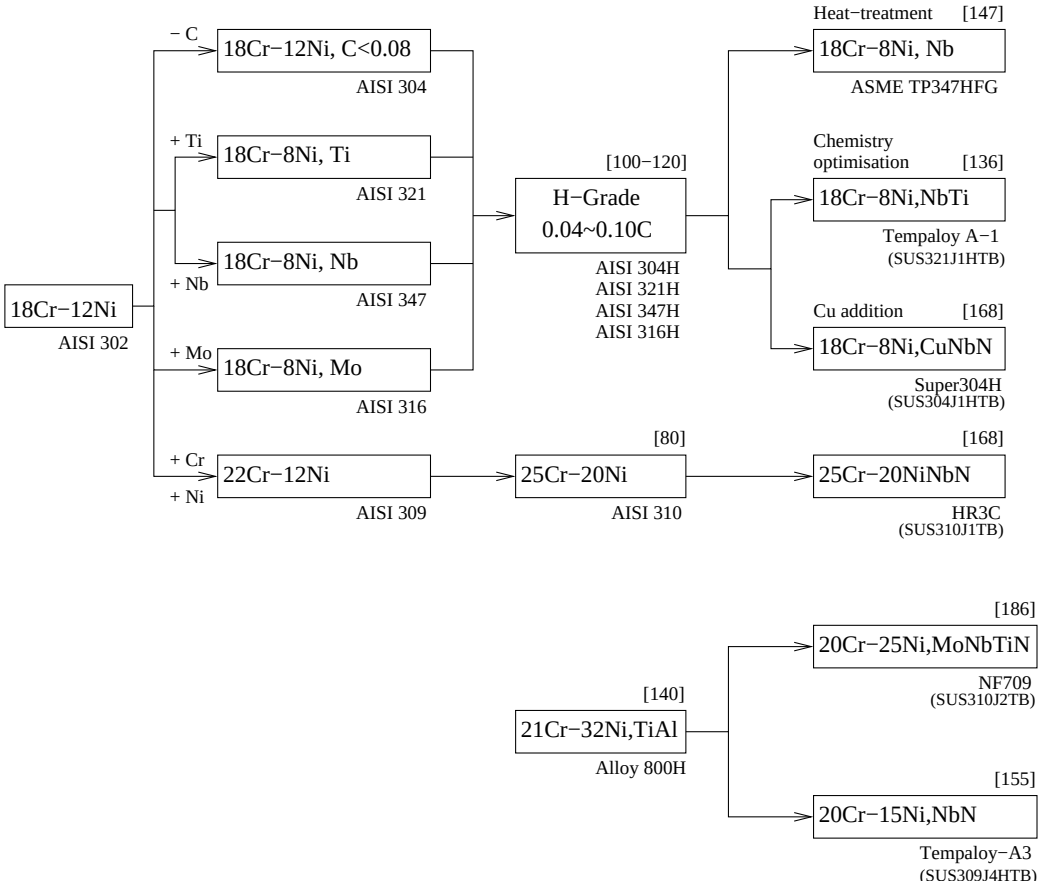

Figure 1.3: The development progress of austenitic stainless steels for high temperature applications, after [11]. Numbers in square brackets indicate the 10^5 h creep rupture strength at 600 °C.

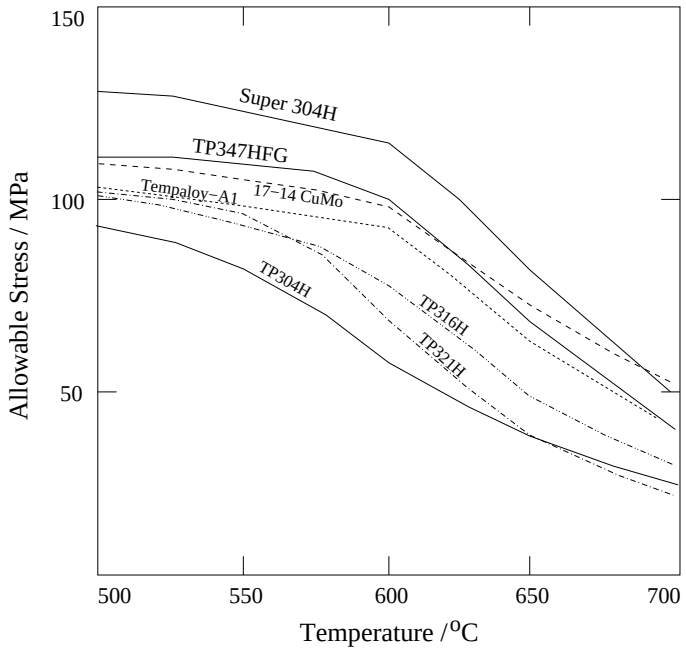

Figure 1.4: The allowable stresses for some austenitic stainless steels for high temperature applications, based on 18Cr-8Ni or 15Cr-15Ni steels. After [11].

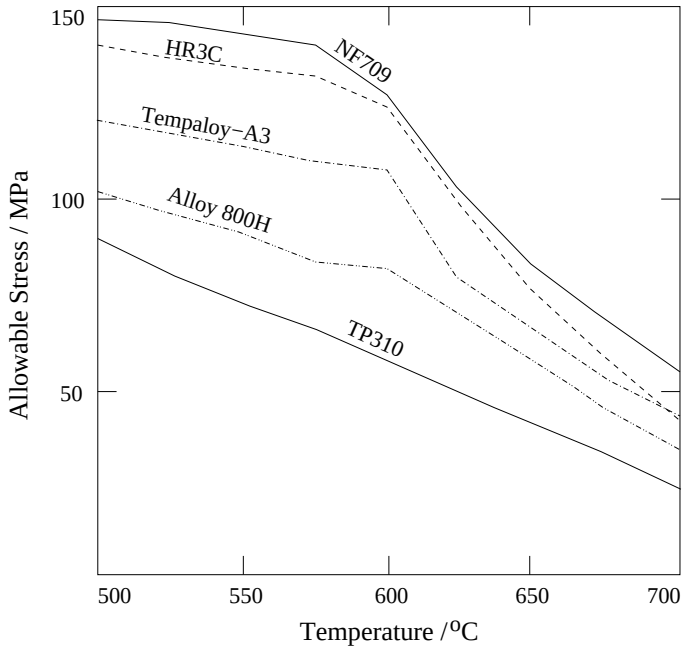

Figure 1.5: The allowable stresses for some austenitic stainless steels for high temperature applications, based on 20Cr-25Ni or other high-Cr, high-Ni steels. After [11].

Chapter 2

Precipitates in creep resistant austenitic stainless steels

The main grades of austenitic stainless steels have been presented in the previous chapter. With excellent corrosion and mechanical properties at high temperatures, they are choice materials for powerplant tubes which have to operate at temperatures above 950K, or for aeroengines.

The important role of precipitation in the achievement of good creep properties has been understood for long and extensively studied. Although some phases are now well documented, there are still contradictions and missing thermodynamic data, in particular, there is only a limited amount of information about phases like Z-phase or Cr_3Ni_2SiN which can be predominant precipitates in nitrogen-bearing steels.

This chapter is a review of common precipitates in austenitic stainless steels, in particular wrought heat-resistant steels of the AISI 300 family or 20/25 steels. Precipitates forming in age-hardening austenitic stainless steels are only briefly presented, having been previously reviewed by other authors, and can be considered out of the scope of this work.

2.1 Carbides and nitrides in austenitic stainless steels

2.1.a MX precipitates

The formation of MX precipitates in austenitic stainless steels occurs when strong carbide/nitride formers (Ti, Nb, V, Zr, Ta...) are added to the alloy.

These additions have two purposes:

- stabilising the alloy against intergranular corrosion. When stabilisation is the first aim, a stabilising heat-treatment is conducted at 840-900 °C for several hours before service. Most of the carbon is then 'tied-up' by precipitation of MC.
- Providing good creep resistance: when this is the first aim, a solution heat-treatment is given in order to dissolve as much MX as possible. Subsequent precipitation occurs during creep and increases strength. A typical solution treatment is 30-60 min at temperatures between 1100 and 1250 °C.

The second use is the one we will focus on.

Many studies have concentrated on MX precipitation, but also on the appropriate content necessary to obtain the best properties. The solubility of the MX precipitates and the stoichiometry are essential in determining the behaviour of the steel with regard to precipitation.

i Structure and features of precipitation

MX carbonitrides have a NaCl fcc (face-centred cubic) structure, with lattice parameters as listed in table 2.1.

MX	a, Å	reference
NbN	4.39	JCPDS 38-1155
NbC	4.47	JCPDS 38-1364
TiN	4.24	JCPDS 38-1420
TiC	4.33	JCPDS 32-1383

Table 2.1: Lattice parameter of some MX precipitates (JCPDS: Joint Committee of Powder Diffraction Standard).

Often, measured lattice parameters have intermediate values, reflecting the existence of a solid solution between the different carbonitrides.

MX precipitates usually form on dislocations within the matrix, on stacking-faults (most often with TiC), on twin and grain boundaries. They have a characteristic cuboidal shape after sufficient ageing.

ii Solubility of MX carbides in austenite

Stabilisers such as Ti or Nb have long been known to reduce the solubility of carbon in austenite. Early studies of the problem consisted in the determination of two parameters: H, the heat of solution, and A, a constant as in:

$$\log[\mathrm{M}][\mathrm{X}] = A - \frac{H}{T}$$

where [M] is the weight percent of stabilising element in solution in the matrix, and similarly for [X]. The product [M][X] is often referred to as the solubility product. Strictly speaking, H is expressed in K.

The two following relationships can be found in many publications (e.g. [4, 6]):

$$\log[\mathrm{Ti}][\mathrm{C}] = 2.97 - \frac{6780}{T(\mathrm{K})}$$
$$\log[\mathrm{Nb}][\mathrm{C}] = 4.55 - \frac{9350}{T(\mathrm{K})}$$

They are essentially valid for a typical 18/12 steel, the concentrations are in weight percent. For a 20/25 steel, Kikuchi *et al.* [12] used for TiC H=10475, A=3.42 and for NbC, H=7900 and A=4.92, but it is not clear whether these values have been measured for 20/25. The solubility is, as shown in their work, an important factor in the achievement of good creep properties: they showed that adding M and X in excess of their solubility limits resulted in coarse MX in the matrix and induced faster coarsening of MX which later precipitated. However, until this limit is reached, the more M and X added the better because more MX particles will be formed.

It is therefore clear that knowing the solubility limits of MX carbides is important. However, modern high-temperature austenitic stainless steels often contain both carbon and nitrogen, and more than one strong carbide former (Ti+Nb, Nb+V...), and relationships as above are of limited use when it comes to estimate the solubility of multicomponent carbonitrides (e.g. (Ti,Nb)(C,N)).

Recently, some studies proposed different approaches to the problem of the solubility of multicomponent carbonitrides in austenite [13, 14, 15]. For example, Rios [13] proposed for Nb(C,N):

$$(\%\mathrm{Nb})\left[(\%\mathrm{C})/\mathrm{K}_{\mathrm{C}}^{1.15} + (\%\mathrm{N})/\mathrm{K}_{\mathrm{N}}^{1.15}\right]^{0.87} = 1$$

where

$$\log\ K_C = \Delta G^{\circ}_{NbC_{0.87}}/RT$$
$$\log\ K_N = \Delta G^{\circ}_{NbN_{0.87}}/RT$$

where $\Delta G^{\circ}_{NbC_{0.87}}$ is the Gibbs energy of formation of $NbC_{0.87}$ with infinite dissolution in the austenite as the reference state. However, one must notice that all these studies deal with MX in austenite for micro-alloyed steels. It seems clear, from the literature, that the presence of Ni and Cr introduces a further difficulty in austenitic stainless steels, the main one being the formation of Z-phase.

There is a general agreement that Z-phase (CrNbN) forms in Nb stabilised austenitic stainless steels, with a sufficient amount of nitrogen. In fact, it seems that as soon as 0.06N wt% is present in a typical 347 steel, Z-phase can be expected [16].

Moreover, in Cr/Ni steels, MX precipitates have been reported to start growing largely under-stoichiometric [17, 18]. No approaches have been found that dealt with the solubility of multicomponent carbonitrides in austenitic stainless steels susceptible of Z-phase formation. Indeed, Z-Phase is even absent from the SGTE (Scientific Group Thermodata Europe) thermodynamic databases accessed by programs such as MT-DATA or Thermo-calc.

iii Formation and stoichiometry of MX precipitates

A number of studies have been devoted to the determination of the correct quantities of M and X to use in order to have the best mechanical properties. As stated above, one factor is the solubility of MX. This has been clearly outlined by the work of Kikuchi *et al.* [12].

The second factor is the proportion of each element that has to be added, in such a way as to maximise the amount of precipitation for a given product [M][X]. It is also important to know, if stoichiometry is not respected, which of the elements is in excess, as this may influence the precipitation sequence.

Wadsworth *et al.* [19] proposed a quantitative approach to stoichiometry and showed that the amount of precipitate that can form drops quite sharply when M and X are not added in proportions corresponding to the composition of the expected carbide (figure 2.1). Using the data of Keown and Pickering [20], they showed that best creep lives were obtained when the Nb/C ratio was matching the stoichiometry Nb_4C_3 (for 18/12 or 18/10).

Other studies have shown that best creep life in 20/25 alloys was obtained for a Nb/C

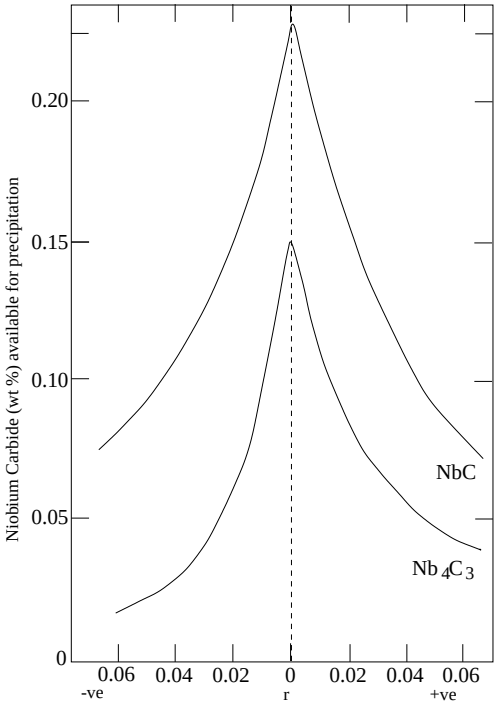

Figure 2.1: The amount of niobium carbide available for precipitation at 923 K (after solution treatment at 1373 K) as function of the degree of deviation from stoichiometry r, defined by $r = pB_T - qA_T$, where p and q are the mass fractions of A and B in the compound AB_n, and A_T and B_T the mass fraction of these elements in the alloy. After [19].

atomic ratio of 1/1 [12, 21]. The work done by Kikuchi *et al.* [12] does not highlight any serious contradiction since the first composition they tried around the atomic ratio 1:1 was 2:1, which means that any variation within this interval was not investigated. However, Adamson and Martin [21] have results for the weight ratios 8:1 and 10:1 (respectively atomic ratios 1:1 and 4:3), but find better creep properties for the 1:1 atomic ratio. A possible explanation is that NbC actually forms with the stoichiometry 1:1 in 20/25 steels.

It seems important to note that all these studies rely on relatively short term creep tests (as an average, less than 1000 h). No study has been found which confirms the importance of a stoichiometric addition on long term creep properties. Moreover, this explanation of the good creep properties of steels with stoichiometric additions of M and X assumes that MX precipitates form with their final stoichiometry, which has been proved wrong by different authors, as explained below.

The non-stoichiometry of MX precipitates in 18/12 austenitic stainless steels has been

confirmed by atom-probe analysis [17, 18]. It was noticed that MX was largely sub-stoichiometric for short ageing (typically 3 h at 750 °C), and contained a large amount of Cr substituting for M (Ti,Nb,V...). The following explanation was proposed: as MX has a lattice parameter larger than that of the austenite, a flow of vacancies is needed for the growth of MX and stress is generated. The substitution of M by Cr and the low carbon content both reduce the lattice parameter. Moreover, Cr is readily available while M has to diffuse over long distances. The formation of sub-stoichiometric, carbon-depleted MX precipitates is therefore kinetically advantageous. In more theoretical terms, this corresponds to two effects. Capillarity is likely to modify substantially the local equilibrium as the precipitates are very small. In fact, the composition changes reported in these references correlate with size changes. The second effect is the modification of local equilibrium to satisfy simultaneously the flux balance for different solutes. This could affect strongly the composition of MX, since the diffusivities of the elements involved are very different. It would similarly correlate with a size change unless the precipitates are only coarsening.

However, stoichiometric carbides still have a lower free energy and, during further ageing, they grow at the expense of sub-stoichiometric ones. This is because, according to Andrén *et al.* [17], the diffusivity of metallic elements within MX precipitates is so small that these precipitates can not change composition.

2.1.b Z-Phase

Z-phase is a complex carbonitride which forms in Nb stabilised austenitic stainless steels containing a relatively high level of nitrogen. It has only recently been discovered, with its structure being fully determined by Jack and Jack in 1972 [22], and it appears from the most recent reviews (e.g. [4]) that the conditions of its formation are not very clear, and even less is its relative stability when compared to other carbonitrides.

i Structure and composition

The structure of Z-Phase is commonly accepted to be the one described by Jack and Jack [22]: it has a tetragonal unit cell (space group P4/nmm), with a=3.037 Å and c=7.391 Å. The unit cell is obtained by ordering of Cr, Nb and N atoms, the formula being $Cr_2Nb_2N_2$ per unit cell. Vodárek [23] reports the following orientation relationship

for Z-phase in a type 316LN:

$$(001)_Z \parallel (001)_\gamma$$
$$[1\bar{1}0]_Z \parallel [100]_\gamma$$

In contrast to MX precipitates, it seems that Z-phase dissolves little (if at all) substitutional elements. Raghavan *et al.* [24] suggest that it can dissolve carbon and write CrNb(CN), without giving any evidence for this. The absence of a CrNbC phase suggests that if carbon can dissolve in Z-phase, it can only do so within small limits. Also, when Nb is in sufficient quantity, both Z-phase and NbC are found.

ii Occurrence

Z-phase is seldom reported, even in alloys liable to form it on ageing. This could be due to its composition and its general features of formation which are not very different from common MX precipitates.

It generally forms on grain-boundaries, very rapidly, but also on twin boundaries and within the matrix, where it is associated with dislocations [25]. When it forms, it is usually as a fine dispersion of particles [24, 25, 16], which makes it an interesting phase when good creep properties are sought. The morphology has been reported to be either cuboidal [25] or rod-like [17].

There is a good agreement that it forms at high temperatures: Raghavan *et al.* [24] report its formation during annealing (1 h at 1300 K) of a 18/12 containing 0.3Nb wt% and 0.09N wt%, with an orientation relationship indicating precipitation in the solid state. After ageing 8000 h at 866 K, it is still the predominant precipitate. Few $M_{23}C_6$ and σ-phase particles are present. These authors indicate that a 10 s heat-treatment at 1573 K is sufficient to dissolve all the Z-phase particles, which is not inconsistent with the work of Robinson *et al.* (quoted in [24]) which locates the solvus of Z-phase to be between 1573 K and 1623 K in a steel containing larger amounts of niobium and nitrogen.

Robinson and Jack [25] report the formation of Z-phase in a 20Cr/9Ni steel containing 0.38N wt% and 0.27Nb wt% between 700 and 1000 °C. At 1000 °C Z-phase is the first and only phase formed. It is found uniformly distributed after 30 min but coarsens rapidly. At 700 °C it starts to precipitate in the matrix after 16 h. At lower temperatures, Vodárek *et al.* [26] report a considerable dimensional stability of Z-phase in a type 316LN, with a mean size of 6 nm after 82 h at 650 °C and 12 nm after 37890 h at the same temperature.

Thorvaldsson and Dunlop [27], studying the effects of stabilising elements in austenitic stainless steels, used a 18/12 steel with 0.4V, 0.13Nb and 0.43N at%. After 5000 h at 750 °C, no Z-phase had formed, but a (Nb,V)(C,N) fcc carbonitride formed instead. Andrén *et al.* [17], with a steel of the same composition, in very similar conditions, found, on the contrary, that the MX precipitate had always a stoichiometry not far from $MX_{0.5}$, and contained sensibly as much chromium as Nb+V. However, the characteristic tetragonality was not observed and the authors suggested that they found a precursor state of the fully ordered Z-phase.

iii Considerations on the stability of Z-phase

It seems quite reasonable to propose that Z-phase is the stable Nb containing phase in austenitic stainless steels with high nitrogen: Hughes [16] suggests that it can be expected in a typical 347 steel as soon as the weight percentage of N is greater than 0.06. Knowles [28] finds Z-phase in a 20/25 0.41Nb wt% steel with 0.028N wt%, which could indicate that chromium and/or nickel content play an important role in the solubility of this phase.

The problem arises, in many steels, to know whether NbC or Z-phase is the more stable. Very few studies have dealt with additions of Nb, C and N together in a way that could determine which phase is more stable: often Nb is in excess and both NbC and CrNbN form. Uno *et al.* [29] found that only Z-phase formed in a 18/12 Nb steel with carbon and nitrogen, the niobium content being lower than that required to combine either all C or all N. This would indicate that Z-phase is fast enough to form first when competition between NbC and CrNbN is likely to occur. On the other hand, Knowles [28] reported Nb(C,N) after 2 h at 850 °C in a 20/25 steel, transforming to Z-phase with further ageing. From the precipitation behaviour of NF709 [7], where Z-phase is reported after ageing times of 10^4 h at 750 °C, and C containing phases are $M_{23}C_6$ and M_6C one can infer that Z-phase is more stable than NbC and that the latter will dissolve for the former if Nb is in too small quantities. However, Raghavan *et al.* [24] deduce from a comparison between 347 (18/12 with 0.8Nb and 0.07C wt%) and 347AP (18/12 with 0.3Nb, 0.09N, 0.009C wt%) a greater stability of NbC, since Z is found to precipitate from the solid state but the NbC is found as residual particles. The conclusions of such a comparison have to be examined carefully as the compositions were different.

iv Conclusions on Z-phase

Generally, one can conclude that Z-phase precipitation is not fully understood. Points of agreement are its stability at high temperature and the features of its precipitation (fine dispersion). Proposed solvus temperatures differ between the various studies, but these differences are consistent with different compositions. It is difficult as yet to build a coherent view of the different kinetics observed. It is not clear whether Z-phase actually forms from MX precipitates as suggested by the results of Knowles [28] and Andrén *et al.* [17], or directly as suggested by Robinson *et al.* [25]. These observations could be reconciled if one could prove that the driving force for the formation of Z-phase in a 20Cr 10Ni (Robinson *et al.*) is significantly different than that in a 18/12. The importance of Z-phase in both ferritic and austenitic power plant steels, renders particularly necessary the assessment of the ternary system Cr, Nb, N to provide the thermodynamic parameters required for any prediction.

2.1.c $M_{23}C_6$

i Structure and composition

$M_{23}C_6$ is a more general notation for $Cr_{23}C_6$, as often, Ni, Mo and Fe are found to substitute partially for chromium. It is the main carbide in non-stabilised C-containing austenitic stainless steels; nitrogen bearing steels form Cr_2N. It has a fcc structure (and space group Fm3m) of lattice parameter varying between 10.57 and 10.68 Å, which is about three times that of the austenite. It is often reported to grow with a cube to cube orientation relationship:

$$\{100\}_\gamma \parallel \{100\}_{M_{23}C_6}$$
$$\langle 010\rangle_\gamma \parallel \langle 010\rangle_{M_{23}C_6}$$

It is most of the time the main carbide found in austenitic stainless steels. Although it can be only metastable, it is always found in the early stage of precipitation because it nucleates very easily.

ii Morphologies and locations

$M_{23}C_6$ is most of the time reported to precipitate on the following nucleation sites, and in this order: grain boundaries, incoherent and coherent twin boundaries, intragranular sites. In Nb stabilised grades, it is sometimes reported to nucleate on undissolved (that

is, during the solution treatment) niobium carbonitrides. Generally, $M_{23}C_6$ only shows {111} and {110} interface planes. This has been explained by Beckitt and Clarck [30], who showed these planes have the best atomic correspondence with the austenite.

Precipitation on grain boundaries The precipitation of $M_{23}C_6$ has been the focus of many investigations, motivated by its importance in terms of corrosion resistance. $M_{23}C_6$ on grain boundaries is often associated with intergranular corrosion. It is found after very short ageing times (30 min at 750 °C, [31]), even in stabilised steels. It causes the grain boundary to move, and therefore shows on one side, the new grain boundary, while the other has a serrated aspect composed by the {111} interfaces. These precipitates are usually large. When boron is added, the number density of $M_{23}C_6$ particles along the grain boundaries increases [32], with beneficial effect for the creep rupture strength, as the grain boundary sliding and surface cracking are reduced. Other effects of boron in $M_{23}C_6$ will be dealt with later.

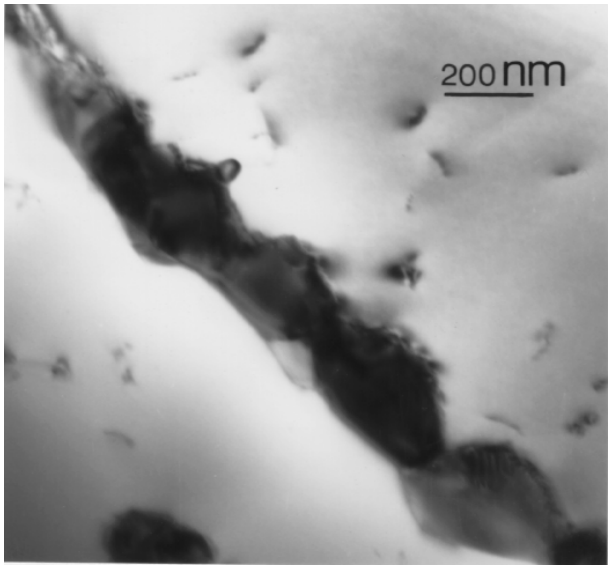

Figure 2.2: $M_{23}C_6$ on grain boundary.

Precipitation on incoherent and coherent twin boundaries On incoherent and coherent twin boundaries, $M_{23}C_6$ forms long plates parallel to the twin boundaries. The plates are, as for any form of $M_{23}C_6$ in austenitic stainless steels, bounded by {110} and {111} planes only. The large faces are {111} planes parallel to the twin boundaries.

Plates are initially growing from the incoherent twin boundary, but some are found later apparently detached from the boundary. Precipitation on the coherent boundary occurs more slowly than on incoherent ones. The mechanism of their formation has been subject

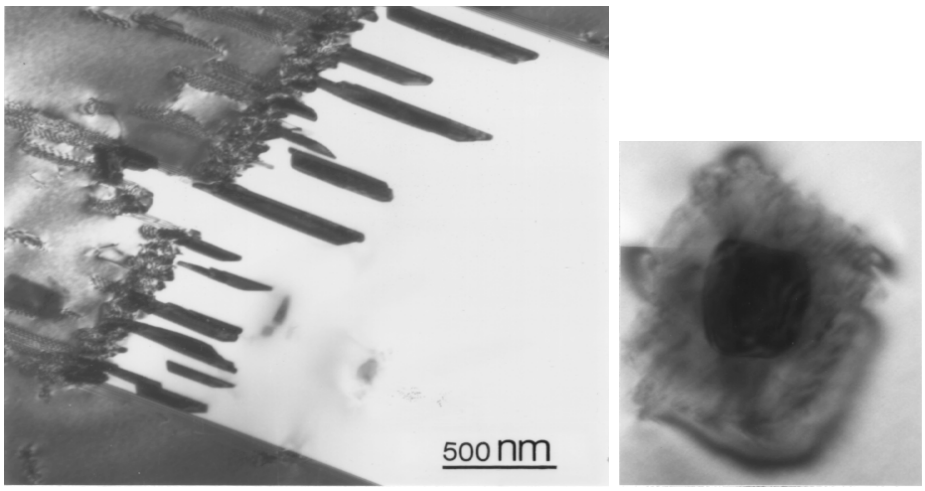

Figure 2.3: Plates of $M_{23}C_6$ growing from an incoherent twin boundary (left), and around a Nb(C,N) precipitate (right), work done for this project.

to controversy: Beckitt and Clarck [30] suggested that carbides growing on the incoherent twin boundary repel Shockley partial dislocations in the twin, and these cause nucleation of new plates in the twin. But detailed observations have lead Singhal and Martin [33] to conclude that stacking faults were first growing in the twin. $M_{23}C_6$ would then nucleate on the Shockley bounding dislocation and grow in the stacking fault, possibly helped by an enrichment of this stacking fault in chromium. Both fail to explain why these plates most of the time stand separated from the boundary and from each other (according to these mechanisms, they should be connected to the incoherent twin boundary by a stacking fault). Another mechanism has been proposed more recently by Sasmal [34]). Noticing that plates do not form away from the boundary or on coherent twin boundaries if the samples are directly put at ageing temperature after the solution treatment, Sasmal suggested that the formation of plates of $M_{23}C_6$ close but detached from the incoherent twin boundaries, and on coherent ones, was an effect of residual stress developed in these regions. One could here argue that stress only influences the formation: if it favours the formation of $M_{23}C_6$ plates parallel to the twin boundaries, there should still be a small percentage of plates growing in other equivalent directions.

Intragranular precipitation In the austenite grains, $M_{23}C_6$ precipitates as cuboids or plates. The latter have the same characteristics as the plates growing from twin boundaries. The cuboids grow on dislocations until they form a continuous chain sharing their corner. These chains can form branches, forming secondary stringers of $M_{23}C_6$. Beckitt and Clarck [30] have proposed a satisfactory explanation for the formation of these secondary stringers: the growth of primary $M_{23}C_6$ generates dislocations on which further precipitation can occur. The direction of these secondary stringers is that expected by the mechanism, that is the direction of usual edge dislocations in austenite.

Another kind of intragranular precipitation has been reported by Sasmal [35]. Plates of $M_{23}C_6$ can form around undissolved Nb carbonitrides in Nb stabilised steels. In this case, the large faces are {110} and the edges are {111}. The reasons for this change are not clear, although a contribution of the strain around the undissolved particle is invoked.

iii Role of other alloying elements

$M_{23}C_6$ is, initially, a chromium-iron carbide. However, its composition is susceptible to large variations. For example, in a typical 2.25Cr1Mo wt% steel, $M_{23}C_6$ has a composition of about 0.3Fe, 0.38Cr, 0.1Mo, 0.22C mole fraction (calculated with MT-DATA), while in a typical 304 it is closer to 0.04Fe, 0.65Cr, 0.11Mo, 0.22C. There is also evidence that, for a given steel composition, $M_{23}C_6$ composition undergoes large changes in the early stages of the precipitation. Lewis and Hattersley [31] quote a study by Philibert *et al.* in which the authors propose that M_7C_3 forms in the early stages of ageing in a 18/8 steel, as the Fe/Cr ratio is more consistent with the known composition of this phase. Similarly, Marshall [5] quotes a study in which the authors show that up to 40 wt% Fe can be found in $M_{23}C_6$ in the early stages of precipitation, and that the Mo content also increases with time. It is proposed here that these composition changes can be explained by the growth mechanism involved. In a multicomponent alloy, the interface has to move at a rate which is consistent with the flux of each element, in order to maintain local equilibrium. Therefore, the interfacial compositions are not in general given by a tie-line passing through the bulk composition, but by an alternative tie-line which permits the flux-balance (details are out of the scope of this review, see for example [36] or [37]).

In the same way, on the interstitial lattice, B can substitute for C; however in very small quantities. Boron is of particular interest as it promotes the formation of intragranular $M_{23}(C,B)_6$. There is some controversy about the mechanism involved, but it is possible

that B increases the lattice parameter of $M_{23}C_6$, therefore reducing the mismatch with the austenite. The presence of B in $M_{23}C_6$ has been shown using atom probe field ion microscopy (APFIM, e.g. [38]). The same is not true for nitrogen. It has long been believed to have a small solubility in $M_{23}C_6$ (e.g. [39]). However, recent experimental results supported by *ab initio* calculations indicate zero solubility of nitrogen in $M_{23}C_6$, the structure of which is destabilised if a small amount of carbon is replaced by nitrogen [10].

Except in the fine intragranular form, $M_{23}C_6$ precipitation is not desirable for good creep properties. It is often associated with intergranular corrosion, as its formation along the grain boundaries causes a local depletion in chromium and possibly local loss of the stainless property (the steel is then said to be sensitised, *i.e.* susceptible to intergranular corrosion).

iv Solubility and kinetics of precipitation

The solubility of carbon in austenite, with regard to $M_{23}C_6$, has been described by empirical relationships such as [40]:

$$\log [\mathrm{C}]_{\mathrm{ppm}} = 7.71 - \frac{6272}{T(\mathrm{K})}$$

As can be seen in figure 2.4, this is valid for a typical 18/12 steel, but one should be careful as it is sensibly modified by the chromium and nickel content. Increasing the chromium content reduces the solubility of carbon in austenite. It also increases the kinetics of $M_{23}C_6$ precipitation, as does an increase in carbon content: from 0.02 to 0.08C wt%, the nose of the C-curve is shifted from 100 h to 0.1 h.

$M_{23}C_6$ first precipitates on grain boundaries, then, with increasing time, on incoherent twin boundaries, coherent twin boundaries and finally in the matrix on dislocations. In the matrix, it forms as evenly spaced angular blocks. At long ageing times, grain boundary carbides can form a completely interlocked structure.

The kinetics of precipitation are affected by Mo, which stabilises the carbide and accelerates its formation. On the other hand, nitrogen is well-known to retard both the formation and coarsening rates of $M_{23}C_6$, and an often proposed explanation is that nitrogen reduces the diffusivity of Cr and C in the austenite [6], [12]. However, Degalaix and Foct [41] found that if the carbon content was higher than 0.08 wt%, increasing the nitrogen content could have the opposite effect. More recent investigations indicate that

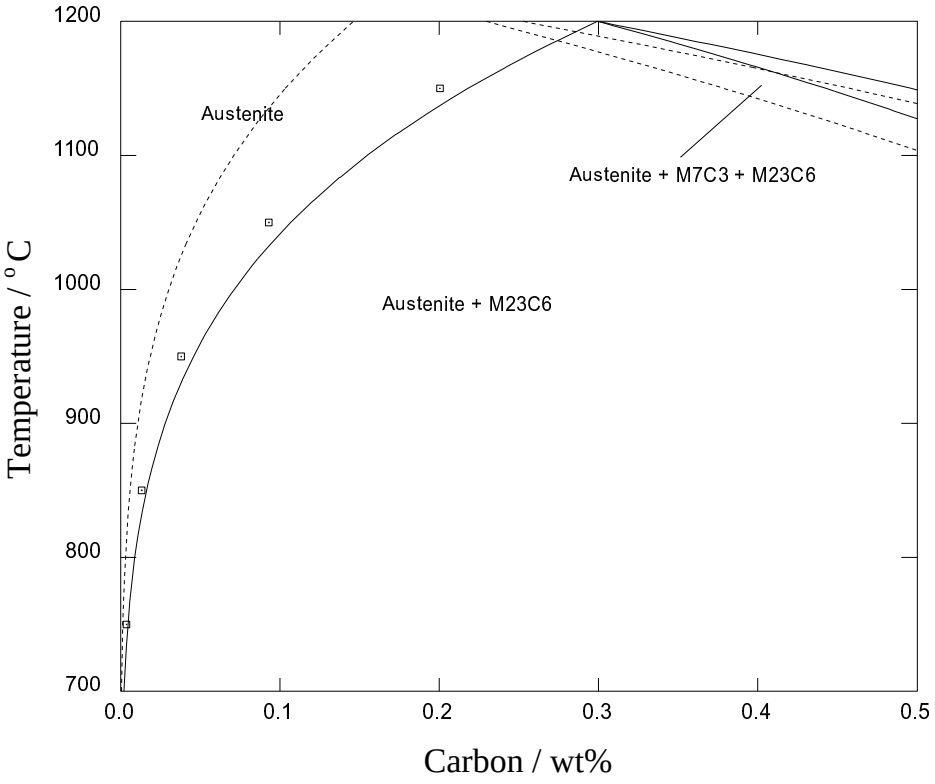

Figure 2.4: Solubility of C in austenite with regard to $M_{23}C_6$ precipitation. Calculated with MT-DATA (allowing for austenite, $M_{23}C_6$, M_7C_3 and liquid, with elements Fe, Cr, Ni, 0.3Si, 1.0Mn wt%). Solid lines for 18/12 and dashed lines for 20/25. The squares correspond to the empirical relationship from [40].

N actually enhances the diffusion of substitutional elements by increasing the formation of vacancies, but delays the nucleation of $M_{23}C_6$, the structure of which is destabilised when carbon is partially substituted by nitrogen [10].

v Relative stability of $\mathbf{M_{23}C_6}$

In a simple type 304 steel, $M_{23}C_6$ is often the only carbide found at any ageing time. Although sometimes M_6C is found [42], it is as a minor phase and no mention is made of an instability of $M_{23}C_6$ with regard to M_6C. When molybdenum is added (type 316), $M_{23}C_6$ can partially transform to M_6C (see further); it is however always reported that $M_{23}C_6$ remains the main carbide even after long ageing. In fact, $M_{23}C_6$ and M_6C also coexist in the X5CrNiMo1713 (17Cr, 13Cr, 5Mo wt%) studied by Thier *et al.* [43]. This is not the case when niobium is involved in the formation of M_6C, which seems then more

stable and becomes the dominant carbide at long ageing times [44].

In stabilised grades, the situation is much more complex: from the literature found, it is not possible to state clearly whether $M_{23}C_6$ is sometimes first formed or always follows MX precipitation, nor which phase is the more stable on long term ageing.

Thorvaldsson and Dunlop [27, 45, 46], studying the effect of different stabilising elements and their combinations, found that $M_{23}C_6$ was more stable than TiC, but less than NbC. This is consistent with Grot and Spruiell [47], who found formation of $M_{23}C_6$ in a type 321 after long term ageing, and with Kikuchi *et al.* [12] for a 20/25. These authors concluded that TiC retards the precipitation of $M_{23}C_6$ but does not suppress it.

On the other hand, Bentley and Leitnaker [48], studying a type 321 steel having been in service for 17 years at 600 °C did not find any $M_{23}C_6$ and concluded that TiC was more stable. Lai [49] observed no $M_{23}C_6$ in a type 321 used up to rupture (16000-29000 h at 600 °C).

Obviously, considerations of the relative stabilities of the two phases only make sense if the titanium content is enough to combine all carbon present, as in the opposite case, $M_{23}C_6$ forms with the excess carbon. The studies in which $M_{23}C_6$ formation appears as an anomaly deal with steels in which Ti content is higher or equal than that required for full stabilisation.

The agreement is better for NbC, which is more stable than $M_{23}C_6$. However, $M_{23}C_6$ can form as a transient phase.

2.1.d M_6C

M_6C is also known as η-carbide, but will be referred to as M_6C to avoid confusion with η-phase (Laves phase). It generally refers to a phase of very variable composition. In most cases, it is formed only after long ageing times, and therefore is quite little documented. Moreover, its appearance and disappearance are strongly linked to that of other constituents and it is difficult to give it any absolute position in a TTP (Time Temperature Precipitation) diagram.

i Structure and composition

M_6C is a diamond-type fcc carbide whose lattice parameter varies between 10.95 and 11.28 Å. Its space group is Fd3m, which distinguishes it from $M_{23}C_6$ and G-phase which both are fcc of similar lattice parameters, but have a Fm3m space group. The η-carbide

structure is described by Stadelmaier [50]. This structure encompasses a wide range of compositions and only the ones which are commonly found in creep- resistant austenitic stainless steels will be reviewed here.

M_6C composition can be molybdenum-rich ($(FeCr)_{21}Mo_3C_6$) or niobium-rich (Fe_3Nb_3C). The molybdenum rich Fe_3Mo_3C (a=11.11 Å) was reported in high Mo steels, but never in austenitic steels [51]. Instead, a fraction of molybdenum is replaced by iron or chromium, and the lattice parameter is reduced (a=10.95 Å) [51]. The composition reported by Brun *et al.* [52] in a 316 steel containing Ti shows substantial amounts of Ni also dissolving in M_6C (see table 2.2).

Element	Si	Mo	Ti	Cr	Mn	Fe	Ni
at%	4.5	6.5	0.8	30	0.5	26.7	31

Table 2.2: Composition of M_6C as measured by Brun *et al.* in a 316 steel containing titanium.

Silicon has been reported to dissolve in this phase to form M_5SiC, but such a phase is very seldom found. Other elements which can be included in the general notation M are Ni, Ti, Co. In NF-709 (a 20/25 Nb stabilised, with 0.17N wt%), long-term ageing allows formation of Cr_3Ni_2SiC; such a composition has been reported by Williams *et al.* in a study of irradiated type 316 [53] and by Titchmarsh *et al.* in a similar steel [54], at rather low temperatures (466 °C) but not above 670 °C. Its formation in such steels is linked with the segregation effects caused by irradiation, in particular the Si segregation to point defect sinks. This particular composition has a lattice parameter of 10.62 Å (JCPDS 17-330), which makes it extremely similar to $M_{23}C_6$ from a structural point of view. Although always referred to as Cr_3Ni_2SiC, its actual composition includes substantial amounts of Mo and Fe (see table 2.3), the concentrations of which increase with temperature [53]. Williams [53] therefore proposed the more general formula $(Cr, Mo)_3(Ni, Fe)_2SiC$.

Temperature	Cr	Mo	Si	Ni	Fe
500 °C	35	11	20	24	10
600 °C	32	15	20	24	10

Table 2.3: Some compositions (at%) of Cr_3Ni_2SiC in irradiated 316, from [53].

Jargelius-Peterson [55] found a nitrogen rich similar phase (Cr_3Ni_2SiN) after furnace ageing of a 20Cr25Ni5Mo0.2N steel. It is reported after 5 h and 3000 h at 850 °C,

therefore being probably an equilibrium phase. In agreement with the observation that the Mo content increases with temperature, the composition found here includes as much as 25 wt% Mo (this is also due to the larger Mo content of the alloy).

ii Occurrence and stability

Mo rich compositions

In a type 316 steel, the composition of M_6C is close to $(FeCr)_{21}Mo_3C_6$. Weiss and Stickler [51] proposed that it is formed as follows:

$$M_{23}C_6 \longrightarrow (FeCr)_{21}Mo_3C_6 \longrightarrow M_6C$$

It is not reported by Minami *et al.* [44] after 10000 h at 750 °C (instead, χ-phase is found), neither by Lai and Meshkat [56] after 10000 h at 600 and 650 °C, nor by Barcik [57] for the same time, up to 900 °C. However, it was found by Stoter [58] in a specimen of 316 having been in service at 650 °C for 28000 and 60000 h, in very small amounts and always associated with $M_{23}C_6$.

Nitrogen seems to have a large influence on M_6C formation: Thier *et al.* [43] did not find this carbide after 1000 h in a type 316 with 0.037N wt%, but found it after only 1 h ageing at 900 °C when the nitrogen content was 0.069 wt%. Gavriljuk and Berns [10] suggest that the calculations performed by Jargelius-Petterson [59] raise controversy, as she shows that an increase of nitrogen in a 20Cr, 25Ni, 4.5Mo wt% steel reduces the driving force for M_6C. However, one must notice that M_6C is quite poorly described in the SGTE databases, as it only contains information about the Mo-rich carbide, that is to say it describes only one of the possible compositions of the η-structure. In this regard, it is possible to say that the η-structure is in both cases stabilised but with different compositions. In particular, Jargelius-Petterson [59] reports that M_5SiN is always present and favoured by high nitrogen contents. It seems therefore that nitrogen generally stabilises the η-structure, but the composition of this phase varies with the alloy.
In type 321 (Ti-stabilised), none of the studies found reports M_6C.

Nb-rich compositions

In type 347, on the contrary, the presence of Nb seems to promote the formation of a niobium rich M_6C. Care should be taken as Powell *et al.* [60] have given sensible arguments showing that G-phase and M_6C had often been mistaken. However, if the structures are very similar, the composition should differentiate clearly Fe_3Nb_3C or Cr_3Ni_2SiC (as

in NF709) from $Ni_{16}Nb_6Si_7$. The experimental methods must be linked with the results of the different studies. In general, Nb-rich M_6C seems to form only on long-term ageing. Kikuchi *et al.* [12] do not report it after 1000 h at 700 °C in a 20/25. In a 18/8 steel, it is reported between 600 and 800 °C by Minami *et al.* [44] at very long time (∼50000 h) for 600 °C but faster (∼2000 h) for 800 °C. They proposed a sequence illustrated in figure 2.5. This mechanism implies excess of Nb is present. If Nb is less than that required for

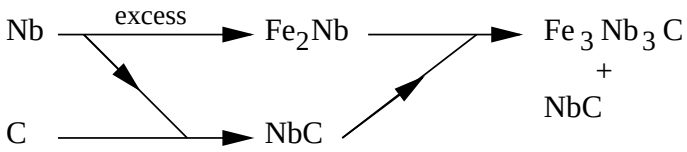

Figure 2.5: Precipitation sequence leading to M_6C when Nb is in excess, as proposed by Minami *et al.* in [61]

combination of all carbon, no such phase is observed (steel Tempaloy A1 in [44], similar to a 304 with 0.13Nb, 0.06Ti, 0.07C wt%)

In 20/25 alloys, as written above, M_6C and G-phase have probably been often mistaken (e.g. [62]) in early studies where identification relied on X-ray or electron diffraction only. It is difficult to conclude which phase forms preferentially: Ramaswamy *et al.* [63] report M_6C in a 20/25 with low Si content (0.03 wt%), but other studies report G-phase (Si content 0.4-0.7 wt%).

When nitrogen is present (in 347 or in 20/25) in sufficient quantities, Z-phase forms and it is difficult to have an idea of its stability with regard to M_6C.

Cr_3Ni_2SiX and G-Phase

G-phase, which is considered further, is an alternative Si-rich phase to Cr_3Ni_2SiC. As mentioned above, the composition Cr_3Ni_2SiC is very seldom reported in the literature. Titchmarsh and Williams have reported its formation in irradiated steels of composition close to that of 316 with addition of 1.8wt% Nb. They noted [54] and provided evidence [64] that G-phase formed preferentially only when carbon was not available.

In 20/25-Nb-C steels though, Powell *et al.* [60, 65], and Ecob *et al.* [66] have found G-phase and observed that NbC partially transforms to G-phase with time. It seems reasonable to propose that in 20/25, G-phase is stabilised with regard to Cr_3Ni_2SiC, probably because of the larger Ni content.

However, in NF709 [7] (composition in table 1.1), Cr_3Ni_2SiC is reported. This is inconsistent with the studies quoted above which seem to indicate G-phase as a more stable phase. It is not clear however whether the presence of carbon or nitrogen was investigated or the composition Cr_3Ni_2SiC assumed. Investigations of the exact nature of this precipitate are required to determine whether it is a nitride or a carbide. A nitride would be expected as it would not be incoherent with the former observations that G-phase is more stable than Cr_3Ni_2SiC and that the η-structure is stabilised by nitrogen.

2.2 Intermetallic phases

2.2.a Sigma phase

σ-phase is a well-known intermetallic phase which forms in the Fe-Cr system, with a composition FeCr. In highly alloyed steels, its composition is variable. Its precipitation is associated with embrittlement. In creep resistant steels, it has a detrimental effect on creep properties when precipitated on grain boundaries, but little effect when it precipitates intragranularly.

i Structure and Composition

σ-phase has a tetragonal unit cell (space group $P4_2/mnm$) with a=8.80 Å and c=4.54 Å (FeCr). This unit cell contains 30 atoms. Reported orientation relationships are [6]:

$$(111)_\gamma \parallel (001)_\sigma$$
$$\left(0\bar{1}1\right)_\gamma \parallel (140)_\sigma$$
or
$$(111)_\gamma \parallel (001)_\sigma$$
$$\left(\bar{1}10\right)_\gamma \parallel \left(\bar{1}10\right)_\sigma$$

The composition varies quite widely and it is difficult to give a formula. For example, Jargelius-Petterson [59] reports the following range of composition for σ-phase in a 20/25 with Mo content varying between 4.5 and 6.0 wt%:

Element	Si	Cr	Mn	Fe	Ni	Mo
wt%	0-1	27-32	1-9	35-43	8-15	10-16

for a type 316 [39], a typical composition is (other elements not given):

Element	Fe	Cr	Mo
wt%	44	29.2	8.3

ii Occurrence

An in-depth review of σ-phase precipitation in Cr-Ni austenitic steels has been done by Barcik [67]. σ-phase precipitates first on triple points then on grain faces. After long term ageing at high temperature, it also forms on incoherent twin boundaries and intragranular inclusions. The mechanism of nucleation is still a matter of controversy, particularly on the role of δ-ferrite and $M_{23}C_6$ in the nucleation process. Studies have reported its formation associated with the dissolution of $M_{23}C_6$, but also independently [6]. It is found in most of the grades of austenitic stainless steels: type 304, 316 (Mo), 321 (Ti stabilised) and 347 (Nb stabilised) (e.g. [44]). However, it forms after different times. The 25Cr-20Ni steels can exhibit as much as 20 wt% of σ-phase.

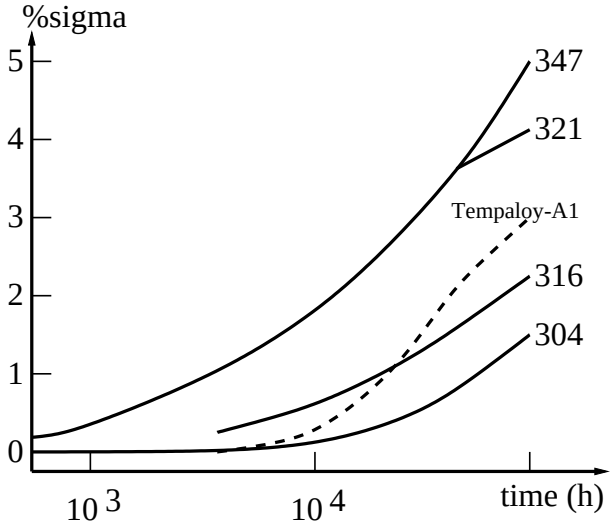

Figure 2.6: Precipitation of σ-phase in different grades of austenitic stainless steels. Tempaloy-A1 is an 18/10 with a Nb/C ratio of 1.86, whereas the 347 has a ratio of 17.40. The percentage is the area etched by KOH. After [44].

In stabilised grades, its formation is faster than in other grades: Minami *et al.* [44] report precipitation of σ-phase after 1000 h at 700 °C in 347 and 321 (347 precipitating σ-phase slightly faster than 321). In 304, 316 and Tempaloy-A1, σ-phase is found in significant quantities only after 10000 h (fig 2.6). It is worth noting that Tempaloy-A1 is Nb stabilised, but with a Nb/C ratio of 1.86, while this ratio is 17.40 in the 347. This

correlates well with the fact that σ-phase forms when the carbon content falls below a critical value and the chromium equivalent is higher than 18 wt%. In the 347 steel, almost all the carbon is rapidly precipitated as NbC, while the low Nb content of Tempaloy-A1 leaves some carbon in solution. The different trend for 321 could be linked to the instability of TiC with regard to $M_{23}C_6$. The precipitation of $M_{23}C_6$ lowers both the carbon and the chromium content. The results of Grot and Spruiell [47] show on the contrary no σ-phase forming up to 2000 h in a type 321. σ-phase is also found in 20/25 (fig 2.7). Different factors affect the formation of σ-phase. Elements like Cr, Nb, Ti or Mo are known to promote σ-phase formation. Silicon promotes and accelerates its formation. In general, the formation of σ-phase in austenite is about 100 times slower than in ferrite. Consequently, the presence of δ-ferrite accelerates σ-phase precipitation. [67]

A method has been developed by Woodyatt *et al.* [6] to estimate the σ-forming tendency of an alloy, based on the electron vacancy number $\overline{N}_v$:

$$\begin{aligned}\overline{N}_v &= 0.66\mathrm{Ni} + 1.71\mathrm{Co} + 2.66\mathrm{Fe} + 4.66(\mathrm{Cr} + \mathrm{Mo} + \mathrm{W}) \\ &\quad +5.66\mathrm{V} + 6.66\mathrm{Zr} + 10.66\mathrm{Nb} \quad \text{at\%}\end{aligned}$$

If $\overline{N}_v$ is higher than 2.52, the alloy should form σ-phase.

2.2.b Laves phase

Laves phase is found in various grades of austenitic stainless steels. It is often a minor constituent. It precipitates intragranularly in the form of equiaxed particles, occasionally on grain boundaries [51]. Whether Laves phase has a detrimental effect or not on creep properties is still discussed. In niobium stabilised steels however, it is likely that Laves phase are detrimental because they allow formation of M_6C (see below).

i Structure and composition

Laves phase is a hexagonal phase of space group $P6_3/mmc$, with a=4.73 Å and c=7.72 Å. The main factor determining its formation being the relative atomic size of the constituent atoms, the ranges of composition are quite small. Jargelius-Petterson [59] measured the following composition for Laves phase in a 20/25 with 5Mo wt%:

After 10 min at 850 °C						
Element	Fe	Mo	Cr	Ni	Mn	Si
wt%	29 ± 2	36 ± 2	19 ± 2	13 ± 1	1.5 ± 0.8	1.8 ± 0.5
After 3000 h at 850 °C						
wt%	37 ± 1	35 ± 1	12 ± 1	14 ± 1	~ 0	0.7 ± 0.2

This shows that Laves phase probably does not form at its exact equilibrium composition. In stabilised grades, Fe_2Nb or Fe_2Ti (more seldom) can form.

Denham *et al.* [68] proposed for Fe_2Nb the following orientation relationships:

$$(0001)_{Fe_2Nb} \parallel (111)_\gamma$$
$$(10\bar{1}0)_{Fe_2Nb} \parallel (\bar{1}10)_\gamma$$

ii Occurrence

In type 304, Laves phase is not found, due to the absence of Mo, Nb or Ti. In type 316, which contains typically 2-2.5Mo wt%, it is found after relatively long ageing times: Minami *et al.* [44] report its formation after a minimum of 1000 h, between 625 and 800 °C. The experimental results of Lai [69] are in agreement with the dissolution of Fe_2Mo above 800 °C. Coherently, White and Le May [70] do not report any Laves phase precipitation between 640 and 800 °C for ageing times up to 900 h. Weiss and Stickler [51] report a slightly higher maximum temperature for Laves precipitation in type 316 as they found it up to 815 °C. Its formation interacts in a competitive way with that of σ and χ phases. For example, the presence of δ-ferrite delays its formation because it enhances that of σ and χ phases.

In titanium stabilised grades, the formation of Fe_2Ti is never reported in compositions similar to that of a 321 steel. Minami *et al.* do not report it for ageing times up to 50000 h between 600 and 750 °C, in a type 321. However, it is found by Beattie and Hagel [71] in a A286 type alloy, containing 16Cr, 26Ni and 1.8Ti wt%, after 1000 h at 815 °C. This is directly related to the large amount of Ti used in such steels compared to a typical 321.

In niobium stabilised steels, Fe_2Nb is frequently reported after long ageing times, but as a transient phase which disappears for Fe_3Nb_3C. It is reported to form in a type 347 with 0.87Nb and 0.05C wt%, after 1000 h between 650 and 800 °C, and disappear after 5000-10000 h [44]. However, its formation is dependent on the availability of niobium. In the same study, the steel Tempaloy-A1 (18/10 with 0.13Nb for 0.07C wt%) does not

precipitate Laves phase after ageing treatments up to 25000 h. Instead, only NbC is found (figure 2.5). The same results are reported by Raghavan *et al.* [24], who found NbC and Laves phase in a type 347 with 0.8Nb and 0.07C wt% (8000 h at ~600 °C), but only Z-phase in a modified 347 with 0.3Nb and 0.09N wt%. It is therefore probable that both NbC and Z-phase are more stable than Fe_2Nb.

2.2.c χ phase

χ phase is most of the time a minor intermetallic phase. It is mainly found in type 316 above 750 °C

i Structure and composition

χ phase is a bcc (body-centred cubic) phase of space group $I1\bar{4}3m$. The unit cell contains 58 atoms and has a lattice parameter varying between 8.807 and 8.878 Å.

A typical composition is $Fe_{36}Cr_{12}Mo_{10}$ but the phase has a high tolerance for metal interchanges. The structure has large holes which allow presence of carbon, sometimes making this phase better described as a $M_{18}C$ carbide. It nucleates on grain boundaries, incoherent twin boundaries but also intragranularly on dislocations.

ii Occurrence

Although it is sometimes (but seldom) present in very small quantities in 321 [47], χ phase is only a significant phase in type 316, when the ageing temperature is high enough. For example, it is reported by Minami *et al.* for times up to 25000 h and temperatures between 700 and 850 °C, and by Lai *et al.*, as being the main phase with σ-phase between 715-850 °C for times up to 5000 h, but not by Stoter [58] after 28000 and 60000 h at 650 °C.

2.2.d G-phase

G-phase is a silicide forming in austenitic stainless steels stabilised with Ti or Nb. It has been first reported by Beattie and Versnyder in 1956, in a A286 type steel, that is, a precipitation-hardening 26Ni-15Cr with variable (0 to 2.3wt %) Ti and Al contents. It has long been believed to form only under irradiation in steels of the 300 series and in 20/25 steels. However, Powell *et al.* showed, in 1985 [60] that it formed under normal ageing in 20/25 Nb stabilised alloys, in the temperature range 500-850 °C, and suggested that it had been identified as M_6C in earlier studies of the same steel.

i Structure and composition

G-phase has a general formula $A_{16}D_6C_7$ where A and D are transition elements, and C a group IV element [66]. A is usually nickel, D niobium [60, 65, 66] or titanium [49]. Ecob *et al.* [66] mentioned the possibility of substitution, in small quantities, of D (*ie* Nb or Ti) by Fe or Cr, and Powell *et al.* [60] measured the following composition:

Element	Ni	Nb	Si	Fe	Cr
wt%	51	29	14	4.5	1.5

Table 2.4: Composition of G-phase measured in [60]

Lai found a titanium-containing G-phase in a type 321 steel, and gives a composition sensibly richer in nickel (table 2.5). Note that none of these compositions clearly shows

Element	Ni	Ti	Si	Fe	Cr
wt%	63.3	20.9	12.2	3.47	0.13

Table 2.5: Composition of G-phase measured in [49]

substitution of D when trying to match the stoichiometric formula.

G-phase has a fcc structure with a lattice parameter of 11.2 Å, this corresponds to a content of 116 atoms per unit cell. The space group for this structure is Fm3m. It is remarkable that the lattice parameter seems to be the same for $Ni_{16}Nb_6Si_7$ [60, 65] and $Ni_{16}Ti_6Si_7$ [49, 71]. In a earlier study, Sumerling *et al.* [62], studying a 20/25 Nb stabilised steel, found a lattice parameter of 11.25 ± 0.05 Å for a phase they identified as M_6C.

As mentioned before, Powell *et al.* have suggested that G-phase was identified as M_6C in early works on 20/25 Nb steels, because of close compositions and structures. A detailed investigation of the structure is sufficient to solve the problem [66], but additional evidence has been sought by the use of EELS (Electron Energy Loss Spectroscopy) (as in [60]) or a wavelength-dispersive crystal spectrometer in SEM (as in [49]), both techniques making possible quantitative measurements of light elements (C,N). These studies have confirmed the absence of interstitial elements in G-phase.

ii Occurrence of G-phase in austenitic stainless steels

The general features of G-phase formation are:

1. It forms very predominantly on grain-boundaries (from where its name).

2. It is now clear that it forms in 20/25 Nb stabilised steels and to an extent which depends on the Si content.

3. It has also been reported in a type 321 steel, but other results are contradictory.

Ti-rich G-phase

In one of the first studies on G-phase [71], the Ti-rich G-phase is reported in a A286 type steel. It is not clear in what conditions of temperature and time it forms, as it was often found to resist the solution-treatment. However, G-phase was not found in the alloy containing only 0.01Si wt%, but formed at higher contents, and the volume fraction increased with the Si content. Adding 2 wt% of Al suppressed the formation of G-phase. This work also included a steel in which the Ti content is more similar to that used in the 300 series, and no G-phase was found.

The only report found of Ti rich G-phase in type 321 has been quoted above [49]. Three out of seven type 321 steels show G-phase after 16000h and 50000h at 600 °C. The common factors between the three type 321 steels which are found to form Ti rich G-phase in this study are their small grain sizes and an excess of Ti with regard to the amount of carbon present. However, in similar conditions, other studies [44, 48]) do not report G-phase.

Nb-rich G-phase

In 20/25-Nb-C stabilised steels, it is now clear that G-phase can form [60, 65, 66] and, following the suggestion of Powell *et al.* [60], the works of Sumerling *et al.* [62] and Dewey *et al.* [72] may be regarded as other evidence for G-phase formation if one accepts that M_6C must be read as G-phase. In [62], in particular, the authors measured a lattice parameter of 11.25 ± 0.05 Å which is much closer to the G-phase parameter.

Powell *et al.* summarised their work in a TTP (Time Temperature Precipitation) diagram shown in figure 2.7. In their alloy (0.68Nb, 0.037C, 0.61Si wt%), G-phase forms between 500 and 850 °C, first on residual grain boundary particles of NbC, and only after very long ageing on NbC particles in the matrix. The authors propose that this is due to the easier diffusion of required elements in the grain boundaries.

Ecob *et al.* [66], comparing the occurrence of G-phase in similar 20/25-Nb stabilised steels, noticed that alloys apparently similar in composition exhibited different relative

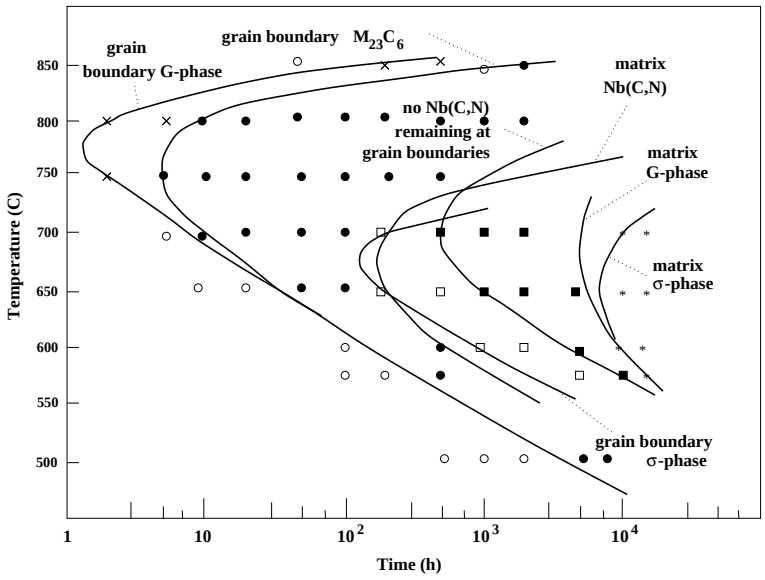

Figure 2.7: TTP diagram from Powell *et al.* [60].

stabilities of NbC with regard to G-phase. They found that an increase in the oxygen content led to a greater instability of NbC with regard to G-phase, and proposed that oxygen and silicon are involved in a co-segregation process, a greater amount of oxygen segregating around NbC leading to a greater segregation of Si in the same way. The silicon rich region is more favourable to G-phase formation.

In 20/25-Nb-N steels however, as it has been discussed in the section regarding M_6C, it seems that Cr_3Ni_2SiN forms preferentially to G-phase. No results could be found that support this hypothesis.

In common 18/12-Nb steels, G-phase seems to be found only under irradiation [54, 53]. Increasing the Si content to 6 wt% resulted in the formation during furnace ageing of Nb G-phase, although provided that carbon was not available to form Cr_3Ni_2SiC. However, no study has been found which reports niobium G-phase in ordinary 18/12 steels.

2.2.e Ni_3Ti and related precipitates

Precipitates such as Ni_3Ti, $Ni_3(Ti, Al)$, are only found in a particular class of austenitic stainless steels: the precipitation hardening ones. A typical steel in this category is A286, a 15Cr-25Ni-Al-Ti steel. They contain titanium and aluminium in quantities substantially larger than the 300 series and related compositions, to form γ' or other Ni, Ti, Al precipitates, as summarised in figure 2.8. However, there are very few studies in which

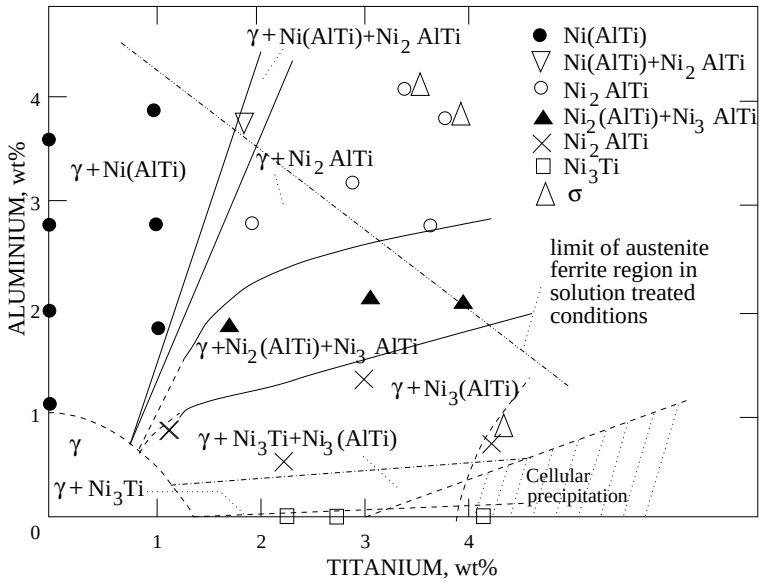

Figure 2.8: Effect of aluminium and titanium on the equilibrium phases present at 800 °C in 15Cr-25Ni austenitic steels, from [73].

the creep properties of these steels are given attention, and long term information is not available (e.g. [74]). For this reason and because the precipitation in these steels has been reviewed in [75], [73], it has been decided not to cover in depth these precipitates. These are [75]:

- γ' is a fcc Ni_3Al or $Ni_3(Ti, Al)$ intermetallic compound of lattice parameter 3.60 Å. It is also the transient structure of Ni_3Ti.
- η is hexagonal (a=5.09 Å c=8.32 Å) and is the equilibrium structure of Ni_3Ti.
- β is NiAl, formed at lower temperatures (up to 700 °C) and short ageing times (10-100h).

2.3 Other precipitates

Attention has been concentrated on precipitates most often reported and studied in creep resistant austenitic stainless steels. However, other phases are sometimes reported depending on the alloying elements.

2.3.a Cr_2N

It forms in non-stabilised austenitic stainless steels with high nitrogen (0.2 wt% at 900 °C with 20Ni wt%) [41]. It has a hcp (hexagonal close-packed) unit cell of lattice parameters a=4.78 Å and c=4.44 Å [6]. Although a major precipitate in high-nitrogen non-stabilised steels, it is not in either nitrogen-bearing non-stabilised creep-resistant austenitic stainless steels because of the lower N content used, or in stabilised nitrogen bearing grades, because Z-phase seems to form preferentially. A detailed review of **Cr_2N** can be found in [10].

2.3.b Pi-nitride

It is reported by Jargelius-Petterson [55, 59] to form in a non-stabilised 20/25 steel with 0.21N wt%. The composition after 10 min at 850 °C is:

Element	Si	Mn	Cr	Ni	Mo	Fe
wt%	1.0 ± 0.2	1.1 ± 0.3	47 ± 1	20± 1	13 ± 1	19 ± 1

It has a cubic structure of lattice parameter a=6.3 Å [55].

2.3.c Titanium carbosulphides

The titanium carbosulphide $Ti_4C_2S_2$ is reported by Lai [49] in different type 321 steels aged at ~600 °C for times between 16000 and 53000 h, and by Minami *et al.* [44] in a similar steel; they clarify that this phase is already present in the solution-treated condition. It has a hcp structure of lattice parameter a=3.21 Å and c=11.12 Å.

2.3.d Copper precipitates

Few data are available concerning the effect of copper in creep resistant austenitic stainless steels. Tohyama *et al.* [76] used 3 wt% copper in Tempaloy-A1, a steel similar to 347, with addition of a small amount of titanium. This results in precipitation of a copper-rich phase, independently of the precipitation of other precipitates. The creep rupture strength is significantly increased in comparison to the original composition.

2.3.e Chromium phosphides

The chromium phospide Cr_3P has been reported by Rowcliffe *et al.* [77], in a 18/10 steel with 0.3 wt% P. It has a tetragonal unit cell with a=9.186 Å and c=4.558 Å.

2.4 Concluding Remarks

An attempt has been here made to review the characteristics of the main precipitates found in austenitic stainless steels. Whereas the early stages of precipitation are quite well understood in the usual grades of austenitic steels, this is far from the case for the new generations of nitrogen-bearing stabilised austenitic steels. There is a lack of knowledge about the phases which precipitate during long-term ageing, particularly with respect to thermodynamic data.

Z-phase, which plays an essential role in recent creep-resistant austenitic or ferritic stainless steels, is not present in the SGTE databases commonly used with thermodynamic calculation packages such as MT-DATA or ThermoCalc. The kinetics of its formation are also rather obscure.

In discussing the stability of M_6C, there is some confusion which arises from the fact that this phase is most often referred to as one particular composition of the η-structure rather than the η-structure itself. Similarly, thermodynamic data are only available for the Mo-rich pole of the η-structure. Other important compositions which are not present in the SGTE databases include Fe_3Nb_3C and Cr_3Ni_2SiX.

The formation of MX precipitates is well documented, but again, thermodynamic data are missing to model the solubility of Cr, which is likely to be important in the kinetics of precipitation. An assessment of the Cr-Nb-N system could help improving the description of NbX precipitates, and would also provide thermodynamic data for Z-phase.

Precipitate	Structure	Parameter (Å)	Composition
NbC	fcc	a=4.47	NbC
NbN	fcc	a=4.40	NbN
TiC	fcc	a=4.33	TiC
TiN	fcc	a=4.24	TiN
Z-phase	tetragonal	a=3.037 c=7.391	CrNbN
$M_{23}C_6$	fcc	a=10.57-10.68	$Cr_{16}Fe_5Mo_2C$ (e.g.)
M_6C	diamond cubic	a=10.62-11.28	$(FeCr)_{21}Mo_3C$; Fe_3Nb_3C; M_5SiC
Sigma	tetragonal	a=8.80 c=4.54	Fe,Ni,Cr,Mo
Laves phase	hexagonal	a=4.73 c=7.72	Fe_2Mo, Fe_2Nb
χ-phase	bcc	a=8.807-8.878	$Fe_{36}Cr_{12}Mo_{10}$
G-phase	fcc	a=11.2	$Ni_{16}Nb_6Si_7$, $Ni_{16}Ti_6Si_7$

Table 2.6: Crystal structure and composition of the main precipitates in austenitic stainless steels

Chapter 3

Modelling precipitation reactions in steels

The formation of an individual particle involves its nucleation and growth. A good thermodynamic description of the phases involved is essential in order to model the kinetics of this reaction. For this reason, this chapter includes a presentation of the CALPHAD method on which are built the SGTE databases used in thermodynamic calculation software such as MT-DATA or ThermoCalc; it then introduces physical models for nucleation and growth. The overall precipitation process must also account for impingement effects. This can be dealt with using the theory for overall transformation kinetics as first expressed by Kolmogorov [78], Johnson and Mehl [79], and Avrami [80].

3.1 Thermodynamic models for solution and compound phases

The use of phase-diagrams has, for long, been seen as being rather academic, because most real materials are multicomponent in nature, while phase diagrams are generally used to represent binary or ternary systems.

The CALPHAD (CALculation of PHAse Diagram) method has altered this viewpoint because it is now possible to predict the phase behaviour of complex, multicomponent systems, based on the extrapolation of thermodynamic properties. At the heart of this method is the calculation of the Gibbs energy of a phase as a function of its composition, temperature and pressure. Once this is possible, the problem of predicting an equilib-

rium is essentially mathematical, although far from simple given the number of variables involved in the minimisation process.

The models in use for the Gibbs energy vary with the nature of the phase considered. The following introduces the problem for pure substances, solutions and sublattice phases, which are the most commonly used in the field of metallurgy. The phases of interest in the present work fall into three categories: MX precipitates (TiN, NbN, *etc.*) are modelled as pure substances, complex carbides (e.g. $M_{23}C_6$, M_6C) and austenite are sublattice phases, while the liquid phase is a random substitutional solution.

The following is essentially based on references [81, 82, 83].

3.1.a Pure substances

For a stoichiometric compound, it is sufficient to know the heat capacity together with reference values to obtain the Gibbs energy at any temperature. The SGTE (Scientific Group Thermodata Europe) databases store the coefficients for the heat capacity at constant pressure, C_P, written as a polynomial of temperature:

$$C_P(T) = A + BT + CT^2 + DT^{-2} \tag{3.1}$$

together with values for $\Delta_f H$, the enthalpy of formation of the substance, and S_{298} the entropy at 298 K. The coefficients are valid only within a given range of temperature, and the database provides parameters as a function of temperature interval.

3.1.b Random substitutional solutions

In random substitutional solutions, such as gas, or simple metallic liquid and solid solutions, the components can mix on any spatial position available to the phase. The Gibbs energy of a solution is traditionally decomposed according to:

$$G = G^\circ + G^{ideal}_{mix} + G^{xs}_{mix} \tag{3.2}$$

where G° is the contribution of the pure components, G^{ideal}_{mix} the ideal mixing contribution and G^{xs}_{mix} the deviation from ideality also known as excess Gibbs energy of mixing.

i Ideal solutions

This is the simplest possible case. The interactions between the different elements are identical and there is no enthalpy change when the solution is formed. The only

contribution to the Gibbs energy change is due to the increase of configurational entropy. This term can be simply calculated using Stirling's approximation for large factorials.

$$\Delta S_{\text{random}} = -R \sum_i (x_i \ln x_i) \tag{3.3}$$

where x_i is the atomic fraction of component i and R the gas constant. The Gibbs energy per mole of solution is therefore:

$$G = \sum_i x_i G_i^\circ + RT \sum_i x_i \ln x_i \tag{3.4}$$

ii Regular and non-regular solutions

In most cases however, there are interactions between the components of a phase. In the case of a binary system AB, the regular model assumes the total energy of solution can be written :

$$E = N_{AA}\varepsilon_{AA} + N_{BB}\varepsilon_{AA} + N_{AA}N_{AB}\varepsilon_{AB} \tag{3.5}$$

where N_{AA} is the number of AA pairs, and ε_{AA} their bond energy, it can be shown that the enthalpy of mixing is:

$$\Delta H_{mix} = \frac{Nz}{2} x(1-x)\left(2\varepsilon_{AB} - \varepsilon_{AA} - \varepsilon_{BB}\right) \tag{3.6}$$

where N is the number of atoms in solution, and z the coordination number of the structure, that is the number of nearest neighbours of any atom.

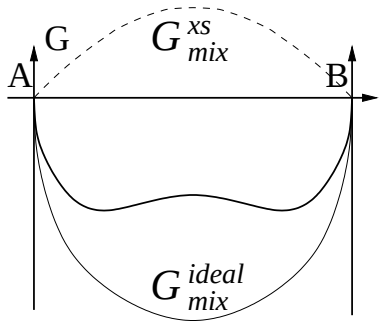

Figure 3.1: Modification introduced by the regular term: this diagram shows the Gibbs energy of mixing with its two contributions as a function of x. If $T < \omega/2R$, the curve has two points of inflection between which there is a miscibility gap; this is the case illustrated here.

For a regular solution, it is also assumed that the entropy of mixing is as given by equation 3.3 so that it does not contribute to the excess Gibbs energy of mixing , therefore G^{xs}_{mix} is:

$$G^{xs}_{mix} = \omega x(1-x) \tag{3.7}$$

where $\omega = Nz/2(2\varepsilon_{AB} - \varepsilon_{AA} - \varepsilon_{AA})$ is a temperature dependent parameter on which depends the behaviour of the solution (figure 3.1). Generalised to a multicomponent random solution, the Gibbs energy per mole is written:

$$G = \sum_i x_i G^\circ_i + RT \sum_i x_i \ln x_i + \sum_i \sum_{j>i} x_i x_j \omega_{ij} \tag{3.8}$$

However, this assumes interactions to be composition independent, which is not realistic in most cases. The sub-regular model, proposed by Kaufman and Berstein, introduces a linear composition dependency and expresses the excess Gibbs energy of mixing as:

$$G^{xs}_{mix} = \sum_i \sum_{j>i} x_i x_j (\omega^i_{ij} x_i + \omega^j_{ij} x_j) \tag{3.9}$$

This is generalised to any composition dependency in the Redlich-Kister power series, which expresses G^{xs}_{mix} as:

$$G^{xs}_{mix} = \sum_i \sum_{j>i} x_i x_j \sum_v \omega^v_{ij} (x_i - x_j)^v \tag{3.10}$$

In the SGTE databases, the individual parameters ω are written:

$$\omega = A + BT + CT\ln T + DT^2 \tag{3.11}$$

and these coefficients are stored for each ω^v_{ij}.

3.1.c Sublattice models

The different expressions for G^{xs}_{mix} presented above are all for solutions where the components can mix freely on the sites available for the phase. In many cases, however, different components mix on different sublattices, as with austenite, where C, N, B mix on the interstitial sublattice, while Fe, Cr, Ni, *etc.* mix on the substitutional one. For a two-sublattice phase, with A and B on the first sublattice, C and D on the second, considering a regular solution, the excess Gibbs energy of mixing is written:

$$G^{xs}_{mix} = y^1_A y^1_B L^\circ_{A,B:*} + y^2_C y^2_D L^\circ_{*:C,D} \tag{3.12}$$

where $L^{\circ}_{A,B:*}$ and $L^{\circ}_{*:C,D}$ are regular solution parameters for mixing on the sublattices irrespective of site occupation of the other sublattice. The mole fractions (e.g. x_A) are now replaced by the occupied site fractions (y^1_A, where 1 denotes the first sublattice). A sub-regular model is introduced by making the interactions dependent on the site occupation of the other sublattice, as:

$$\begin{aligned} G^{xs}_{mix} &= y^1_A y^1_B y^2_C \, L^{\circ}_{A,B:C} + y^1_A y^1_B y^2_D \, L^{\circ}_{A,B:D} \\ &\quad + y^2_C y^2_D y^1_A \, L^{\circ}_{A:C,D} + y^2_C y^2_D y^1_B \, L^{\circ}_{B:C,D} \end{aligned} \tag{3.13}$$

The temperature dependency is obtained by writing the parameters $L^{\circ}_{A,B:C}$ as polynomials of T and $\ln T$, and it is the coefficients of these polynomials which are stored in the SGTE databases.

3.1.d The SGTE databases

The purpose of this section is to describe the limitations of the SGTE databases when dealing with systems such as NF709 (composition in table 1.1). These limitations can be classified in three categories:

- Absence of a phase: this is the case of Z-phase and G-phase for which no information is present in the database.
- Absence of an element within a phase, for example, Nb is not included in M_6C in the databases.
- Absence of parameters: an element can be allowed to enter a phase, but there is no information about its interactions with the other elements. For example, there is no parameter for Nb and N interactions in austenite. When this arises for two elements on a same sublattice, they are modelled as an ideal solution.

i Missing Phases

Two phases reported to form in austenitic stainless steels are not present in the SGTE databases. Z-phase, which forms in the early stages of precipitation in nitrogen-bearing stabilised austenitic stainless steels, and G-phase, which is sometimes reported in 20/25 niobium stabilised steels, after long-term ageing.

ii Missing Solubilities

For many phases, not all the elements which are known to dissolve in the phase are found in the database. In the following table, the substitutions reported in literature are reported, and the substitutions allowed by the SGTE are compared.

Phase	Elements reported in literature	Elements allowed by SGTE
$M_{23}C_6$	Cr Fe Mo C Mn Ni P B N	Cr Fe Mn Ni Mo C
M_6C	Fe Cr Mo Si Nb Ti Ni C N	Fe Cr Mo C
Sigma	Fe Cr Ni Mo Mn	Fe Cr Ni Mo Mn
Laves phase	Fe Ti Nb Mo	Fe Ti Nb Mo

iii Missing Parameters

There are more than 800 parameters missing for the description of all the phases able to form in a system corresponding to NF709. Although some have no importance because they describe phases which are not expected to form, it is difficult to judge of the consequences of most of them. In austenite, for example, most of the interaction parameters for boron with other elements are missing. However, boron may be present in very small quantities. A number of parameters are also missing for niobium and it is more difficult to estimate the consequences.

3.2 The classical theory for nucleation

In this section the main lines of the derivation of nucleation rate as calculated in classical theory are given, together with modifications for nucleation on dislocations, on grain boundaries and for non-spherical shapes.

3.2.a Nucleation rate in the classical theory

At any temperature above absolute zero, composition and structure fluctuations constantly occur in alloys as a result of thermal agitation. These fluctuations can lead to the formation of stable nuclei of a new phase.

In classical theory, the probability P of a fluctuation giving a nucleus leading to an increase of Gibbs energy ΔG is calculated according to the Boltzmann statistics:

$$P(\Delta G) = A \exp\left(\frac{-\Delta G}{RT}\right)$$

Although the nucleus is extremely small, macroscopic thermodynamical variables are used to give an expression for ΔG, because the rate is an average function. Considering the formation of a nucleus of θ in a matrix γ, r being the radius of the nucleus, the change in Gibbs energy is:

$$\Delta G = \frac{4\pi r^3}{3}\Delta G_v + 4\pi r^2 \sigma_{\gamma\theta} \tag{3.14}$$

where $\sigma_{\gamma\theta}$ is the interface energy per unit area between the two phases, and ΔG_v is the Gibbs energy change per unit volume of embryo.

The change in Gibbs energy shows two contributions which act in opposition. In this case, the Gibbs energy change decreases with increasing size only above a critical radius r_c. The critical radius and the activation energy G^* are, assuming a spherical nucleus and

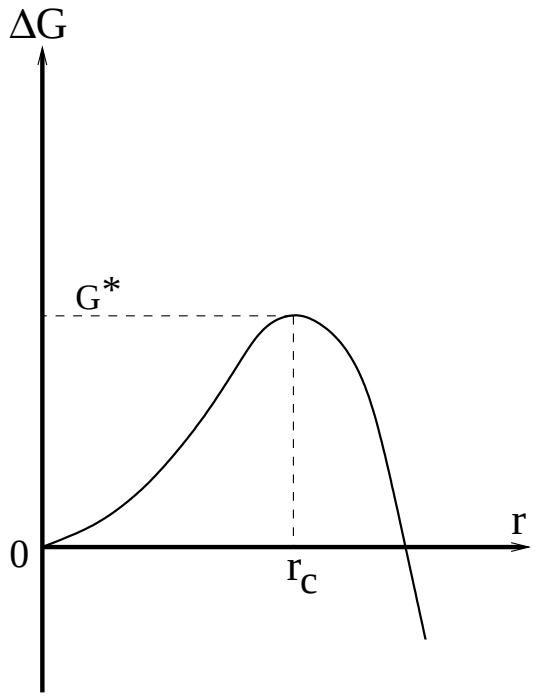

Figure 3.2: Schematic variation of the Gibbs energy change with the size of a nucleus in a supersaturated solution. After [84].

neglecting possible strain effects:

$$r_c = -\frac{2\sigma_{\gamma\theta}}{\Delta G_v} \quad \text{and} \quad G^* = \frac{16\pi}{3}\frac{{\sigma_{\gamma\theta}}^3}{{\Delta G_v}^2} \tag{3.15}$$

The nucleation rate is then derived by considering the frequency with which an atom adds

to a critical radius and makes it stable:

$$I = N \exp\left(-\frac{G^*}{RT}\right) \nu \exp\left(-\frac{G_t^*}{RT}\right) \tag{3.16}$$

where ν is an attempt frequency, often taken as being kT/h, N a number density of nucleation sites and G_t^* the activation energy for transfer of atoms across the $\gamma\theta$ interface.

3.2.b Heterogeneous nucleation

Homogeneous nucleation very seldom occurs in solid-state transformations. The presence of defects, with which is associated a given energy, provides sites for preferential nucleation. In austenitic stainless steels, MX carbides nucleate intragranularly on dislocations, and most of the other carbides occur on the austenite grain boundaries.

i Nucleation on dislocations

When a nucleus forms on a dislocation, the Gibbs energy change is not given by (3.14), as the strain energy field associated with the dislocation is locally suppressed [84]. The Gibbs energy change per unit length for a cylinder of radius r forming around the dislocation is:

$$\Delta G = \pi r^2 \Delta G_v + C_{12} - \frac{1}{2} Bb \ln(r) + 2\pi\sigma_{\gamma\theta} r \tag{3.17}$$

where b is the magnitude of the Burgers vector of the dislocation and B a term which depends on its nature (edge, screw or mixed). The solution for $\partial\Delta G/\partial r = 0$, if it exists, is given by:

$$r = \frac{\sigma_{\gamma\theta}}{2\Delta G_v}\left[1 \pm \left\{1 - \frac{\Delta G_v \; Bb^2}{\pi\sigma_{\gamma\theta}}\right\}^{1/2}\right] \tag{3.18}$$

The quantity $\alpha^D = \Delta G_v Bb/(\pi\sigma_{\gamma\theta}^2)$ determines the behaviour of the nucleus: if $\alpha^D > 1$, the energy decreases continuously as the radius increases. If $\alpha^D \leq 1$, there are two solutions and the activation energy G_d^* is the difference between the Gibbs free energy at the two extrema.

The nucleation rate in this case is a function of the dislocation density:

$$I = {N_v}^{1/3} l_d \frac{kT}{h} \exp\left(-\frac{G_d^* + G_t^*}{RT}\right) \tag{3.19}$$

where N_v is the number of atoms per unit volume and l_d is the length of dislocation per unit volume.

ii Grain boundary nucleation

Nucleation on grain boundaries is treated in a similar way: the formation of a nucleus is helped because it suppresses a high energy defect in the crystal. In this case, the

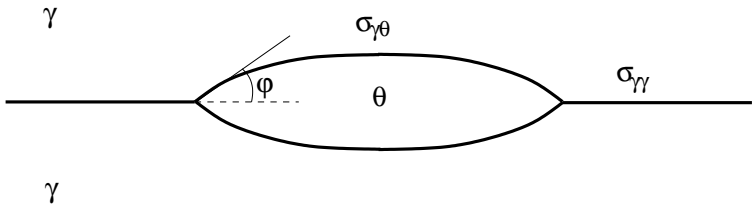

Figure 3.3: Nucleation on a grain-boundary as described by Clemm and Fisher. Adapted from [84].

activation energy is found to be:

$$G_B^* = \frac{4}{27}\frac{\{\eta_{\gamma\theta}\,\sigma_{\gamma\theta} - \eta_{\gamma\gamma}\,\sigma_{\gamma\gamma}\}^3}{\eta_\theta{}^2 \Delta G_v{}^2} \tag{3.20}$$

where $\sigma_{\gamma\gamma}$, $\sigma_{\gamma\theta}$ are the interfacial energies for the grain boundary and the interface precipitate-matrix respectively. $\eta_{\gamma\gamma}$, $\eta_{\gamma\theta}$ are shape factors which relate the area of the interfaces $\gamma\gamma$ and $\gamma\theta$ to the radius of the particle, while η_θ is a shape factor for the volume of the precipitate. In the case described by figure 3.3, they are:

$$\begin{aligned} \eta_\theta &= 2\pi\left(\frac{2 - 3\cos\theta + \cos^2\theta}{3}\right) \\ \eta_{\gamma\gamma} &= \pi \sin^2\theta \\ \eta_{\gamma\theta} &= 4\pi\,(1 - \cos\theta) \end{aligned} \tag{3.21}$$

Johnson *et al.* [85] derived expressions for the activation energy for faceted homogeneous nucleation and for various shapes of grain boundary nucleation. They showed that a change in shape left the critical radius unchanged, but modified the activation energy.

3.2.c The driving force for nucleation

The preceding sections show the need to know the chemical driving force for nucleation ΔG_v. The precipitation of θ in a matrix γ leads to a reduction of Gibbs energy, $\Delta G_\circ$ as illustrated in figure 3.4. The corresponding Gibbs energy change per unit of precipitate is given by $\Delta G_n = \Delta G_\circ / f$ where $f = (\overline{x} - x^{\gamma\theta})/(x^{\theta\gamma} - x^{\gamma\theta})$ is the fraction of precipitate, $\overline{x}$ being the bulk composition (mole fraction), $x^{\gamma\theta}$ the composition of the matrix

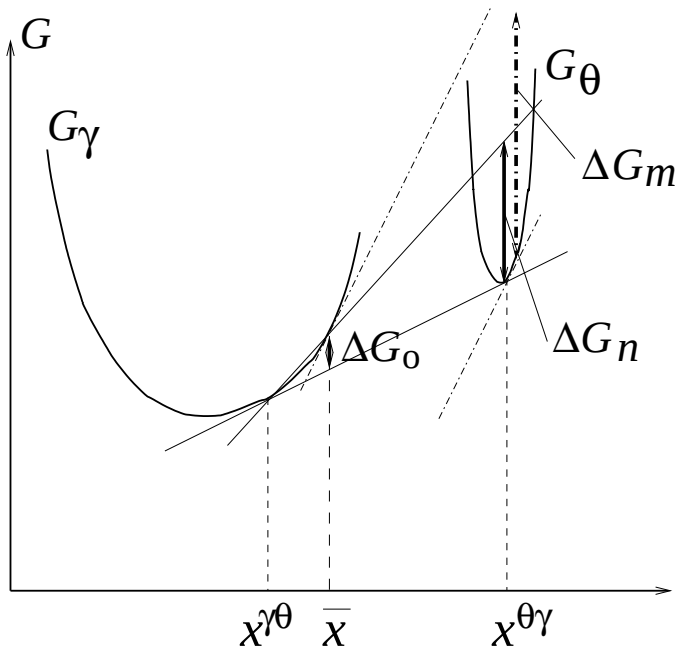

Figure 3.4: An illustration of the construction for finding the driving force for nucleation, $x^{\gamma\theta}$ is mole fraction of solute in the matrix in equilibrium with the precipitate, $\overline{x}$ the bulk mole fraction.

γ in equilibrium with the precipitate θ, and $x^{\theta\gamma}$ the composition of the precipitate θ in equilibrium with the matrix γ. However, the composition of the matrix hardly changes as a consequence of the nucleation, and ΔG_n does not represent correctly the Gibbs energy change during this phenomenon. Furthermore, the composition of the nucleus need not be that corresponding to equilibrium ($x^{\theta\gamma}$), since an alternative composition may lead to a larger Gibbs energy change. The composition that maximises the Gibbs energy change at the nucleation stage is given by the parallel tangent construction [86] as illustrated in figure 3.4. ΔG_m is therefore a better estimate of the driving force for nucleation.

3.3 The growth of precipitates

3.3.a Rate control

The velocity of the interface between matrix and precipitate depends on the mobilities of atoms in the matrix and is related to the atom transfer across the interface. The processes are in series. When the majority of free energy is dissipated in the diffusion of

solute ahead of the interface, the growth is said to be diffusion controlled. It is interface-controlled otherwise. Figure 3.5 illustrates the solute concentration profile in both cases. In the case of diffusion-controlled growth, the interface compositions are given by the

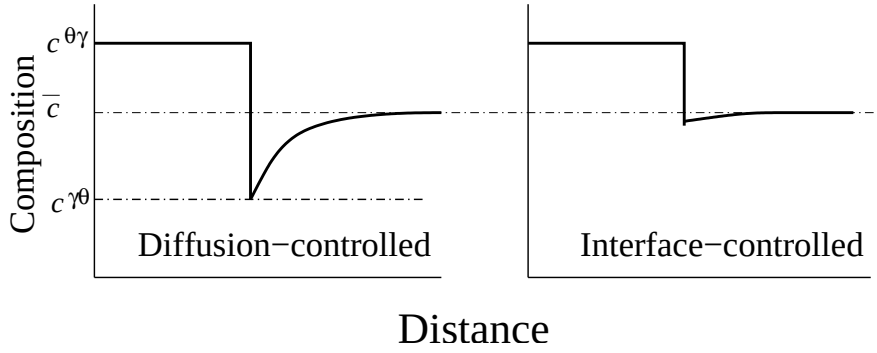

Figure 3.5: Schematic illustration of the solute concentration profile at the interface between the precipitate θ and the matrix γ. $c^{\gamma\theta}$ is the concentration of solute of the matrix in equilibrium with θ, $c^{\theta\gamma}$ that of the precipitate in equilibrium with γ, and $\overline{c}$ is the bulk concentration.

equilibrium phase diagram, as illustrated in figure 4.1.

The following describes, as an example, the Zener model for the growth of a planar interface with a constant far-field concentration ($\overline{c}$), in a binary system. More rigorous models and extension to multicomponent systems are discussed in chapter 4.

3.3.b Zener model for diffusion-control growth

The solute concentration profile at the interface is illustrated in figure 3.5. A simplification introduced by Zener assumes a linear gradient as illustrated in figure 3.6.

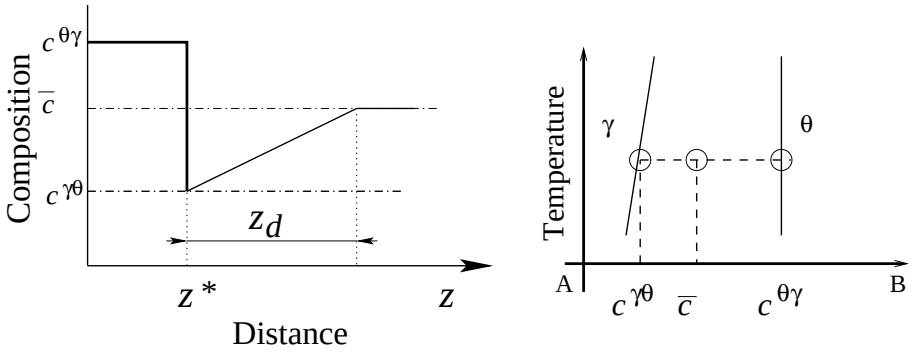

Figure 3.6: The constant concentration gradient approximation [87], and the binary phase diagram showing the composition at the interface $\gamma\theta$.

In this case, the flux of solute arriving at the interface is:

$$J_{z=z^*} = -D \left.\frac{\partial c}{\partial z}\right|_{z=z^*} = -D\frac{\overline{c} - c^{\gamma\theta}}{z_d} \tag{3.22}$$

where z^* is the position of the interface, D the diffusion coefficient of the solute in the matrix, and c the concentration of solute. This flux must equal the rate at which the solute is partitioned:

$$\psi(c^{\theta\gamma} - c^{\gamma\theta}) = |J_{z=z^*}| \tag{3.23}$$

where ψ is the growth rate. z_d can easily be estimated using the mass conservation:

$$\frac{1}{2} z_d(\overline{c} - c^{\gamma\theta}) = z^*(c^{\theta\gamma} - \overline{c}) \tag{3.24}$$

Introducing the dimensionless supersaturation $\Omega = (\overline{c} - c^{\gamma\theta})/(c^{\theta\gamma} - c^{\gamma\theta})$, and combining equations 3.22, 3.23 and 3.24, the velocity is given by:

$$\psi = \frac{\mathrm{d}z^*}{\mathrm{d}t} = \frac{D}{2}\,\Omega\,\frac{\overline{c} - c^{\gamma\theta}}{c^{\theta\gamma} - \overline{c}}\,\frac{1}{z^*} \tag{3.25}$$

Most of the times, it can be assumed that $(c^{\theta\gamma} - \overline{c}) \simeq (c^{\theta\gamma} - c^{\gamma\theta})$, then:

$$\psi = \frac{\mathrm{d}z^*}{\mathrm{d}t} = \frac{D}{2}\Omega^2\frac{1}{z^*} \tag{3.26}$$

Integration leads to:

$$z^* = \Omega\sqrt{Dt} \tag{3.27}$$

The precipitate size therefore varies with the square root of time, giving the classical parabolic law for one-dimensional growth in a binary system.

3.3.c Capillarity effects on the interface compositions

As explained above, in diffusion-controlled growth, the interface compositions are given by the equilibrium phase diagram. However, these diagrams are calculated assuming phases extending indefinitely, that is without surfaces. In the case of precipitation, this is not always a realistic approximation, and the influence of surface energy has to be accounted for.

When a small particle with a curved interface grows, the work done to increase the interface area is not negligible and results in a modification of the expected composition. This is known as the Gibbs-Thomson or *capillarity* effect [84].

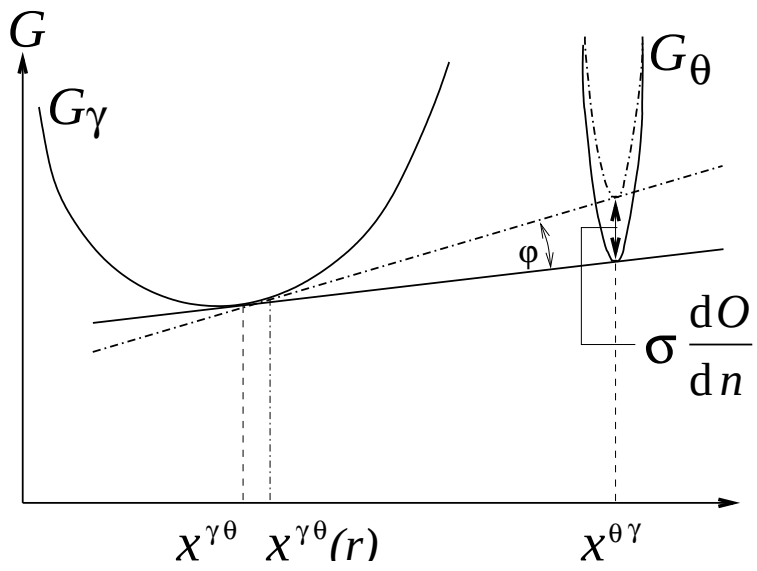

Figure 3.7: Schematic illustration of Gibbs energy and interface composition changes due to the capillarity effect in a binary system. This is a simplified case where the composition of the precipitate is assumed to be constant.

For a curved interface, the increase in Gibbs energy due to the expanding area is given by (figure 3.7), [84]:

$$G_\theta(r) - G_\theta = \sigma_{\theta\gamma}\frac{\mathrm{d}O}{\mathrm{d}n} \tag{3.28}$$

where $\sigma_{\theta\gamma}$ is the energy per unit area of the interface between the matrix and the precipitate, and $\mathrm{d}O/\mathrm{d}n$ is the increase of interface area when a mole of component is transfered to the precipitate.

For a spherical geometry, the term $\mathrm{d}O/\mathrm{d}n$ becomes $2V_m^\theta/r$ where V_m^θ is the molar volume of θ and r the radius of curvature. The calculation of the interface compositions change is given further attention in chapter 5.

3.4 Overall transformation kinetics

As mentioned before, to model multiple precipitation reactions, it is necessary to account for the impingement effects. There are two such effects: *soft-impingement* occurs because of the diffusion fields overlap, while *hard-impingement* is due to contact between the particles.

3.4.a Soft-impingement

In an overall model for precipitation, soft-impingement can be dealt with by using the mean field approximation, in which $\overline{c}$ is not a function of spatial coordinates. It is reduced in agreement with the amount of solute partitioned into the growing precipitates.

Although the validity of this approximation can be discussed when localised precipitation phenomena are dealt with, it is nevertheless extremely useful to avoid recurring to a model requiring spatial coordinates.

3.4.b Hard-impingement: the Avrami equation

We consider the precipitation of θ in a matrix γ, whose initial volume is V. The nucleation and isotropic growth rates, respectively I and ψ are known. The volume of a precipitate nucleated at time τ is, at time t:

$$w_\tau = C\psi^3(t-\tau)^3$$

where C is a shape factor, $4\pi/3$ if the precipitate is spherical.

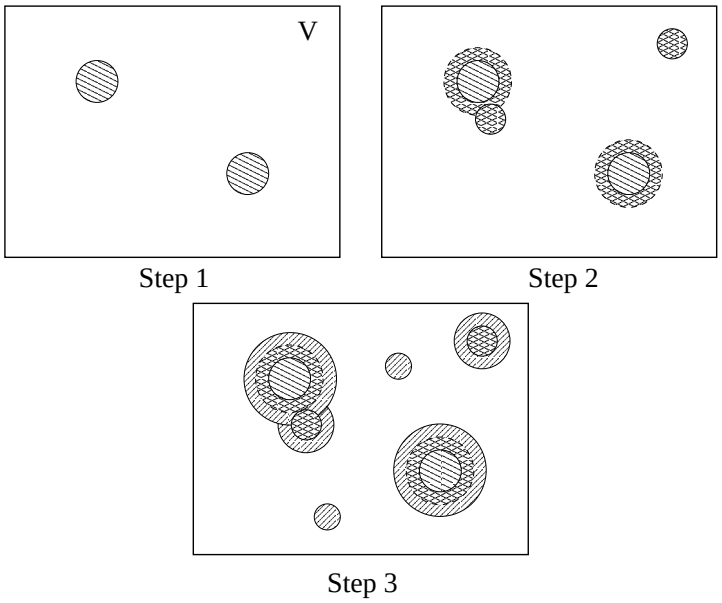

Figure 3.8: The different contributions to the extended volume.

The basic assumption at this stage of the derivation of Avrami's equation is that nucleation and growth occur both in the transformed and untransformed regions, although

it is clear that in reality, neither nucleation nor growth are possible in transformed regions. With this assumption, the number of particles nucleated between τ and $\tau + \mathrm{d}\tau$ is simply $IV\mathrm{d}\tau$, and therefore the contribution of these particles to the total volume of θ at time t is :

$$\mathrm{d}V_\theta^e = w_\tau IV\mathrm{d}\tau$$

The superscript e signifies that this is not a real volume, but an extended volume, because of the assumption made above. The total extended volume is simply the sum of all contributions from particles nucleated between 0 and t:

$$V_\theta^e = \int_{\tau=0}^{t} w_\tau IV\mathrm{d}\tau$$

The change in real volume can be derived by writing:

$$\mathrm{d}V_\theta = \left(1 - \frac{V_\theta}{V}\right)\ \mathrm{d}V_\theta^e$$

i.e. the change in real volume is the proportion of the change in extended volume which occurred in the untransformed volume. Assuming I and ψ to be independent of time, an analytical solution for the volume fraction of θ is immediately derived:

$$V_f(\theta) = 1 - \exp\left(-\frac{CI\psi^3 t^4}{4}\right)$$

3.4.c Modification for simultaneous reactions

Obviously, the Avrami equation as introduced above is only able to deal with a single reaction, or a succession of independent reactions. This is not satisfying for the description of multiple precipitation reactions which clearly interact with each other, by competing for solute and nucleation sites. Robson and Bhadeshia [88] proposed a modification of this equation as follows.

If two phases θ and γ can form from a volume V of γ with different growth and nucleation rates, we still can write the contribution of the ones nucleated between τ and $\tau + \mathrm{d}\tau$ as:

$$\begin{aligned} \mathrm{d}V_\theta^e &= C\psi_\theta^3 I_\theta V(t-\tau)^3\mathrm{d}\tau \\ \mathrm{d}V_\gamma^e &= C\psi_\gamma^3 I_\gamma V(t-\tau)^3\mathrm{d}\tau \end{aligned} \qquad (3.29)$$

but when correcting for the extended volume:

$$\mathrm{d}V_\theta = \left(1 - \frac{V_\theta + V_\gamma}{V}\right) \mathrm{d}V_\theta^e$$
$$\mathrm{d}V_\gamma = \left(1 - \frac{V_\theta + V_\gamma}{V}\right) \mathrm{d}V_\gamma^e$$

The extension to multiple reactions is immediate:

$$\mathrm{d}V_j = \left(1 - \frac{\sum_i V_i}{V}\right) \mathrm{d}V_j^e \tag{3.30}$$

However, such systems have no general analytical solution if no relationship is assumed between the parameters of the two phases (nucleation and growth rates).

3.5 Summary

The CALPHAD method, which is at the heart of the prediction of the phase behaviour of complex systems, has been presented briefly, together with the format of the SGTE databases used with most thermodynamic calculation packages such as MT-DATA or ThermoCalc.

Physical models for nucleation and growth of a single particle rely on the availability of thermodynamic information such as the Gibbs energy change during precipitation, or the equilibrium interface composition. Simple models have been presented for nucleation and growth, the latter being given more attention in chapter 4.

The overall precipitation phenomenon cannot be modelled accurately without accounting for interactions between the different particles. Soft-impingement can be dealt with using the mean-field approximation while the concept of extended volume, modified for multiple precipitation reactions, provides a solution to the hard-impingement problem.

Chapter 4

The growth rate of precipitates

4.1 Introduction

Calculating the diffusion-controlled growth rate is a problem which has received considerable attention, but for which solutions can still be classed in two categories. On the one hand, relatively complex mathematical approaches are used to solve the growth equation with as few assumptions as possible, or to account rigorously for the geometry of the growing particles, *etc.* (e.g. [89, 90, 91]). However, such approaches are difficult to use for practical purposes, as they often introduce quantities which are not known (for example, the cross-diffusion coefficients). On the other hand, solutions which are of practical interest rely on approximations which can be judged more or less important, but allow the calculations to be performed relatively easily and use parameters known for most materials (e.g. [92, 88, 93]).

In this work, an attempt is made to build as general a model as possible, while avoiding unnecessary approximations. For this reason, when possible, the diffusion coefficients of the components involved in the growth of the different precipitates found in austenitic stainless steels are calculated internally, and the use of MT-DATA removes the need for inputs such as the maximum volume fraction of a given phase, its composition, driving force, *etc.*

4.2 Calculation of the diffusion coefficients

4.2.a Calculation of the carbon diffusivity

As can be seen from the published literature [94], the diffusivity of carbon in austenite in the Fe-Cr-Ni-C system is strongly dependent on the composition. There are two main advantages in calculating the carbon diffusivity within the framework of any model created, rather than having it as an input. One is to considerably ease the task of the user who does not have to find a value in the literature for the particular composition being used. The other is that it may allow extrapolation to values which might not be found in the literature. The calculation of the carbon chemical diffusivity was done as suggested by Jönsson [94]. In his assessment of the carbon mobility in C-Cr-Fe-Ni alloys, Jönsson uses the multicomponent diffusion theory [95] and writes the chemical diffusivity of carbon, under the assumption that the concentration gradients of substitutional elements are negligible throughout the specimen, as:

$$\tilde{D}_C = RTy_{Va}M_C\Psi \tag{4.1}$$

where $\tilde{D}_C$ is the chemical diffusivity of carbon, y_{Va} the fraction of vacant sites on the interstitial sublattice, M_C the mobility of carbon, and Ψ the thermodynamic factor defined by:

$$\Psi = \frac{c_C}{RT}\frac{\partial \mu_C}{\partial c_C} \tag{4.2}$$

where C_C is the molar concentration of carbon. Jönsson then expresses the mobility M_C as:

$$M_C = M_\circ \exp\left(\frac{-Q_c}{RT}\right)\frac{1}{RT} = \frac{1}{RT}\exp\left(\frac{\Delta G_C^*}{RT}\right) \tag{4.3}$$

where $M_\circ$ is a frequency factor, Q_C an activation enthalpy and $\Delta G_C^* = RT\Phi_C - Q_C$, with Φ_C defined by $M_\circ = \exp(\Phi_C)$. Using the CALPHAD approach to model the composition dependency of the mobility, it is easier to fit the quantity ΔG_C^* than the frequency factor and activation enthalpy separately [94]. The quantity ΔG_C^* is therefore fitted using a sublattice model 4.4:

$$\Delta G_C^* = \sum_i \sum_j y_i y_j \Delta G_C^{*\,i:j}$$

$$+\sum_i \sum_{j>i} \sum_l y_i y_j y_l \left(\sum_r {}^r\Delta G_C^{*\,i,j:l} (y_i - y_j)^r \right)$$
$$+\sum_i \sum_l \sum_{m>l} y_i y_l y_m \left(\sum_r {}^r\Delta G_C^{*\,i:l,m} (y_l - y_m)^r \right) \quad (4.4)$$

where the indices indicate which species occupies the different sublattices, separated by a colon, for example $\Delta G^{*\,Cr:Va}$ is for Cr on the first sublattice with nothing on the second (vacancy), $\Delta G^{*\,Fe,Cr:Va}$ is an interaction parameter for Fe and Cr on the first sublattice with nothing on the second. y_i is the fraction of the sites occupied by species i on its sublattice. If necessary, the individual parameters $\Delta G_C^{*\,i:j}$ are expressed as polynomials of the temperature.

Jönsson [94] provides the parameters for the mobility of carbon in austenite for Fe-Cr-Ni-C alloys, so that the influence of the Cr, Ni and C content on the diffusion coefficient of carbon in this phase can be calculated. These data have been used to calculate the diffusion coefficient of carbon within a FORTRAN (formula translation) program written to model the nucleation and growth of precipitates in austenitic stainless steels. The influence of other elements commonly found in such steels (e.g. Mo, Mn, Si, N, *etc.*) is only present as a modification of the site occupancy fractions for Fe, Cr, Ni and C, but there are no specific parameters. As is explained later, this FORTRAN program is interfaced with a library of subroutines which enable the use of MT-DATA internally. Therefore it is not a problem to calculate terms such as Ψ defined by equation 4.2. Typical calculated values are shown in table 4.1.

Material	NF709	AISI 304
$\tilde{D}_C$ / m^2 s^{-1}	4.87×10^{-13}	5.86×10^{-13}

Table 4.1: Typical calculated values for the chemical diffusivity of C in austenite at 1023 K, composition of these two steels can be found in table 1.1.

4.2.b The diffusivity of Fe, Cr and Ni

The same approach was used for Fe, Cr and Ni which allows diffusivity coefficient to be calculated within the program mentioned above, parameters were found in [36] and [96]. Table 4.2 shows examples of calculated diffusion coefficients for Cr, compared with values found in literature:

Material	Calculated	Literature
AISI 316 [97]	8.9×10^{-19} m^2 s^{-1}	6.2×10^{-19} m^2 s^{-1}
16Cr-14Ni [98]	5.54×10^{-19} m^2 s^{-1}	5.50×10^{-19} m^2 s^{-1}

Table 4.2: The diffusion coefficient of Cr in AISI 316 at 750 °C as calculated and found in different studies.

4.3 Calculation of the growth rate

The problem of calculating the growth rate is two-fold: firstly, it is necessary to be able to calculate the growth rate as a function of the supersaturation, that is as a function of the concentration profile at the interface. Secondly, it is necessary to determine the interface compositions which in turn fixes the supersaturation.

4.3.a Calculating the growth rate in a binary system

This section deals with the diffusion-controlled growth of a precipitate θ in a matrix γ, for a binary system. Under these conditions, the flux of solute in the matrix is given by:

$$J = -D\nabla c \tag{4.5}$$

where J is the flux of solute, D its diffusion coefficient in the matrix and c the molar or mass concentration, depending on the flux of interest. The growth rate ψ of θ is usually calculated by solving the diffusion equation, and equating the flux of solute to the amount incorporated into θ (figure 4.1 and equation 4.6):

$$\psi \left(c^{\theta\gamma} - c^{\gamma\theta} \right) = J \tag{4.6}$$

where $c^{\theta\gamma}$ is the concentration of solute in the precipitate in equilibrium with the matrix and $c^{\gamma\theta}$ the composition of the matrix in equilibrium with the precipitate. As is shown in figure 4.1, it is essential that the interface compositions are known in order to solve the problem. Under the assumption of local equilibrium, these are given by the equilibrium phase diagram. There are various effects which might cause a departure from local equilibrium, such as the effect of interface energy, the existence of stresses and the solute-drag effect (a review of these effects can be found in [99]). Much work has been dedicated to the treatment of multicomponent capillarity, which is presented in chapter 5. Other effects are assumed to be negligible.

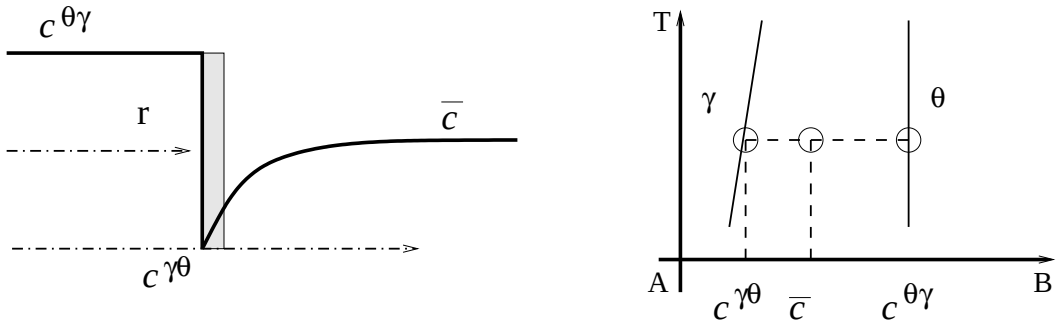

Figure 4.1: The concentration profile of the solute as a function of the distance from the interface matrix / precipitate. r is the coordinate of the interface between the matrix and the precipitate, $\overline{c}$ is the bulk alloy composition. The shaded area represents the amount of solute incorporated in the precipitate during a small amount of time. It must be equal to the amount of solute brought at the interface by the diffusion in the matrix.

For planar, cylindrical or spherical geometries, the growth rate can be generally expressed by [84]:

$$\psi = \frac{S\sqrt{D}}{2\sqrt{t}} \tag{4.7}$$

where ψ is the velocity of the interface, t is the time, and S is the solution of:

$$S^j = 2\ \Omega\ \frac{\exp(-\frac{S^2}{4})}{\Phi_j(S)} \tag{4.8}$$

where Ω, the supersaturation, is defined by $\Omega = (\overline{c} - c^{\gamma\theta})/(c^{\theta\gamma} - c^{\gamma\theta})$, and j is 1,2 or 3 depending on the geometry of the problem: planar, cylindrical and spherical respectively. $\Phi_j(S)$ is given by:

$$\Phi_j(S) = \int_S^\infty u^{1-j} \exp\left(-\frac{S^2}{4}\right) \mathrm{d}u \tag{4.9}$$

In cases where Ω is very close to 0 or very close to 1, asymptotic expansions can easily be found for the planar and spherical cases, by rewriting Φ using the erfc function and expanding the latter to the first terms of its equivalent series. The following results are obtained:

For small supersaturations ($\Omega \to 0$):

$$S^{\text{planar}} = \frac{2}{\sqrt{\pi}}\Omega \tag{4.10}$$

$$S^{\text{spherical}} = \sqrt{2\Omega} \tag{4.11}$$

For large supersaturations ($\Omega \to 1$):

$$S^{\text{planar}} = \sqrt{\left(\frac{2}{1-\Omega}\right)} \tag{4.12}$$

$$S^{\text{spherical}} = \sqrt{\left(\frac{6}{1-\Omega}\right)} \tag{4.13}$$

i Calculation of the exact solution

Although equation 4.8 can be solved using a FORTRAN program, this is not straightforward, particularly at large supersaturations, where the different terms have to be calculated in a carefully chosen order to avoid exceeding the limits of most computers. Instead,

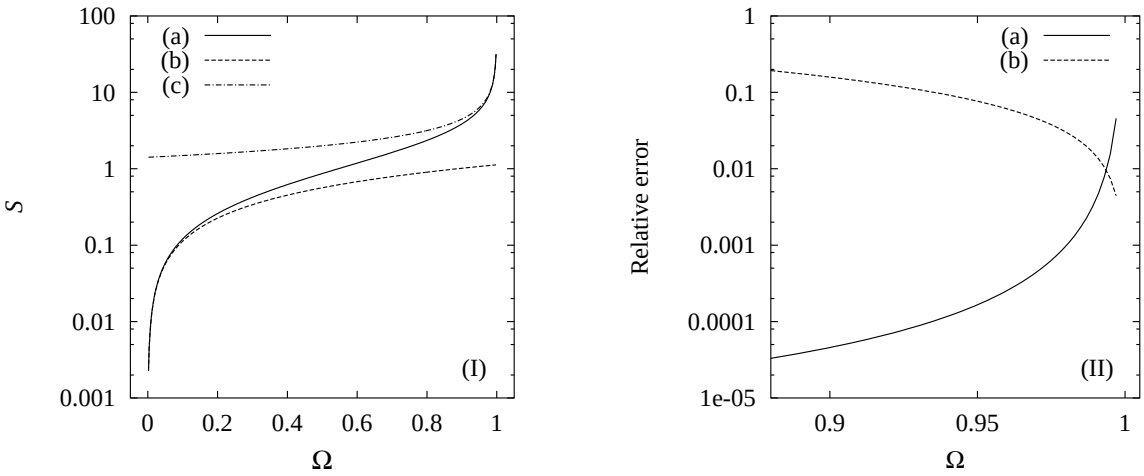

Figure 4.2: (I) The exact solution for the growth of a planar interface (a), and the approximations for small (b) and large (c) supersaturations. (II) The relative error (error due to method / exact solution) due to the use of equation 4.12 (a) and to the linear interpolation between calculated points (b).

a freely available mathematic package called SciLab (http://www-rocq.inria.fr/scilab/) was used to create a file containing the solutions for 500 points between 0 and 1. Intermediate values are found by linear interpolation. However, at large supersaturations, the error caused by this method becomes important. By comparing the relative error obtained by the linear interpolation and the use of the asymptotic expansions (figure 4.2), it was possible to optimise the use of one or another method as a function of the supersaturation.

As can be seen in figure 4.2, the relative error is always kept below 1% if the solution is calculated using equation 4.12 when $\Omega > 0.994$ while the linear interpolation between pre-calculated points gives a very reasonable error down to $\Omega = 0$. A similar method was used to calculate the growth rate of a spherical interface, and gave $\Omega = 0.990$ as the value above which it was preferable to use equation 4.13. A considerable calculation time is gained by this procedure, which almost reduces the calculation of S to a memory access.

4.3.b Calculation of the growth rate in a multicomponent alloy

The extension of the method described above is far from straightforward, as different effects appear in multicomponent systems, which, it is shown in this section, can not be reasonably neglected.

i The flux balance

The discussion that follows considers a ternary system as an example, but can be extended easily to a larger number of components.

Figure 4.3 illustrates the case of a ternary system in which a matrix γ is in equilibrium with a precipitate θ. The bulk composition corresponds to point P, and the equilibrium tie-line is that going through P. This tie-line defines diffusion profiles as illustrated, for which the supersaturations are all equal.

However, the elements involved often have very different diffusivities. For example, with Cr and C in austenite, the diffusion coefficients differ by a ratio of about about 10^6 at 750 °C. Therefore the concentration profiles defined by the mass-balance tie-line do not, in general, satisfy the following set of equations for a unique interface velocity ψ:

$$\begin{aligned} J_1 &= \psi \left(c_1^{\theta\gamma} - c_1^{\gamma\theta} \right) \\ J_2 &= \psi \left(c_2^{\theta\gamma} - c_2^{\gamma\theta} \right) \end{aligned} \tag{4.14}$$

or, taking the problem in the other sense, the diffusion profiles of the different elements, as fixed by the mass-balance tie-line, lead to different values of the interface velocity.

But there is no reason to select the equilibrium tie-line, that going through P, as the one defining the interface compositions. The mass-balance equations are no longer the determining constraints and must be replaced by equations 4.14. The tie-line fixed by these conditions will be referred to as the flux-balance tie-line.

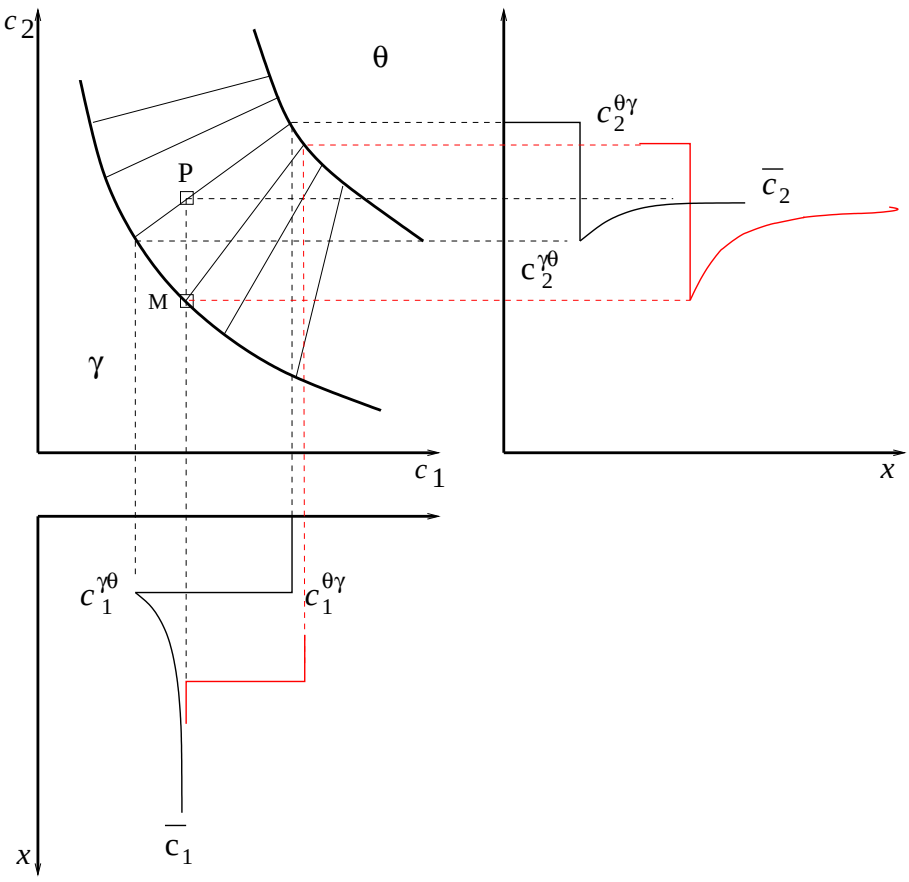

Figure 4.3: The flux-balance fixed tie-line going through M, can be quite different from the mass-balance fixed one, that passes through P, the bulk composition. In the case where 1 diffuses much faster than 2, its gradient may be strongly reduced.

ii The problem of identifying the flux-balance tie-line

Although the problem of identifying the flux-balance tie-line has received attention in a number of studies [89, 90], it remains, in practice, difficult to solve. If one is to account for this effect within a model describing the evolution of the precipitation, one needs to have access to the entire phase diagram for the phases concerned, and not, as is the case with binary system, just the interface compositions.

Earlier approaches by Fujita and Bhadeshia [93] have used simple analytical expressions to fit the phase boundary in the ternary system of interest. However, there are serious limitations to this method: first, the use of the model will be restricted to those systems for which the phase boundary have been fitted by a function, and second, the method is extremely difficult to extend to systems of more than three components.

The application interface of the thermodynamic calculation software MT-DATA [3] was used to provide an algorithm able to solve the problem in any system described in the SGTE (or any other) databases. It consists of a library of subroutines which can be called within a FORTRAN program to perform thermodynamic calculations with MT-DATA.

Before presenting the algorithm which was written to solve this problem in a general manner, it is necessary to look more carefully at the set of equations 4.14, and particularly at the fluxes. In multicomponent system, the flux of component i is related to the various concentration gradients according to:

$$J_i = -D_i \nabla c_i - \sum_{j \neq i} D_{ij} \nabla c_j \tag{4.15}$$

where the cross-diffusion terms ($D_{ij} \nabla c_j$) arise because the gradient of components other than i can modify its chemical potential. In the following, cross-diffusion terms have been neglected. Without this assumption, which is further discussed later, it is not possible to use equation 4.7.

4.3.c An algorithm to determine the tie-line satisfying the flux-balance

In this method, the velocity ψ_i (the index indicating which component profile is used) of the interface is calculated independently for each component composition profile, which implies that cross-diffusion terms in equation 4.15 are neglected. The aim is to find the tie-line for which all the ψ_i are identical. This is in fact reduced to equating the $S_i\sqrt{D_i}$, as shown by equation 4.7.

Figure 4.4 describes how the tie-line satisfying the flux-balance is identified in a pseudo-ternary system. Pseudo-ternary refers to a ternary sub-system of a multicomponent system. We consider here the example of the growth of $M_{23}C_6$. For the mass-balance tie-line, C and Cr have the same supersaturation ($\Omega_C = \Omega_{Cr}$), hence $S_C = S_{Cr}$. However C diffuses much faster than Cr, and therefore ψ_C, as calculated from the C concentration profile, will be much larger than ψ_{Cr}. The tie-line eventually giving $\psi_{Cr} = \psi_C$ considerably reduces Ω_C and increases Ω_{Cr}.

In systems with more than three components, this is repeated in a nested manner. For example, a first modification is done on Mo, which gives a new pseudo-ternary system in

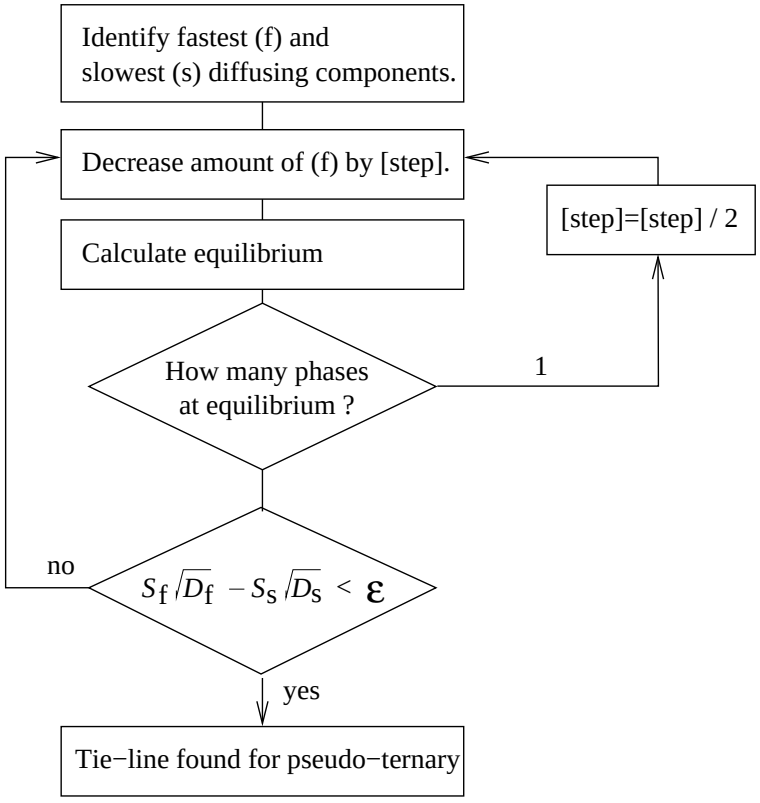

Figure 4.4: The algorithm written to find the tie-line satisfying the flux-balance in any system described in the databases used by MT-DATA; for each component the step is initially set to a tenth of its total amount.

which this algorithm is applied, to Cr and C. When the tie-line is found, the fluxes of Cr and C are identical, and need to be compared to that of Mo. The amount of Mo can then be corrected and the procedure repeated until the tie-line that gives identical fluxes for all elements involved is found.

This method is computer intensive, essentially because it is not possible to interact with MT-DATA on a low level and replace the mass balance constraint directly in the Gibbs energy optimisation process.

4.4 Overall kinetics

The overall kinetic is presented in chapter 6. For comparisons made later, it is however necessary to introduce the concept of soft-impingement.

When many precipitates form in the same matrix, whether they are of same or different nature, they compete for solute. To represent this, the mean-field approximation is used, in which the composition $\overline{c_i}$ is updated to reflect the amount of component i which has been incorporated during a time step by the various precipitates.

4.5 Consequences

4.5.a The growth rate

The growth rate calculated assuming that Cr and C control the process was found to be more than an order of magnitude larger than the one calculated assuming Cr control alone.

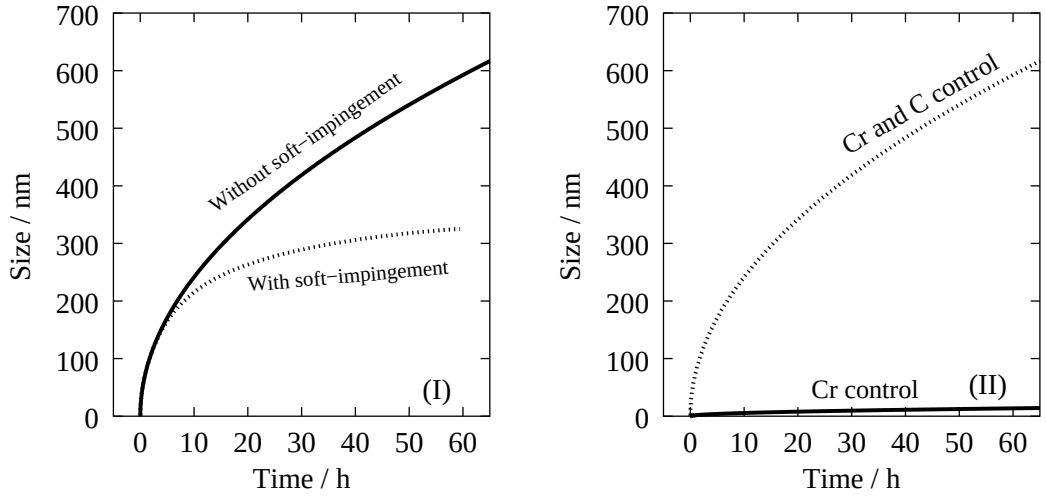

Figure 4.5: (I) Comparison between the calculated growth rates for $M_{23}C_6$ at 650 °C, in AISI 316 [97], with and without soft-impingement, under control of both Cr and C diffusion. (II) Comparison, without soft impingement, of the growth rate of a $M_{23}C_6$ particle nucleated at $t = 0$, at 650 °C, under Cr control alone, and Cr and C control.

Figure 4.5(I), shows the predicted radius of a $M_{23}C_6$ precipitate nucleated at $t = 0$, with and without accounting for soft impingement, which can have a strong effect on the growth rate. Since the purpose is here to compare the growth rates under different hypotheses and since the role of soft impingement is itself dependent on the growth rates, this effect has been removed to facilitate further comparisons. This means that

growth curves can only be representative of the real phenomenon at the early stages of the precipitation.

Figure 4.5(II) compares the growth rate under Cr and C diffusion control and under Cr diffusion control alone. In this situation, because of the very large difference between the diffusivity of carbon and chromium in austenite, the tie-line found to satisfy the flux-balance is virtually bringing the carbon gradient to zero (tie-line going through M in figure 4.3). As a consequence, at the early stages of precipitation, the composition of $M_{23}C_6$ and of the surrounding austenite, are expected to be fairly different from the equilibrium values.

4.5.b The composition of $M_{23}C_6$ in the Fe-Cr-Ni-C system

Several observations can be found which report an increasing Cr/Fe ratio during the growth of $M_{23}C_6$ (section 2.1.c). Table 4.3 shows the expected $M_{23}C_6$ composition at equilibrium, and the composition at the beginning of precipitation. As observed, the Cr/Fe ratio is much smaller at the onset of precipitation than for the equilibrium.

	Element	Fe	Cr	Mo	Mn
650 °C	Wt% (I)	4.7	64.61	9.95	0.001
	Wt% (II)	49.12	20.05	10.12	0.006
800 °C	Wt% (I)	7.9	62.37	9.03	0.005
	Wt% (II)	31.46	38.50	9.31	0.016

Table 4.3: The substitutional composition of $M_{23}C_6$ in two different cases: I is for the mass balance and II for the flux balance as calculated in this project. The steel composition was 17.5 Cr, 12.3 Ni, 2.5 Mo, 1.6 Mn, 0.07 C wt%, as in [97].

4.5.c Number of components accounted for

The number of components that can be accounted for in the calculation is firstly limited by the thermodynamic databases. Phases such as NbN, TiN and similar phases are modeled as pure substances in the SGTE databases, so that it is not possible to predict a change of composition, although, as explained in chapter 2, many works have reported variations in the composition and stoichiometry of these phases during growth.

In the case of $M_{23}C_6$, the elements Fe, Cr, Mo, Mn, Ni, and C can be included.

However, including minor elements such as Mo, Ni and Mn has little influence over the growth rate calculated with Cr and C diffusion, but greatly increases the computation time. For this reason, in the above calculations and following comparisons, only the diffusion of Cr and C have been used to calculate the growth rates.

4.6 Comparisons and discussions

Figure 4.6 shows the experimental results obtained by Záhumenský *et al.* [97] for a AISI 316 steel at 650 °C and 800 °C. As can be seen, the agreement is relatively poor since the experimental points lie in between the two curves corresponding to the Cr diffusion-controlled growth and the multicomponent growth (accounting for Cr and C diffusion). Furthermore, while the above method predicts a reduction of Cr/Fe well below 1 (40 Fe,

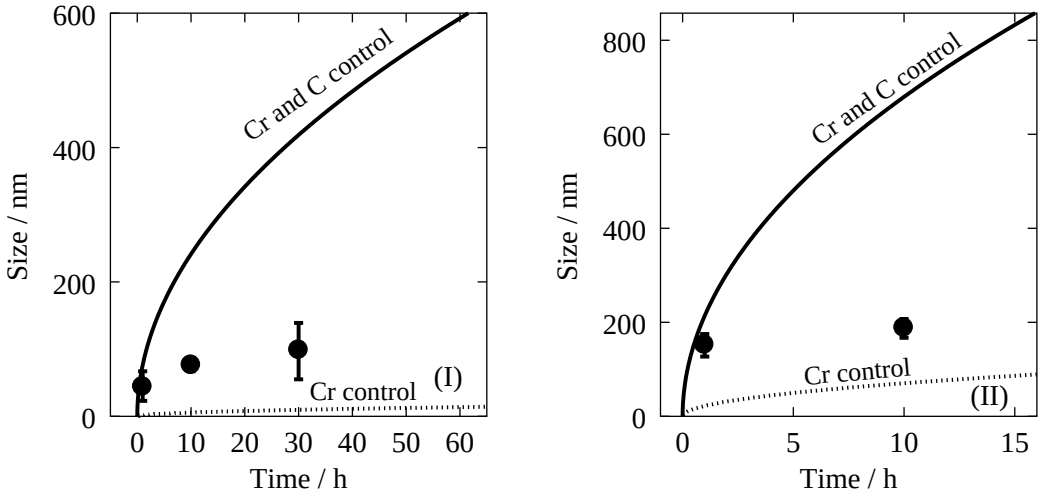

Figure 4.6: Comparison between predicted (lines) and measured (points) radii of $M_{23}C_6$ for the AISI 316 steel in [97], at (I) 650 °C and (II) 800 °C.

30 Cr wt%), the measurements made by Boeuf *et al.* [100] on an AISI 304 stainless steel report a Cr/Fe ratio slightly greater than 2 in the same conditions.

The overprediction of the radius can be partially attributed to the fact that soft-impingement is not accounted for. As shown in figure 4.5, soft-impingement flattens the growth curve considerably and quite early. But it appears that the difference is larger than could be attributed to this effect alone. Also, the absence of soft-impingement cannot explain why the compositions are different from the observations made by Boeuf *et al.*

As mentioned before, this method is based on the commonly used (e.g. [92, 88, 93]) assumption that the cross-diffusion terms in equation 4.15 are negligible, however, both the exaggerated growth rate and composition change indicate that this is not the case. Applying equation 4.15 to the example of $M_{23}C_6$, two fluxes have to be considered:

$$\begin{aligned} J_{\mathrm{C}} &= -D_{\mathrm{C}}\nabla c_{\mathrm{C}} - D_{\mathrm{CC}r}\nabla c_{\mathrm{C}r} \\ J_{\mathrm{C}r} &= -D_{\mathrm{C}r}\nabla c_{\mathrm{C}r} - D_{\mathrm{C}r\mathrm{C}}\nabla c_{\mathrm{C}} \end{aligned} \tag{4.16}$$

When the tie-line reaches point M in figure 4.3, the carbon gradient is almost reduced to zero, but there is a strong gradient of chromium concentration, so that even if $D_{\mathrm{CC}r} \ll D_{\mathrm{C}}$, it is not possible to conclude that $D_{\mathrm{CC}r}\nabla c_{\mathrm{C}r} \ll D_{\mathrm{C}}\nabla c_{\mathrm{C}}$ since $\nabla c_{\mathrm{C}r} \gg \nabla c_{\mathrm{C}}$.

Difficulties arising from the inclusion of cross-diffusion terms have been presented before. However, the following solution avoids this difficulty: in the most general formalism, it is a gradient of activity that drives diffusion. By reducing the gradient of carbon activity rather than its concentration gradient, it can be ensured that the carbon flux is really reaching a minimum. Furthermore, it can be considered, at this point, that the effect of the remaining carbon gradient on the activity of chromium is negligible, therefore allowing to identify $J_{\mathrm{C}r}$ to $-D_{\mathrm{C}r}\nabla c_{\mathrm{C}r}$. This means that the growth rate can be calculated by using the diffusion of chromium alone at the point where there is no carbon activity gradient. The following section describes the implementation of this method and the results obtained.

4.7 Improvement in the calculation of the flux-balance tie-line

Instead of reducing the carbon gradient and finding the tie-line which gives identical fluxes (under the assumption that cross-diffusion is negligible), the algorithm described in figure 4.4 was modified to find the interface composition for which the activity of carbon was equal to the far-field one. When this tie-line is found, the velocity of the interface is assumed to be that given by the diffusion of chromium.

As shown in figure 4.7 the agreement between the calculated and measured radii of $M_{23}C_6$ in AISI 316 is considerably improved. Without doubt, the overpredicted size of $M_{23}C_6$ after 10 h at 800 °C is due to the absence of soft-impingement, this temperature

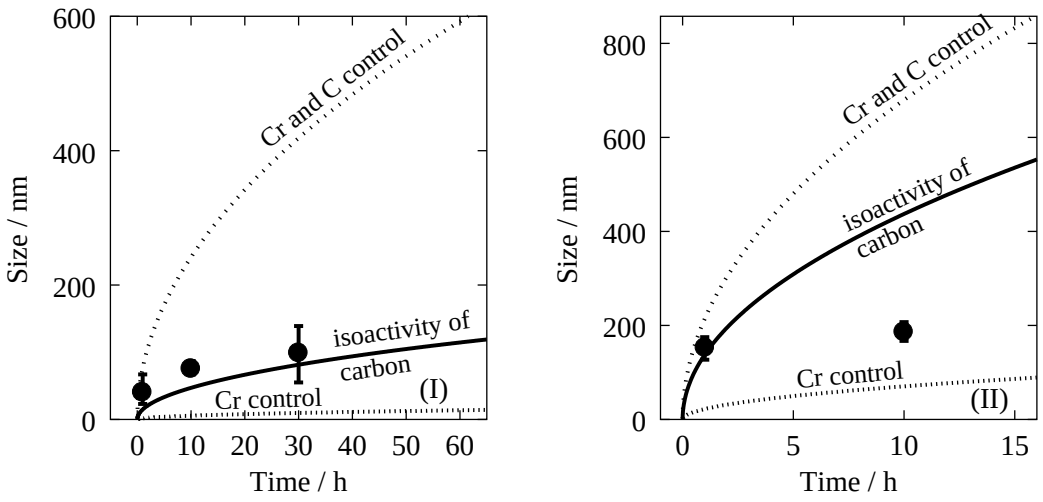

Figure 4.7: The radius of $M_{23}C_6$ at (I) 650 °C and (II) 800 °C. The agreement is best for the growth rate calculated with no gradient of carbon activity.

corresponding roughly to the nose of the TTT (time temperature transformation) curve for this category of steels [4], where the transformation is finished in a matter of hours.

The composition of $M_{23}C_6$ at the beginning of precipitation was calculated for the AISI 304 studied by Boeuf *et al.* [100]. Table 4.4 sumarises the observed initial Cr/Fe ratio and the calculated ones, using a zero gradient of carbon concentration and a zero gradient of carbon activity. The last method, which gives very satisfying predictions of the radius, also predicts well the Cr/Fe ratio.

	Cr/Fe ratio
Equilibrium	12
Boeuf *et al.* at $t = 0$	**2.1**
Flux balance	0.72
Carbon isoactivity	**2.2**

Table 4.4: The Cr/Fe ratio in $M_{23}C_6$ in different cases, for the AISI 304 steel studied by Boeuf *et al.*. The last method clearly gives satisfying agreement with experimental results.

4.8 Summary and conclusions

A FORTRAN program has been written, interfaced with the thermodynamic calculation software MT-DATA, to solve the problem of growth in multicomponent systems. It is shown that, although this approximation has been often used, neglecting the cross-diffusion terms is particularly inappropriate when trying to equate the fluxes, and lead to unrealistic results. A method has been proposed to solve the problem more rigorously without having to include such terms, by considering the activity of carbon. This last method predicts correctly not only the growth rate, but also the change in the $M_{23}C_6$ composition.

Chapter 5

Capillarity in multicomponent systems

In the preceding chapter, it was assumed that the interface between the matrix and the growing precipitate was under local equilibrium, therefore allowing the use of the equilibrium phase diagram to determine its composition. It was also mentioned that several effects may invalidate this hypothesis. In particular, capillarity, which is a modification of the interface equilibrium due to the contribution of the interface energy, affects particularly the early stages of growth. Capillarity is also at the origin of the coarsening phenomenon.

Because the problem of multicomponent capillarity has no simple solutions, many works have used the Gibbs-Thomson equation developed for a binary system. In this chapter, the validity of this approach is discussed, and two better methods are proposed and compared.

5.1 Introduction

As presented in chapter 3, the CALPHAD method allows predictions of the phase behaviour of complex, multicomponent systems. Software such as MT-DATA or ThermoCalc use thermodynamic databases to calculate equilibrium phase compositions and amounts for given composition, temperature and pressure. However, the equilibrium at an interface between two phases can be modified by curvature, an effect commonly referred to as "capillarity", and most often described by the Gibbs-Thomson equation (e.g. [101]

page 149). These concepts have been introduced in chapter 3.

There are two aspects in the treatment of the capillarity problem. One solution is to re-calculate the thermodynamic equilibrium when the Gibbs free energy of one phase is raised by an amount which allows for the creation of new interfacial energy as the particle grows (Eq. 22.29 in [84]). This is possible using thermodynamic calculation packages such as MT-DATA, as described later.

On the other hand, there is an interest in being able to estimate the capillarity correction without such software, particularly when this correction has to be estimated within a separate model. For binary solutions, this can be done using the Gibbs-Thomson equation, or a generalised form for multicomponent alloys.

In the following, a two-phase system is considered, with the matrix referred to as γ and the precipitate as θ. The problem is to estimate how the equilibrium between the two phases is modified when the Gibbs energy of θ is raised by a given amount, in the case of capillarity, $\sigma_{\gamma\theta}\,\partial O/\partial n$; $\sigma_{\gamma\theta}$ being the γ/θ interface energy per unit area, and $\partial O/\partial n$ the increase in area when the number of moles n of θ increases.

5.2 Capillarity effects in a binary two phase system

The solution of the capillarity problem in a binary, two-phase system is well known and is presented here to be used as a guide towards the solution in a ternary system. This section is essentially after Hillert [101]. A binary system A-B is considered, with two phases γ and θ.

The precipitate θ is here considered to have a fixed chemical composition. Figure 5.1 illustrates the problem: the Gibbs free energy of θ (G_θ) is raised by a term $\sigma_{\gamma\theta}\,\partial O/\partial n$. The mathematical treatment is however more readable and easier to develop rigorously if the Gibbs energy addition is written in a general manner, $V_m^\theta\,\Delta P$ where V_m^θ is the molar volume of θ and $\Delta P = \int \mathrm{d}P$ a pressure increase.

The initial interface compositions are given by the two contact points of the common tangent to the γ and θ free energy curves. If the difference in composition between the matrix and the precipitate is sufficiently large, when compared to the composition change due to capillarity, the addition of $V_m^\theta \mathrm{d}P$ causes the slope of the common tangent to change as:

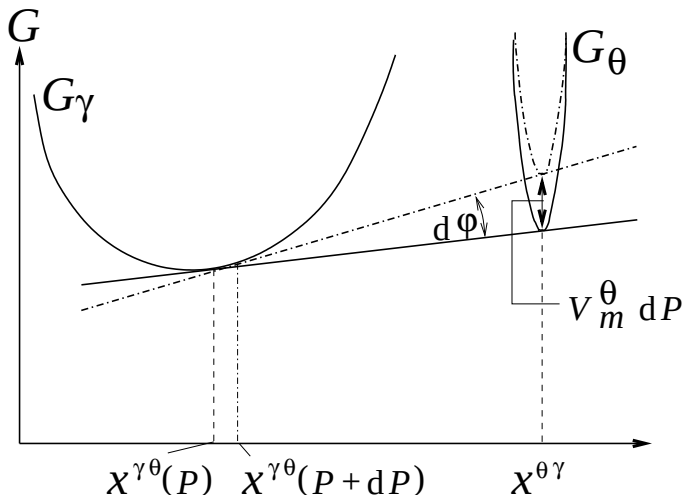

Figure 5.1: The effect of an increase in the Gibbs energy of a stoichiometric compound θ on the matrix composition. G denotes the Gibbs energy of the phase identified by the subscript.

$$(x^{\theta\gamma} - x^{\gamma\theta})\mathrm{d}\varphi = V_m^\theta \mathrm{d}P \tag{5.1}$$

where $x^{\theta\gamma}$ is the mole fraction of solute in phase θ in equilibrium with γ, similarly for $x^{\gamma\theta}$; $\mathrm{d}\varphi$ is the difference between the slopes at the two contact points (figure 5.1):

$$\mathrm{d}\varphi = \left.\frac{\partial G_\gamma}{\partial x^\gamma}\right|_{x^{\gamma\theta}(P+\mathrm{d}P)} - \left.\frac{\partial G_\gamma}{\partial x^\gamma}\right|_{x^{\gamma\theta}(P)} = \frac{\partial^2 G_\gamma}{\partial {x^\gamma}^2}\,\mathrm{d}x^{\gamma\theta} \tag{5.2}$$

where $\mathrm{d}x^{\gamma\theta} = x^{\gamma\theta}(P+\mathrm{d}P) - x^{\gamma\theta}(P)$ is the composition change of the matrix in equilibrium with the precipitate. Assuming a dilute solution:

$$\frac{\partial^2 G_\gamma}{\partial {x^\gamma}^2} = \frac{RT}{x^\gamma} \tag{5.3}$$

therefore:

$$\mathrm{d}x^{\gamma\theta} = \frac{x^{\gamma\theta}}{x^{\theta\gamma} - x^{\gamma\theta}} \frac{V_m^\theta \mathrm{d}P}{RT} \tag{5.4}$$

and for a reasonably small change, it is possible to integrate assuming that $x^{\theta\gamma} - x^{\gamma\theta}$ is constant:

$$\ln \frac{x^{\theta\gamma}(P)}{x^{\theta\gamma}(P=0)} = \frac{V_m^\theta \Delta P}{RT(x^{\theta\gamma} - x^{\gamma\theta})} \tag{5.5}$$

This is valid regardless of the nature of the Gibbs energy increase; in the case of capillarity with a spherical interface of radius r, $P = 0$ corresponds to a flat interface, that is $r = \infty$, and the increase of Gibbs energy is $2V_m^\theta \sigma_{\gamma\theta}/r$, so that:

$$\ln \frac{x^{\theta\gamma}(r)}{x^{\theta\gamma}(r=\infty)} = \frac{2V_m^\theta \sigma_{\gamma\theta}}{r} \frac{1}{RT(x^{\theta\gamma} - x^{\gamma\theta})} \tag{5.6}$$

5.3 Ternary systems

Probably because the literature does not offer a simple solution for multicomponent capillarity, various works dealing with multicomponent alloys have used either the standard form of the Gibbs-Thomson equation, or methods based on it.

For example, Faulkner [102] used directly the Gibbs-Thomson equation to calculate the influence of the curvature of $M_{23}C_6$ on the expected chromium content of the surrounding austenite, in an austenitic steel (Fe-18Cr-10Ni-Mn-C wt%). Such a procedure was recognised to be incorrect by Fujita and Bhadeshia [93] since the binary equation gives a different critical radius (at which growth becomes impossible) for each of the solutes in a multicomponent solution. However, the technique used by Fujita and Bhadeshia, who used the Gibbs-Thomson equation for a particle with a fixed radius and then calculated the capillarity corrected phase boundary, also has its problems. In a multicomponent system, the different components are not independent, and this does not appear when equation 5.6 is applied in turn to each component.

Consider now a ternary system *A*-*B*-*C* where *C* is the solvent. The mole fractions of *A* and *B* in both the matrix (γ) and the precipitate (θ) are likely to be modified by the curvature of the interface and are therefore functions of r.

The derivation of a correct set of equations is better understood with the help of figure 5.2. MN is an equilibrium tie-line as shown in figure 5.2. Since it is assumed that the composition of θ is constant, the new tie-line M′N′ will remain in the same vertical plane. Equation 5.1 becomes:

$$Z \, \mathrm{d}\varphi = V_m^\theta \, \mathrm{d}P \tag{5.7}$$

where Z is the distance between the compositions defined by M and N. Considering the change of slope along the tie-line, it can be shown, using the same idea as in equation 5.2,

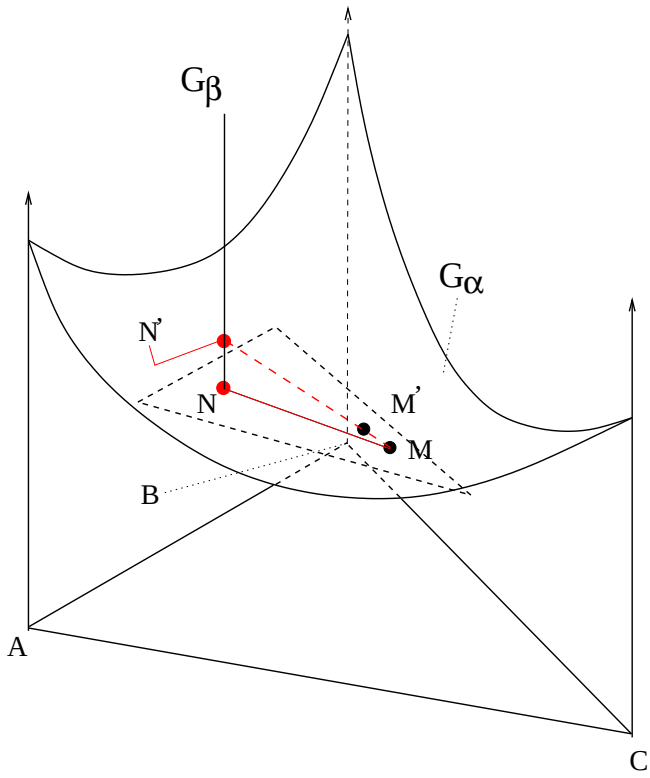

Figure 5.2: The effect of raising the molar Gibbs energy of the θ phase in a ternary system. The points of contact with the tangent plane, M and N move to M' and N'. $G_\theta + V_m^\theta \mathrm{d}P$ has its minimum value at N'.

that:

$$V_m^\theta \, \mathrm{d}P = \left(a \frac{\partial^2 G_\gamma}{\partial {x_A^\gamma}^2} + b \frac{\partial^2 G_\gamma}{\partial x_A^\gamma \partial x_B^\gamma} \right) \mathrm{d}x_A^\gamma + \left(b \frac{\partial^2 G_\gamma}{\partial {x_B^\gamma}^2} + a \frac{\partial^2 G_\gamma}{\partial x_A^\gamma \partial x_B^\gamma} \right) \mathrm{d}x_B^\gamma \tag{5.8}$$

where $a = (x_A^\theta - x_A^\gamma)$ and $b = (x_B^\theta - x_B^\gamma)$. Equation 5.8 is in fact similar to the one proposed by Morral and Purdy [103], since $V_m^\theta \, \mathrm{d}P$ is replaced by $2V_m^\theta / r$ for a spherical particle:

$$(\Delta x^{\gamma\theta}) \, [G] \, [\Delta x^\gamma) = \frac{2\sigma_{\gamma\theta} V_m^\theta}{r} \tag{5.9}$$

where ( ] indicates a row vector, while [ ) a column vector, and the matrix $[G]$ is defined by:

$$G_{ij} = \frac{\partial^2 G_\gamma}{\partial x_i \partial x_j} \tag{5.10}$$

If a dilute solution is assumed, the cross derivatives are zero and the others can be estimated as in equation 5.3. Given that $\mathrm{d}x_A^\gamma / \mathrm{d}x_B^\gamma = (x_A^\theta - x_A^\gamma)/(x_B^\theta - x_B^\gamma)$, equation 5.8

becomes:

$$\begin{aligned} \mathrm{d}x_A^\gamma &= \frac{a x_A^\gamma x_B^\gamma}{a^2 x_B^\gamma + b^2 x_A^\gamma} \frac{V_m^\theta \mathrm{d}P}{RT} \\ \mathrm{d}x_B^\gamma &= \frac{(x_B^\theta - x_B^\gamma)}{(x_A^\theta - x_A^\gamma)} \mathrm{d}x_A^\gamma \end{aligned} \tag{5.11}$$

These equations involve, as expected, both x_A^γ and x_B^γ; the system can easily be integrated numerically, and there is no difficulty in generalising to any number of components. For n components a system of $(n-1)$ equations are obtained.

It is noticeable that the interdependence does not require the presence of thermodynamic interactions between the components, as equation 5.11 has been derived assuming an ideal solution. Rather, the interdependence can be explained, geometrically, by the need to consider the slope along the tie-line. Applying directly the Gibbs-Thomson equation is equivalent to consider individually the components of this slope along the axis x_A and x_B.

It would be useful to compare these solutions against an exact calculation done using MT-DATA, in which the capillarity effect can be incorporated by raising the free energy of one of the phases by a quantity $\Delta P\, V_m^\theta$, equivalent to $\sigma \partial O / \partial n$.

5.4 An exact calculation using MT-DATA

Softwares such as MT-DATA rely on thermodynamic solution models to estimate the Gibbs energy of a given phase. Such models have been presented in chapter 3. The Gibbs energy of a phase like austenite is usually calculated using a sublattice model [81], which involves, in particular, terms called unaries ($G^0_{i:j}$ in eq. 5.12) which, for the example of a phase with two sublattices, contribute to the total free energy as follows:

$$G_{unaries} = \sum_{i \in I} \sum_{j \in II} y_i^I y_j^{II} G^0_{i:j} \tag{5.12}$$

where I is the first sublattice and II the second, i are all the elements able to enter the first sublattice and j those entering on the second, y_i^I the site fraction occupancy on the first sublattice by element i. Most commonly, temperature and pressure dependence of

the unaries are described using the G-HSER format [83]:

$$G^{T,P} - H^{SER} = a + bT + cT\ln T + eT^2 + fT^3 + i/T + \int_0^P V_m^{P,T}\mathrm{d}P \qquad (5.13)$$

in which $G^{T,P}$ is the molar Gibbs energy at (T, P) and H^{SER} is the enthalpy of the element or substance in its defined reference state at 298.15 K. Although the data contained in the SGTE solutions and substances databases do not include any pressure dependent terms for most of the condensed phases, it is possible to construct modified databases containing such terms. In the case of a sublattice model, one has to modify all the unaries for a given phase. By inserting a constant molar volume in the databases, one can, while using MT-DATA, add a given Gibbs energy to the phase of interest by setting the pressure to the appropriate value. As an example, table 5.1 lists all the non-zero unaries data for $M_{23}C_6$ (three sublattices).

Cr:Cr:C	Fe:Cr:C	Mn:Cr:C	Ni:Cr:C	V:Mn:C
Cr:Fe:C	Fe:Fe:C	Mn:Fe:C	Ni:Fe:C	
Cr:Mn:C	Fe:Mn:C	Mn:Mn:C	Ni:Ni:C	
Cr:Mo:C	Fe:Mo:C			
Cr:Ni:C	Fe:Ni:C			
Cr:V:C	Fe:V:C	Mn:V:C		V:V:C

Table 5.1: Some unaries data for $M_{23}C_6$. Missing unary like Mn:Mo:C have to be created so that the sum in equation 5.12 adds up to one mole of component. However, most of the time, missing unaries may make insignificant contributions as they involve minor elements.

For phases such as NbN, TiN, *etc...* which are modelled as pure substances, however, the SGTE databases often only contain coefficients to describe the temperature dependence of the heat capacity. This format does not accept pressure dependent terms and it was therefore necessary to create datasets in the G-HSER format for the relevant phases. In the C_P-format [83], the variation of the heat capacity within the temperature range i, for which $T \in [T_{min,i}, T_{min,i+1}]$ where $T_{min,i}$ is the minimum temperature for the range i, is given by:

$$C_{Pi}(T) = A_i + B_i T + C_i T^2 + D_i T^{-2} \qquad (5.14)$$

with possibly a transition term $\Delta_t \mathrm{H}_i$ between the ranges i and $i+1$, the parameters required for the G-HSER format can be calculated from the relationships between Gibbs

energy and heat capacity:

$$
\begin{aligned}
a_i &= \mathrm{H}(T_{min,i}) - A_i\,T_{min,i} - B_i\,T_{min,i}^2/2 - C_i\,T_{min,i}^2/3 + D_i/T_{min,i} \\
b_i &= A_i - \mathrm{S}(T_{min,i}) + A_i\,\ln(T_{min,i}) + B_i\,T_{min,i} + C_i\,T_{min,i}^2/2 - D_i/(2\,T_{min,i}^2) \\
c_i &= -Ai \\
d_i &= -B_i/2 \\
e_i &= -Ci/6 \\
f_I &= -D_i/2 \\
\mathrm{H}(T_{min,i}) &= \Delta_f\mathrm{H}(298) + \sum_{j<i}\left(\int_{T_{min,j}}^{T_{min,j+1}} C_{Pj}\mathrm{d}T\right) + \sum_{j<i}(\Delta_t\mathrm{H}_j) \\
\mathrm{S}(T_{min,i}) &= \mathrm{S}_{298} + \sum_{j<i}\left(\int_{T_{min,j}}^{T_{min,j+1}} \frac{C_{Pj}}{T}\mathrm{d}T\right) + \sum_{j<i}\left(\frac{\Delta_t\mathrm{H}_j}{T_{min,j+1}}\right)
\end{aligned}
\tag{5.15}
$$

where enthalpies and entropies, $\Delta_f\mathrm{H}(298)$, S_{298}, and the $\Delta_t\mathrm{H}_j$ are found in the databases.

A pressure dependence term was added to various precipitates expected to form in steels, so as to increase the molar Gibbs energy of the phases of interest by 10^{-6} J per Pa. In this way, setting a pressure of 1 Pa allows the user to perform an ordinary equilibrium calculation since the added Gibbs energy is negligible. Databases incorporating such

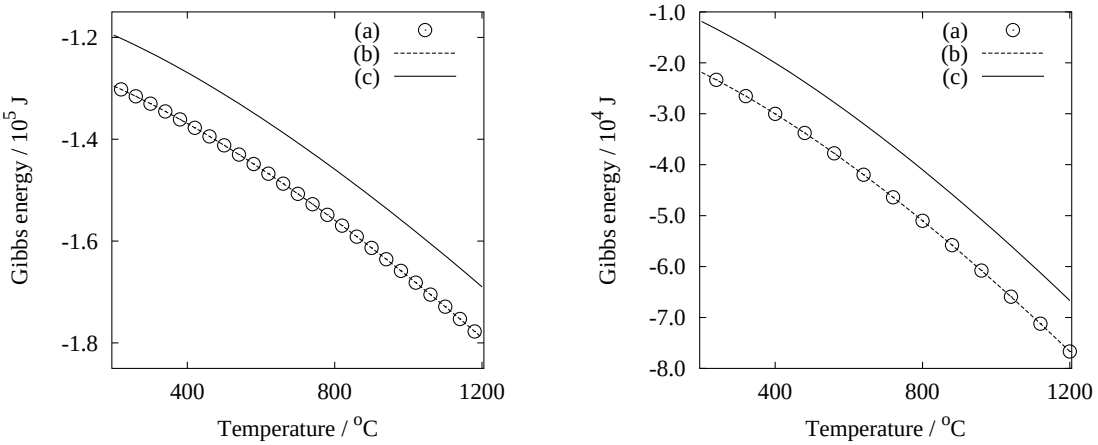

Figure 5.3: Verification of the effect of pressure setting on the Gibbs energy of NbN and $M_{23}C_6$ calculated with MT-DATA. The calculation using the original database (a) is identical to that with the modified database and the pressure set to $P = 1$ Pa (b). Setting the pressure to $P = 10^{10}$ Pa raises the Gibbs energy of the phases by 10^4 J per mole of components (c).

modifications have been created for $M_{23}C_6$, HCP_A3 (e.g. Cr_2N, Mo_2C), NbN, TiN, NbC and TiC, $NbC_{0.479}$, $NbC_{0.877}C$ and $Nb_{0.98}C$. Figure 5.3 shows the Gibbs energy of NbN and $M_{23}C_6$ calculated in different conditions. By setting the pressure to 1 Pa when using a thermodynamic calculation software such as MT-DATA or ThermoCalc in conjunction with the modified databases, the user can calculate the ordinary equilibrium (because the Gibbs energy increase is negligible), while the equilibrium when G_θ is raised by 500 J would be calculated by setting the pressure to 5×10^8 Pa.

5.5 Comparisons and comments

5.5.a The dilute solution approximation

To validate the simple expression proposed for a ternary system (equation 5.11), a system consistent with the approximations made above (precipitate of fixed composition, ideal solution) was chosen: Fe, Nb, C, allowing austenite (γ) and NbC. Because NbC is modelled as a pure substance, its composition cannot change as assumed in the derivation.

By setting a small total amount of Nb (0.03 mole %) and C (0.06 mole %) in the austenite, it is possible to match reasonably well the approximation of a dilute solution, as shown in table 5.2. The second part of this table is for the example used later and shows that the dilute solution approximation does not lead to significant error. When the

For $x^\gamma_{Nb} = 0.0003$ and $x^\gamma_C = 0.0006$, at 1173 K				
	Calculated with MT-DATA		Ideal solution approximation	
	Nb	C	Nb	C
Nb	3.25×10^7	-2.98×10^5	3.25×10^7	0
C	-2.98×10^5	1.63×10^7	0	1.62×10^7
For the composition chosen in example (0.2 Nb, 0.1 C wt%):				
	Calculated with MT-DATA		Ideal solution approximation	
	Nb	C	Nb	C
Nb	8.33×10^6	-2.97×10^5	8.32×10^6	0
C	-2.97×10^5	2.23×10^6	0	2.15×10^6

Table 5.2: The Hessian matrix of G (that is $\left[\partial^2 G_\gamma \,/\, \partial x_i \partial x_j\right]_{(i,j)}$) (J / mol) calculated with MT-DATA (left) and calculated using the dilute solution approximation (right).

concentration is further raised, RT/x_i^γ is still a good approximation for $\partial^2 G_\gamma / \partial x_i^{\gamma\,2}$, but the cross derivatives cannot reasonably be neglected.

5.5.b Effect of a Gibbs energy increase

In this example, the precipitate is NbC, which is modelled as a pure substance. The composition change of the matrix (γ) in equilibrium with NbC when the latter's Gibbs energy is increased by a constant term is considered.

Table 5.3 shows the expected composition change of the austenite in equilibrium with NbC at 1200 K, comparing the results of equation 5.5 and of equation 5.11 integrated to the value calculated with MT-DATA. The bulk composition is 0.2 wt% Nb, 0.1 wt% C. In this case, the C is in excess for the formation of NbC, and the modification of the Nb

	$\Delta x_C^{\gamma\theta}$ calculated with:		
PV_m^θ / (J/mol)	MT-DATA	Eq. 5.5	Integration of Eq. 5.11
1000	$\mathbf{2.4 \times 10^{-6}}$	7.74×10^{-4}	$\mathbf{2.4 \times 10^{-6}}$
5000	$\mathbf{1.85 \times 10^{-5}}$	6.03×10^{-3}	$\mathbf{1.84 \times 10^{-5}}$

Table 5.3: The modification of the carbon content (mole fraction) of the matrix in equilibrium with NbC when a constant Gibbs free energy is added, as calculated by MT-DATA and according to different equations.

content is well approximated by any formula. If the situation is opposite (Nb in excess), the effect of capillarity on Nb is overestimated by equation 5.5.

This shows clearly that a straightforward application of the Gibbs-Thomson formula leads to an error which can be large. With the correct multicomponent treatment (Eq. 5.11), the agreement is excellent.

Figure 5.4 shows the shift of the austenite/austenite+NbC boundary when the molar Gibbs energy of NbC is raised by 10000 J/mol. It should be noticed that, although the boundary calculated according to the method proposed by Fujita and Bhadeshia [93] does not lie very far from the exactly calculated one, the error on individual points is significant.

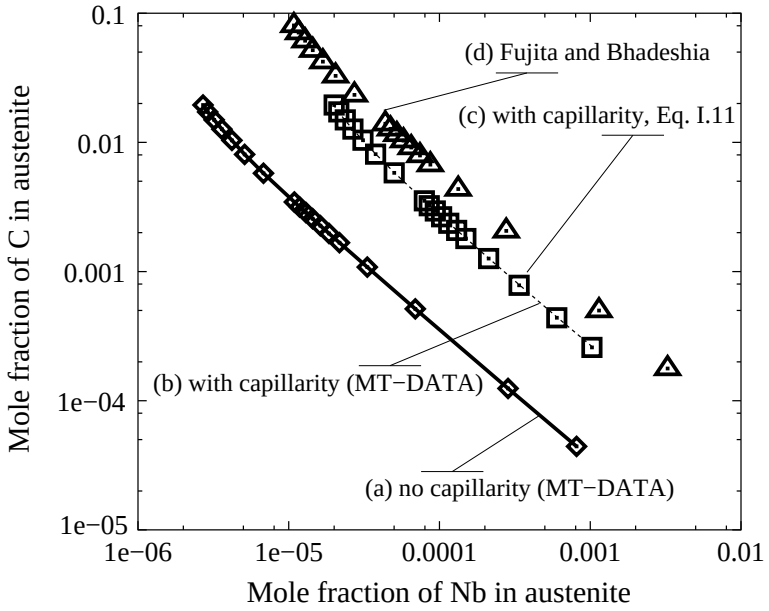

Figure 5.4: The shift of the $\gamma/\gamma + \mathrm{NbC}$ boundary at 1200 K for $\mathrm{P}V_m^\theta = 0$ (a), calculated with MT-DATA for $\mathrm{P}V_m^\theta = 10000$ J/mol (b), for the same addition using Fujita and Bhadeshia's method (c) and using equations 5.11 (d).

5.6 Consequences and conclusions

5.6.a Example

To illustrate the effect of the correction proposed to the Gibbs-Thomson equation, the model proposed by Fujita and Bhadeshia [93] for Mo_2C precipitation was used. The program available on MAP (http://www.cam.ac.uk/map/mapmain.html) was used as provided, then corrected to estimate capillarity effects using the system of equations 5.11.

Figure 5.5 shows the differences between the two curves; when additions of Mo and C are nearly stoichiometric, the error due to the use of the standard Gibbs-Thomson equation is relatively small (see figure 5.4, an example with Nb and C) and only the last part of the curve in which the transformation is mainly due to growth of the existing precipitates is significantly affected. When the additions of Mo and C are far from stoichiometric, the error is more important and so is the difference between the two curves. The trend is expected: it has been shown that use of the Gibbs-Thomson equation leads to large overestimation of the capillarity effect, and consequently, the effect on kinetics is exaggerated.

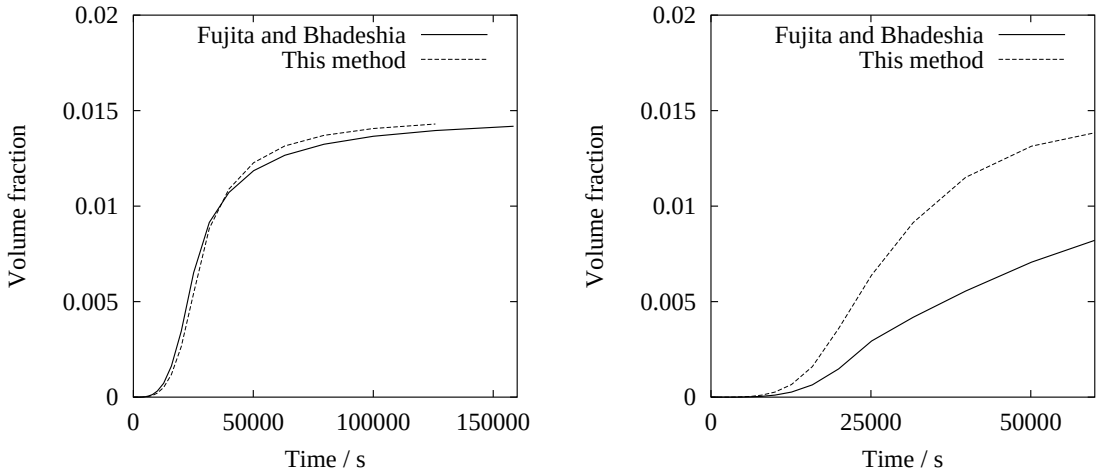

Figure 5.5: The volume fraction of Mo_2C in Fe-Mo-C steel. On the left, with all parameters as given on MAP (http://www.cam.ac.uk/map/mapmain.html), the initial mole fraction of Mo is twice that of C. On the right, the mole fraction of Mo and C have been chosen so as to give about the same amount of Mo_2C, but with a Mo addition ten times that of carbon, and the error due to the use of the Gibbs-Thomson equation is much larger, as can be seen on figure 5.4 with Nb and C for example.

5.6.b Conclusions

The Gibbs-Thomson equation has been applied in a number of studies dealing with multicomponent alloys, for example [93, 102]. It has been shown that the error can be large. This means that estimation of the coarsening rate, and of the influence of interface curvature on the kinetics of precipitation might be overestimated.

A simple solution has been proposed for a ternary system, one which can easily be extended to any number of components. It shows excellent agreement with the exact recalculation of the modified equilibrium when the assumptions are justified, that is in the case of a precipitate with fixed composition, in a matrix behaving like a dilute solution. When the precipitate is a solution whose composition is likely to change, the equation proposed estimates quite well the matrix composition change, but can not be applied to the precipitate, for which the approximation of dilute solution can not be made. It seems that solving analytically the problem of the precipitate composition change would be as complicated as recalculating the equilibrium, which can be made easily with thermodynamic calculation packages like MT-DATA.

Chapter 6

Overall transformation kinetics

6.1 Introduction

The model for the estimation of the growth rates of precipitates has been presented in chapter 4. Being able to predict correctly the growth rate is a first and important step; however, the overall transformation kinetics are also strongly dependent on the nucleation rate, and on the impingement effects described in chapter 3.

This chapter presents the methods used to estimate the overall transformation kinetics for multiple, simultaneous precipitation reactions in austenitic stainless steels.

6.2 Nucleation

Models for the nucleation rate have been presented in chapter 3. In the classical nucleation theory, the nucleation rate for a phase θ is given by:

$$I_\theta = N \exp\left(-\frac{G^*_\theta}{RT}\right) \nu \exp\left(-\frac{G^*_t}{RT}\right) \tag{6.1}$$

where G^*_θ is the activation energy for the nucleation of θ and G^*_t the activation energy for transfer of atoms across the $\gamma\theta$ interface; N is the number density of nucleation sites and ν is an attempt frequency taken as being kT/h. For a spherical precipitate θ, the activation energy for nucleation is given by:

$$G^*_\theta = \frac{16\pi}{3} \frac{\sigma^3_{\gamma\theta} {V_m^\theta}^2}{\Delta G^2_{m,\theta}} \tag{6.2}$$

where $V_m^{\theta\,2}$ is the molar volume of θ, $\sigma_{\gamma\theta}$ the energy per unit area of the interface γ/θ, $\Delta G_{m,\theta}$ the driving force for the precipitation of θ, per mole of components in θ. This unusual reference is prompted by the need to use a definition compatible with MT-DATA, in which the most reliable reference quantity is not the number of moles of a phase but the number of moles of components in a phase. Most of the times, these quantities are different, as for example, 1 mole of components in TiC corresponds to 0.5 mole of the phase. The molar volumes need to be defined accordingly, with, in the case of interstitial phases such as austenite, an additional complication introduced by the fact that not all component contribute to the volume, but only the substitutional one. However, calculating the number of moles of substitutional elements with MT-DATA is not a difficulty.

6.2.a Calculating the driving force for nucleation

The Gibbs energy change for precipitation reaction $\gamma \longrightarrow \gamma\prime + \theta$, where $\gamma\prime$ refers to austenite with a composition different from that of γ, can be written:

$$(n_0 - n_\theta)G_{\gamma\prime} + n_\theta G_\theta - n_0 G_\gamma \tag{6.3}$$

where n_0 is the initial number of moles of components in γ, n_θ the number of moles of components in θ at equilibrium and G_θ the Gibbs energy of θ per mole of component.

In most cases, the molar Gibbs energy of the precipitate is actually higher than that of the parent phase, and the main contribution to the driving force comes from the composition change of the latter. Table 6.1 illustrates this by giving examples of molar Gibbs energy for austenite, $M_{23}C_6$ and σ-phase. Obviously, the driving force for nucleation

	Austenite	$M_{23}C_6$	σ-phase
Gibbs energy (J/moles of components)	-50.53×10^3	-50.96×10^3	-45.99×10^3

Table 6.1: The molar Gibbs energy of austenite, $M_{23}C_6$ and σ-phase for a steel of composition 18 Cr, 12 Ni, 1 Mo, 1.5 Mn, 0.4 Si, 0.5 Nb, 0.05 Ti, 0.06 C wt%, at 750 °C. The formation of σ-phase is essentially justified by a reduction of the austenite molar Gibbs energy, rather than the formation of a phase of lower Gibbs energy as is the case for $M_{23}C_6$.

can not be estimated by $G_\theta - G_\gamma$ as this would imply that σ-phase never forms in alloys in which it is expected. The composition change contribution must be included, so that the driving force is best estimated by equation 6.3, divided by n_θ.

An additional difficulty has been presented in chapter 3: the most probable composition for the nucleus of θ is that for which the driving force for nucleation is maximum. However the method of the parallel tangents becomes increasingly difficult to implement mathematically as the number of components increases; furthermore, the Gibbs energy of the phases involved is not easily accessible as an analytical function of the composition. Approximating G_θ to the equilibrium value is however reasonable in these systems, since precipitates tend to have a very limited domain of existence, *ie* very sharply peaked Gibbs energy curves in the composition space. This is illustrated in figure 6.1. For the limit corresponding to fixed composition compounds, there is no difference.

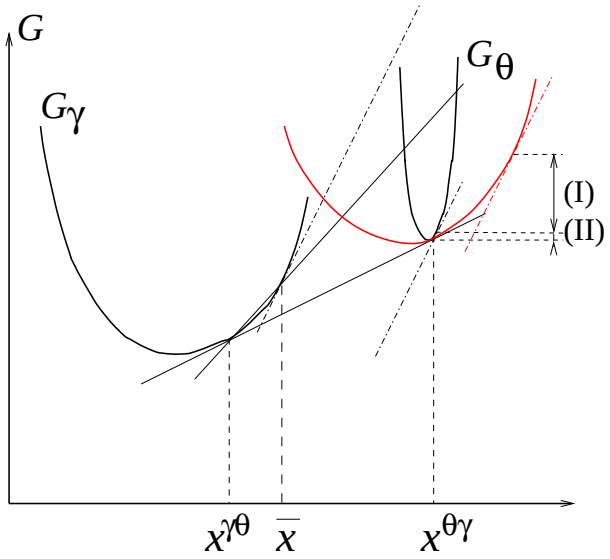

Figure 6.1: The parallel tangent construction as explained in chapter 3, for two cases: for precipitates, which often have limited domains of existence over the compositions space, approximating G_θ to the equilibrium value leads only to a small error (II). When θ is a more extended solid solution, the Gibbs energy of the most probable composition can be significantly different from that of the equilibrium composition (I).

Because the FORTRAN computer program written to model the precipitation kinetics is interfaced directly with MT-DATA, a software package to perform thermodynamic calculations with the use of the SGTE databases, it is possible to calculate the driving force for nucleation at each stage of the precipitation sequence. This avoids assumptions as to its evolution with time as needed to be made in the programs developed by Robson and Bhadeshia [88], or Fujita and Bhadeshia [93]. In these models, the initial driving force had to be given as an input, and the program then assumed a linear decrease as the

	$\Delta G_{m,\sigma}$
At $t = 0$	-77.7 J/mol
After formation of NbC and TiC	-130.0 J/mol

Table 6.2: The driving force for nucleation of σ-phase at the onset of precipitation, and after precipitation of TiC and NbC in an alloy of composition 18 Cr, 12 Ni, 1.0 Mo, 1.5 Mn, 0.5 Nb, 0.05 Ti, 0.06 C wt%, at 750 °C. The carbon depletion caused by TiC and NbC causes an increase in the driving force for σ-phase formation. Effects of this type cannot be identified when only the initial driving force is provided to the program which then assumes it to decrease with the supersaturation of Cr (in the case of σ phase).

supersaturation is reduced. By this method, it is impossible to grasp effects such as that of carbon on the formation of σ-phase: when carbon precipitates as NbC or TiC, the driving force for σ-phase formation is increased, although the supersaturation of chromium, the principal alloying element forming σ-phase, is not affected.

The use of MT-DATA as a slave application allows such interactions to be properly taken into account as a function of time, without any assumption about the evolution of the driving force or the precipitation sequence.

6.2.b The unknowns in the nucleation rate

The parameters N, $\sigma_{\gamma\theta}$ and G_t^* in equation 6.1 have to be determined for each phase in order to calculate the nucleation rate. The values that can be attributed to these parameters are bounded by physical considerations and comparisons. G_t^* can be attributed the value of the activation energy for self-diffusion of the principal element entering the precipitate, while the literature can also provide approximate values for the interfacial energy between precipitate and matrix.

However, because of the large influence these parameters have on the nucleation rate, in particular N, the most important constraints derive from the need to obtain a sensible evolution of the volume fraction of the precipitates. The parameters N and σ are therefore best seen as fitting parameters.

Figure 6.2 illustrates the influence of N, the nucleation site density, and $\sigma_{\gamma\theta}$, the interface energy per unit area, for the formation of $M_{23}C_6$ in an AISI 316 steel at 800 °C. Both have a considerable influence on the overall transformation rate, with up to 8 orders

of magnitude difference when the interfacial energy changes between 0.15 and 0.25 J/mol.

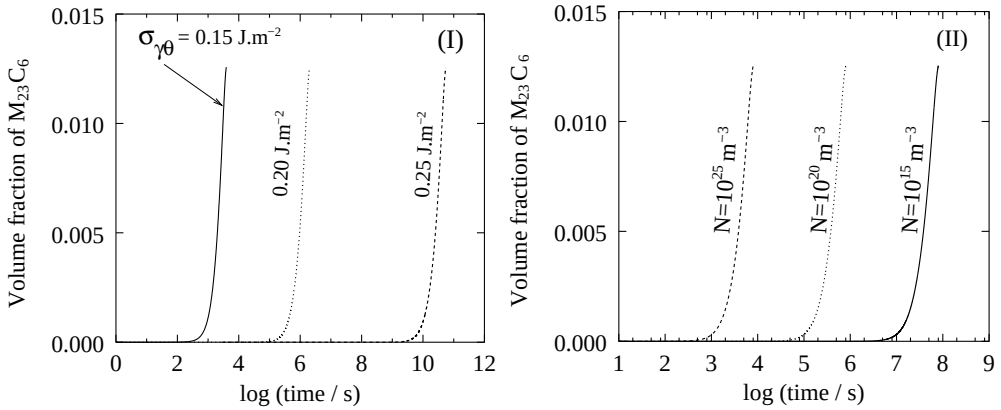

Figure 6.2: The effect of (I) the interfacial energy $\sigma_{\gamma\theta}$ with $N = 10^{19}$ m^{-3} and (II) the nucleation site density N with $\sigma_{\gamma\theta} = 0.2$ J m^{-2} on the the overall kinetics of $M_{23}C_6$ formation in an AISI 316 steel, all calculations are for 800 °C.

Although there is a considerable amount of literature regarding precipitation in austenitic stainless steels, there is virtually no reliable quantitative study of the precipitation sequence. Identical difficulties in obtaining volume fraction have been met in this work and are presented in chapter 8. The published literature mostly reports TTP (time temperature precipitation) diagrams such as figure 2.7. Such diagrams do not provide quantitative data since they neither indicate the end of precipitation, nor the exact start: there is no standard quantity defining the onset of precipitation, which depends on the experimental methods used.

The values adopted later are therefore based on an attempt to match predictions with general observations reported in TTP diagrams.

6.3 Overall transformation kinetics

To estimate the overall transformation kinetics, it is necessary to account for both soft and hard impingement. Figure 6.3 illustrates, in a simplified manner, the functioning of the FORTRAN program interfaced with MT-DATA, used to estimate the overall kinetics of simultaneous precipitation reactions.

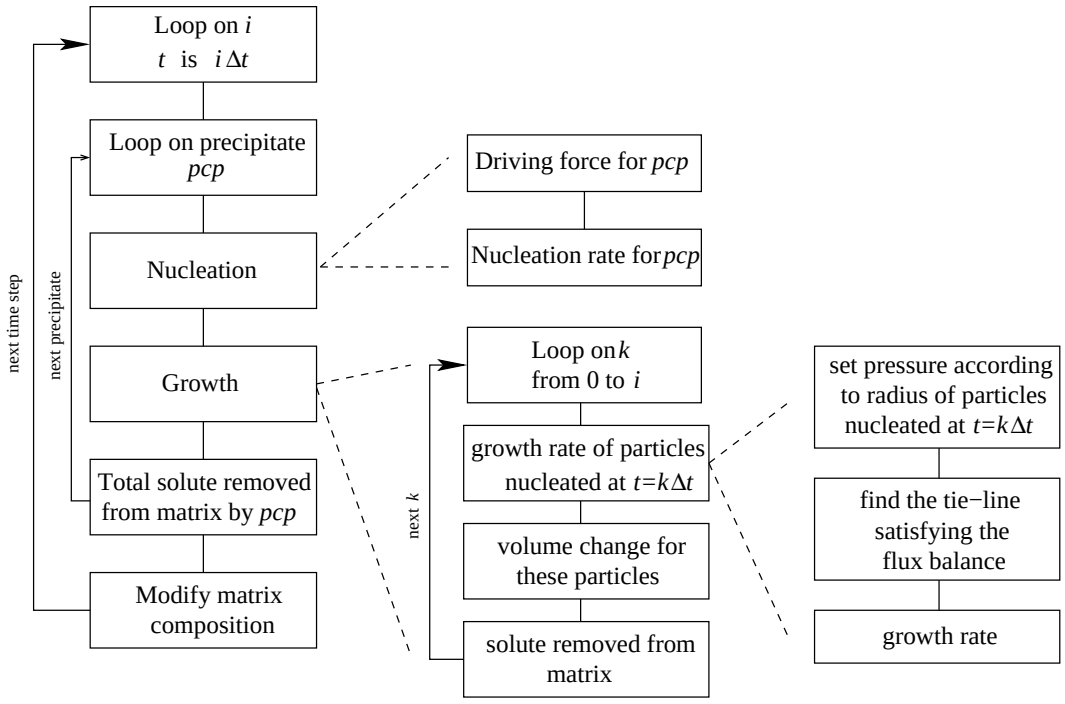

Figure 6.3: Simplified illustration of the functioning of the FORTRAN program written to estimate the evolution of simultaneous precipitation reactions. t is the time and Δt the increment, pcp is a variable identifying the phases allowed to form.

During a time step, the program considers in turns all the different phases allowed to enter the calculation, and calculates the volume increase from each of them. This increment, is, as explained in chapter 3, an extended volume, and has to be corrected according to [88]:

$$\mathrm{d}V^{f,\theta} = \left(1 - \sum_{k} V_{f,k}\right) \mathrm{d}V^{e}_{f,\theta} \tag{6.4}$$

where $\mathrm{d}V_{f,\theta}$ is the change in volume fraction of θ, $V_{f,k}$ the volume fraction of precipitate k, and $\mathrm{d}V^{e}_{f,\theta}$ the change in extended volume fraction of θ. However, in the present case, this

correction is of negligible consequence, as precipitation phenomena involve small volume fractions.

Consider component i, for which the amount $\overline{c_i}V_{f,\gamma}+\sum_k V_{f,k}c_i^{k\gamma}$ is constant due to mass conservation, and therefore, the matrix composition changes according to the increment of precipitate θ (noting that $V_{f,\gamma} = 1 - \sum_k V_{f,k}$) as follows:

$$\mathrm{d}\overline{c_i} = \frac{\left(\overline{c_i} - c_i^{\theta\gamma}\right)\mathrm{d}V_{f,\theta} - \overline{c_i}}{V_{f,\gamma}} \tag{6.5}$$

where $\mathrm{d}\overline{c_i}$ is the change of matrix composition. This quantity is calculated in turn for each precipitate, and the matrix composition is updated at the end of the time step. The program also verifies that the composition change is small compared to the content of the matrix, so as to ensure the step size is not too large.

The method described in figure 6.3 requires significant computing power. Each loop to identify a tie-line can take up to 50 iterations (figure 4.4), each including an equilibrium calculation. This is repeated as many times as is the current time step, that is, step 1000 requires 1000 iterations to calculate the growth rate of all the precipitates nucleated at earlier times. The whole process is also repeated as many times as there are precipitates. Typical calculation times are 2-3 days on 64 bits, 450 MHz processor machine. When capillarity effects are neglected, however, the tie-line is unique to all precipitates of the same nature and there is no need to calculate one for each different nucleation time.

6.4 The tie-line shifting phenomenon

As explained in chapter 4, the composition of precipitates such as $M_{23}C_6$ is expected to be modified by the need to satisfy the flux balance at the interface matrix/precipitate. The tie-line satisfying the flux-balance at the onset of precipitation does not generally go through the bulk composition. However, as the precipitation reaction progresses, the matrix composition is modified, and as a consequence, the tie-line satisfying the flux-balance shifts towards the one going through the bulk composition P (figure 6.4).

Many studies have reported composition changes in $M_{23}C_6$ as its precipitation progresses [100, 67, 104]: the Cr content increases while the Fe content decreases. This was correctly reproduced by the model, as illustrated in figure 6.5, which shows the Cr and Fe content of $M_{23}C_6$ in an AISI 316 steel, as precipitation progresses.

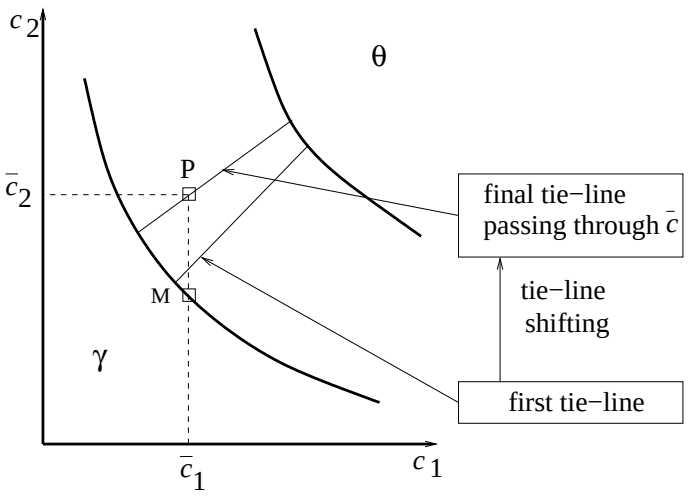

Figure 6.4: Illustration of the tie-line shifting phenomenon. As the supersaturation of elements 1 and 2 decreases, the tie-line satisfying the flux-balance approaches that going through point P, the bulk composition.

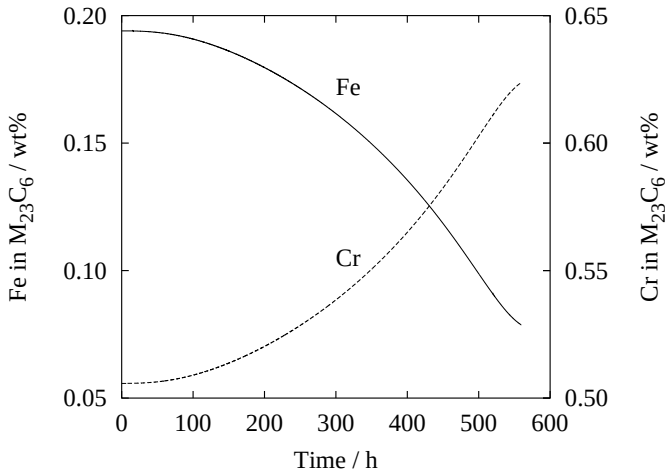

Figure 6.5: Verification of the tie-line shifting phenomenon during the precipitation of $M_{23}C_6$ in an AISI 316 steel at 800 °C. The initial Fe content is larger than expected from an equilibrium calculation, while the Cr is lower. As precipitation reaches completion, both the Fe and Cr contents return to their equilibrium values.

Similar observations have been made for MC type carbides (e.g. NbC, TiC), as mentioned in chapter 2: these carbides grow with a chromium content much larger than is the equilibrium value, and with a carbon content below a 1:1 atomic stoichiometry. However, because they are modelled as pure substances in the SGTE databases, it is not possible to reproduce these composition changes.

6.5 Multiple precipitation reactions

One of the main advantages of the model developed is its ability to cope with as many simultaneous precipitation reactions as required by the user, provided that thermodynamic data are available in the databases used by MT-DATA.

6.5.a Precipitates drawing from the same solute

The various phases likely to form in austenitic stainless steels frequently draw on one or two similar solutes. For example, $M_{23}C_6$ and TiC compete for carbon, σ-phase and $M_{23}C_6$ for chromium, *etc.*

When strong carbide formers such as Ti or Nb are added in sufficient quantities, $M_{23}C_6$ is not expected to be present at equilibrium. It is however usual to observe the latter forming at early stages of the ageing. The AISI 321 steel (17.1Cr, 12.6Ni, 1.5Mn, 0.5Si, 0.49Ti, 0.11C wt%) as studied by Thorvaldsson [105] is a good example of the importance of interactions in precipitation sequences. Table 6.3 gives the equilibrium state, as calculated with MT-DATA for this steel, at 750 °C.

Phase	volume fraction / %
σ-phase	0.058
TiC	0.74

Table 6.3: The equilibrium at 750 °C for the AISI 321 steel studied by Thorvaldsson *et al.* [105], calculated with MT-DATA.

It is noticeable the σ-phase is predicted to be present at equilibrium, although there is no driving force for its formation when considering the transformation of the initial austenite, or even after solution treatment at 1250 °C. Table 6.4 gives the austenite composition after solution treatment at 1250 °C.

Element		Cr	Ni	Mn	Si	Ti	C
Bulk composition	**wt %**	17.2	12.6	1.5	0.5	0.49	0.11
After sol. treat.	**wt %**	17.14	12.63	1.503	0.501	0.302	0.063

Table 6.4: The bulk composition and the austenite composition after solution treatment at 1250 °C for the AISI 321 steel studied by Thorvaldsson [105].

As illustrated in figure 6.6, the kinetics of formation of TiC are affected by the formation of $M_{23}C_6$, which also draws carbon from the matrix. $M_{23}C_6$ is not expected as an equilibrium phase, but forms for kinetic reasons.

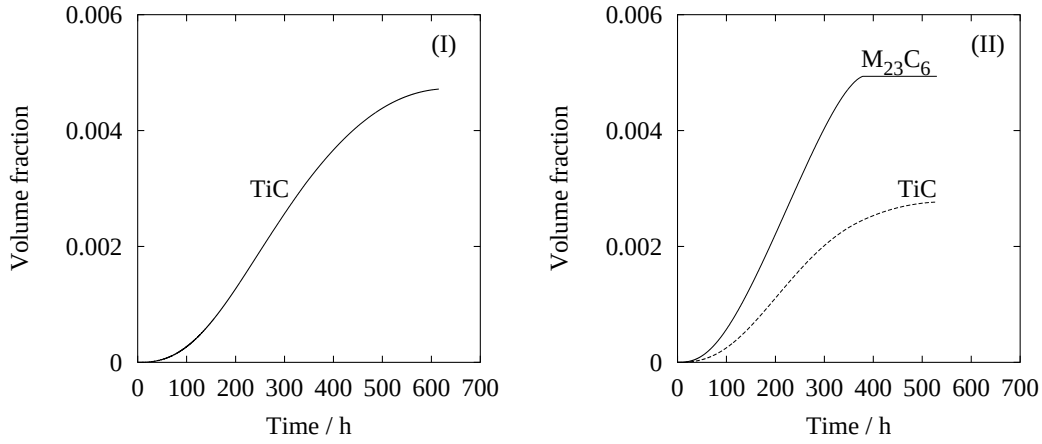

Figure 6.6: The predicted kinetics of formation of TiC in the AISI 321 steel studied by Thorvaldsson [105], (I) allowing only TiC and (II) allowing $M_{23}C_6$ and TiC, showing clearly the interactions as the two precipitates compete for carbon. $M_{23}C_6$ is not expected to be an equilibrium phase but forms for kinetics reasons.

Although interactions between precipitates are expected such as those presented in figure 6.6, a valid prediction is still required to show TiC as the only phase remaining after sufficient ageing, as given by the equilibrium calculation. For this, the model needs to account for the dissolution of transient phases.

6.5.b Dissolution of precipitates and transient phases

To illustrate the method used to implement the dissolution of precipitates, the example of the AISI 321 steel above is used again.

Figure 6.6 (II) shows that, after some time, $M_{23}C_6$ precipitation reaches completion. However, TiC, more stable than $M_{23}C_6$ according to MT-DATA, keeps on drawing carbon from the matrix, leading to the situation illustrated in figure 6.7: when precipitation of $M_{23}C_6$ is completed, the composition of the matrix is given by M′, which is on the tie-line going through the bulk composition P. This tie-line shifting phenomenon was explained previously. During the next time step, TiC draws carbon from the matrix, explaining the shift (1) of point M′, but also increases its own volume fraction. Since the matrix chromium content is not affected by the formation of TiC, but its volume fraction is

slightly reduced, the chromium concentration, and of any other element not included in TiC, is increased. This explains the shift (2) in the change from M′ to M″.

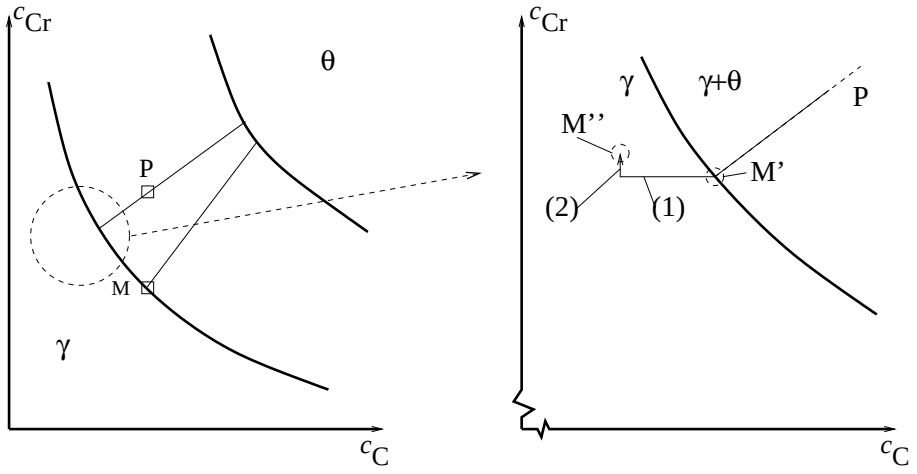

Figure 6.7: Illustration of the matrix composition change resulting from the continued formation of TiC when $M_{23}C_6$ precipitation is completed.

It is important to notice that both shifts (1) and (2) are very small, as they correspond to the quantity of solute drawn during a single time step, the latter being set so as to prevent composition modifications which are not negligible compared to the matrix content, as explained earlier. Here again, the tie-line giving the interface composition during dissolution is expected to be the one respecting the iso-activity of carbon. However, because M″ is very close to M′, the shift is of negligible proportion. Another consequence is that the supersaturation (although negative) is very small, and therefore simplified model such as Zener's approximation presented in equation 3.26 can be used.

The case when a phase dissolves with a larger negative supersaturation is different and cannot be treated with these approximations. For example, when $M_{23}C_6$ formed during service at about 700 °C is dissolved during solution treatment at 1200 °C, the point representing the bulk composition in the phase diagram is at a non-negligible distance from the $\gamma/\gamma + \theta$ boundary. Therefore the above treatment for the dissolution of phases is essentially valid for transient phases.

Figure 6.8 illustrates the predicted behaviour of the AISI 321 steel whose composition is given in table 6.4. Comparisons with experimental results are reasonably satisfying, since results by Thorvaldsson *et al.* [105] suggest that, for this steel, precipitation of TiC is completed after about 1000 h. However, the authors report a dissolution of TiC for

$M_{23}C_6$ and not the opposite. As reported in chapter 2, this observation is controversial. The dissolution cannot be predicted if the phase stability calculations indicate TiC as the equilibrium precipitate.

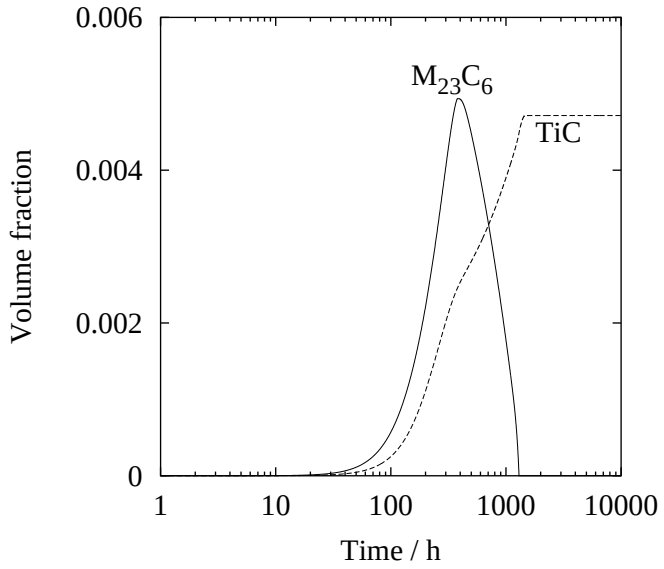

Figure 6.8: The calculated volume fraction of $M_{23}C_6$ and TiC as a function of time in an AISI 321 steel, during ageing at 750 °C. $M_{23}C_6$ is expected as a transient phase only. The volume fraction of TiC does not include the amount left undissolved after solution treatment.

Table 6.3 shows that σ-phase is also expected at equilibrium in the considered AISI 321 steel. However, it is neither predicted by the present model nor observed by Thorvaldsson [105]. The model does predict a non-zero driving force for its formation, when precipitation of TiC has almost reached completion. This is because both the low carbon and high chromium expected at that stage are favourable to σ-phase formation. Nevertheless, this driving force is too low for the formation of σ-phase to occur in an observable time.

6.6 Predicting the behaviour of different steels.

As mentioned earlier, there is little quantitative information regarding precipitation in austenitic stainless steels. Furthermore, results obtained by different methods differ significantly. For example, the work used in the previous section, from Thorvaldsson and

Dunlop [105], indicates that the maximum volume fraction of MC type carbides is reached after about 1000 h, on the basis of TEM investigations. On the other hand, Thorvaldsson *et al.* [104], in a different publication on a similar steel, in identical conditions, report the maximum volume fraction of MC type carbides to be reached after 3 to 8 hours, on the basis of resistance measurement.

This renders difficult if not impossible the task to estimate the adjustable parameters N and $\sigma_{\gamma\theta}$ for these phases. However, the time scale for the formation of such carbides and nitrides remains small in comparison with the typical lifetime, and therefore the error introduced in the precipitation sequence is of little consequence.

6.6.a The formation of σ-phase in the AISI 300 series

The case of σ-phase, which incidentally is believed to be more relevant to long term creep properties than the various carbides, is better defined. Minami *et al.* [44] provide data on the microstructural evolution of the main AISI 300 series steels, which have been used to refine the parameters N_σ and $\sigma_{\gamma\sigma}$. The use of equation 6.1 to predict the nucleation rate for σ-phase leads however to meaningless values of these parameters: only with interfacial energies close to zero and extremely large N_σ would a sufficient nucleation rate be obtained. Observation of σ-phase in such steels also indicates a difficulty in nucleation, as this phase is almost exclusively found on grain boundary triple points.

A simple model was therefore used to estimate triple point nucleation. Triple point nucleation can be integrated within the model without loss of consistency: the points can be assumed to be uniformly distributed in space and therefore the treatment of the hard and soft impingement remains valid. This is not the case for grain surface nucleation, where both soft and hard impingement effects may be strongly localised.

A simple modification to equation 3.20 was done to account for the extra amount of grain boundary surface eliminated when nucleation occurs on a triple point:

$$G_B^* = \frac{4}{27} \frac{\left\{ \eta_{\gamma\theta}\, \sigma_{\gamma\theta} - \frac{3}{2} \eta_{\gamma\gamma}\, \sigma_{\gamma\gamma} \right\}^3}{{\eta_\theta}^2 {\Delta G_v}^2} \tag{6.6}$$

where the different terms are as defined in equations 3.21.

6.6.b σ-phase in AISI 304

The case of AISI 304 is interesting to start with because σ-phase is the only phase expected, with the exception of $M_{23}C_6$ which is precipitated in the very early stages of

ageing. The absence of interaction with other precipitation phenomena simplifies greatly the determination of the parameters N_σ and $\sigma_{\gamma\sigma}$.

i Parameters optimisation

For a given ageing temperature, there is an infinite number of combinations of parameters $N_\sigma, \sigma_{\gamma\sigma}$ to obtain a similar result for the volume fraction as a function of time. For example, a greater interfacial energy renders nucleation more difficult but N_σ can be raised to compensate.

However, if N_σ and $\sigma_{\gamma\sigma}$ have been chosen too large for example, the nucleation rate will be overestimated at lower temperatures and, and underestimated at higher temperatures. Therefore, values for N_σ and $\sigma_{\gamma\sigma}$ have to be obtained that fit published data over a range of temperatures.

For N_σ, a first guess can be made by estimating the number of triple points per unit volume ($10^{10} - 10^{14}$ m^{-3}), while the value of the interfacial energy for a grain boundary was used as a starting point for $\sigma_{\gamma\sigma}$.

ii Results

With $N_\sigma = 3 \times 10^{12}$ m^{-3} and $\sigma_{\gamma\sigma} = 0.283$ J/m^2, good agreement could be obtained between the predictions and both the time temperature precipitation diagram and the quantitative measurements obtained by Minami *et al.* [44], as illustrated in figure 6.9.

The disagreement at high temperatures is essentially due to thermodynamic data on which the model rely: MT-DATA predicts an equilibrium amount of σ-phase which is not consistent with the observation made by Minami *et al.*, and it is therefore not surprising that the kinetics of its formation is underestimated.

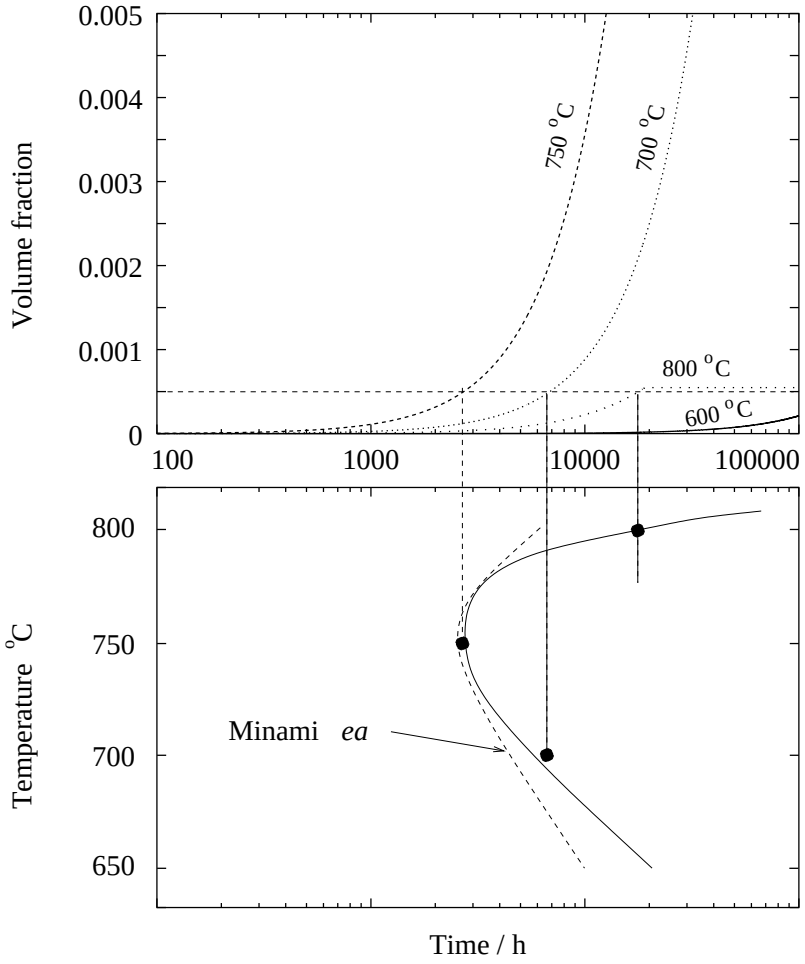

Figure 6.9: TTP (Time Temperature Precipitation) diagram for the formation of σ in an AISI 304 steel of composition: 18.7Cr, 9.0Ni, 1.73Mn, 0.6Si, 0.05C wt%. Predictions are compared to the TTP diagram obtained by Minami *et al.* [44]. The detection limit is assumed to be a volume fraction of 0.05 %. $M_{23}C_6$ is found at all times and temperatures, both experimentally and in predictions.

6.6.c Other steels in the AISI 300 series

i Observed and predicted trends

Figure 6.10, after [44] shows the evolution of the volume fraction of σ-phase as a function of ageing time at 700 °C, in different steels of the AISI 300 series. It has been proposed that the very low carbon level of the austenite in steels such as AISI 321 or AISI 347 is responsible for the rapid formation of σ-phase (chapter 2).

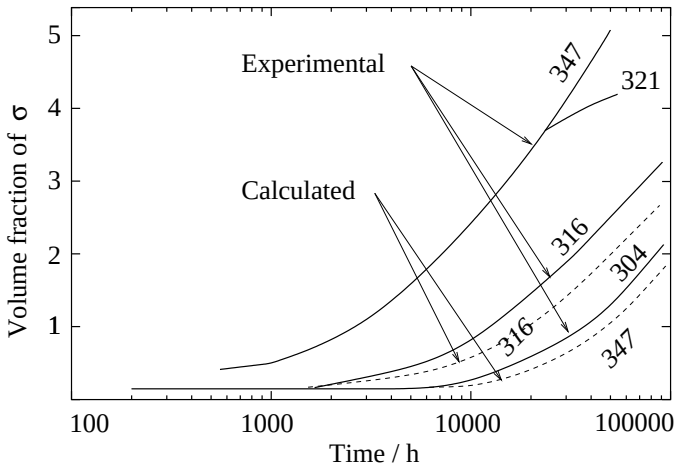

Figure 6.10: The rate of formation of σ-phase at 700 °C in different steels of the AISI 300 series, after [44]. Both 321 and 347 contain strong carbides formers (Ti and Nb respectively) which reduce the austenite carbon content to almost zero. Dashed lines show the predictions with the parameters obtained by fitting the curve for the AISI 304 steel.

Because of variations in the grain size, or thermo-mechanical history, it is probable that the values of N_σ and $\sigma_{\gamma\sigma}$ will have to be slightly adjusted. However, with the exception of AISI 316 in which σ-phase is predicted to form slightly faster than in AISI 304, the predictions show a trend opposite of that reported by Minami *et al.* [44], as illustrated in figure 6.10: σ-phase is predicted to form at a slower rate in AISI 321 and 347. Table 6.5 shows the driving force for the formation of σ-phase in these different steels, at the end of the carbides formation, where it is expected to be greatest.

The prediction of a slower formation of σ-phase in AISI 321 and 347 compared to 304 can therefore be expected from the thermodynamic data underlying the model, since the classical theory for nucleation predicts a greater nucleation rate when the driving force is larger.

It seems reasonable to assume that the growth rate of σ-phase does not vary signifi-

Element wt%	Cr	Ni	Mn	Si	Ti	Nb	C	ΔG_m J/mol
AISI 304	18.20	9.07	1.73	0.60			2.15×10^{-3}	-209.7
AISI 347	17.68	10.45	1.65	0.59		0.48	4×10^{-5}	-169.7
AISI 321	17.64	10.53	1.76	0.59	0.15		6×10^{-5}	-176.1
AISI 316 (2.3 Mo)	16.09	12.01	1.83	0.64			5.4×10^{-4}	-288.4

Table 6.5: The composition of 4 different steels studied by Minami *et al.*, after precipitation of all carbides, calculated with MT-DATA, and the driving force for the formation of σ-phase from the austenite of this composition, expressed in joules per mole of components. All calculations are for 700 °C.

cantly between the different steels; this is supported by the fact that the slopes in figure 6.10 are similar. Therefore, as already proposed in the literature (e.g. [67]), the cause is most likely to be found in the nucleation process, although the above results on the driving force indicate that classical theory may not provide an explanation.

ii Is the classical theory for nucleation failing ?

The former section indicates that, although the driving force for the nucleation of σ-phase is expected to be lower in AISI 347 when compared to AISI 304, nucleation actually occurs significantly faster in the former.

Because the different steels present reasonably similar nucleation site densities, it seems justified to propose as above, that the prefactor N in the nucleation rate equation 6.1 does not vary significantly between two steels. However, further examination of the classical theory will reveal that this assumption may be erroneous.

One of the first steps of the nucleation theory consists in counting the number of nuclei which have reached the critical radius, and to which is associated an energy G^*_θ, as explained in chapter 3. This is done by assuming that the probability of finding such nuclei is given by a Boltzmann distribution:

$$N_{critical\ nuclei} \propto \exp\left(\frac{-G^*_\theta}{RT}\right) \tag{6.7}$$

However, it must not be forgotten that such an equation actually gives the probability for a fluctuation of composition/structure of energy G^*_θ. For the sake of simplicity, structure fluctuations are neglected in the following discussion.

In a binary alloy, there is an equivalence relationship between a composition fluctuation of given spatial extension, and a fluctuation of given energy. This is illustrated schematically in figure 6.11.

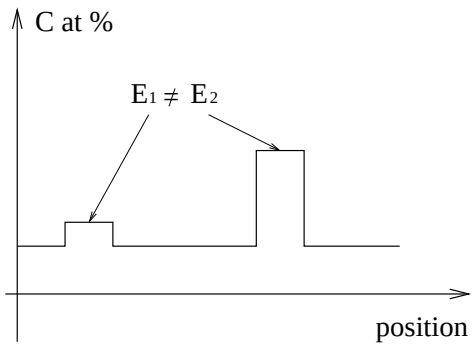

Figure 6.11: In a binary alloy, for example Fe-C, fluctuations of the carbon content are uniquely associated to an energy which can therefore be written E(C).

In this case, it is reasonable to assume that the prefactor N does not include any composition dependencies, which are all present in the exponential term.

The situation is however different in multicomponent alloys. In the following, the hypothetical case of the nucleation of σ-phase in a Fe-Cr-C system is considered as an example and fluctuations in both the carbon and chromium content are examined. As illustrated schematically in figure 6.12, a number of different fluctuations may have the same energy.

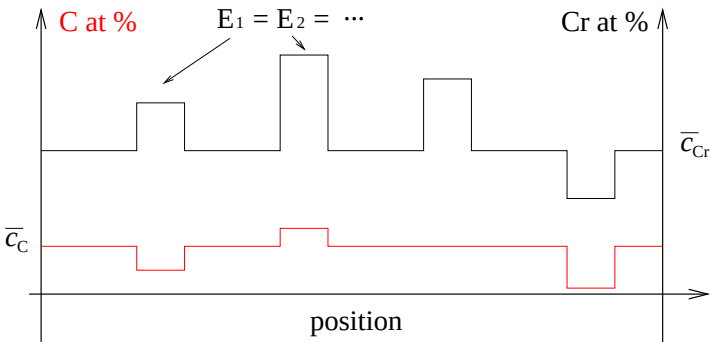

Figure 6.12: Schematic illustration of composition fluctuations in a Fe-Cr-C alloy. Different fluctuations may be associated with the same energy, but not all are events leading to the formation of a nucleus.

However, only a fraction of the composition fluctuations of energy G^*_θ is of interest for the nucleation of σ-phase. Therefore, the probability to form a critical nucleus is better written $f \exp\left(-G^*_\theta/RT\right)$ than $\exp\left(-G^*_\theta/RT\right)$, where f is the fraction of the fluctuations of

energy G_θ^* that may lead to the formation of σ-phase. Equation 6.1 can then be re-written:

$$I_\theta = f N_0 \exp\left(-\frac{G_\theta^*}{RT}\right) \nu \exp\left(-\frac{G_t^*}{RT}\right) \tag{6.8}$$

This never appears in practice since the prefactor is fitted as a single entity, and it is probably difficult to estimate f on a theoretical basis.

It is now considered, as a simple model, that composition fluctuations leading to the formation of a σ-phase nucleus are those raising simultaneously the Cr content above, and lowering the C level below, critical values, since the carbon solubility in σ-phase is close to zero. Figure 6.13 illustrates two different cases: when the average carbon content of the austenite ($\overline{c_C}$) is relatively high, the fraction of the fluctuations of identical energies which brings the carbon content below the critical level is smaller than when $\overline{c_C}$ is low.

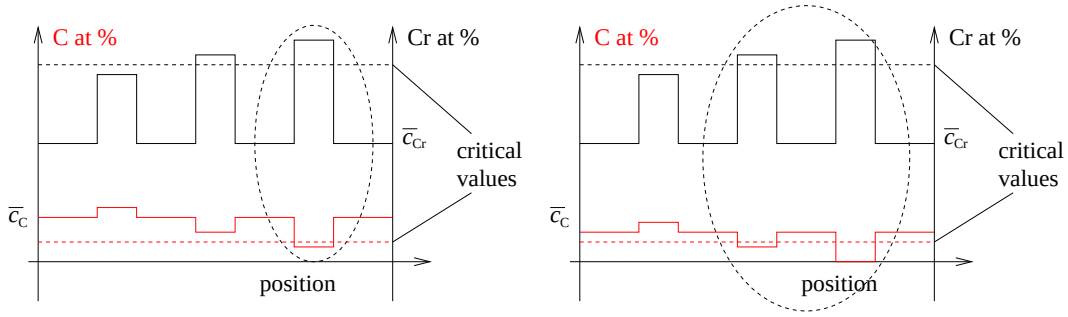

Figure 6.13: Schematic illustration of different composition fluctuations in two cases. The fractions of the fluctuations which can lead to the nucleation of σ-phase is higher when the average carbon content of the austenite is lower.

Using again the calculated carbon content of the austenite (table 6.5), and attributing a factor f_{304} and f_{347} to the steels of same names, we can expect, on the basis of the above argument, $f_{304} \ll f_{347}$ since the austenite carbon content is much lower in the AISI 347 steel. Having fitted $N_{\sigma,304} = N_0 f_{304}$ to experimental data, it is now expected that the prefactor $N_{\sigma,347} = N_{\sigma,304}(f_{347}/f_{304})$ be much larger than $N_{\sigma,304}$.

Further validation is obtained when considering the case of the AISI 316 steel, in which the rate of σ-phase formation is also under-estimated. Following identical reasoning, and since the austenite carbon content is lower in the AISI 316 steel than it is in 304 (table 6.5), the fraction f_{316} is expected to be larger than f_{304} and consequently the prefactor $N_{316} = N_{304}(f_{316}/f_{304})$ larger than the experimentally derived N_{304}. This would lead to a shift to the left of the curve, consistent with observations.

Finally, the tendency to underestimate the kinetics of σ-phase formation at lower temperatures for the reference steel, as visible in the TTP diagram 6.10, could also be explained by the austenite carbon content decreasing with the temperature, as shown in figure 6.14.

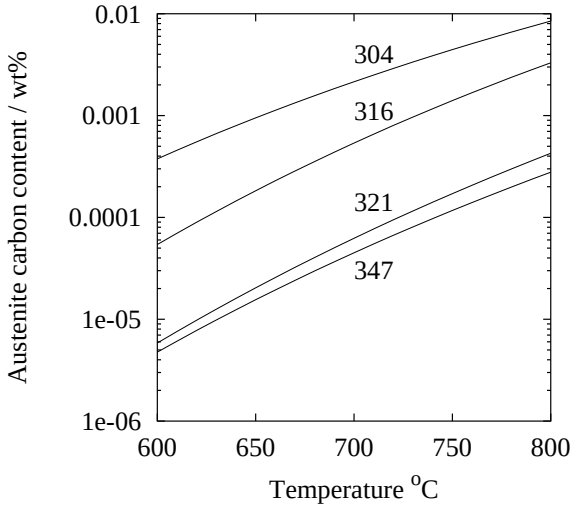

Figure 6.14: The carbon content of the austenite after precipitation of all carbides in different steels from the AISI 300 series, calculated with MT-DATA.

Figure 6.15 shows that better agreement is obtained for increasing N as the carbon content decreases. However, due to the restricted amount of quantitative data available, it was not possible to obtain a relationship between N and the carbon content of the austenite. Such a relationship would only hold for a given steel, as the introduction of additional elements such as Mo should, according to the explanation proposed above, further modify the prefactor N.

The example used above is based on a ternary system, and it should be underlined that in a system with many more components, there will be an even greater number of composition fluctuations of identical energies, which will be of no interest for the nucleation of a given phase. Therefore one can expect the factor f to decrease in general, as the number of components increases.

In conclusion, it is shown that, in multicomponent alloys, it is not reasonable to expect the prefactor N_σ to be independent of the composition of the steel. The composition dependency is only qualitatively explicited here but is opposite of the more intuitive argument provided by Fujita and Bhadeshia [93], which proposes that N is expected to

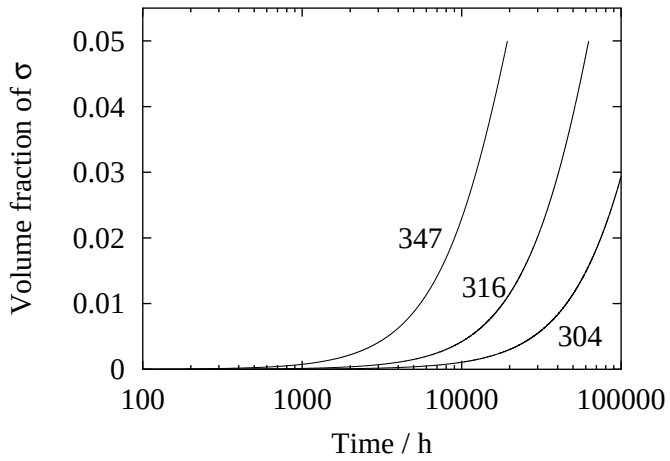

Figure 6.15: The predicted amount of σ-phase forming at 700 °C in different steels of the AISI 300 series is in better agreement with observations when allowing an increasing prefactor N as the carbon content decreases. Here, $N = 3 \times 10^{12}$ m^{-3} for 304, $N = 4 \times 10^{12}$ m^{-3} for 316 and $N = 8 \times 10^{13}$ m^{-3} for 347.

increase as the driving force (the volume fraction) for precipitation increases. In the present case, the steels with lower driving forces are actually expected to have the largest N_σ, although it should not be concluded that there is a correlation between the two.

6.6.d Other phases and difficulties

As mentioned earlier, there are significant experimental uncertainties which render difficult the task of identifying the parameters N and σ for each phase.

Of greater importance are the discrepancies between the observed behaviours of steels and the thermodynamic data on which this model relies, or the absence of such data.

Figure 6.16 shows the complete precipitation sequence for an AISI 316 steel, at 700 °C, which is in good agreement with the work of Minami *et al.* [44]. However, at 750 °C, χ phase is found experimentally, but is not predicted to form by the model. This is because, according to MT-DATA, the driving force for its formation is zero throughout the precipitation sequence.

Similar problems occur with Nb rich steels (AISI 347) in which Fe_2Nb and Fe_3Nb_3C are expected to form when Nb is in excess (chapter II). Although the formation of the former is correctly predicted, its dissolution for the latter cannot be accounted for, since there are no thermodynamic data for Fe_3Nb_3C.

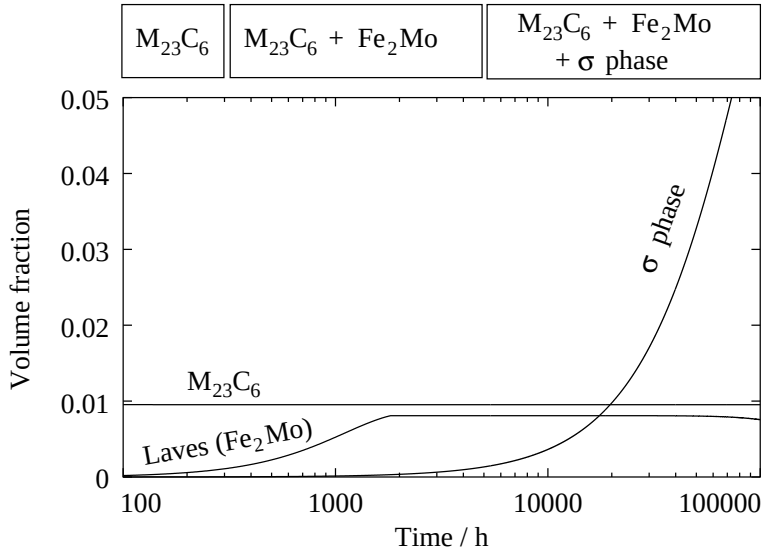

Figure 6.16: The evolution of the volume fraction of different phases in an AISI 316 steel at 700 °C, and on the upper part, the phases observed experimentally by Minami *et al.* [44].

Phases such as Cr_3Ni_2SiX or Z-phase are not represented in the SGTE database, therefore making impossible any meaningful prediction on nitrogen bearing steels.

6.7 Practical aspects of the software

Figure 6.17 illustrates the overall functioning of the software. As mentioned earlier, it is interfaced with the thermodynamic calculation package MT-DATA, and has been written so as not to implicitly incorporate knowledge about the phases. That is to say, none of the algorithms contain assumptions about what component may control the growth or dissolution of any precipitate, nor about which precipitate may form or not. Therefore any correction or addition in the databases is immediately reflected in the model, which can be used with any phase described in the thermodynamic databases.

Physical information about the phases is stored in a separate file, which contains the lattice parameter, number of atoms per unit cell, temperature dependency of the lattice parameter if known, and the nucleation parameters N and σ.

The solution treatment is modelled by assuming that equilibrium is reached at the given temperature. For example, when predicting the evolution of the microstructure of

an AISI 347 steel, it is essential to include a solution treatment, at typical temperatures of 1100-1200 °C which calculates the amount of undissolved phases and sets a new bulk composition before proceeding with the ageing.

By default, the diffusion coefficients are calculated for Fe-Cr-Ni-C alloys, as explained in chapter 4, however the user has the possibility to enter alternative values for a different system.

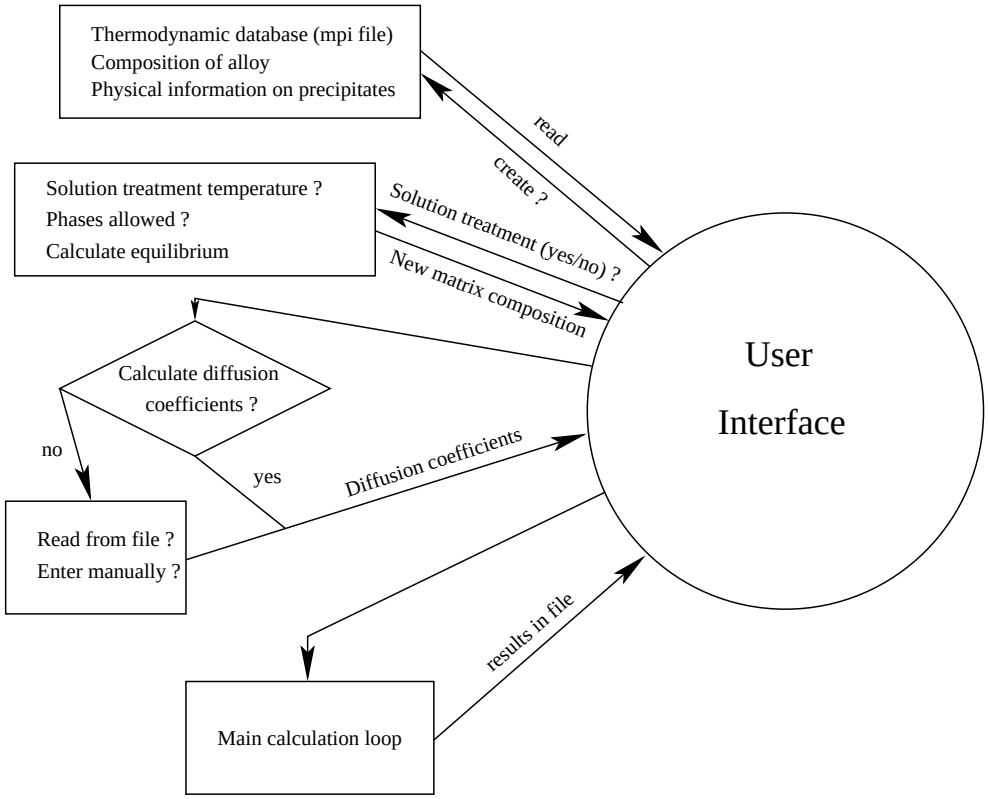

Figure 6.17: General functioning of the software developed in interface with MT-DATA, which can be used with any phase present in the SGTE databases provided that informations such as lattice parameters, interfacial energies, *etc* are present or provided.

Finally, the program is written in a modular manner which allows for easy modifications or additions.

6.8 Summary and conclusions

A general model for multiple precipitation reactions in multicomponent systems has been created using the thermodynamic software MT-DATA as part of a FORTRAN program. Effects particular to multicomponent systems have been shown to have significant importance and have been accounted for. This includes a treatment of the flux-balance problem and of multicomponent capillarity.

A major difficulty remains in the lack of reliable quantitative experimental data. However, general semi-quantitative aspects are very well predicted considering the relative simplicity of the model, which, for example, does not account for the role of grain boundaries. This causes an over estimation of the overall growth rate, as the actual hard impingement effects are underestimated for phases growing on grain boundaries.

A further effect of the multicomponent nature of the systems considered appeared in the calculation of the nucleation rate. It was shown that examining the nucleation rates in terms of driving force only, could lead to considerable error. An argument was proposed to explain that the prefactor N in the classical nucleation theory was itself strongly dependent on the composition. This implies the existence of strong limitations in the predictive power of any model based on the classical theory for nucleation, as the value of N may have to be fitted for each single composition. It seems important to reconsider the classical theory for nucleation and adapt it so as to deal with multicomponent effects.

Chapter 7

Experimental Procedures

7.1 Introduction

The experimental work consists essentially of the identification of different kinds of precipitates formed during ageing treatments.

As has been outlined in the presentation of precipitated phases in austenitic stainless steels, the identification of carbides, nitrides and intermetallic phases is not straightforward, bearing in mind that:

- The size of the precipitates ranges from about 15 nm to 5 μm. For the smallest particles, only TEM (transmission electron microscopy) is appropriate, but it is not for the largest as very few are likely to be found in the observable area of a thin foil. The larger particle are also not expected on carbon replicas, because the film is not strong enough to hold them. Diffraction patterns are also difficult to obtain from large particle.

- Some precipitates have similar crystal structures and lattice parameters (e.g. $M_{23}C_6$, M_6C, G-phase). Therefore, any technique which relies solely on structure determination is susceptible to error.

- Some precipitates have similar compositions, so that 'fingerprinting techniques' based on microanalysis can be ambiguous when used on their own.

It clearly is necessary to use complementary techniques. The experimental procedure is depicted in figure 7.1.

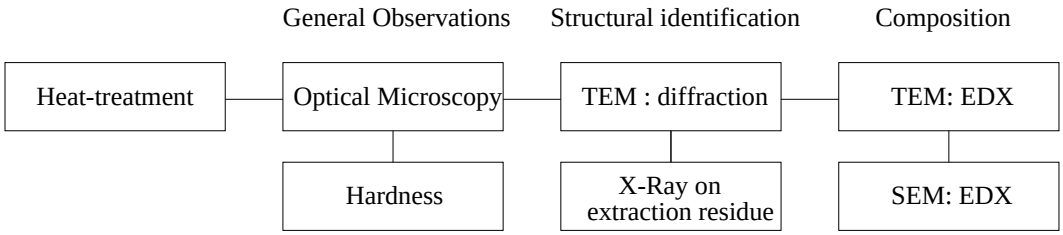

Figure 7.1: Complementary techniques used for identification of precipitates and general observations of ageing effects. TEM: transmission electron microscopy. EDX: energy dispersive X-ray analysis. SEM: scanning electron microscopy.

7.2 Materials and heat-treatments

Two steels where provided by National Power: NF709, and a variant called NF709R (both manufactured by Nippon Steel). NF709, based on 20/25 austenitic stainless steels, has been designed recently and is regarded as the best creep resistant austenitic stainless steel available today. The chemical compositions are given in table 7.1. The steels were

NF709	Cr	Ni	Mn	Mo	Si	Nb	Ti	N	C	B	P
wt%	20.28	24.95	1.00	1.50	0.41	0.26	0.05	0.167	0.06	0.005	0.006
NF709R	Cr	Ni	Mn	Mo	Si	Nb	Ti	N	C	B	P
wt%	22.22	25.34	0.92	1.40	0.38	0.24	0.05	0.170	0.03	0.005	0.022

Table 7.1: Composition of steels studied. NF709R is a variant of the first steel provided, NF709, with increased Cr and reduced C.

received in the form of tubes from which two kinds of specimens were made. Rods of 3 mm in diameter and various lengths were machined; they were used to prepare thin foils. Sections of the tubes were cut so as to provide samples for replication, optical microscopy, hardness, *etc...* (figure 7.2). The grain size was smaller along the inner and outer walls of the tubes. The longitudinal sections were made carefully so as to cross the tube and present some regions from the outer wall and the middle of the tube wall.

Pairs of each kind (rod and piece) of sample were sealed in silica tubes under a pressure of argon of about 0.1 atm. They were water quenched at the end of the heat-treatment.

Both NF709 and NF709R were aged at 750 °C and 800 °C for up to 15000 h.

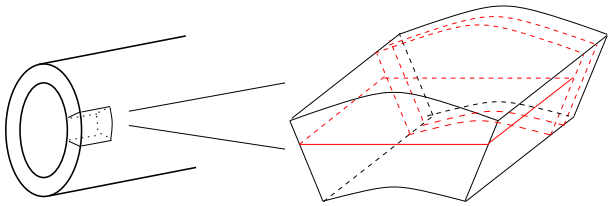

Figure 7.2: Preparation of specimen from received tubes. Longitudinal sections were used for SEM and preparation of replicas, transverse sections for optical microscopy and hardness. The samples are typically 1 cm long and 5 mm thick.

7.3 Optical microscopy

The specimens for optical microscopy were hot mounted with conductive bakelite powder, ground with silicon carbide paper down to 1200 grit and then polished with 6 and 1 μm diamond paste. Electrolytic etching was done in a solution of 10% oxalic acid in distilled water, at about 5 V. This electrolyte attacks the precipitates and σ-phase, but not the matrix. Grain boundaries are only revealed after about 60 s when they are precipitate free.

Using a solution of 10% HCl in methanol also gave satisfying results (6 V for 10 to 30 s). This electrolyte attacks the matrix but not the precipitates.

A selective etchant was also used to reveal σ-phase. The samples were electrolytically etched (5 to 10 s at 1.5-3 V) in a solution of 56 g KOH for 100 ml of water. This colours σ-phase brown.

Optical microscopy gives a general impression of the amount of precipitates and on their locations (grain boundary, twin boundary, intragranular). Phases such as grain-boundary σ-phase can be identified readily.

7.4 X-ray analysis of extraction residues

Each kind of precipitate makes only $< 1\%$ in volume of the bulk sample. For this reason, X-ray diffraction on a bulk specimen is unlikely to provide accurate information about precipitates. A method commonly used to avoid this difficulty involves the electrolytic dissolution of the matrix, leaving residues which can be analysed by X-ray diffraction.

Details of the experimental settings are shown in figure 7.3, together with a typical

X-ray spectrum of extracted residues. Specimens of a few hundred milligrammes were

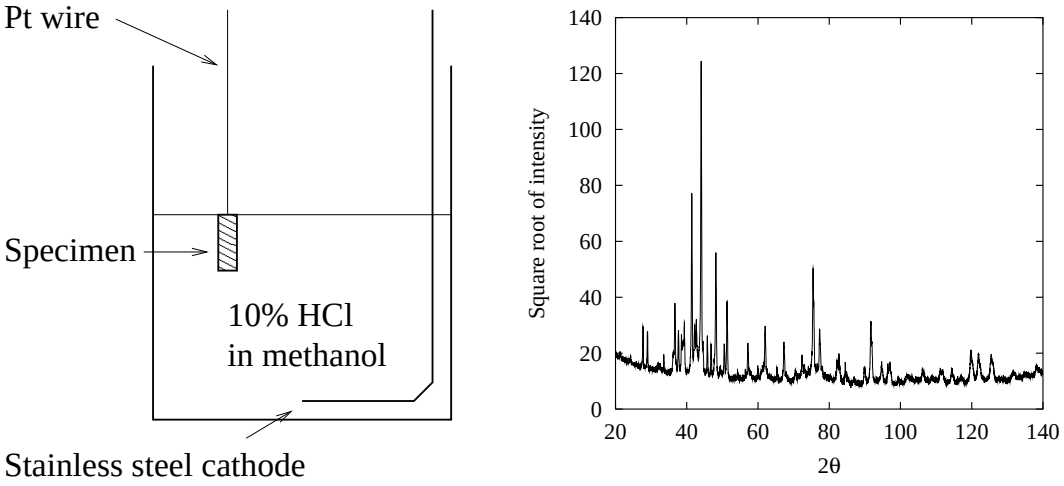

Figure 7.3: The experimental settings used to electrolytically dissolve samples of NF709. A typical X-ray spectrum of extracted residues is illustrated on the right.

dissolved electrolitically in a solution of 10% HCl in methanol. The ensemble made by the platinum wire and the specimen (figure 7.3) was weighed before and after dissolution, with a precision balance, so as to provide an estimate of the amount of steel dissolved. The residues were filtered using a 0.2 μm membrane filter (filtering using a 0.1 μm was not possible within a reasonable amount of time). The filter was then allowed to dry for one day. It was weighed before and after filtration, so as to measure the amount of residue collected.

The filter was then placed in a 2-θ X-ray diffractometer. Identification of the different phases was often made difficult because of the overlapping of many peaks. An analysis was also performed on the filter by itself in order to remove any peak coming from it.

This technique is very useful when used in conjunction with other identification methods. The main advantages are that it should reveal all of the precipitates present, that the amount of material investigated at once is far greater than with most of the other methods (scanning electron microscopy, transmission EM, *etc...*) and that it can give, in principle, quantitative information. It is also relatively easy to implement when compared to methods such as TEM for which the sample preparation can be much more time consuming.

The disadvantages are that no information are obtained about the morphology, distribution or location of the precipitates. In practice, quantitative information can only be

obtained if the absorption coefficients (μ) or their ratio (μ/μ_{cor}) to a that of a reference phase (corundum) are known, which was not the case for most of the phases found in the present work. Another limitation concerns the size of the precipitates. Comparison with the phases detected with this method and those found using TEM show that the smallest precipitates are most probably dissolved.

7.5 Transmission electron microscopy

This is by far the most important experimental method in this project justifying a more detailed presentation of specimen preparation and precipitate identification.

7.5.a Preparation of samples

i Carbon replicas

Carbon replicas were prepared on samples mounted in the same way as for metallographic specimens. At first, the polished surface was lightly etched with a 10% HCl in methanol solution, which attacks the matrix but not the carbides (oxalic acid cannot be used as it attacks the carbides but not the matrix).

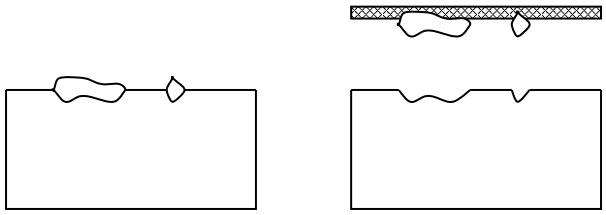

Figure 7.4: Preparation of carbon replicas. On the left a schematic drawing of the etched sample. On the right, the carbon film has extracted the precipitates

A carbon film was then applied on the surface using a vacuum vaporising system. The thickness of the film is a critical factor: too thin and it will be destroyed by the electron beam. By contrast, a thick film is difficult if not impossible to lift. The film was cut on the surface into small squares, the specimen was electrolytically etched in the same solution, rinsed in methanol and then in distilled water. The pieces of film were collected on 3 mm diameter copper grids. For specimens aged over long periods of time (2500 h and more), it became increasingly difficult to obtain nice replicas. This was attributed to the density of precipitation and the presence of very large particles on the grain boundaries.

Carbon replicas offer a much larger observable area than thin foils, but it is more difficult to tilt to a major zone axis, because of the very small size of the diffracting particle. Also, it is possible that some particles are not extracted.

ii Preparation of thin foils

Thin foils were cut from the 3 mm rods to about 100 μm, then ground with silicon carbide paper (1200 grit) on both sides, until the thickness was about 50 μm. Care was taken to avoid deformation which can cause the formation of martensite.

The foils were then electropolished using a twin-jet electropolisher initially with a solution of 5% perchloric acid, 15% glycerol in 80% methanol. Although some thin foils were satisfactory, the repeatability was low and another solution was used, made of 5% perchloric acid in 2n-ethoxy-butanol, which gave more satisfying results.

Although thin foils offer a much smaller observable area, the presence of the austenitic matrix greatly simplifies tilting as it is possible to take advantage of the orientation relationships which often exist between it and the variety of precipitates.

7.5.b Identification of precipitates with TEM

Two microscopes were used for this work, a Philips CM30 capable of acceleration tensions of 300 kV, and a JEOL 2000FX (200 kV). Both were fitted with an energy dispersive X-ray analysis (EDX) facility and an electron energy loss spectrometer (EELS). Therefore both structure and chemical composition could be investigated.

i Structure identification: electron diffraction

Conventional selected-area diffraction and convergent beam electron diffraction techniques were used. The latter was required to identify independently small precipitates on carbon replicas; it was also useful when tilting the sample to a major zone axis. A schematic drawing of both techniques is found in figure 7.5. In conventional diffraction, the distance between two different spots in the pattern (R_{hkl}) is related to the spacing d_{hkl} for the planes of Bragg indices hkl by:

$$d_{hkl} = \frac{R_{hkl}}{L\lambda} \tag{7.1}$$

where L is called the camera length although it is not strictly related to any real length in the microscope. λ is the wavelength associated with the electrons for a given acceleration

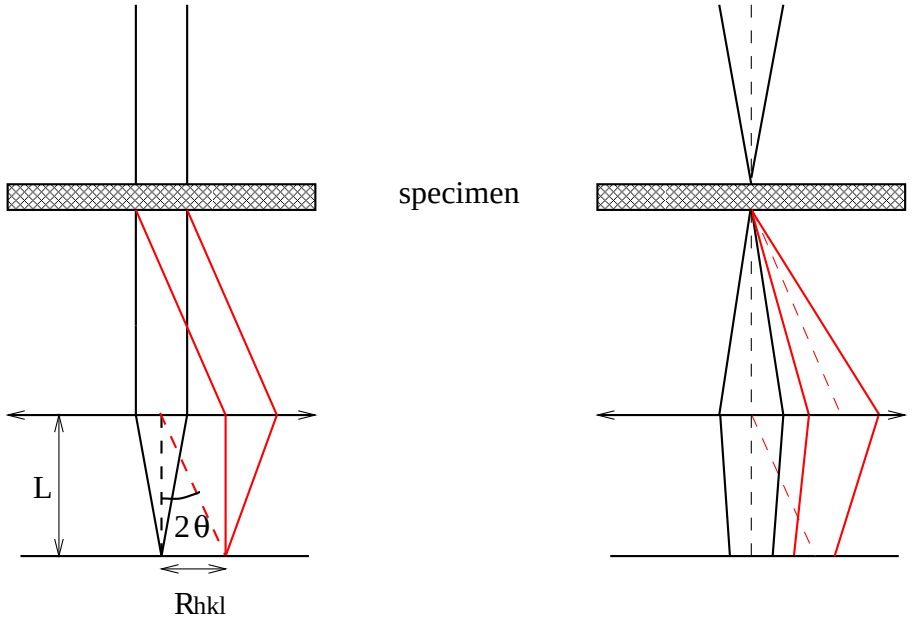

Figure 7.5: Schematic drawing of conventional diffraction pattern formation and convergent beam diffraction. In CBED, the points are replaced by discs which can contain supplementary structural information.

voltage, calculated with:

$$\lambda = \frac{12.26}{\sqrt{V(1+0.979.10^{-6})}} \text{ Å} \tag{7.2}$$

where V is the acceleration voltage and λ is given in Angströms. This formula account for relativistic corrections. The wavelength is 0.025 Å at 200 kV and 0.019 Å at 300 kV. For more accuracy, $L\lambda$ is often found by calibration with a gold thin foil. The following values were provided for 200 kV (JEOL 2000):

L,cm	$L\lambda$ measured, mm Å	$L\lambda$ theoretical
50	12.81	12.5
60	14.95	15
80	20.10	20
100	24.17	25
120	29.09	30
150	36.03	37.5
200	48.01	50

It can be noticed that these values are all less than 4% different from the theoretical ones.

It is possible to identify precipitates with conventional diffraction patterns, by trying to match against expected patterns. However, to distinguish $M_{23}C_6$ and M_6C for example,

which are both fcc (face centred cubic) and of similar lattice parameter, particular care is required (in this case, M_6C has a diamond-cubic structure for which reflections with h, k, l all even but $h + k + l \neq 4n$ are absent). The presence of the first order Laue zone (FOLZ) can also reveal features which help distinguish these carbides. Diffraction on its own is little appropriate to distinguish between different type of MX precipitates which all have a similar lattice parameter. On some replicas or foils, it is difficult to isolate one particular carbide because of the very small sizes. For this reason, CBED was used. In CBED, the incident electron beam is not parallel but convergent. This allows a reduction in probe size to a minimum of 10 nm, whereas it can hardly be less than 500 nm in conventional diffraction. Points are replaced by discs which contain information related to the space group of the precipitates. In fact, this space group can be determined from a suitable CBED pattern.

The systematic presence of Kikuchi's lines helps tilting of the specimen to a major zone axis. The CBED pattern (provided that it is not formed of blank disks) from a major zone axis can be related immediately to a particular precipitate with the help of reference.

However, to obtain a fine CBED pattern is time consuming and often, by the time the specimen had been oriented, the contamination blurs out the information in the discs.

ii Composition identification: EDX

In EDX or XEDS (X-ray energy dispersive spectrometry), the characteristic X-rays emitted by the different atoms as a consequence of their ionisation under the electron beam are used to identify them.

To perform EDX analysis in the TEM, the specimen was tilted to 45°; the live time was 100 s. The dead time was kept below 20%.

EDX analysis was particularly useful on carbon replicas, where the precipitates are separated from the matrix. In thin foils, the size of most of the particles is so small that EDX patterns often contain an important contribution from the matrix. Most of the phases, once characterised by diffraction and composition, can be directly identified from their EDX pattern.

Chapter 8

Precipitation behaviour of NF709 and NF709R under static ageing at 750 °C and 800 °C

8.1 Introduction

NF709, a 20Cr-25Ni austenitic steel, manufactured by Nippon Steel, is currently set as a standard for its creep and corrosion resistance. Studying its microstructural evolution during ageing at elevated temperatures is of great interest, both to ensure that no phase forms which is detrimental to creep properties and which could invalidate the extrapolations of short-term creep tests, and to identify a precipitation sequence which cannot be deduced from the existing literature. NF709 has a composition which distinguishes it from the existing 20/25, as it contains a unique combination of carbon and nitrogen together with niobium and titanium.

8.2 Material and experimental procedures

Two grades of NF709 were provided by National Power. The compositions are given in table 8.1. Little information could be obtained about the production route and the exact heat treatment: NF709R was cold-drawn, solution treated at 1200 °C and water quenched; the duration of the solution treatment is unknown. The solution-treatment temperature for NF709 is also unknown but is stated to be above 1100 °C. The experimental methods

NF709	Cr	Ni	Mn	Mo	Si	Nb	Ti	N	C	B	P
wt%	20.28	24.95	1.00	1.50	0.41	0.26	0.05	0.167	0.06	0.005	0.006
NF709R	Cr	Ni	Mn	Mo	Si	Nb	Ti	N	C	B	P
wt%	22.22	25.34	0.92	1.40	0.38	0.24	0.05	0.17	0.03	0.005	0.022

Table 8.1: Compositions of the two grades of NF709 provided by National Power. In both cases, S is 0.001 wt%

mentioned below are described in greater detail in chapter 7.

Samples were sealed in argon and aged in furnaces at 750 and 800 °C. Specimens for optical microscopy were electrolytically etched with a solution of 10% (by mass) oxalic acid in distilled water for general etching, and in a solution of 56 g / 100 ml KOH in distilled water for outlining σ-phase, according to the procedures described in [8].

Thin foils for TEM (transmission electron microscopy) examination were electropolished using a solution of 5% perchloric acid in 2n-ethoxy-butanol, in a twin-jet electropolisher.

Extraction was performed by dissolving the matrix electrolytically with a solution of 10% HCl in methanol at 5-6 V. The residues were then filtered with a membrane filter of 0.2 μm pore size. It was verified by prolonged centrifugation that no detectable amount of particles were left in the solution after filtration. X-ray analysis was performed in a 2-θ diffractometer.

8.3 As-received material

8.3.a Prediction of the phases present in the as-received state

It is difficult to make meaningful predictions for the as-received state as the exact conditions of solution treatment are not known. Table 8.2 shows the predicted phases and their amounts at the given solution treatment temperatures, 1100 °C for NF709 and 1200 °C for NF709R.

Since both tubes underwent different solution treatments and probably different mechanical treatments, it was necessary to characterise the as-received condition thoroughly. The two materials had substantially different initial hardnesses and grain sizes (table 8.3).

	NbN wt%	TiN wt%
NF709	0.260	0.064
NF709R	0.200	0.063

Table 8.2: Predicted equilibrium precipitates and their weight fractions at the solution treatment temperatures for each steel.

	HV 10 kg	Average grain size
NF709	178 ± 1.0	51 μm
NF709R	162 ± 1.6	90 μm

Table 8.3: Initial hardnesses and grain sizes of NF709 and NF709R. Grain sizes calculated according to [106].

The X-ray analysis of extraction residues showed further differences between the two steels. As indicated in table 8.4, NF709 does not seem to contain any Z-phase in the as-received state but instead contains substantial amounts of NbN. By contrast, NF709R does not show NbN but traces of Z-phase.

	NbC (38-1364)	NbN (38-1155)	TiC (32-1383)	(Nb,Ti)C (47-1418)	TiN (38-1420)	CrNbN (25-0591)
NF709		VS		VS	VS	
NF709R					S	VW

Table 8.4: Results of X-ray analysis of extraction residues for the two as-received materials (VS: very strong, S: strong, W: weak, VW: very weak).

These results are in agreement with SEM (scanning electron microscopy) observations. Relatively large precipitates are found in both steels (up to 3 μm for TiN and 1 μm for NbX). Their sizes are typical of residual precipitates, which are not dissolved during the solution treatment. But, while TiN is found in both steels, the EDX (energy dispersive X-ray) spectra of Nb rich particles revealed the presence of a substantial amount of Cr, giving a composition closer to that expected for Z-phase.

Because it was not clear whether this difference should be attributed to a different solution treatment or to the difference in chemical composition, samples of both steels were solution treated 2 h at 1200 °C. Both steels reacted fairly differently, with NF709 showing exaggerated grain growth and presenting a bimodal grain size distribution, while NF709R still presented a normal grain size distribution (see figure 8.2). In both cases, the weight fraction of filtered residues was smaller than in the as-received state. X-ray

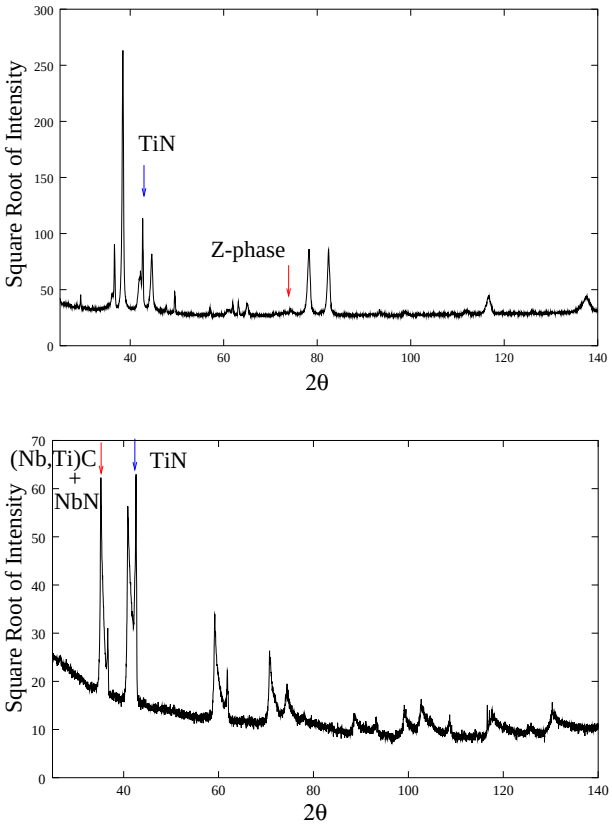

Figure 8.1: X-Ray diffraction on extraction residues for as received NF709R, the main peaks for identified phases are given, other peaks are all related to one of the two phases or the Al support

analysis did not reveal any change in the nature of the phases present (see table 8.4), which were the same as for the as-received samples. The new grain sizes are given in table 8.5.

	HV 10 kg	Average grain size
NF709	157 ± 2	$146 \pm 30\mu$m
NF709R	158 ± 2	$128 \pm 10\mu$m

Table 8.5: Hardness and grain size of NF709 and NF709R after 2 h at 1200 °C. Grain size calculated according to [106].

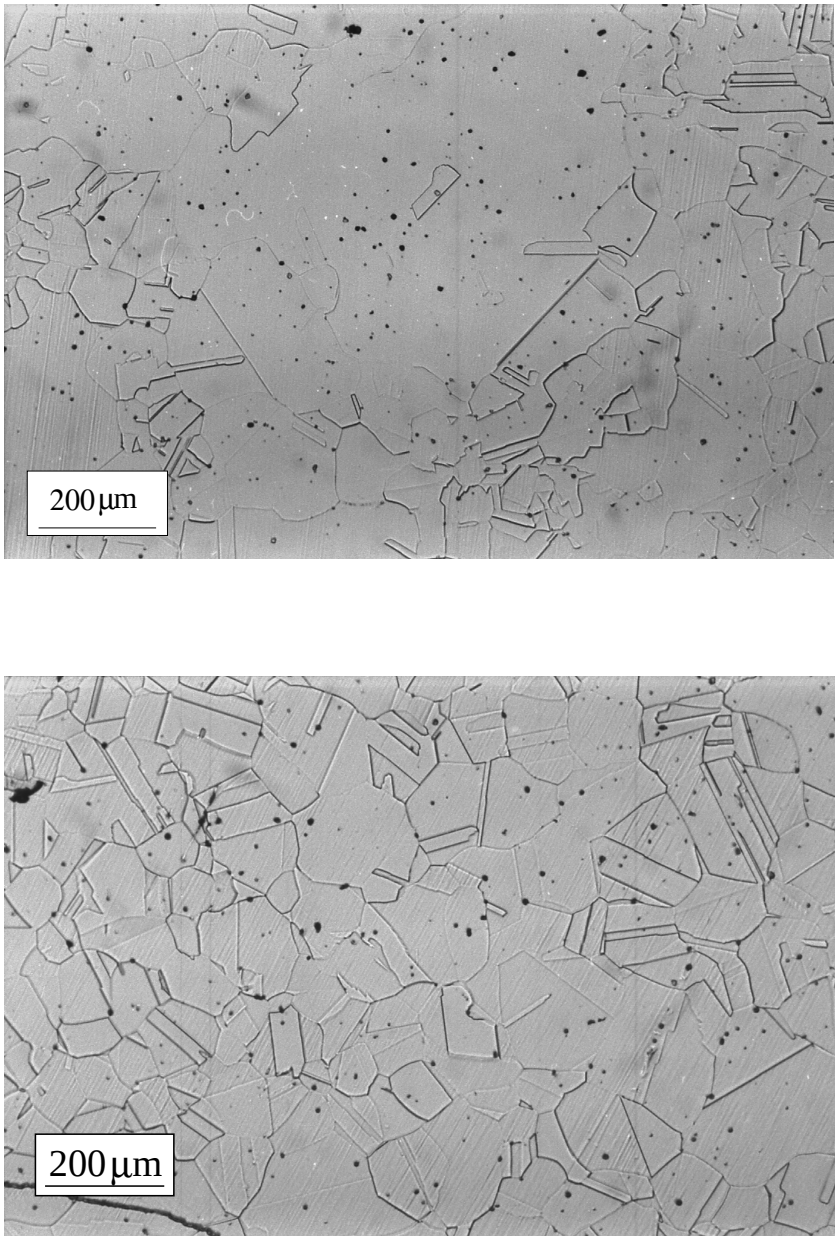

Figure 8.2: Microstructure of NF709 and NF709R after 2 h at 1200 °C. Etched 60 s in a 10 wt% solution of oxalic acid in water.

8.4 Short term ageing

Specimen of NF709 and NF709R were aged for 1 h, 100 h (NF709) and 200 h at 750°C. Extraction results (figure 8.3) show that the precipitation of $M_{23}C_6$ occurs at very early stages, although subsequent changes in the X-ray spectra of the residues indicate it is not yet completed.

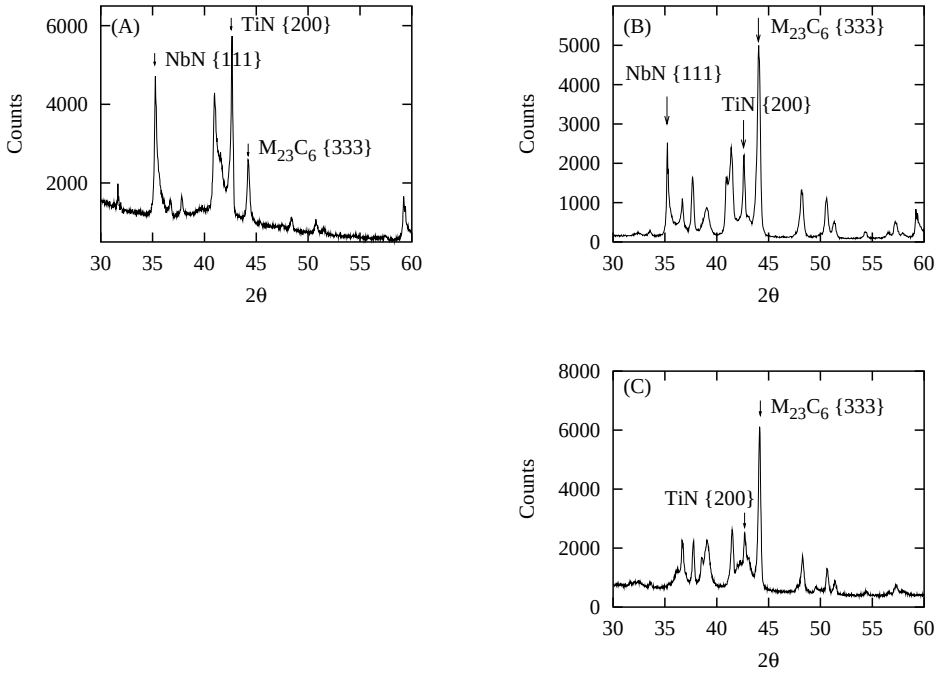

Figure 8.3: X-ray analysis of extracted residues for NF709 aged 1 h (A) and 200 h (B) at 750 °C, and NF709R aged 200 h (C) at 750 °C. Only the most intense peak for each phase is indicated, all other peaks have been identified as belonging to the identified phases, but are not indexed for clarity.

The morphology and distribution of the precipitates differs significantly between the two variants of NF709. Figure 8.4 shows optical micrographs of NF709 and NF709R aged 200 h at 750 °C. The alignment of precipitates observed in the 22Cr variant is not found in the 20Cr sample. Both steels show relatively intense precipitation on grain boundaries, incoherent twin boundaries, and, to a lesser extent, on coherent twin boundaries.

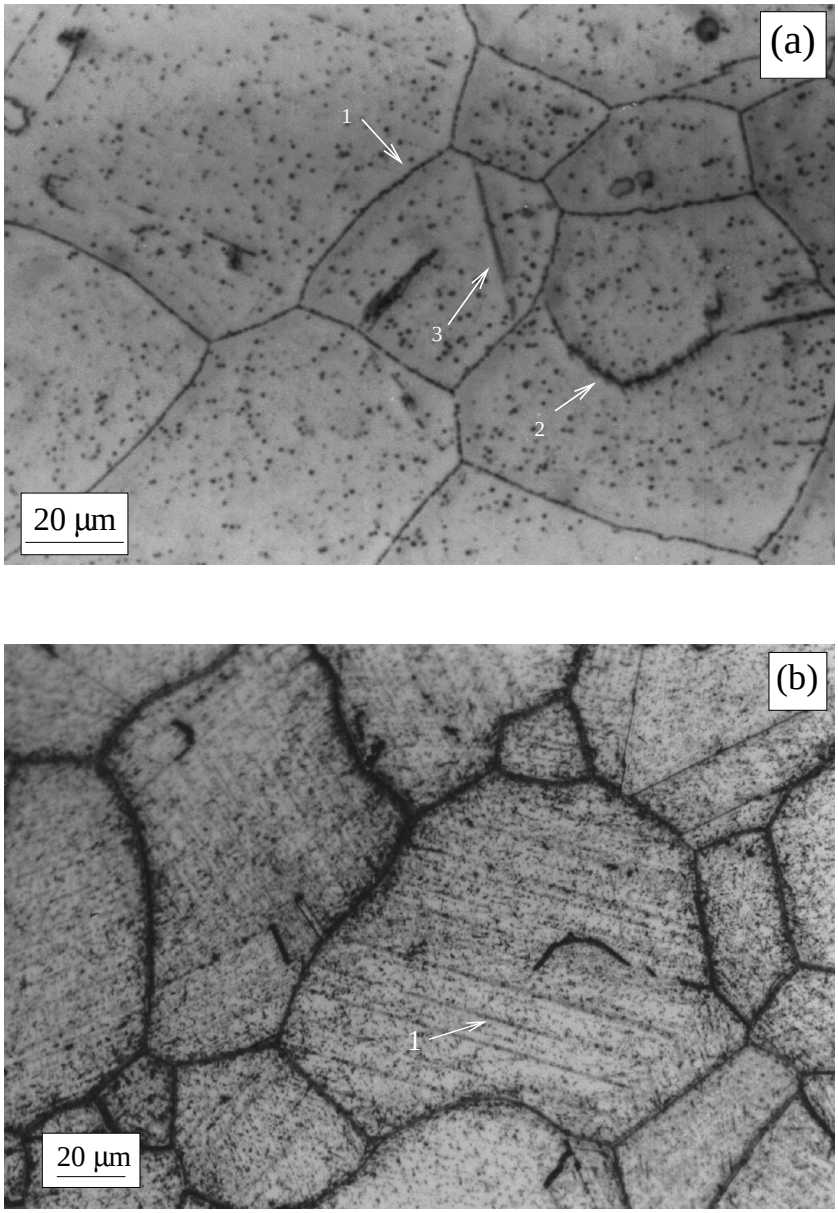

Figure 8.4: NF709 (a) and NF709R (b) after 200 h at 750 °C, etched 10 s in a 10 wt% solution of oxalic acid in water. (a/1) points to grain boundary precipitates, (a/2) to incoherent twin boundary precipitates and (a/3) to coherent twin boundary precipitates. (b/1) shows alignment of precipitates.

8.4.a TEM identification of the phases present in NF709

In addition to the phases identified by X-ray analysis of extracted residues, TEM investigation of carbon replicas revealed the formation of Z-phase (CrNbN) on dislocations, as shown in figure 8.5.

$M_{23}C_6$ was found at numerous sites, as shown in figure 8.6: strong presence on grain boundaries, with a globular morphology, on incoherent and coherent twin boundaries with a plate morphology, and around residual NbX residual precipitates. All these occurrences are well documented and have been reported on numerous occasions, with the exception of the formation of plates around residual NbX particles which is more seldom reported (chapter 2). As reported in the literature, $M_{23}C_6$ has a cube-to-cube orientation relationship with the austenite, and its lattice parameter is three times that of the matrix; typical diffraction patterns appear as shown in figure 8.6 (d) and (f). After identification by diffraction and EDX, it became evident that EDX fingerprints were sufficient to distinguish $M_{23}C_6$ and Z-phase without possible confusion.

It is interesting to note the differences between the results obtained by X-ray analysis of extracted residues, and those obtained using TEM, particularly with regard to Z-phase. Although this phase is found with the latter, it was not detected with the former method. One of the possible causes is the size of the Z-phase precipitates. As can be seen in figure 8.5, these are seldom more than 50 nm in length after 200 h of heat treatment at 750 °C. This is significantly smaller than the 200 nm pore size of the membrane filter. To verify whether Z-phase particles were retained by the filter, the filtered solution was centrifuged. Since no deposit was found after prolonged centrifuging, it can be concluded that Z-phase was either dissolved or its quantity was too small to give a significant signal. Z-phase is found, with this method, in the as-received NF709R because it is present as residual particles, that is, coarse particles formed during solidification and undissolved by the solution treatment. By contrast, Z-phase formed during ageing was never found in the extracted residues.

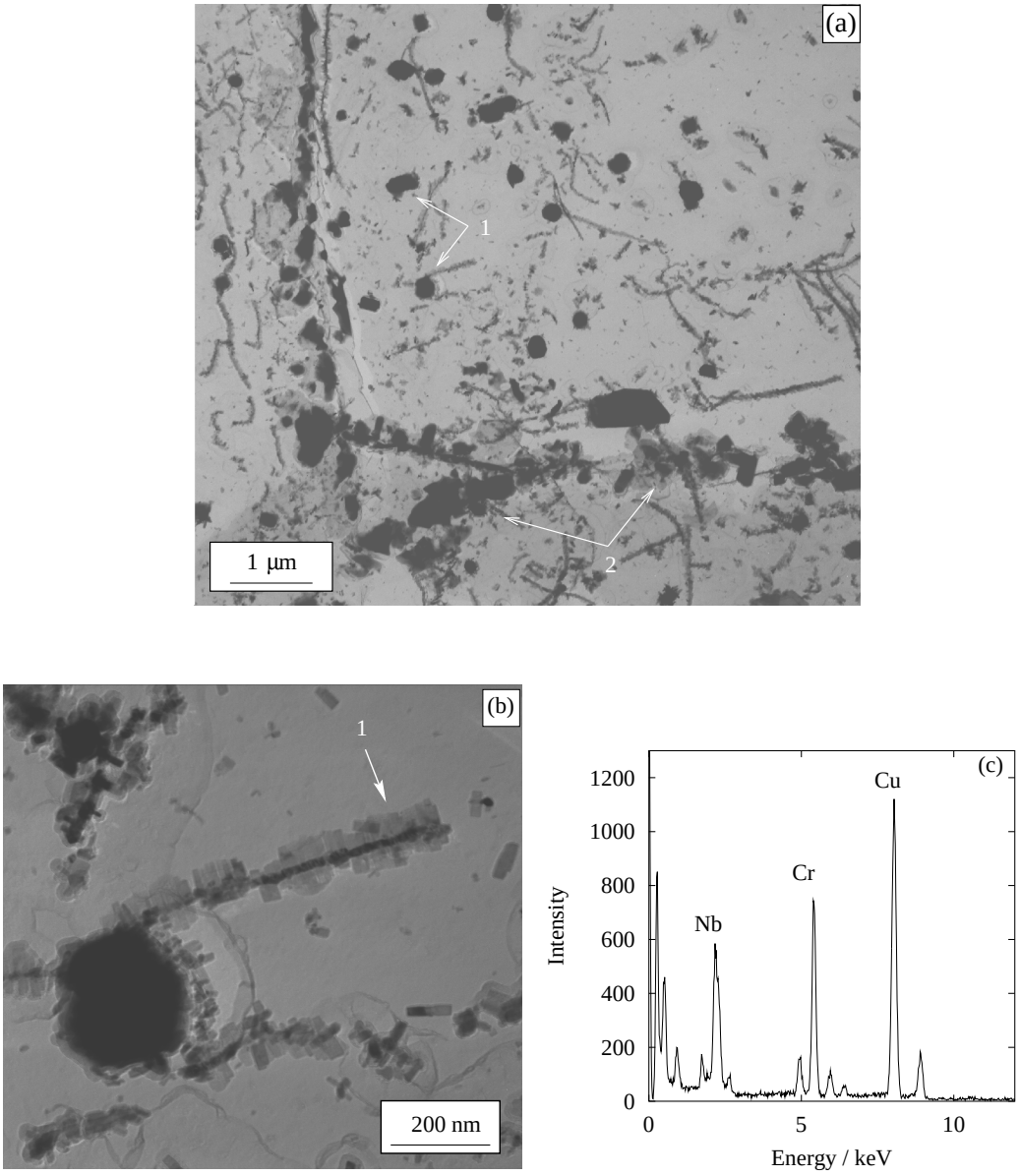

Figure 8.5: Transmission electron micrographs of a carbon replica of NF709 after 200 h at 750 °C, (a) low magnification image, with $M_{23}C_6$ on (a/1) residual NbN and on (a/2) grain boundaries; (b) high magnification image showing (b/1) Z-phase precipitates on a dislocation, and (c) EDX spectrum from the particles identified by the arrow in (b), the strong copper signal comes from the grid supporting the replica.

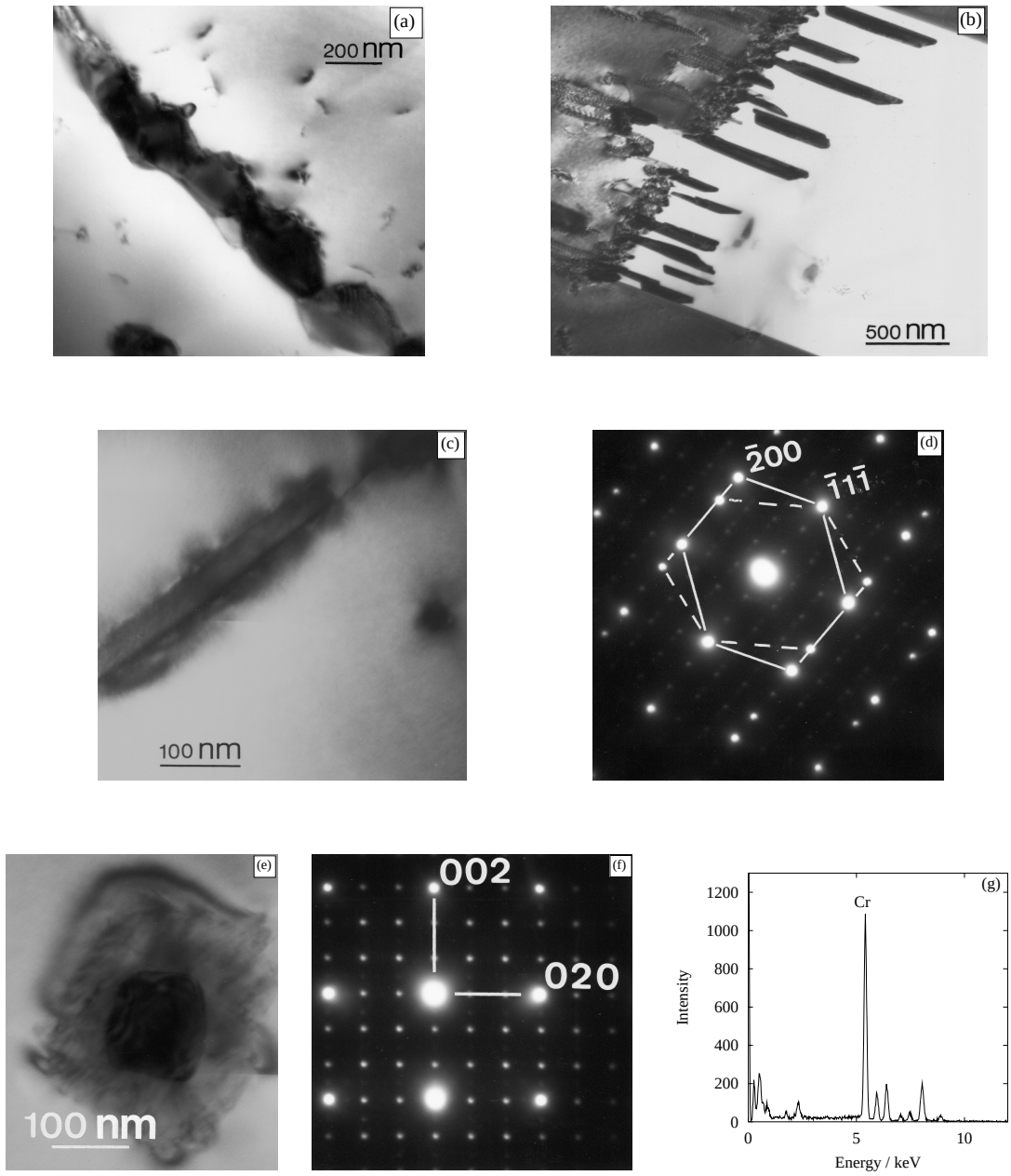

Figure 8.6: The various locations and morphologies of $M_{23}C_6$ in NF709 after 100 h at 750 °C: (a) forming on grain boundaries, (b) as plates on incoherent twin boundaries, and (c) on coherent twin boundaries (less frequent). (d) Diffraction pattern from the precipitate shown in (c), the indexed points are for austenite and show the two orientations on each side of the twin boundary; $M_{23}C_6$ has a lattice parameter about three times larger than that of austenite, but has the same structure and a cube-to-cube orientation relationship. (e) Plate forming around a NbX residual particle (formed during solidification and undissolved by the solution treatment), (f) typical diffraction pattern from $M_{23}C_6$ with the austenite points indexed, and (g) typical EDX spectrum.

8.4.b $M_{23}C_6$ after very short ageing

The precipitation of $M_{23}C_6$ is well advanced after 200 h at 750 °C. Both optical microscopy and TEM reveal continuous arrays of relatively coarse precipitates on the grain boundaries. Very short term aging was performed at 750 °C to estimate the speed of transformation and to verify whether the predicted composition shift was observed (chapter 6).

Figure 8.7 shows $M_{23}C_6$ precipitates on grain boundaries in NF709, after 1 h at 750 °C. The composition, after correction to include the expected mass fraction of carbon (which is not measured by EDX) is presented in table 8.6. The Fe content is significantly larger than the equilibrium value.

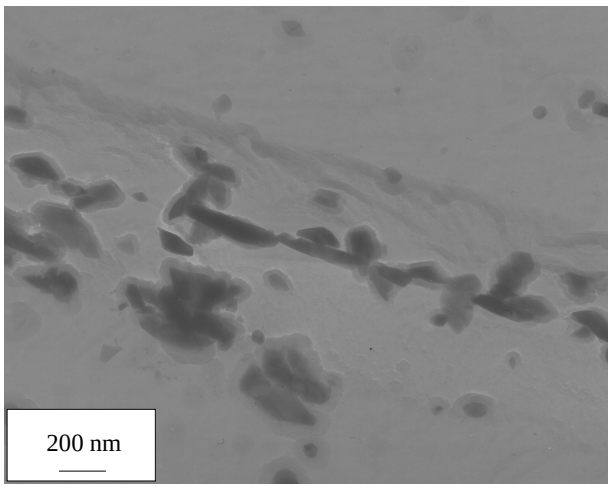

Figure 8.7: Transmission electron micrograph of a carbon replica of NF709 after 1 h at 750 °C, showing $M_{23}C_6$ formed on grain boundaries.

Element	Cr	Fe	Ni	Mo
Wt%	55.0	16.8	3.2	10.8

Table 8.6: The average composition of $M_{23}C_6$ after 1 h at 750°C.

8.4.c TEM identification of phases in NF709R

The same phases were identified in NF709R as in NF709. Figure 8.8 shows coarse $M_{23}C_6$ precipitates formed on the grain boundaries, in NF709R after 200 h at 750 °C.

However, the aligned precipitates visible in figure 8.4 were identified as Z-phase and are therefore present in quantities significantly greater than in NF709. Also, the aligned particles observed (figure 8.8 (a)), which clearly correspond to precise crystallographic planes, are not found in NF709. TEM investigation of thin foils of the as-received NF709R did not reveal an obvious difference in dislocation density, therefore making it difficult to explain the difference in the way the precipitation of Z-phase occurs in the two steels.

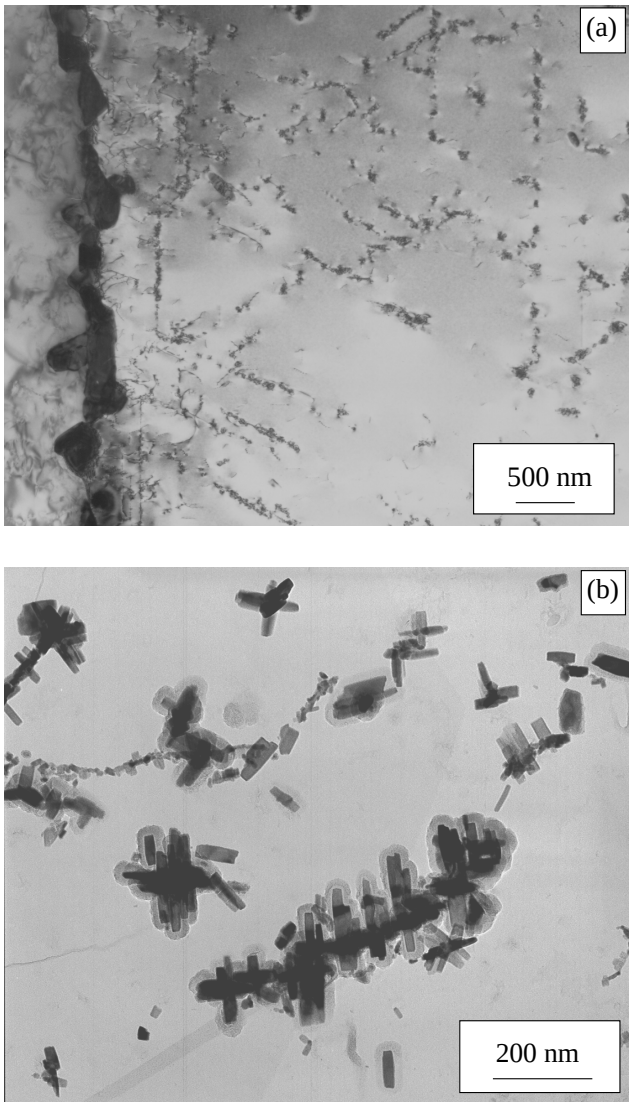

Figure 8.8: TEM micrographs (a) of a thin foil of NF709R after 200 h at 750 °C, showing a grain boundary decorated by $M_{23}C_6$ and alignment of Z-phase particles, (b) of a replica at higher magnification, showing Z-phase particles growing on a dislocation.

8.5 NF709 aged 2500 and 5000 h at 750 and 800 °C

Figure 8.9 shows optical micrographs of NF709 aged 2500 and 5000 h at both temperatures: both the grain and incoherent twin boundaries are covered with coarse precipitates, together with most of the coherent twin boundaries. Interesting results could be obtained

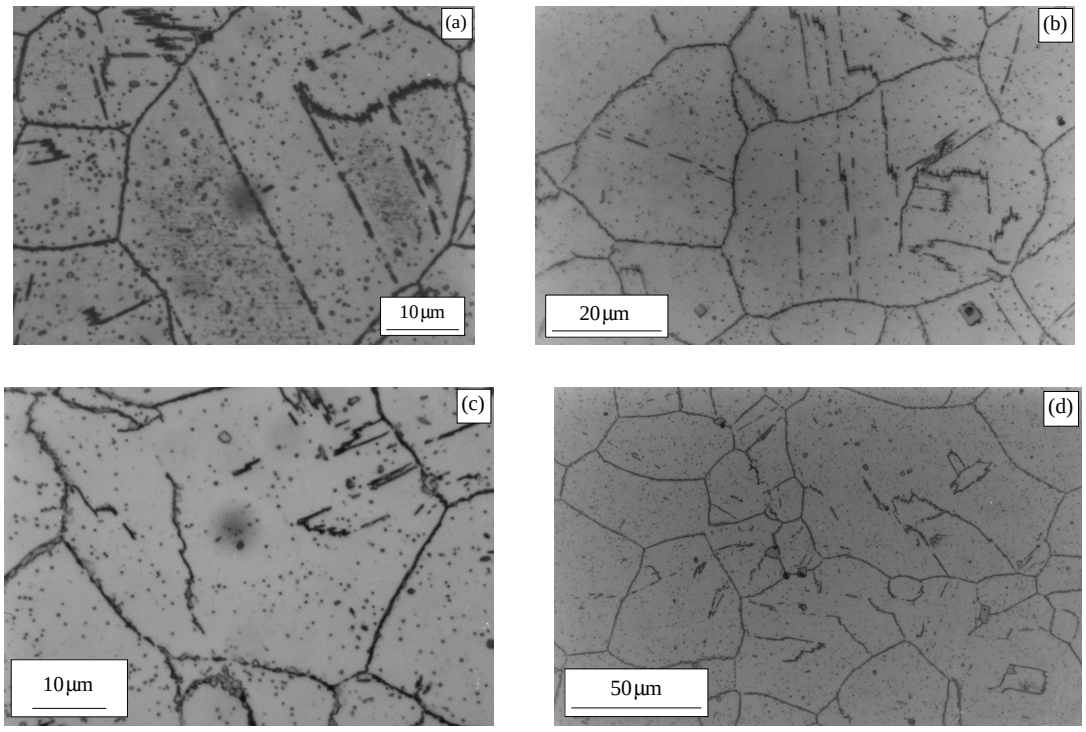

Figure 8.9: Optical micrographs of NF709 aged (a) 2500 h, (b) 5000 h at 750 °C, and (c) 2500 h, (d) 5000 h at 800 °C

from X-ray analysis of extracted residues: the relative intensity of the main peak for NbN is clearly reduced between the samples aged 2500 h and 5000 h at 800 °C, as illustrated in figure 8.10. This can be attributed to a dissolution of the residual NbN to the profit of Z-phase (CrNbN).

A careful examination of the X-ray spectra, for both 2500 h and 5000 h at 800 °C, also revealed a separation in the $M_{23}C_6$ peaks which was not detected by automated methods. As illustrated in figure 8.10 (c), this is true for specimen aged at 800 °C but not at 750 °C were only a small shoulder is visible near the top of the peak. Two distinct lattice parameters could be estimated corresponding to a cubic phase and a cubic diamond

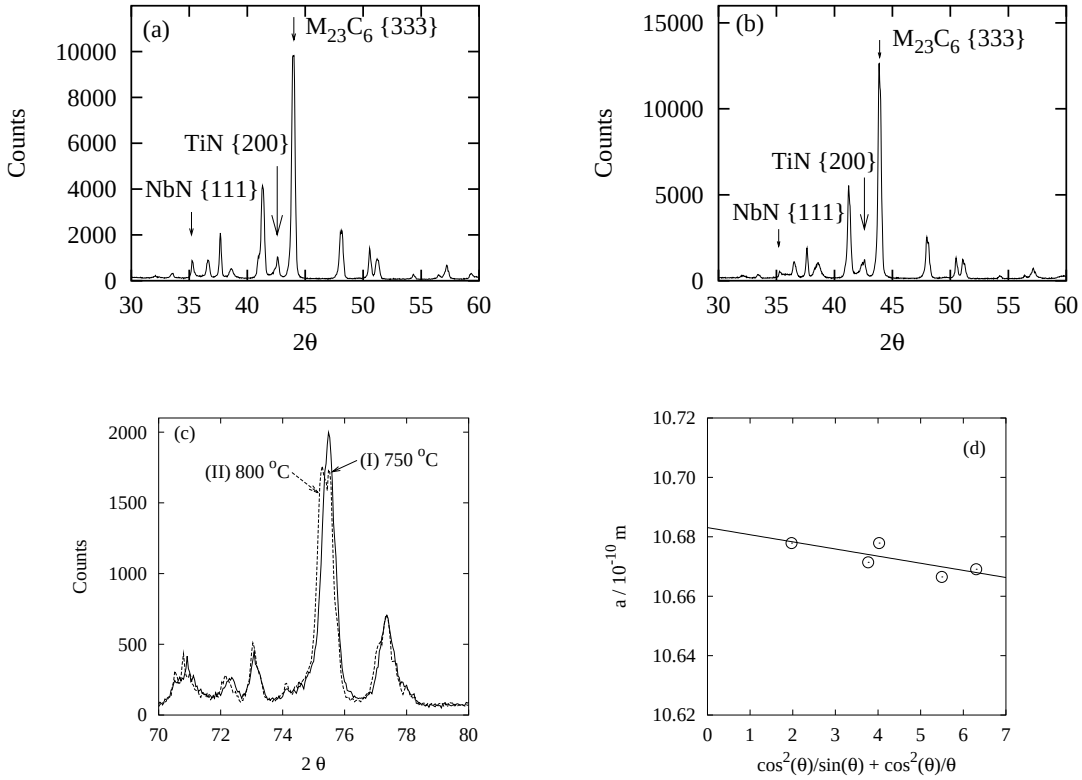

Figure 8.10: X-ray spectrum of extracted residues from NF709 aged (a) 2500 h and (b) 5000 h at 800 °C, and (c) comparison between the 2500 h at 750 °C and 800 °C showing a clear separation in the {660} peak of $M_{23}C_6$ at 800 °C; (d) accurate determination of the lattice parameter of $M_{23}C_6$ in NF709 after 2500 h at 800 °C, giving $a = 10.683$ Å

phase ($h + k + l$ all even with $h + k + l \neq 4n$ were absent so that the peaks for these indices were unique rather than showing the separation illustrated above). The measured lattice parameters are plotted as a function of $\cos^2(\theta)/\sin(\theta) + \cos^2(\theta)/\theta$, the Nelson-Riley function, and extrapolated to $\theta = 90°$ to minimise errors due to absorption [107]; this is illustrated in figure 8.10 (d). Table 8.7 presents the different lattice parameters measured for these ageing times. The lattice parameter measured for the diamond cubic phase, later identified as Cr_3Ni_2SiN is significantly greater than the one reported for Cr_3Ni_2SiC (10.62 Å, JCPDS 17-0330). Taking account of the literature covered in chapter 2, there is no previous record of the lattice parameter of Cr_3Ni_2SiN. The shoulder visible in figure 8.10 (c), for the peak (I) is evidence that the lattice parameter of this phase, formed at lower temperature, is significantly closer to that of $M_{23}C_6$. This might be related to the

composition change of Cr_3Ni_2SiX (where X refers to C or N): Williams [53] reported a significant increase in the Mo content of this phase with temperature (about 7 wt% per 100 °C), which could explain the significant change in the lattice parameter.

Phase / Ageing time	2500 h	5000 h
$M_{23}C_6$	10.683 Å	10.684 Å
Cr_3Ni_2SiN	10.713 Å	10.722 Å

Table 8.7: The lattice parameters of $M_{23}C_6$ and Cr_3Ni_2SiN at 800 °C for two different ageing times.

TEM examination of thin foils confirmed the presence of a new phase whose composition matches closely the reported compositions of Cr_3Ni_2SiX; diffraction confirmed a lattice parameter close to 10.7 Å, and the diamond-cubic structure for which particular extinction rules exist which have been mentioned earlier. This was, however, only seen in a few diffraction patterns; the presence of the unexpected diffraction spots (e.g. 200) in many others was attributed to double diffraction, as strong diffracted beams from the austenite may act as secondary diffraction sources.

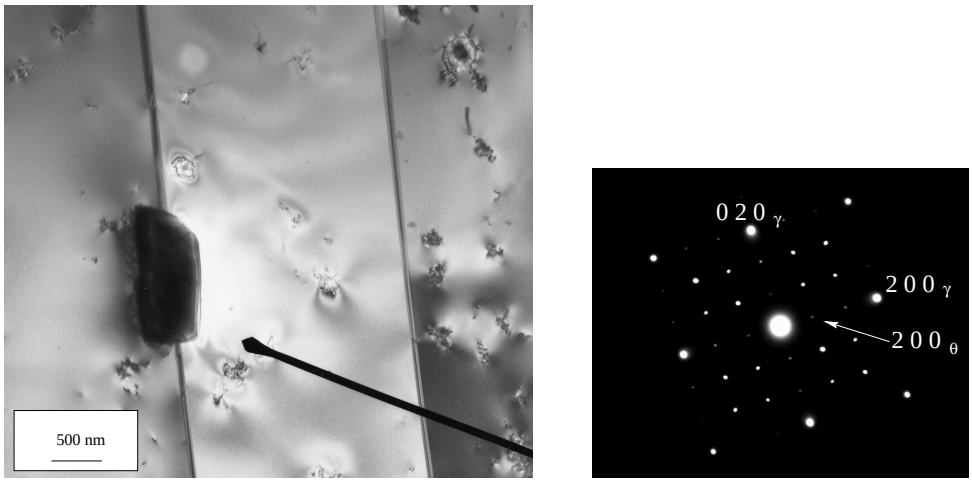

Figure 8.11: TEM micrographs of a thin foil of NF709 after 2500 h at 750 °C, showing a coarse Cr_3Ni_2SiN precipitate on a coherent twin boundary. Diffraction pattern of Cr_3Ni_2SiN precipitate, zone axis 001, indexed for austenite (γ) and Cr_3Ni_2SiN (θ), showing partial extinction of 200 from the precipitate (θ).

8.6 NF709R aged 2500 and 5000 h at 750 and 800 °C

As will be shown in this section, the precipitation sequence for the 22Cr version is fairly different from that of NF709, in spite of their relatively similar chemical compositions.

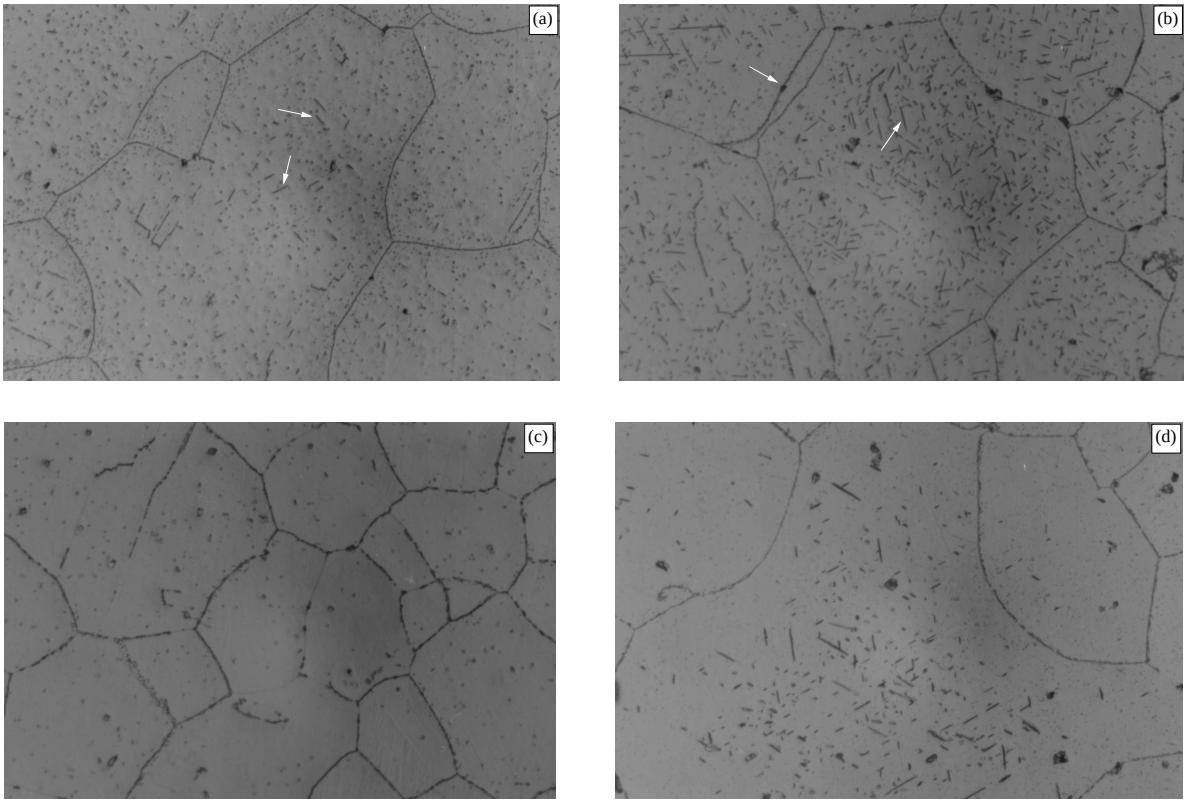

Figure 8.12: Optical micrographs of NF709R, aged (a) 2500 h and (b) 5000 h at 750 °C, and (c) 2500 and (d) 5000 h at 800 °C. The arrows point to σ-phase, which, after 2500 h at both temperatures or 5000 h at 800 °C is found only in the largest austenite grains.

After 2500 h at 750 °C, the microstructure reveals relatively dense intragranular precipitation. Precipitates of new morphologies are found on grain boundaries, similar to those shown in figure 8.12 (b), and within the grains, as pointed in figure 8.12 (a). The latter are found only in large grains. The same observations can be made after 5000 h at 800 °C, although to a lesser extent, as illustrated by figure 8.12 (c) where most of the smaller grains do not show new precipitates at the grain boundaries or new intragranular precipitates.

After 5000 h at 750 °C, the quantity of the coarse grain-boundary and, particularly,

of the plate-shaped precipitates has considerably increased, as shown by figure 8.12 (b); while at 800 °C, the plate-shaped intragranular particles are still essentially found in the larger grains.

Both these new particles were identified, using SEM, as σ-phase, of composition close to 44Cr 40Fe 10Ni 6Mo, at%, which is in satisfying agreement with the 46Cr 38Fe 10Ni 6Mo predicted with MTDATA for the same temperature.

The intragranular presence of σ-phase only in large grains is explained easily in terms of heterogenous nucleation: σ-phase nucleation is easier on sites such as triple points and grain boundaries. In grains of small sizes, the amount of surface for a given volume is more than in large grains, and there is therefore a greater number density of easy grain boundary nucleation sites for σ-phase. Because nucleation is more difficult within the grain, the tendency is for σ-phase to form intragranularly only if grain boundary sites are not available, and if the driving force for nucleation is large enough.

As is the case for NF709, a separation is observed between $M_{23}C_6$ and Cr_3Ni_2SiN, in the X-ray diffraction spectra of extracted residues, for NF709R, after 5000 h at 800 °C but not at 750 °C. As shown in figure 8.13, the separation is not as well defined as in NF709, and accurate lattice parameters could not be determined. However, two peaks are clearly overlapping, the one corresponding to the smaller lattice parameter this time having an intensity of only 50% of the other. This can be explained by the composition modifications presented by NF709R: the elements likely to control the amount of Cr_3Ni_2SiN such as Si or N are present in similar quantities, while the amount of C is halved, and as a consequence, the amount of $M_{23}C_6$ is reduced.

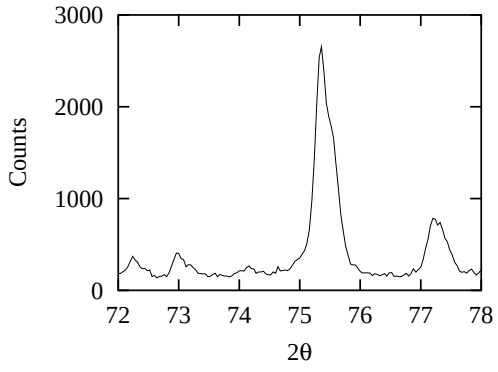

Figure 8.13: The {660} peak for $M_{23}C_6$ and Cr_3Ni_2SiN in NF709R after 5000 h at 800 °C, showing less separation than in NF709, shown in figure 8.10(c).

Electron diffraction and EDX in TEM confirmed the presence of σ-phase, as illustrated in figure 8.14 (c), while replicas revealed the presence of aligned Z-phase precipitates as observed after 200 h, figure 8.14 (a).

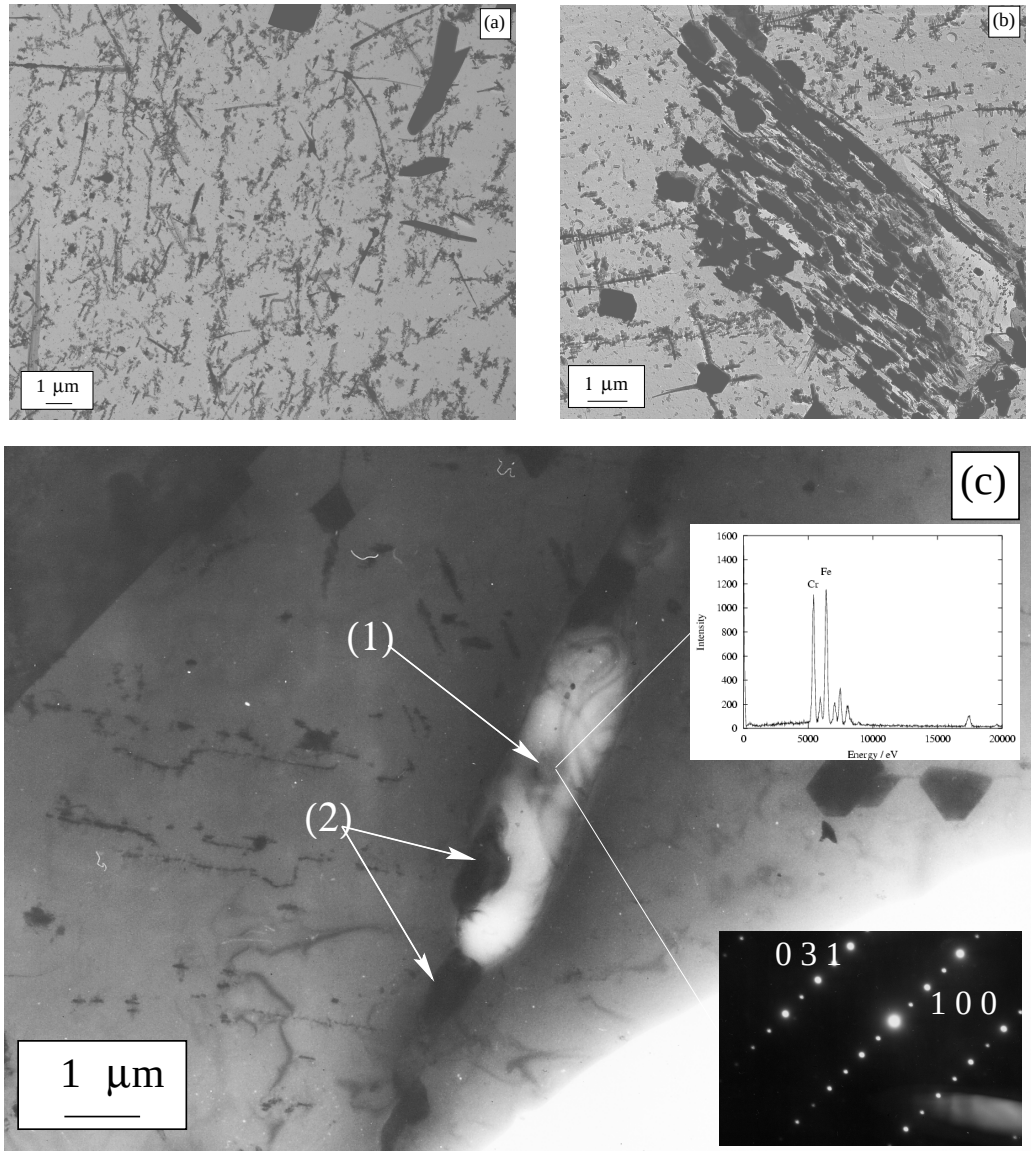

Figure 8.14: Carbon replicas of NF709R after 2500 h at 750 °C showing (a) the Z-phase precipitates as found after 200 h, and (b) coarse Cr_3Ni_2SiN and $M_{23}C_6$ precipitates on an incoherent twin boundary. (c) Thin foil of NF709R after 5000 h at 750 °C showing a large (c/1) σ-phase particle together with (c/2) Cr_3Ni_2SiN on a grain boundary.

8.7 Longer term ageing of NF709 and NF709R

All specimens were aged at least 10000 h at both temperatures, the longest ageing treatment reaching 17500 h at 750 °C for NF709R. Only results up to 10000 h are presented here.

Figure 8.15 shows optical micrographs of NF709 and NF709R after 10000 h at 750 °C and 800 °C. The precipitation is clearly denser in the specimen aged at 750 °C, with

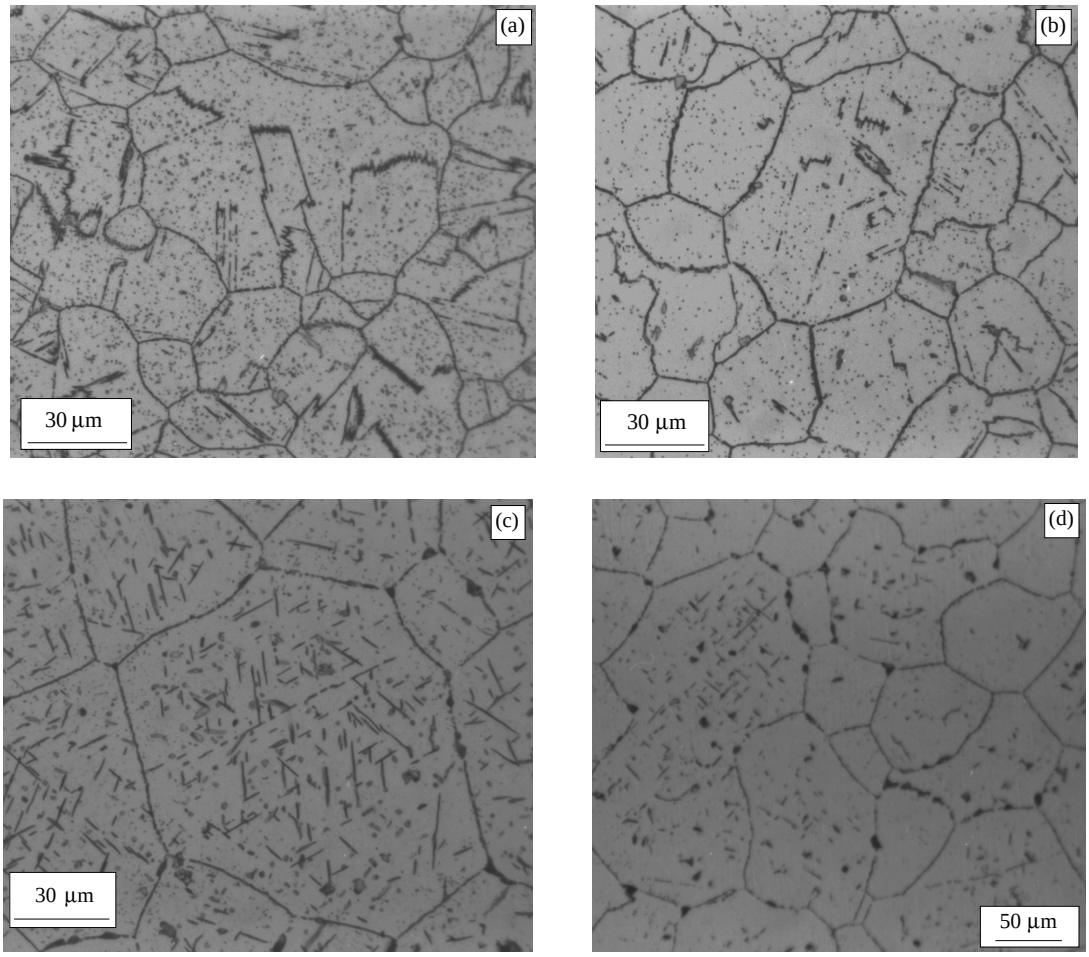

Figure 8.15: Optical micrographs of NF709 and NF709R aged 10000 h at 750 °C (a and c respectively) and 800°C (b and d respectively).

NF709 showing a stronger presence of $M_{23}C_6$ and Cr_3Ni_2SiN on twin boundaries and intragranularly (figure 8.15 (a) and (b)); NF709R shows a more even distribution of σ-

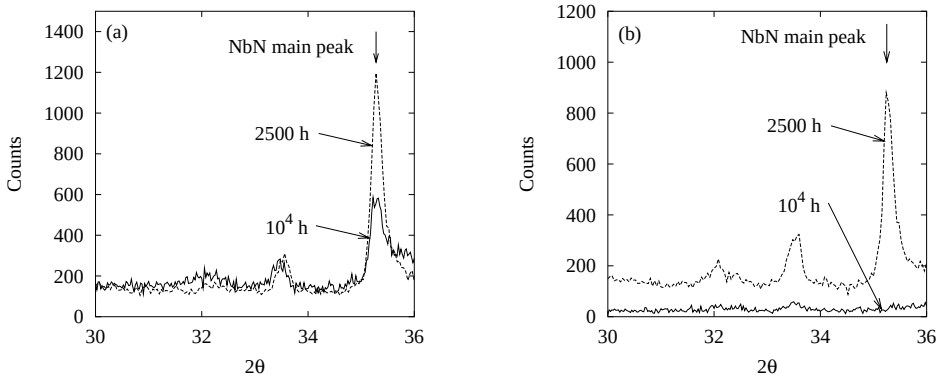

Figure 8.16: The main diffraction peak for NbN, (a) at 750 °C and (b) 800 °C for NF709 aged 2500 and 10000 h.

phase plates at 750 °C (figure 8.15 (c)). Following heat-treatment at 800 °C, σ-phase is present on grain boundaries and intragranularly (mainly in the larger grains) in NF709R.

The X-ray analysis of extracted residues revealed that, in NF709, NbN completely disappeared following heat-treatment at 800 °C and almost so at 750 °C (figure 8.16). This most likely follows the formation of CrNbN (Z-phase). As mentioned earlier, Z-phase, which is observed in transmission electron microscopy is not found using this method, probably because small CrNbN particles are dissolved during the extraction process. As for specimens aged 2500 and 5000 h, a separation is visible between $M_{23}C_6$ and Cr_3Ni_2SiN in the specimen aged at 800 °C but not for 750 °C; the lattice parameters were calculated to be:

Phase / Ageing time	5000 h	10000 h
$M_{23}C_6$	10.684 Å	10.679 Å
Cr_3Ni_2SiN	10.722 Å	10.712 Å

Table 8.8: The lattice parameters of $M_{23}C_6$ and Cr_3Ni_2SiN at 800 °C for two different ageing times.

Using TEM, it was possible to confirm the nature of the intragranular plates: figure 8.17(a) shows a thin foil of NF709R after 10000 h at 750 °C, in which large plates of σ-phase are found. The dislocations are decorated with Z-phase in a similar fashion as shown in previous figures. Large Cr_3Ni_2SiN particles were also found both on grain boundaries and intragranularly as illustrated in figure 8.17 (b) and (c).

Figure 8.18 shows precipitation on an incoherent twin boundary and on a grain boundary in NF709 after 10000 h at 750 °C. The particles have coarsened considerably when compared with similar observations after 100 h, as in figure 8.6 (b).

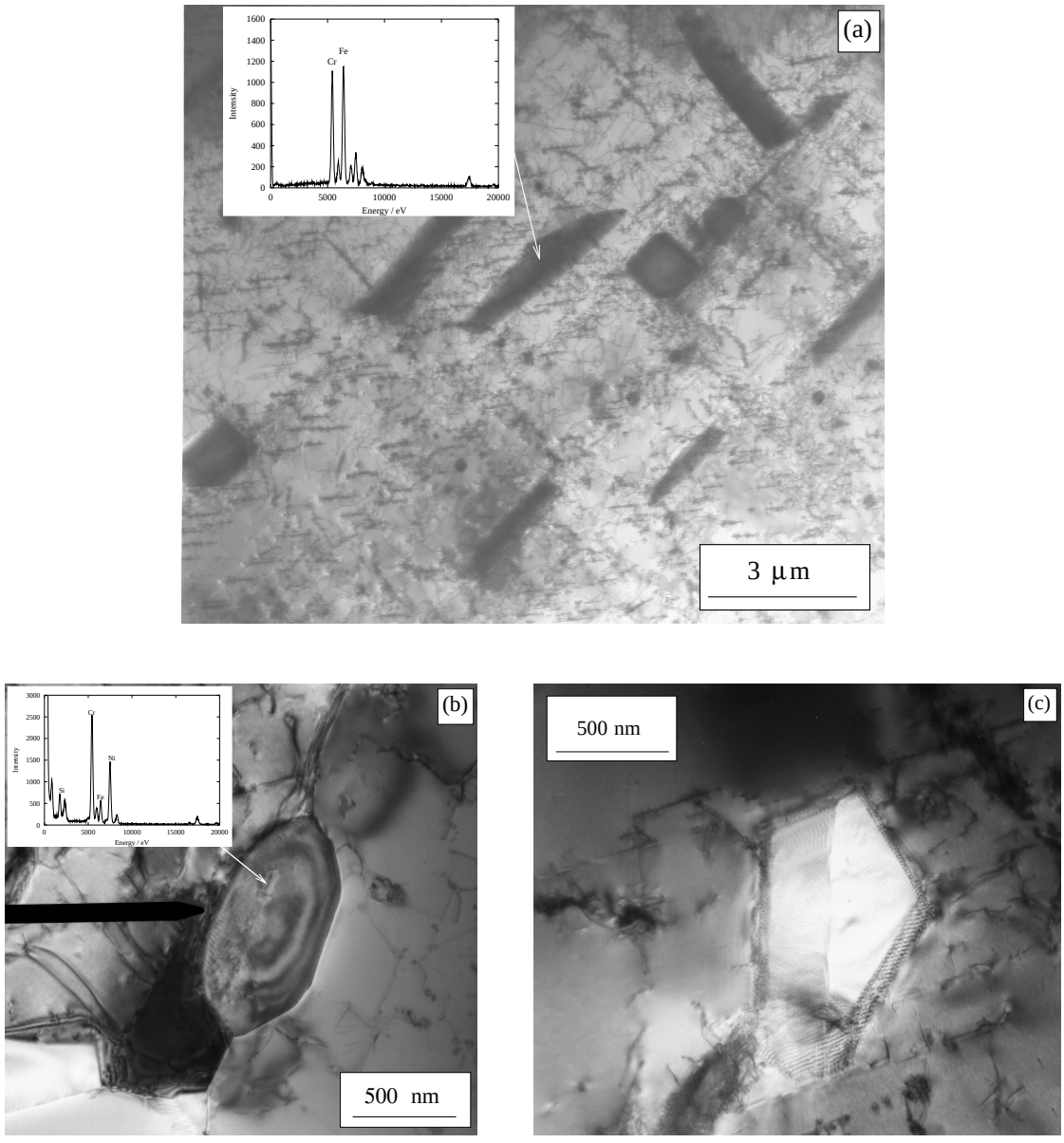

Figure 8.17: Transmission electron micrographs of a thin foil of NF709R aged 10000 h at 750 °C: (a) intragranular plates of σ phase and dislocations decorated by Z-phase. Cr_3Ni_2SiN (b) on grain boundary and (c) as an intragranular plate.

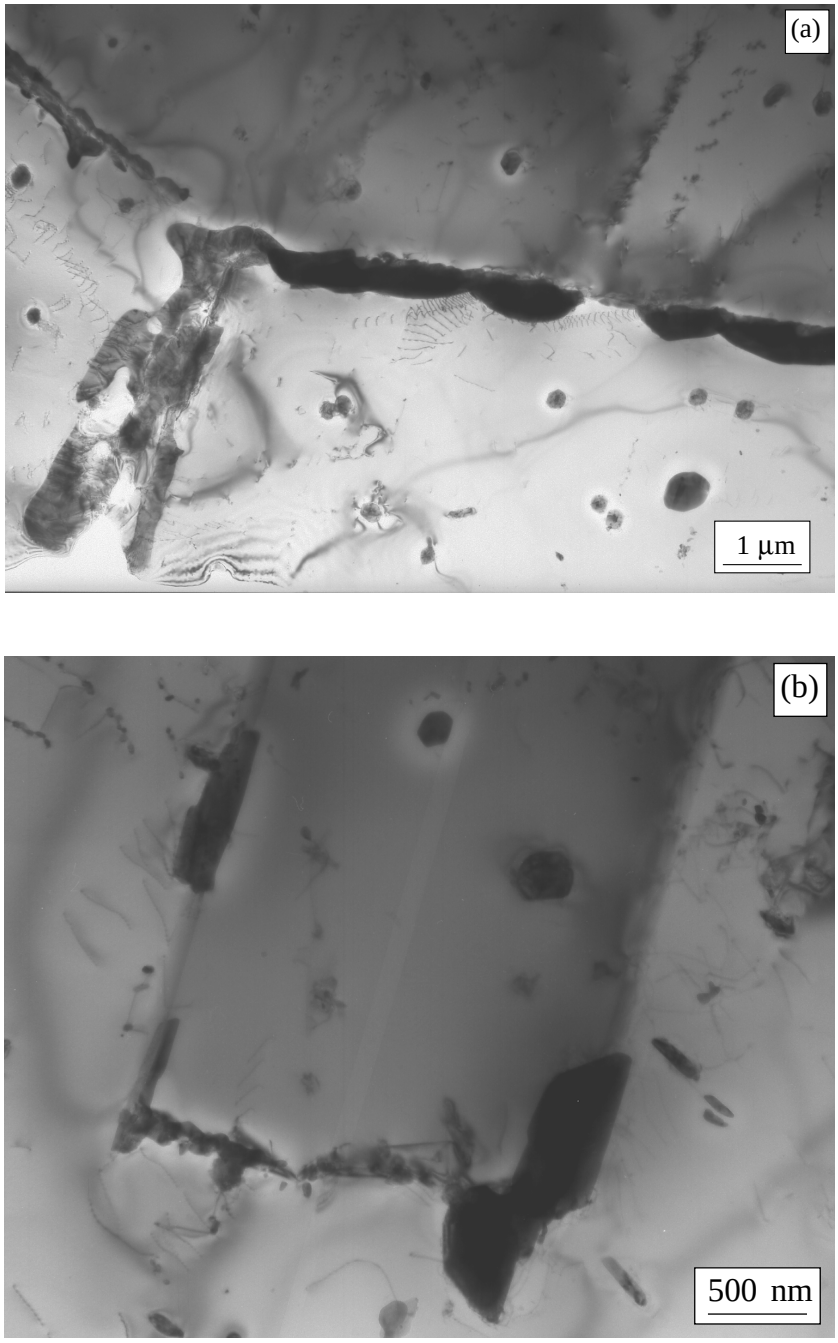

Figure 8.18: Transmission electron micrographs of a thin foil of NF709 after 10000 h at 750 °C, showing considerable coarsening of precipitates when compared to similar observations at shorter ageing times.

8.8 Summary and Discussion

8.8.a Summary

Table 8.9 summarises the phases observations at different times for NF709 and NF709R aged at 750 °C and 800 °C.

Time (h)	0	200	2500	5000	10000
NF709	NbN TiN (Nb,Ti)C	$M_{23}C_6$(+) Z-phase(+) NbN(-) TiN (Nb,Ti)C	$M_{23}C_6$(+) Cr_3Ni_2SiN(+) Z-phase(+) TiN NbN(-) (Nb,Ti)C	$M_{23}C_6$(+) Cr_3Ni_2SiN(+) Z-phase(+) TiN NbN(-) (Nb,Ti)C	$M_{23}C_6$(+) Cr_3Ni_2SiN(+) Z-phase(+) TiN NbN(-) (Nb,Ti)C
NF709R	TiN Z-phase	Z-phase(+) $M_{23}C_6$(+) TiN	Z-phase(+) $M_{23}C_6$(+) Cr_3Ni_2SiN(+) σ(+) TiN	Z-phase(+) $M_{23}C_6$(+) Cr_3Ni_2SiN(+) σ(+) TiN	Z-phase(+) $M_{23}C_6$(+) Cr_3Ni_2SiN(+) σ(+) TiN

Table 8.9: Summary of the different phases identified over the ageing treatments at 750 and 800 °C. (+) indicates a phase forming during the ageing treatment, (-) a phase dissolving. The same phases were identified at 800 °C although the quantities were, in some cases such as σ-phase, obviously different.

8.8.b Cr_3Ni_2SiN and G-phase in 20Cr/25Ni steels

Although M_6C is a quite frequently reported carbide in ferritic and austenitic steels containing Mo, as Fe_3Mo_3C, the structure sometimes referred to as η encompasses a much wider composition range [50] from $M_3M'_3X$ to $M_3M'_2SiX$, where M indicates a substitutional element such as Fe or Cr, while X indicates an interstitial element such as C or N. η is a diamond cubic structure whose lattice parameter varies in the range 10.6-12.4 Å.

Cr_3Ni_2SiX is a particular composition of the η structure, whose lattice parameter is 10.62 Å (JCPDS 17-330), which makes it extremely similar to $M_{23}C_6$ from a structural point of view, although the latter is cubic while the former is diamond-cubic. Very few studies report its presence under normal ageing conditions, while it is more frequently found in irradiated austenitic stainless steels.

In 1981, Titchmarsh and Williams [54] reported its presence in FV548, a Nb stabilised version of type 316 stainless steel. In this steel, Cr_3Ni_2SiC is not found under normal

In study	Cr	Ni	Mo	Mn	Si	Nb	C	N
Titchmarsh *et al.* [54]	16.5	12.0	1.44	1.14	0.35	0.92	0.11	-
Jargelius-Pettersson [55]	19.8	25.0	4.59	1.44	0.54	-	0.014	0.210
Powell *et al.* [60]	19.4	24.4	-	0.74	0.61	0.68	0.037	0.01

Table 8.10: Composition (wt%) of the steels investigated in some of the studies quoted.

ageing condition and its formation is attributed to the unusual segregation phenomena occurring in irradiated steels. In particular, point defect sinks are often surrounded by an increased amount of Si, because it is bound to the defects, and Ni, because it is slower than other elements to diffuse away from the sink. In both the works of Titchmarsh and Williams [54] and of Williams [53], the carbon content of Cr_3Ni_2SiC is assumed. This is supported by the fact that G-phase, another Ni, Si rich phase of composition close to $Ni_{16}Nb_6Si_7$ and space group Fm3m, forms instead of Cr_3Ni_2SiC in variants with a low level of carbon (0.02 wt%). A phase similar to Cr_3Ni_2SiC is reported by Jargelius-Peterson [55] in a 20/25 N-bearing steel, but as a nitride rather than a carbide.

The substitutional content of Cr_3Ni_2SiC undergoes significant changes as the temperature of ageing is modified. Williams [53] reports increasing amounts of Mo and Fe substituting for Cr and Ni respectively, when the ageing temperature increases. He therefore proposes the more general formula $(Cr, Mo)_3(Ni, Fe)_2SiC$. This study also gives evidence against the idea that Cr_3Ni_2SiC forms from $M_{23}C_6$ by infiltration of Ni and Si.

It is interesting to now study closely the precipitation of G-phase and η carbide under conventional ageing in 20/25 steels. The former phase is reported in various studies on 20/25-Nb stabilised steels [60, 65, 66], while report of the latter was only found for a 20/25 N-bearing steel, where it is rather a nitride than a carbide. Powell *et al.* [60, 65] and Ecob *et al.* [66] have found G-phase in a 20/25 Nb stabilised steel, and observed that NbC partially transforms to G-phase with time. Ecob *et al.* [66] have related the increasing relative instability of NbC compared to G-phase, in three different steels, to the amount of oxygen present in the steels. To justify this observation, they proposed that Si segregation was following oxygen segregation to the NbC particles, therefore creating the thermodynamic conditions required for the formation of G-phase. Nickel segregation may not be required in such steels, since the Ni content is more than double that of AISI 316 stainless steel.

On the basis of these observations, it is possible to argue that G-phase is more stable than Cr_3Ni_2SiC in these steels: segregation provides the increased Si level required, while the dissolution of NbC is expected to raise locally the carbon level. Both phenomena are expected to be favourable to the formation of Cr_3Ni_2SiC, which is nevertheless not observed.

It seems therefore reasonable to say that if either phase was to be found in NF709 or NF709R, it would be G-phase. However, none is observed, while Cr_3Ni_2SiN is present in significant quantities. In chapter 2, it has been proposed that observations on the effect of nitrogen on the formation of M_6C were better understood by considering M_6C and other compositions as occurrences of the same η structure. Again, the results here support the idea that the η structure is generally stabilised by nitrogen, whether its composition is Mo-rich or Ni/Si-rich.

8.8.c σ-phase formation and effect on mechanical properties

The difference between NF709 and NF709R is noticeable given the relatively small composition changes. As explained in chapter 2, σ-phase formation is favoured by both a high Cr and a low C content. The presence of σ-phase in NF709R but not in NF709 is therefore not surprising and is in fact predicted from the SGTE (Scientific Group Thermodata Europe) databases, using MT-DATA:

	NF709	**NF709R**
750 °C	0.8	5.9
800 °C	0	2.45

Table 8.11: The amount of σ-phase in wt%, predicted with MT-DATA for NF709 and NF709R, allowing for austenite, $M_{23}C_6$, M_6C, NbN, NbC, TiN, TiC, and σ-phase.

The role of σ-phase on mechanical properties, and particularly on creep strength, in austenitic stainless steels, is not clearly defined, and some attribute the main cause of a reduction of toughness to the general formation of carbides and nitrides [108].

The formation of copious amounts of σ-phase caused great concern about the ductility of NF709R after long term service. The results of creep tests provided by Nippon Steel were examined to identify the possible effects of the presence of this phase on the creep ductility. It is not clear what were the exact compositions of the steels used in the tests,

as only a label "22Cr" would distinguish some of the compositions tested. It was assumed that the "22Cr" labelled data were for NF709R while all others were for NF709.

As can be seen in figure 8.20, the results are the opposite of the expectations, with NF709R showing significantly better creep ductility, even for specimens with a rupture life of 5000 h and more, where σ-phase is expected in significant quantities.

An additional experiment was carried out to verify the deformation behaviour of the steels provided: after ageing 10000 h at 750 °C, samples of both NF709 and NF709R were deformed 30% in compression.

Figure 8.19 shows that grain boundary cracking was observed at various places in NF709, but nowhere in NF709R. Moreover, the micrographs show that the intragranular plates can deform to a limited extent.

These observations support the fact that carbide and nitride precipitation in general, rather than σ-phase alone, cause the embrittlement in these steels.

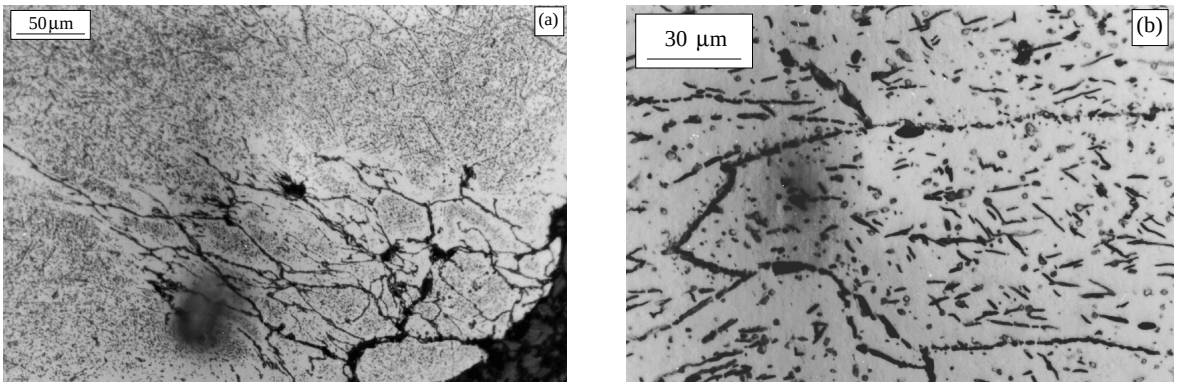

Figure 8.19: Optical micrographs of (a) NF709 and (b) NF709R deformed by 30% in compression after ageing 10000 h at 750 °C. Grain boundary cracking is observed at the corners of the specimen in NF709 (nowhere in the bulk material), not in NF709R. The intragranular plates of σ-phase are found to deform to a limited extent.

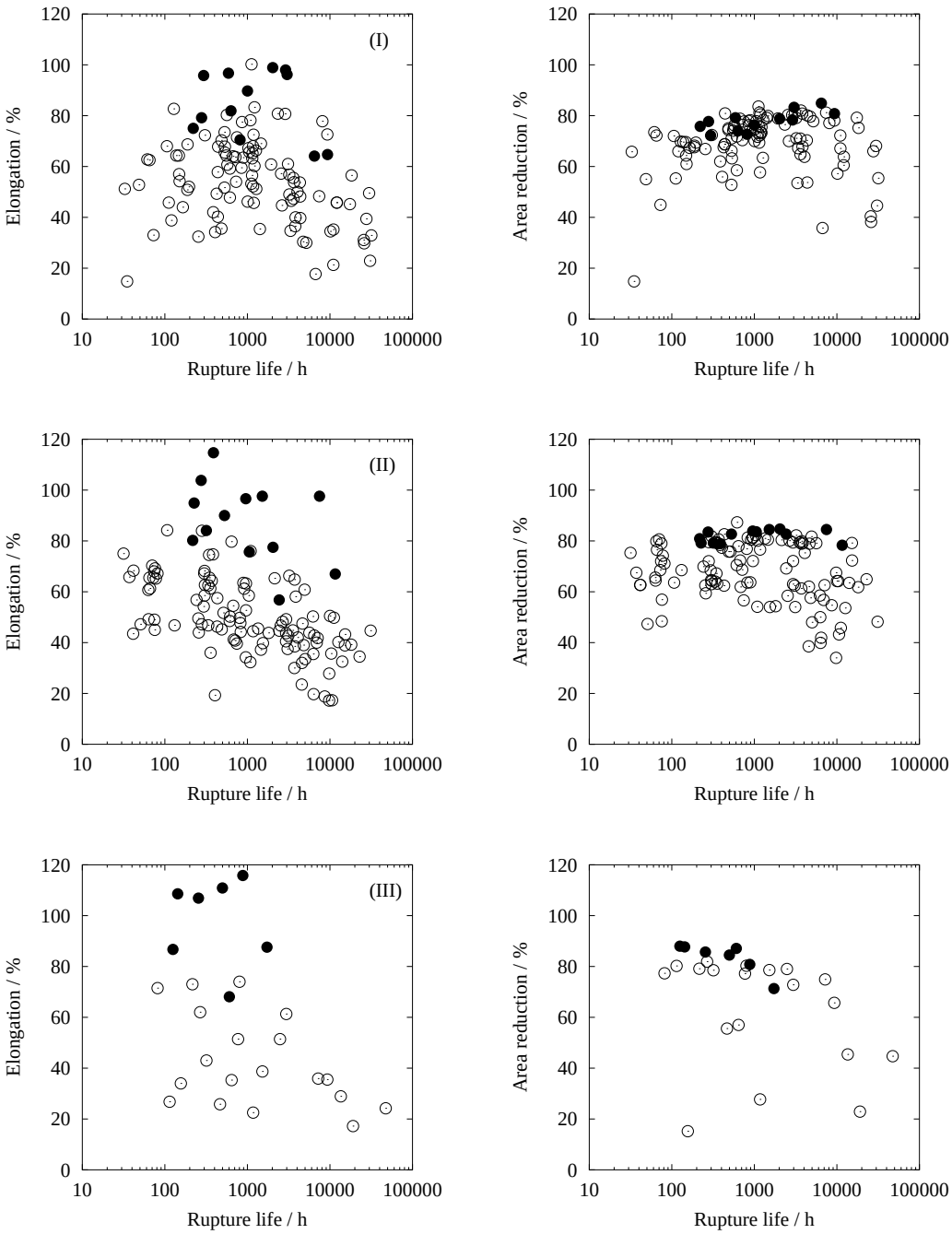

Figure 8.20: Creep elongation and reduction of area for the creep tests results provided by Nippon Steel at (I) 700 °C, (II) 750 °C, (III) 800 °C. ○ are for NF709, ● for NF709R.

8.8.d Quantifying the precipitation

The task of quantifying the amount of the different precipitates found in both NF709 and NF709R after different ageing times appeared impossible in practice. In the following, the different methods are presented with their limitations.

i Optical microscopy and scanning electron microscopy

For obvious reasons, most of the precipitates are not visible in optical microscopy. Small precipitates are not visible, while larger ones cannot be distinguished by morphology alone. Only σ-phase quantities could be estimated because of its particular appearance in scanning electron microscopy, when using backscattered electrons images (figure 8.21).

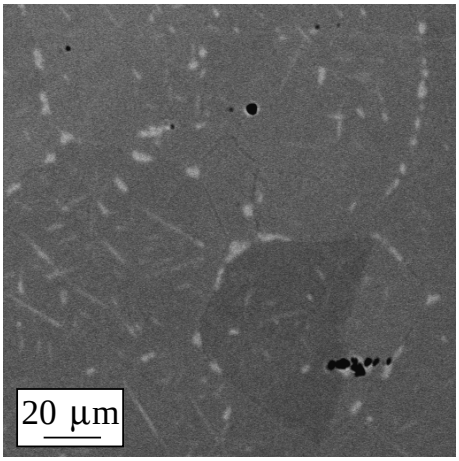

Figure 8.21: Backscattered electron image of grain boundary and intragranular σ-phase formed in NF709R after 10000 h at 750 °C, obtained in scanning electron microscopy. Because σ-phase does not contain interstitial elements such as C or N, it has, in average, a greater atomic number than the matrix and appears brighter. Carbides and nitrides, by contrast, are in average lighter than the matrix and appear darker, as can be seen on some grain boundaries.

ii X-ray analysis of extracted residues

The problem of quantifying the amount of the different phases present in a powder from its X-ray diffraction spectrum is well established. It is not possible to compare directly the areas of the peaks because different phases have different absorption coefficients which account for much of the intensity observed. In general, for a phase α in a polyphase specimen [109]:

$$I_{(hkl)\alpha} = \frac{K_e K_{(hkl)\alpha} X_\alpha}{\rho_\alpha \left(\mu/\rho\right)_s} \tag{8.1}$$

where $I_{(hkl)\alpha}$ is the intensity of the (hkl) diffracted line for phase α, K_e a constant for identical experimental settings, $K_{(hkl)\alpha}$ a constant for each diffraction line (hkl) of the phase α in the melange, ρ_α the density of the phase α, $(\mu/\rho)_s$ the mass attenuation coefficient of the polyphase specimen, and X_α the mass fraction of α in the melange.

Because the mass attenuation coefficient depends on the X_j:

$$\left(\frac{\mu}{\rho}\right)_s = \sum_j \left(\frac{\mu}{\rho}\right)_j \tag{8.2}$$

the problem is mathematically undetermined.

The conventional method to work around this difficulty consists of using a reference compound (corundum) added to the powder in a known quantity. With the help of calibration values providing the ratio of the intensity of a reference peak of the phase to quantify to that of corundum, it is possible to work out an amount present as a ratio of that of corundum. However, this requires that $I/I_{corundum}$ are known. This was only the case for $M_{23}C_6$ and σ-phase, but the peaks of the latter were for the most part hidden by peaks of other phases.

Further limitations of this method have been presented before concerning the size of the precipitates retained by the filter during filtration and the possible dissolution of the smallest particles.

iii Transmission electron microscopy

The smallest particles can only be seen during transmission electron microscopy, and in the case of Z-phase, only on carbon replicas. In TEM, phases such as $M_{23}C_6$ and Cr_3Ni_2SiN are difficult to distinguish on the basis of their morphology alone, and the use of EDX analysis is essential. This makes extremely time-consuming the identification of a number of particles large enough to provide reliable quantitative data, without mentioning the corrections required because TEM is in practice the observation of a projected volume.

A TEM based technique appears to be a promising method for reliable quantitative observations. Energy filtered TEM is similar to electron energy loss spectroscopy, but the whole image instead of a single beam is filtered according to the energy of the electrons. In this way, a composition map can be more or less easily obtained. However, the method is still under development and remains extremely time-consuming.

8.9 Conclusion

The precipitation sequence of NF709 and NF709R have been studied for heat-treatments of different duration at 750°C and 800°C. It has been shown that, despite their similar chemical compositions, these steels exhibit different precipitation behaviour. In particular, there is evidence that the nitride CrNbN, known as Z-phase, is more stable at higher temperatures in NF709R than in NF709. Also, σ-phase is found in copious quantities in the latter but not in the former.

With support of the existing literature, the formation of Cr_3Ni_2SiN in both NF709 and NF709R is taken as evidence that the η structure is generally stabilised by nitrogen.

To verify whether the formation of σ-phase was detrimental to the mechanical properties, the creep data provided by Nippon Steel were examined and aged specimens were deformed, with a unique conclusion that NF709R exhibits superior ductility when compared with NF709.

Different experimental techniques have been used together as it has been demonstrated that each presents serious limitations in a different domain of observation. In particular, evidence is given that small precipitates dissolve during the electrolytic dissolution of the austenite.

Chapter 9

Modelling the creep rupture life of austenitic stainless steels

Being able to predict quantitatively the creep rupture life of a steel, or its 10^5 h creep strength is of enormous interest for the design of alloys and their use in the power generation industry. Although tests cannot be avoided, a good quantitative model allows a considerable reduction in the number of trials needed to match the expected properties.

When complex properties such as creep life or toughness are addressed, physical models are mostly of qualitative use, but are yet not able to deliver accurate quantitative predictions as a function of the large number of controlling variables. Such problems have long been solved using empirical modelling and experience. Most widely used are probably the multi-linear and polynomial regressions (for example, in NRIM datasheet 6B, the tensile strength is modelled using a 3rd order polynomial). The methods have some advantages: they require a small number of coefficients and are generally simple to calculate. On the other hand, their flexibility is limited. They do not allow sufficient interactions between the different input variables and consequently their range of validity may be narrow. However, the continuous increase in computing power allows much more complex regression methods to be implemented relatively easily.

9.1 Neural Networks for empirical modelling

All regression methods can be described generally in terms of neural networks. To define a neural network, it is first necessary to present the single neuron.

9.1.a The single neuron

A single neuron has a given number of inputs x_i, and an output y. A weight w_i is associated with each input. The activation a of the neuron is defined by:

$$a = \sum_i w_i x_i \tag{9.1}$$

Equation 9.1 sometimes takes the form $\sum_i (w_i x_i + h)$, where h is called the bias, but in practice, this additional term is included in the general notation by considering w_0 associated with the constant input 1.

A single neuron output is a function of its activation $y(a) = f(a)$, where the function f depends on the problem considered.

9.1.b More complex networks

The standard feedforward networks used in this work consist of 2 layers of neurons interconnected as described in figure 9.1. These networks are also referred to as three layers network which are the inputs, the hidden units and the output. The second layer

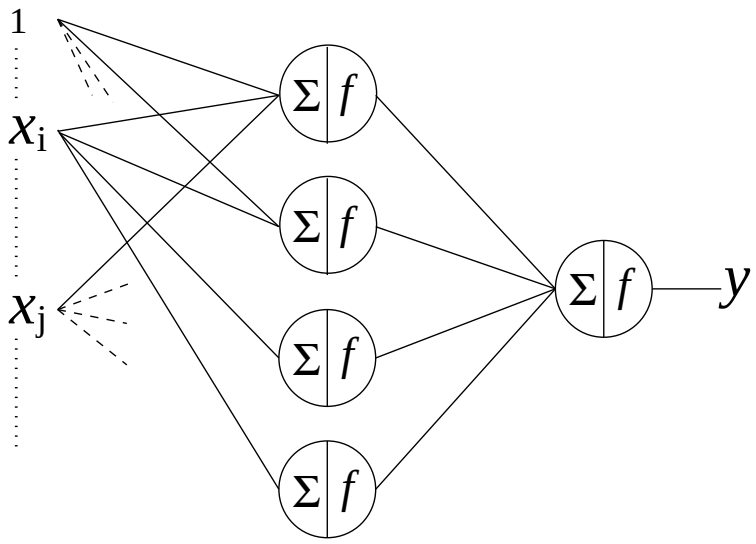

Figure 9.1: A three layers feedforward network identical to the one used in this work. The activation function of the neurons in the first layer is a tanh, and is linear in the second one. The complexity of the model is controlled by the number of hidden units.

is often referred to as 'hidden layer' and its neurons as hidden units. Their activation

function is non-linear, in the present case a tanh function. The third layer performs a linear combination of each hidden unit output.

9.1.c Neural Network as a regression tool

In supervised learning, the network is presented with a data set $D = \left\{\mathbf{x}^{(n)}, \mathbf{t}^{(n)}\right\}$, and the weights are adjusted so as to minimise an error function. In the light of the description of a single neuron, performing a linear regression on a data set D can be described as training a single neuron with a linear activation function. In the case of the two layer network in figure 9.1, the learning process is equivalent to a multiple, non-linear regression. The existence of an intermediate layer also allows the model to identify interactions between variables.

9.1.d Learning and making predictions

The algorithm used to train the models has been written by D.J.C. Mackay. It implements a particular learning method using Bayesian statistics to infer the most probable distribution for the weights given the data.

i A simple example of inference

A good example to illustrate Bayes rule is that of someone drawing balls from 11 urns each containing 10 balls. Of the 10 balls in each urn, u are black, and the rest are white. Given that the person draws N times (replacing the balls on each occasion) from a chosen

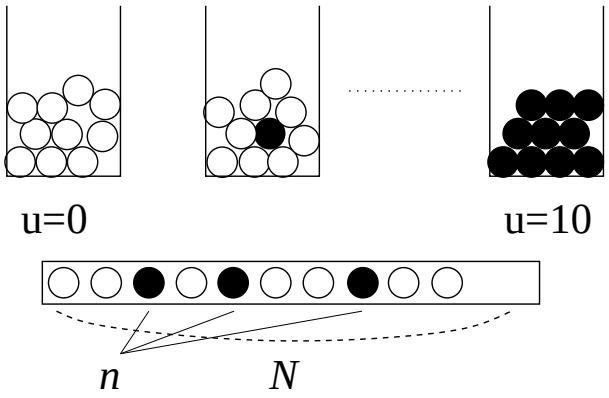

Figure 9.2: A person is drawing N times from a same urn u chosen among ten and presents the result. The problem is to guess which urn the person has chosen and to use this to predict the next draw.

urn, the problem is to guess from which urn u the person has drawn. In this case, Bayes

rules is written:

$$P(u|n,N) = \frac{P(n|u,N)\,P(u|N)}{P(n|N)} \tag{9.2}$$

that is, given that the person has drawn n black balls among N, the probability that urn u was used is the probability of drawing n black balls from u times the probability to chose u, over the overall probability of drawing n balls. This last term is also:

$$P(n|N) = \sum_u P(n|u,N)\,P(u|N) \tag{9.3}$$

To solve the problem, we can first assume (this is our hypothesis H) that the person will chose any of the urns with the same probability, so that $P(u|N)$, which is actually $P(u)$ since it does not depend on the number of draws, is 1/11; this is called the *prior*. For each possible value of u, we can then compute the probability of drawing n black balls, which gives a binomial distribution. If we are simply interested in knowing which urn the person has most probably drawn from, that is to compare the different models, there is no need to calculate the normalising constant $P(n|N)$. The result is a probability distribution on u, which, not surprisingly, is maximum for $n = u$. However, almost all other possibilities have a non zero probability, as can be seen in figure 9.3, apart from the two urns containing either only white or only black balls.

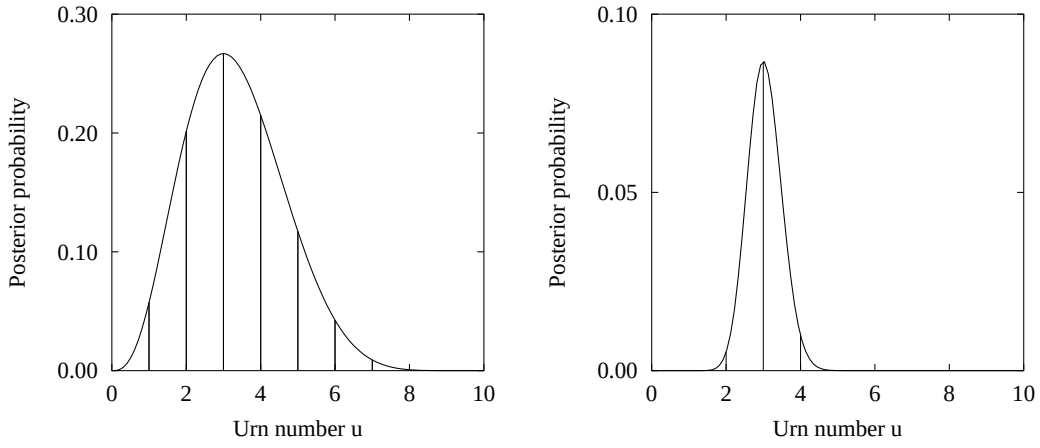

Figure 9.3: The posterior probability for the chosen urn u, when $n = 3$ ($N = 10$). The person has most probably drawn from the urn containing 3 black balls, but the probability that he/she has drawn from other urns is not negligible. The right figure shows that when more data are presented, ($n = 30$, $N = 100$) the probability of $u = 3$ is much greater than $u = 2$ and $u = 4$ and that any other value of u is virtually impossible

An interesting problem is to now use these results to predict how likely the person is to obtain a black ball at the next draw. For this, we consider the different possible values of u with their respective probability; for each of them, the probability of obtaining a black ball is $u/10$, so the overall probability is

$$\sum_{u=1}^{u=10} P\left(u|n,N\right) u/10 \tag{9.4}$$

This process is called *marginalizing* over all the possible values of u.

A traditional statistic approach would have used the most probable hypothesis ($u = 3$) to make this prediction, and would have led to a value of 1/3. In the Bayesian approach, all the possibilities are taken into account, but weighted according to how probable they are.

ii Quantifying the uncertainty

One of the most interesting features of the Bayesian approach to inference problems, is that it provides a quantitative estimation of the uncertainty in fitting a model to the data. Figure 9.3 shows the posterior distributions for $P(u)$ when $n = 3,\ N = 10$ and $n = 30,\ N = 100$. In the first case, the distribution is spread, while it is sharply peaked in the second one. Consequently, the predictions made on the basis of the second model ($n = 30,\ N = 100$) is associated with a much smaller uncertainty than those made using the first set of data. The reader interested in the relatively complex mathematical treatment of this problem can refer to [110].

iii Application to neural network learning

Neural networks are usually trained by minimising an error function such as equation 9.5:

$$\begin{aligned} M(\mathbf{w}) &= \beta E_D + \alpha E_W \\ E_D &= \frac{1}{2}\sum_i \left(t^{(i)} - y^{(i)}\right)^2 \\ E_W &= \frac{1}{2}\sum_i w_i^2 \end{aligned} \tag{9.5}$$

where E_D is the overall error, and E_W the regulariser, used to force the network to use small weights (equations 9.5). α and β are control parameters which largely influence

the complexity of the model. $t^{(i)}$ is the target for the set of inputs $\mathbf{x}^{(i)}$, while $y^{(i)}$ is the corresponding network output.

The method used in this study, developed by MacKay [111], is based on Bayesian probability theory and treats learning as an inference problem.

Rather than trying to identify the best set of weights, the algorithm infers a probability distribution for the weights from the data presented. When making predictions, the variety of solutions corresponding to different possible sets of weights are averaged using the probabilities of these sets of weights, a process called *marginalising*.

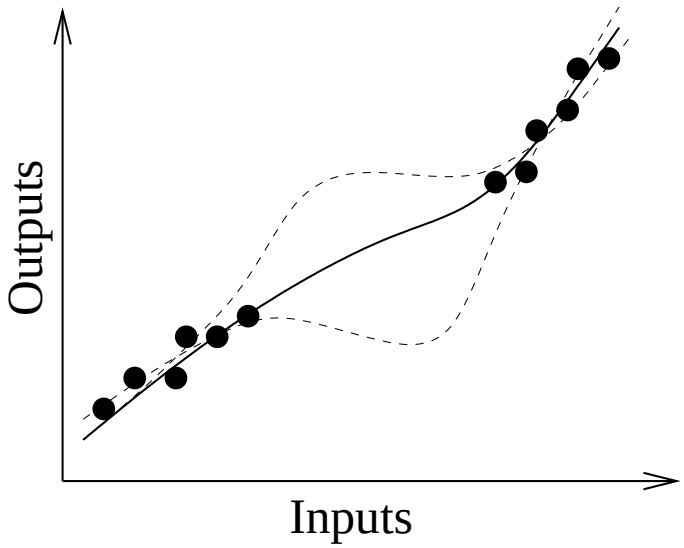

Figure 9.4: Where data are sparse, the probability distribution of the weights is wider, and predictions are accompanied by a larger error bar.

A major consequence is that it is possible to quantify the uncertainty of fitting: if the inferred distribution is sharply peaked in the weight space, the most probable set will give by far the largest contribution to the prediction and alternative solutions will have little importance. As a consequence, the prediction will be associated with a small uncertainty. If on the contrary, the data are such that different sets of weights are similarly probable, alternatives will contribute in similar proportions and the error bar will be large, as typically occurs in regions of the input space where data are scarce or exceptionally noisy. This is illustrated in figure 9.4.

In this context, the performances of different models are best evaluated using the log predictive error (LPE) as defined below. This error penalises wild predictions to a lesser

extent when they are accompanied by appropriately large error bars.

$$\mathrm{LPE} = \sum_m \left[\frac{1}{2} \left(t^{(m)} - y^{(m)} \right)^2 / {\sigma_y^{(m)}}^2 + \log \left(\sqrt{2\pi}\, \sigma_y^{(m)} \right) \right] \tag{9.6}$$

where $\sigma_y^{(m)}$ is related to the uncertainty of fitting for the set of inputs $\mathbf{x}^{(m)}$.

9.1.e Practical aspects of the neural network training

i The overfitting problem

Because of the great flexibility of the functions used in the network, there is a possibility of overfitting data. Two solutions are implemented which contribute to avoid overfitting. The first is contained in the algorithm due to MacKay: the complexity parameters α and β are inferred from the data, therefore allowing automatic control of the model complexity.

The second resides in the training method. The database is equally divided into a training set and a testing set. To build a model, about 150 networks are trained with different numbers of hidden units and seeds, using the training set; they are then used to make predictions on the unseen testing set and are ranked by LPE. Figure 9.5

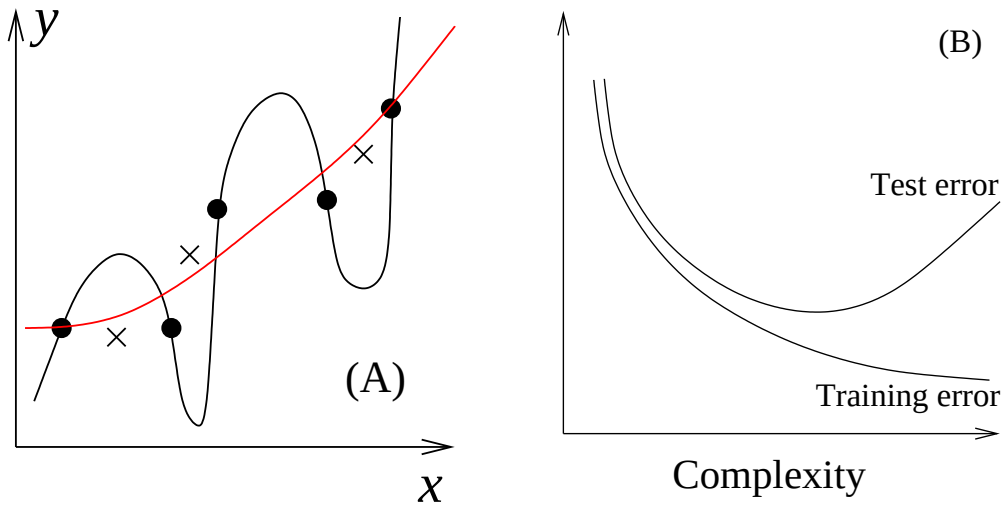

Figure 9.5: (A) When a model has overfitted the training data (•), the error on the test data (×) is larger then for an optimum model which fits the trend but not the noise. (B) illustrates the behaviour of the error on the training and testing sets as a function of the complexity of the model.

illustrates the behaviour of the error on the training and the testing set. Because it is

possible to obtain a near perfect fitting, the error on the training set is always decreasing with increasing complexity. The error on the testing set decreases at first, as the fitting improves, but increases again when overfitting occurs.

ii Choice of variables

Careful selection of the input variables and of the output is essential to the construction of a good model. For example, if a particular combination of two variables is thought to be of particular importance, it can be included as a variable itself. The same applies to functions of relevant variables. In creep problems for example, $\log(t)$ is much more relevant than t, and models trained to predict $log(t)$ perform much better than those with t as an output.

Because the algorithm includes an automatic relevance detection [110], variables which are either redundant or found to be irrelevant are affected a zero weight. There is therefore little to gain in reducing the number of input variables by any other process.

iii Other practical aspects of the training

To ensure a good distribution of the data in the data set, it is first randomised, or rather re-organised, with every odd line being moved to the testing set. However, this procedure has been found to be inappropriate in this particular case, as will be explained later. Another important step is the normalisation, which brings the range of variations of all the variables between -0.5 and 0.5. This is to avoid having very different scales of variations between the different inputs.

9.1.f Committee Model

The complexity of a model depends on its number of hidden units. Therefore, models with different numbers of hidden units will give different predictions.

To explain the origin of another potential difference between models, the example of the urn is useful. To estimate the probability of a black ball being drawn at $N+1$, it was first assumed that the choice of the urn was totally random, *ie* $P(u) = u/11$. However, this might not be the case. Maybe some are easier to access than others ? For example, if urn 4 is much easier to access than urn 3, our final guess of which urn has most probably been used might be changed, particularly if N is relatively small, as in figure 9.3 where 3 and 4 are not far from equiprobable under the assumption $P(u) = 1/11$.

This illustrates the fact that the *prior* $P(u)$ or $P(\Theta|H)$ in the general case, is important

for our predictions.

The same apply when calculating the posterior distribution $P(\mathbf{w}|\alpha, \beta, H)$. For a given number of hidden units, the predictions of a model still depends more or less strongly on the prior distribution of the weights. In practice, the distribution is assumed to be a Gaussian, whose parameters are fixed by a seed.

i The training process

For this reason, the training process involves in fact the training of a large number of models with different numbers of hidden units (typically 1 to 25), and different priors, that is different seeds (typically 5).

These models are then ranked according to how they perform on unseen data. Most of the time, a combination of the best models performs better than a single model.

ii Committee model

To determine the optimum number of models to use in a committee, the combined prediction error is calculated for an increasingly large number of models. Most of the time, this combined error presents a minimum which corresponds to the optimum number of models to be used (see figure 9.6). The committee prediction is the average of

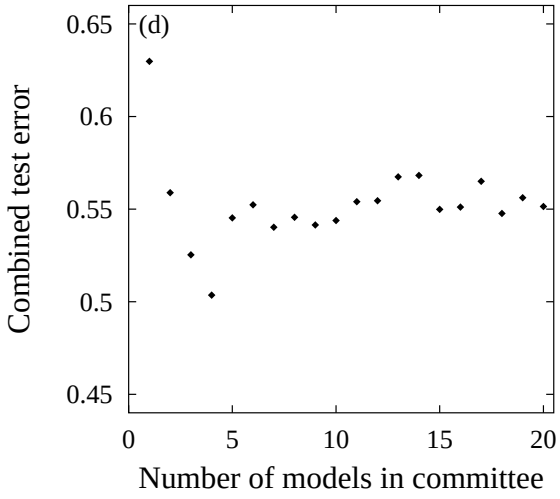

Figure 9.6: An example of the variation of the combined test error when the number of model in the committee is increased. In this case, the optimum number of model is found to be 4

the predictions of the models constituting the committee, while the error is calculated

according to:

$$\begin{aligned} \bar{y} &= \frac{1}{L}\sum_{l} y^{(l)} \\ \sigma^2 &= \frac{1}{L}\sum_{l} \sigma_y^{(l)\,2} + \frac{1}{L}\sum_{l} \left(y^{(l)} - \bar{y}\right)^2 \end{aligned} \tag{9.7}$$

where L is the number of networks in the committee, and, in this particular case, σ is the standard deviation. Note that we now consider the predictions for a given, single set of inputs and that the exponent (l) refers to the model used to produce the corresponding prediction $y^{(l)}$. In practice, an increasing number of networks are included in a committee and their performances are compared on the testing set. Most often, the error is minimum when the committee contains more than one model. The selected models are then retrained on the full database.

9.2 Traditional empirical method for creep strength predictions

The need for quantitative predictions of the creep strength, or the rupture life, of austenitic stainless steels has led to the use of more or less complex regression methods.

For example, the influence of some alloying elements has been studied [6] using linear regression, such as equation 9.8 or 9.9, which estimate the 10^4 h creep rupture stress as a function of the composition in wt%, for AISI 316 and 304 respectively.

$$\sigma_{f,10^4\mathrm{h}} = 173.8 + 7243(\mathrm{B}) + 961.1(\mathrm{N}) + 1145(\mathrm{S}) - 7.5(\mathrm{Cr}) \tag{9.8}$$

$$\sigma_{f,10^4\mathrm{h}} = 90.81 + 115(\mathrm{Mo}) + 498.5(\mathrm{W}) \tag{9.9}$$

The NRIM (National Research Institute for Metals, Japan) uses traditional methods to fit the creep curves of each steel studied. Typically, a time-temperature parameter such as the one given in equation 9.10, is fitted by a polynomial of $\log(\sigma)$ (equation 9.11), and allow, for a given composition, extrapolation to different stresses and temperatures.

$$P = \frac{\log(t_R) - \log(t_a)}{T - T_a} \tag{9.10}$$

$$P = b_0 + b_1 \log(\sigma) + b_2(\log(\sigma))^2 + \cdots + e_i \tag{9.11}$$

where t_R is the time to rupture, T the test temperature, t_a and T_a adjustable parameters, b_i the coefficients of the polynomial and e_i an error term. As can be seen in the datasheet NRIM 28B, these parameters vary significantly even between different heats of the same grade (in this case SUS 347H, an 18Cr-12Ni-Nb wt% stainless steel).

The limitations of such methods are obvious: the composition range is limited to variation within a grade of austenitic stainless steel, or less. Non-linear effects or interactions can not be identified and extrapolations are made without any indications as to whether they are safe or not. However, they are easy to implement and to publish, consisting of a maximum of 10 parameters.

On the other hand, neural network models require substantial computational power, and printing the set of weights making up a single network is not feasible. These limitations, though, are disappearing as it is now possible to publish the software on the world wide web, as it has been done with all the models described here (*www.msm.cam.ac.uk/map*).

9.3 Building a database

A large database was compiled for the creep properties of various grades of austenitic stainless steels: AISI 304 (basic 18Cr-12Ni), AISI 316 (304 + Mo), AISI 321 (304 + Ti), AISI 347 (304 + Nb) and many variants designed for heat-resistant applications (for example, 316 + Ti, Esshete 1250, etc.). It contains a total of about 3500 entries which, as explained above, are equally distributed between the training and testing sets.

Figure 9.7 gives an idea of the distribution of each input against the logarithm of the rupture life. The dataset included all of the following NRIM datasheets : 5B, 6B, 45, 28A, 16B, 26B, 14B, and most of the data published by the British Steelmakers Creep Committee [112] for 304, 316, 321 and 347. Only limited data could be extracted from publications [49, 61, 113, 114, 42, 115, 26, 116, 117, 118, 119, 120, 121, 122, 123, 124]. This is essentially because of non standard pre-test mechanical treatments performed in order to accelerate the evolution of the microstructure.

The data set includes the following variables: test conditions (stress and temperature), chemical composition, solution treatment temperature and time (the latter being available in a very limited number of cases), nature of the quench following, grain size, and logarithm of rupture life. The minimum and maximum values are given in table 9.1. Be-

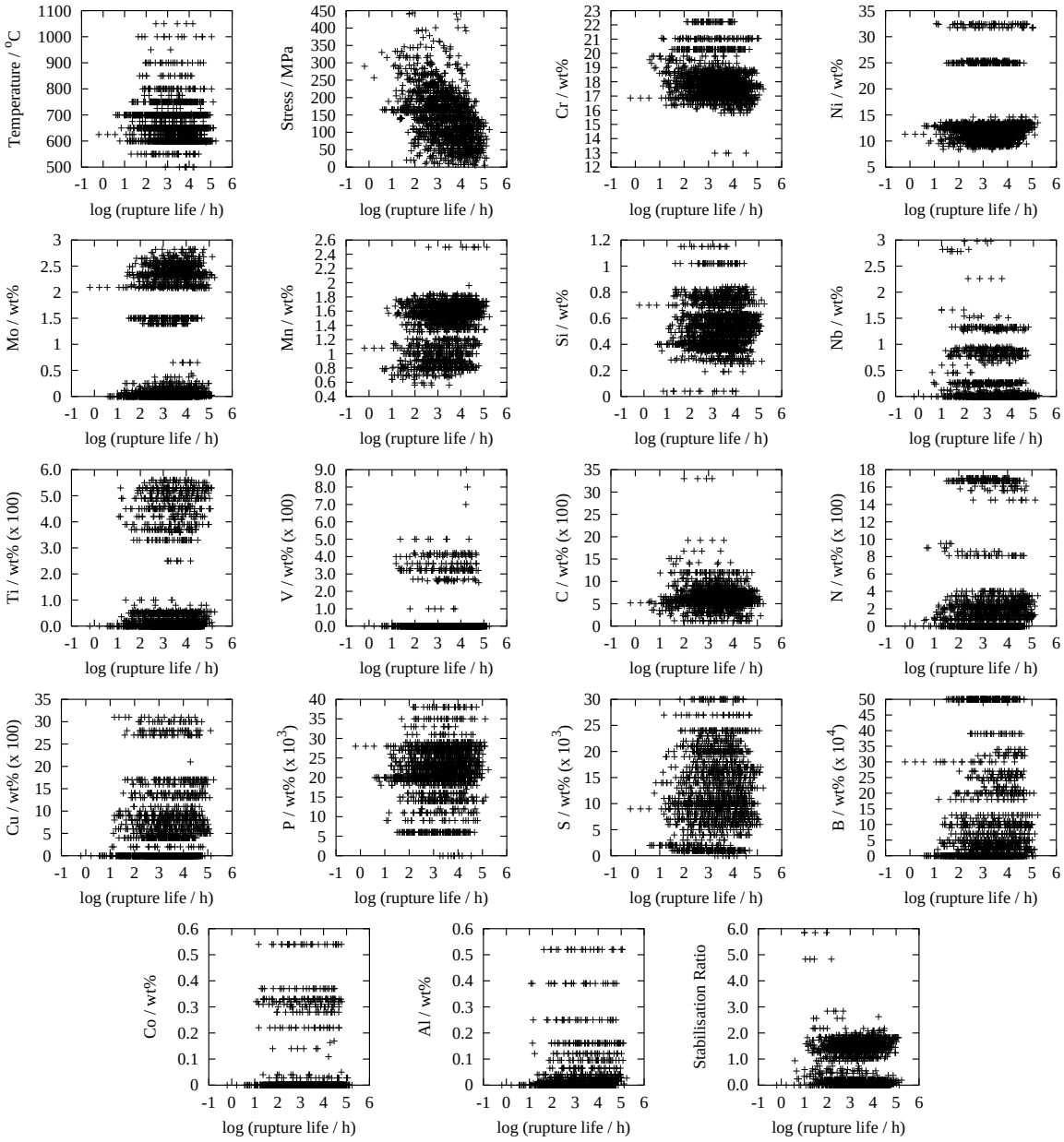

Figure 9.7: The distribution of the different inputs against the log of creep rupture life. This way of representing the data should not hide the possibility of numerous non documented interactions.

cause the algorithm includes an automatic relevance detection [110], variables which are either redundant or found to be irrelevant are affected a zero weight. There is therefore little to gain in reducing the number of input variables by any other process.

Input variable	Minimum	Maximum	Mean	Std deviation
Test Stress (MPa)	5	443	145	72
Test Temperature (°C)	500	1050	667	71
log (rupture life / h)	-0.200	5.240	3.324	0.879
Cr wt%	12.98	22.22	18.08	1.35
Ni wt%	8.40	32.48	13.82	5.47
Mo wt%	0.00	2.82	1.05	1.10
Mn wt%	0.56	2.50	1.36	0.35
Si wt%	0.040	1.150	0.545	0.171
Nb wt%	0.000	2.980	0.242	0.449
Ti wt%	0.000	0.560	0.131	0.199
V wt%	0.000	0.090	0.004	0.011
Cu wt%	0.000	0.310	0.051	0.074
N wt%	0.000	0.170	0.029	0.052
C wt%	0.012	0.330	0.062	0.025
B wt%	0.000	0.005	0.001	0.0016
P wt%	0.000	0.038	0.021	0.0067
S wt%	0.000	0.030	0.012	0.0071
Co wt%	0.000	0.540	0.037	0.1090
Al wt%	0.000	0.520	0.029	0.0804
Solution treatment temperature (°C)	1000	1350	1102	51

Table 9.1: The different inputs in the data set.

Compositional data were often missing. In such circumstances, elements usually known to be deliberate additions were set to zero while impurities were set to the average of the available data (e.g. phosphorus and sulphur). There is undoubtedly a regrettable loss of information when the amounts of elements such as Mo or Nb present as impurities are not given, as there is evidence that these elements have an influence [6].

9.4 Creep rupture life model

It is usual to attempt to predict the rupture strength for a given life time. However, the creep stress is only present as a finite number of discrete values while the rupture life is much more continuously spread, and therefore seemed a more appropriate target.

When training a model, the choice of input variables is of great importance. Also, when a combination of these variables is believed to be of particular importance, the

model can be improved by adding the combination as an explicit variable. The model was trained on the logarithm of the rupture life rather than the rupture life itself, and the calculated stabilisation ratio was used, as given below:

$$\text{Stabilisation Ratio} = \frac{\text{Nb}/8 + \text{Ti}/4}{\text{C} + \text{N}} \tag{9.12}$$

where the concentrations are in weight %. This is because precipitation of MX (where M is either Nb or Ti and X either C or N) is believed to be of particular importance to the creep behaviour of austenitic stainless steels, as will be discussed in more detail later. To avoid biasing the model, the individual variables making up the stabilisation ratio are also included, so that a direct influence of any of them can also be detected. Other input variables are as given in table 9.1.

Because some inputs were not always given (the solution treatment temperature for example), about 1000 amongst the 3500 entries of the database could not be used.

About 130 networks were trained with up to 22 hidden units and 6 different seeds. As expected, the perceived level of noise during training decreases as the model becomes more complex. The results of the training are shown in figure 9.8.

The purpose and method for building a committee model has been discussed earlier. In this case, the optimum committee was found to have 4 members. The perceived significances σ_w for these four models are shown in figure 9.9. They represent the extent to which a particular input explains the variation of the output, rather like a partial correlation coefficient in a multiple linear regression analysis.

The predictions of the final committee model (figure 9.10) contain a very few outliers considering that there is a total of about 2000 points. The improvement is clear compared with the best model alone.

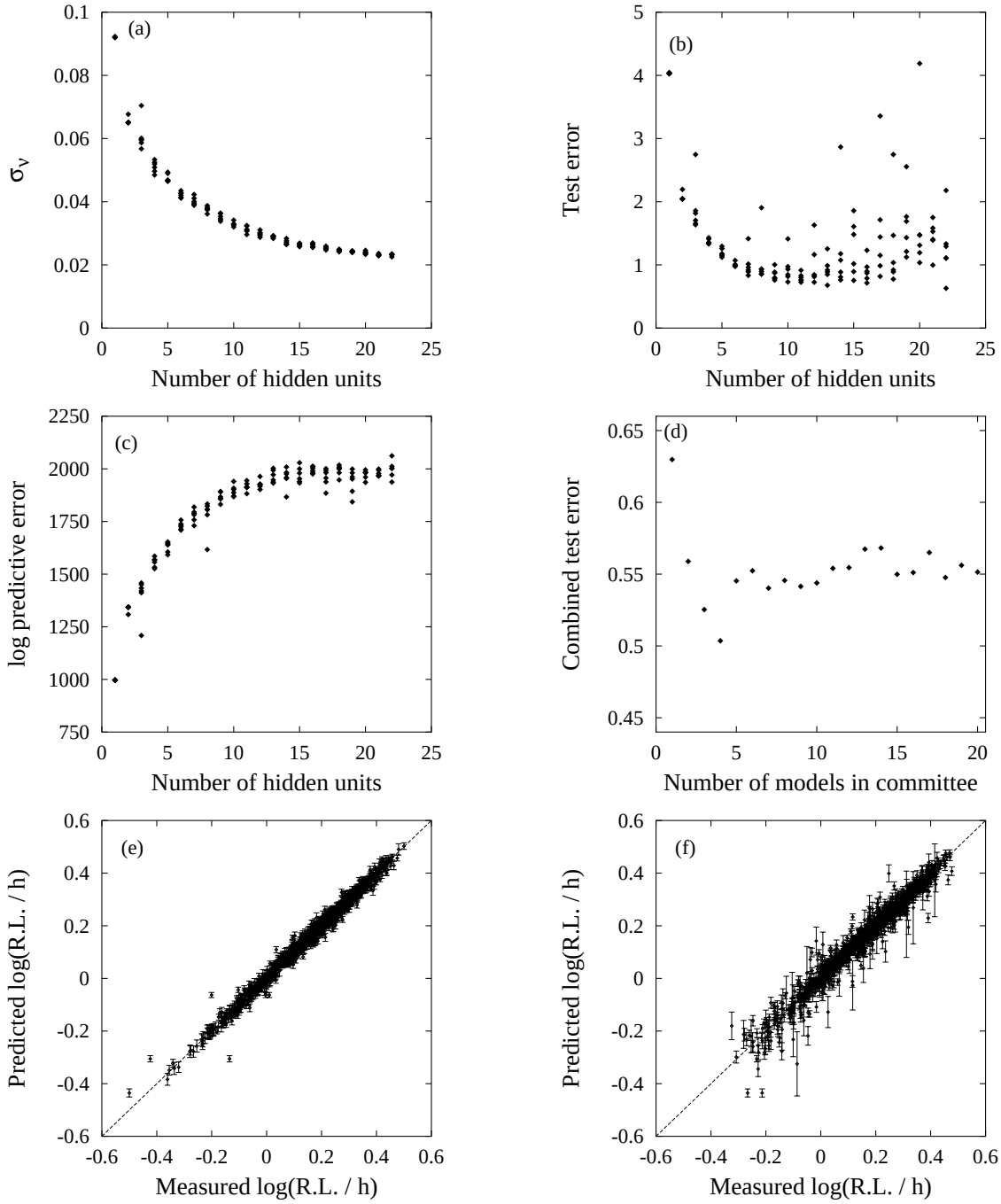

Figure 9.8: The perceived level of noise σ_ν (a), the test error (b), the log predictive error (c) of the models with increasing numbers of hidden units, the combined test error (d) for an increasing number of models in committee, and the performances of the best single model on seen (training set, (e)) and unseen data (testing set (f)). (e) and (f) are plots of the predicted rupture life (R.L.) against the experimental values, in this case both are normalised.

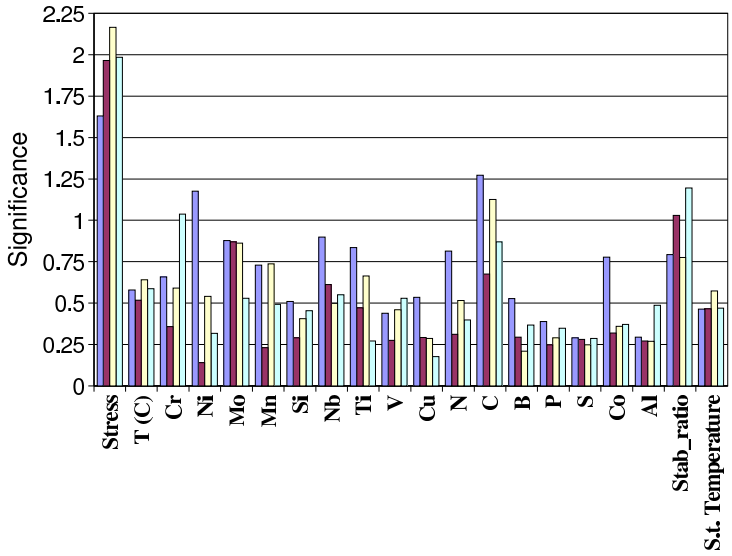

Figure 9.9: The perceived significances σ_w for the first four networks, constituting the committee model for the creep rupture life. S.t. stands for solution treatment.

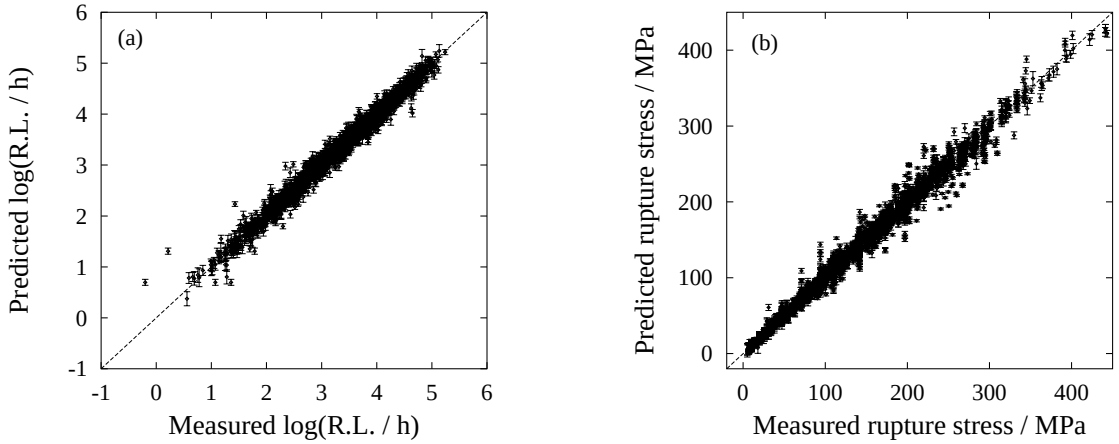

Figure 9.10: The performances of the final committee model on the whole database, for the rupture life model (a) and the creep strength model (b).

9.5 Creep strength model

The creep strength model was built essentially to facilitate quantitative comparisons with literature. In this case, the target was the stress and the life time was an input. The solution treatment temperature was not included to allow use of the entire database.

It seems of little interest to reproduce here all the results from the training such as test error or LPE as a function of number of hidden units as their evolution was similar to that observed for the creep rupture life model. In this case, the optimum number of models in committee was found to be 12. The performance of the committee is shown in figure 9.10.

9.6 Applications

9.6.a Molybdenum in AISI 304 and AISI 316

The difference between AISI grades 304 and 316 resides essentially in the addition of about 2 wt% of molybdenum. The chromium and nickel concentrations are smaller and larger, respectively, for AISI 316 compared to AISI 304. Rupture stresses for 10^4 h at 650 °C are respectively around 80 MPa and 110 MPa [125].

There are no specifications as to what the maximum level of molybdenum should be for the AISI 304 steels. It is common to find up to 0.5 wt% Mo in these steels. For AISI 316, an addition of 2-3 wt% Mo is specified. It has been shown that molybdenum has a beneficial effect on creep strength because of its solution strengthening role, although this effect can disappear after prolonged ageing due to the formation of Mo-rich Laves phase [6].

Figure 9.11 illustrates the predicted effect of molybdenum on the 10^4 h rupture stress. The initial increase is consistent with equation 9.9, which predicts a strong effect of small additions of Mo in 304. The predicted gradient (assuming a linear variation) is 38 MPa / wt% between 0 and 0.02 Mo wt%, which is lower than the one given by equation 9.9. Particularly interesting is that the trend between 0 and 1.1 wt% of molybdenum shows an excellent agreement (correlation 0.995) with a $c^{1/2}$ (where c is the concentration) dependence expected for a solution strengthening mechanism [126].

The flattening of the curve would be consistent with precipitation of a molybdenum

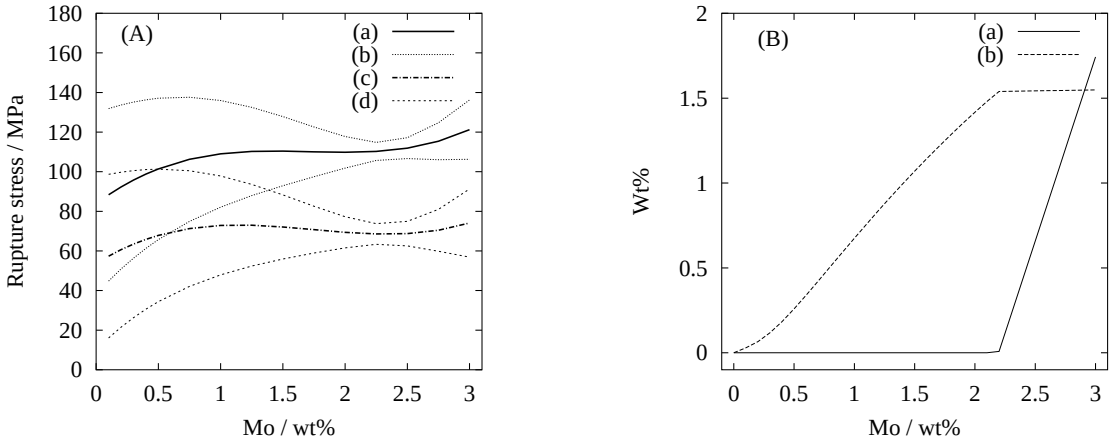

Figure 9.11: (A) The predicted effect of Mo on (a) the 10^4 h and (c) the 10^5 h rupture stress at 650 °C, (b) and (d) are the error bounds for (a) and (c) respectively. (B) MT-DATA prediction for (a) the amount of Laves phase and (b) the amount of Mo in solid solution in austenite for a steel of same composition (phases allowed were austenite, $M_{23}C_6$, M_6C, Laves phase, σ phase, ferrite and liquid). The base composition used can be found in table 9.2.

rich phase, which would keep the matrix content at a constant level. In this regard, the shift of the plateau between the 10^4 h and the 10^5 h rupture stress could be related to the kinetics of this precipitation. Calculations made on this composition with MT-DATA (fig. 9.11B) actually reveal a consistent trend in the Mo content of the austenite when increasing the bulk Mo content, but indicate that Laves phase is only expected for Mo content greater than 2.2 wt%.

9.6.b Chromium and boron

According to equation 9.9, chromium slightly reduces the creep rupture strength. Unfortunately the mechanism does not seem to be understood. It was possible to reproduce this trend for a type 316 steel as illustrated in figure 9.12. The gradient for compositions close to 16 wt% Cr is in very good agreement with the value of 7.5 found in equation 9.9.

Additions of boron have been found to increase substantially the creep life of austenitic stainless steels, as emphasised by the large coefficient it is attributed in equation 9.8. The predicted effect of boron was found to be similar, with a slope of about 5700 MPa / wt% (see figure 9.12).

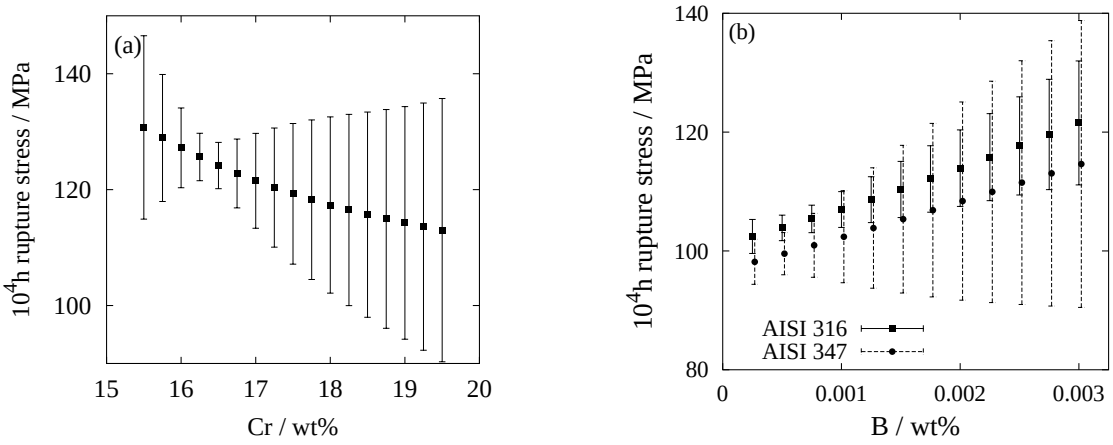

Figure 9.12: (a) The predicted influence of chromium on the 10^4 h rupture stress at 650 °C for a typical 316. (b) The effect of boron on the creep rupture stress for two different steels. Detailed compositions for these examples are given in table 9.2

9.6.c The stabilisation ratio and solution temperature

There has been much work on the influence of the amount of 'stabilising elements' such as Nb, Ti, V or Zr, which prevent the formation of chromium carbides, on the creep properties of austenitic stainless steels. The problem is generally described using a stabilisation ratio (eq.9.12), which is a convenient estimate of the extent to which carbon, nitrogen and the stabilising elements deviate from stoichiometry during compound formation [12, 116, 127].

Keown and Pickering [116] estimated that the best creep properties were obtained for stoichiometric additions of Nb while more recent work [11] claims that 'under stabilising' C is better. This is because data from long term experiments [11] have shown that the trend observed by Keown and Pickering for rather short term experiments (average 3000 h) do not extrapolate well. For Ti on its own, the agreement is that a larger stabilisation ratio produces the optimum creep strength [6]

For short term tests, optimum creep properties have often been found when the precipitation of MX was maximised by using stabilisation equal to or greater that unity. However, according to [6], the creep of austenitic steels is essentially diffusion controlled in service conditions, which could explain why there is no great benefit in maximising the amount of MX precipitates.

Figure 9.13(a), shows that the neural network model was able to reproduce the ex-

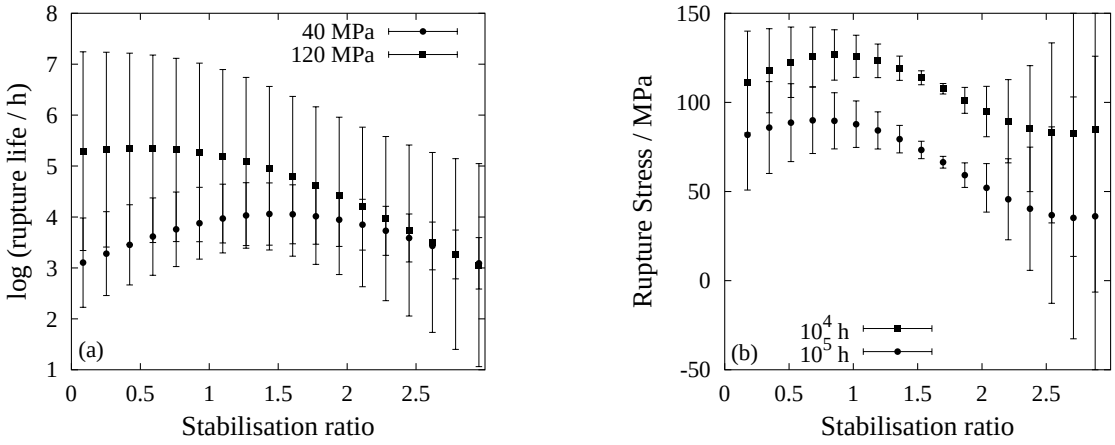

Figure 9.13: (a) The effect of the stabilisation ratio (increase of Nb) on the creep rupture life of a typical 18Cr-12Ni steel at 650 °C. Optimum short term creep properties are obtained for close to stoichiometric additions, while understabilisation is better for long term properties. (b) the effect of an increase of Ti: the stabilisation ratio which produces the optimum creep strength is larger than in (a).

pected trends for Nb additions. For short term tests, the best properties are obtained for a stabilisation ratio equal to or slightly greater than unity. For longer term tests, the influence of stabilising elements is predicted to be less and the optimum addition much below a stoichiometric ratio. On the right of the same figure is the effect of Ti addition on the 10^4 and 10^5 h rupture stress of a typical 18-12 steel, showing that the model correctly predicts best properties at a larger stabilisation ratio, although this ratio still shifts slightly towards understabilisation for longer times.

Figure 9.14 (a), shows the effect of the solution treatment temperature for different levels of Nb (see base composition in table 9.2). This is in very good agreement with the hypothesis [12] that the optimum creep properties are obtained when as much as possible of MX forming elements are put in solution before service: with an increased level of niobium, the solution treatment temperature that dissolves the maximum amount of Nb(C,N) is increased. Figure 9.14(b), is a prediction of the amount of NbC (calculated with MT-DATA [83]) found in a steel of composition equal to that used for the predictions above, (steel with 0.32 Nb wt%). It shows that all of the carbon and niobium are in solution only at temperatures larger than 1250 °C, which closely matches the optimum solution treatment temperature for this composition.

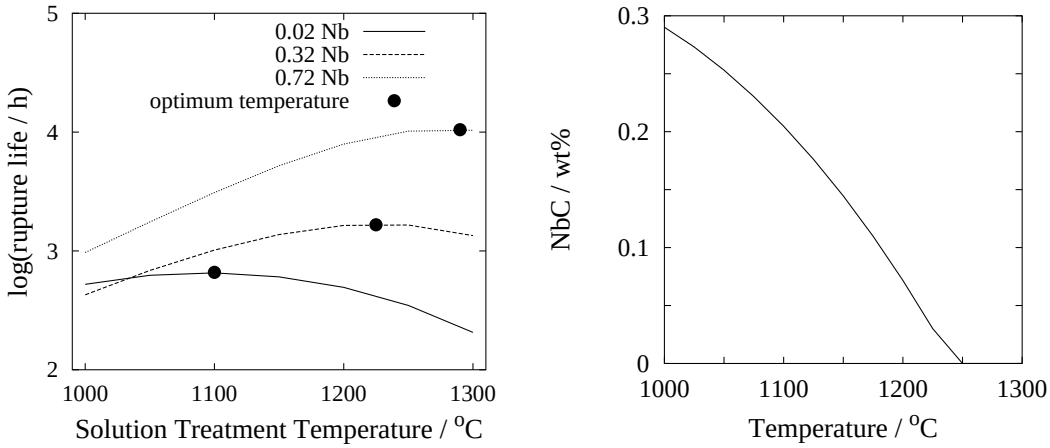

Figure 9.14: (a) the predicted effect of the solution treatment temperature on the creep rupture life of a typical 18-12 steel (see table 9.2). On the right, the amount of NbC present as a function of the solution treatment temperature, in the 0.32Nb wt%, calculated with MT-DATA (allowing for austenite, ferrite, liquid, TiC, NbC, TiN, NbN, $M_{23}C_6$ and σ-phase). The solubility limit corresponds closely to that for which optimum creep properties are predicted.

9.6.d Comparison with other methods

The recent revision of the NRIM (National Research Institute for Metals, Japan) datasheet no. 28 (28B, data for SUS 347H TB) contains considerably more long term data than did the previous version 28A. At the time when the database used in the present work was compiled, these new data were not available and therefore have not been used to train the models. It is interesting to compare the predictions of our model with those made by the NRIM on the same data.

The 10^5 h rupture stress was predicted using the neural network model for two steels of the NRIM 28B datasheet (AEA and AEG), for temperatures ranging between 600 and 750 °C.

Figure 9.15 shows the predictions of the neural network model against those made by the NRIM, using the Orr-Sherby-Dorn method, on the previously published data, and the recent results published in revision 28B. The agreement with experimental data is good, particularly in the case of steel AEG where the neural network produces significantly better predictions than the Orr-Sherby-Dorn method used by the NRIM. It should also be noticed that the trends for both steels have been correctly predicted, despite their apparent similarity in composition (see table 9.2).

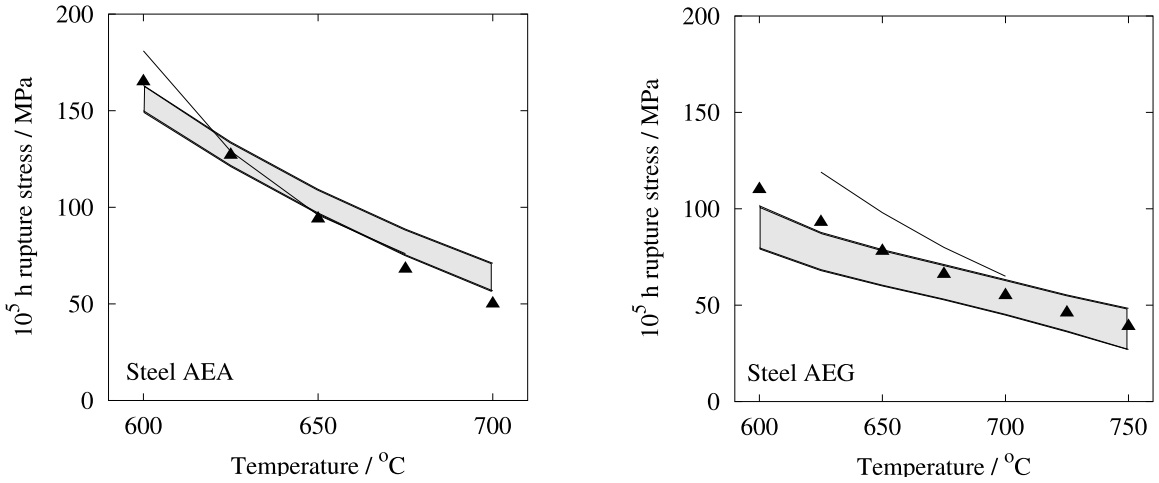

Figure 9.15: Comparison between the neural network model predictions (shaded area), the predictions made by NRIM using the Orr-Sherby-Dorn method (line) and the experimental values published in the recent revision 28B (points). See table 9.2 for full compositions.

9.6.e Software

A number of other trends predicted by the models have been examined, which have been found to be reasonable from a metallurgical point of view, amongst which a positive effect of Cu, of P within a limited range (however this element causes embrittlement and is therefore kept much below the level giving optimum creep rupture strength). The number of possibilities of interactions are such that it is not possible to study them fully. The database used to create the model covers a large range of compositions and its application does not stop at the AISI 300 series. The software capable of doing these calculations can be obtained freely from http://www.msm.cam.ac.uk/map/map.html.

9.7 Summary and conclusions

The creep rupture life for a given stress, and the creep rupture stress for a given life have been analysed using a neural networks method within a Bayesian framework. The data were obtained from a variety of sources and cover a wide range of compositions and heat treatments. The potential of the method is clearly illustrated in its ability to perceive interactions between the different input variables. Predicted trends have been found consistent with those expected and the quantitative agreement was frequently

Fig.	Cr	Ni	Mo	Mn	Si	Nb	Ti	V	Cu
9.11	18.0	12.0	-	1.4	0.6	0	0	0	0
9.12(a)	-	12.1	2.54	1.41	0.46	0	0	0	0
9.12(b) 316	16.42	13.21	2.34	1.51	0.52	0.01	0.011	0	0.14
9.12(b) 347	17.89	12.55	0.11	1.74	0.77	0.77	0.02	0.033	0.09
9.13(a)	18.15	13.3	0	0.75	0.4	0.1	0	0	0
9.13(b)	17.71	12.27	0.02	1.56	0.55	0.005	-	0	0.06
9.14(a)	18	12	0.05	0.8	0.4	0.02	0.02	0	0
9.15(AEA)	17.85	12	0.04	1.71	0.60	0.74	0.019	0.031	0.05
9.15(AEG)	17.56	12.24	0.15	1.81	0.63	0.87	0.019	0.041	0.14

Fig.	N	C	B ppm	P	S	Co	Al
9.11	0	0.06	5	0.02	0.01	0	0
9.12(a)	0	0.04	0.0002	0.019	0.02	0	0
9.12(b) 316	0.034	0.05	-	0.021	0.01	0	0
9.12(b) 347	0.016	0.05	-	0.025	0.007	0.37	0.004
9.13(a)	0.012	0.062	0	0.02	0.002	0	0
9.13(b)	0.014	0.06	5	0.026	0.01	0	0.121
9.14(a)	0.01	0.06	10	0.02	0.002	0	0
9.15(AEA)	0.0284	0.07	12	0.02	0.005	0.29	0.019
9.15(AEG)	0.0222	0.053	27	0.027	0.011	0.30	0.008

Table 9.2: The base compositions of the different examples, in wt%.

satisfying. The model can be applied widely because of its capacity to indicate uncertainty, including both an estimate of the perceived level of noise in the output, and an uncertainty associated with fitting the function in the local region of input space.

Chapter 10

Summary and future work

Following an extensive review of the work done on the topic, it can be said with certainty that precipitation phenomena in austenitic stainless steels are complex, and that controversies persists in many cases.

A part of this work was concerned with the microstructural evolution of a newly designed austenitic stainless steel named NF709, with a particular attention to phases which may be detrimental to long-term creep properties. In this regard, results obtained during this work indicate that the detrimental role of σ-phase is not systematic, as evidence is given that it has little effect on the ductility. It is also shown that significant differences in the precipitation sequences can appear from apparently similar compositions. Furthermore, by combining observations from the literature and the detection of Cr_3Ni_2SiN the role of nitrogen as a stabiliser for the η-structure can be clarified.

Of great interest is also the ability to predict the microstructural evolution of these steels. Based on previous work by Robson and Bhadeshia, and Fujita and Bhadeshia, a model has been created which makes full use of modern thermodynamic calculation tools. This model corrects approximations made necessary when using stand-alone programs, in particular, it is shown that using either the equilibrium tie-line, or the one corresponding to a zero gradient of carbon, is incorrect and does not lead to satisfactory predictions of the growth rate. The problem is only correctly solved when addressing it in terms of activities of the components rather than concentration. Also, the issue of capillarity in multicomponent systems has been examined, and earlier approaches have been corrected. A method has been designed which allows to tackle the problem through modification of the SGTE databases so that capillarity corrections can be calculated directly with MT-

DATA. With the program written so as to avoid too specific solutions, it is hoped that its scope of use will extend beyond austenitic stainless steels in future works.

However, for various reasons, this still has to be considered as a semi-quantitative approach. First, there is a serious lack in available thermodynamic data on phases that are commonly encountered in modern grades of heat-resistant austenitic stainless steels, which strongly limits the number of systems in which meaningful predictions can be made. Furthermore, the model still relies on the mean-field approximation. It is certainly a worthy challenge to overcome this so as to account for localised interactions, or grain-boundary and intragranular precipitation separately. Finally, fundamental reasons have been given which justify a re-examination of the way nucleation theory is used in multicomponent systems, so as to improve the prediction ability of the classical theory.

Given the difficulties in predicting quantitatively the precipitation reactions, it is yet too early to use these calculations as inputs in the further step which is to estimate the mechanical properties. It is clear that a meaningful model based on the precipitation state must include feature such as location, as, for example, grain boundary and intragranular precipitates are known to have different influences, and distribution, as a same phase finely dispersed or present as coarse particles also has different effects.

However, when using powerful empirical methods such as neural network modelling, these difficulties can be avoided; variables such as composition and test conditions can be used directly. With the use of creep data collected from a number of sources, such models have been built to estimate the creep strength and creep life of austenitic stainless steels. Predictions made with these models have been compared to known trends, and shown to grasp properly interactions between different input variables and to be superior to conventional extrapolation methods. It is also interesting to note that the use of physically relevant variables significantly improved the models; for example, the logarithm of time was used rather than time and a variable relevant for the estimation of the quantity of fine MX precipitates was added. This justifies the hope that future models, which may use predicted volume fractions and locations of precipitates as inputs, could help confirming or understanding the role held by the different precipitate phases in determining the creep strength of austenitic stainless steels.

APPENDIX ONE

MAP_STEEL_CREEP_LIFE_AUSTENITIC

This appendix presents the model described in chapter 9 and associated documentation following the MAP format, http://www.msm.cam.ac.uk/map/mapmain.html.

1 Provenance of Source Code

Thomas Sourmail
Phase Transformations and Complex Properties Group,
Department of Materials Science and Metallurgy,
University of Cambridge,
Cambridge, CB2 3QZ U.K.

The neural network program was produced by:
David MacKay,
Cavendish Laboratory,
University of Cambridge,
Madingley Road,
Cambridge, CB3 0HE, U.K.

Added to MAP: June 2001.

2 Purpose

A program for the estimation of the creep life of austenitic stainless steels as a function of elemental composition, test conditions and solution treatment.

3 Specification

Language: C
Product Form: Source Code
Operating System: tested on Solaris, SGI and Linux. Can be compiled on most UNIX systems.

4 Description

MAP_STEEL_CREEP_LIFE_AUSTENITIC contains the programs which enable the user to estimate the creep life of austenitic stainless steels as a function of chemical composition, solution-treatment temperature, and stress and temperature of the creep test. It makes use of a neural network program called *generate44*, which was developed by David MacKay and is part of the *bigback5* program. The network was trained using a large database of experimental results [1]. 4 different models are provided, which differ from each other by the number of hidden units and by the value of the seed used when training the network. It was found that a more accurate result could be obtained by averaging the results from all models [1]. The programs calculate the results of each model and then combines them, by averaging, to produce a *committee result* and error estimate, as described by MacKay [2].

The source code is accompanied by a program to install the program, which should run on most versions of UNIX. Once uncompressed, and once the 'install' program run, the directory contains:

README

A text file containing step-by-step instructions for running the program, including a list of input variables.

MINMAX

A text file containing the minimum and maximum limits of each input and output variable. This file is used to normalise and unnormalise the input and ouput data.

test.dat

An input file containing the input variables used for predictions.

model.gen

This is a UNIX shell file containing the commands required to run the model. It can be executed by typing 'sh model.gen' at the command prompt. This shell file normalises the input data, executes the neural network program, unnormalises the results and combine them to produce the final *committee* result.

.normalise

Hidden executable file, to normalise the input data.

.generate44

Hidden executable file, for the neural network program. It reads the normalised input file

and also uses a configuration file *spec.t* generated by *.generate_spec* and the weight files, located in the subdirectory *c*.

.generate_spec

Hidden executable file, generates the configuration file read by *.generate44*.

.gencom

Hidden executable file, combines the output of the different models in a *committee* result.

.treatout

Unnormalise the results.

SUBDIRECTORY c

_w*f

The weight files of the different models.

***.lu**

Files containing information for calculating the size of the error bars for the different models.

_c*

Files containing information about the perceived significance value [1] for each model.

_R*

Files containing information about the noise, test error and log predictive error [1] for each model.

SUBDIRECTORY d

outran.x A normalised output file which was created during the building of the model. It is accessed by *.generate44*.

SUBDIRECTORY outprdt

out1, out2, *etc.*

The normalised output files for each model.

com.dat

The normalised output file containing the committee results. It is generated by *.gencom*.

5 References

1. Thomas Sourmail, H. K. D. H. Bhadeshia and D. J. C. MacKay, *A neural network model for the creep strength of austenitic stainless steels.*, Materials Science and Technology, *in press.*

2. D. J. C. MacKay, *Mathematical modelling of weld phenomena 3*, eds. H. Cerjak and H. K. D. H. Bhadeshia, Institute of Materials, London (1997) 359, 3. D. J. C. MacKay's website at http://wol.ra.phy.cam.ac.uk/mackay/README.html

6 Input parameters

The input variables are listed in the README file in the corresponding directory. The maximum and minimum values for each variable are given in the file MINMAX.

7 Output parameters

These give the creep life in log h. The output is written in the file result.txt.

Accuracy

A full calculation of the error bar is presented in reference 1.

Program data

See sample file test.dat

Program results

See sample file result.txt

Keywords

Neural networks, creep life, austenitic stainless steels.

APPENDIX TWO

MAP_STEEL_CREEP_STRENGTH_AUSTENITIC

This appendix presents the model described in chapter 9 and associated documentation following the MAP format, http://www.msm.cam.ac.uk/map/mapmain.html.

1 Provenance of Source Code

Thomas Sourmail
Phase Transformations and Complex Properties Group,
Department of Materials Science and Metallurgy,
University of Cambridge,
Cambridge, CB2 3QZ U.K.

The neural network program was produced by:
David MacKay,
Cavendish Laboratory,
University of Cambridge,
Madingley Road,
Cambridge, CB3 0HE, U.K.

Added to MAP: June 2001.

2 Purpose

A program for the estimation of the creep strength of austenitic stainless steels as a function of elemental composition, temperature of creep test and required life.

3 Specification

Language: C
Product Form: Source Code
Operating System: tested on Solaris, SGI and Linux. Can be compiled on most UNIX systems.

4 Description

MAP_STEEL_CREEP_STRENGTH_AUSTENITIC contains the programs which enable the user to estimate the creep strength of austenitic stainless steels as a function of chemical composition, temperature of the creep test and required life. It makes use of a neural network program called *generate44*, which was developed by David MacKay and is part of the *bigback5* program. The network was trained using a large database of experimental results [1]. 14 different models are provided, which differ from each other by the number of hidden units and by the value of the seed used when training the network. It was found that a more accurate result could be obtained by averaging the results from all models [1]. The programs calculate the results of each model and then combines them, by averaging, to produce a *committee result* and error estimate, as described by MacKay [2].

The source code is accompanied by a program to install the program, which should run on most versions of UNIX. Once uncompressed, and once the 'install' program run, the directory contains:

README

A text file containing step-by-step instructions for running the program, including a list of input variables.

MINMAX

A text file containing the minimum and maximum limits of each input and output variable. This file is used to normalise and unnormalise the input and ouput data.

test.dat

An input file containing the input variables used for predictions.

model.gen

This is a UNIX shell file containing the commands required to run the model. It can be executed by typing 'sh model.gen' at the command prompt. This shell file normalises the input data, executes the neural network program, unnormalises the results and combine them to produce the final *committee* result.

.normalise

Hidden executable file, to normalise the input data.

.generate44

Hidden executable file, for the neural network program. It reads the normalised input file

and also uses a configuration file *spec.t* generated by *.generate_spec* and the weight files, located in the subdirectory *c*.

.generate_spec

Hidden executable file, generates the configuration file read by *.generate44*.

.gencom

Hidden executable file, combines the output of the different models in a *committee* result.

.treatout

Unnormalise the results.

SUBDIRECTORY c

_w*f

The weight files of the different models.

***.lu**

Files containing information for calculating the size of the error bars for the different models.

_c*

Files containing information about the perceived significance value [1] for each model.

_R*

Files containing information about the noise, test error and log predictive error [1] for each model.

SUBDIRECTORY d

outran.x A normalised output file which was created during the building of the model. It is accessed by *.generate44*.

SUBDIRECTORY outprdt

out1, out2, *etc.*

The normalised output files for each model.

com.dat

The normalised output file containing the committee results. It is generated by *.gencom*.

5 References

1. Thomas Sourmail, H. K. D. H. Bhadeshia and D. J. C. MacKay, *A neural network model for the creep strength of austenitic stainless steels.*, Materials Science and Technology, *in press.*

2. D. J. C. MacKay, *Mathematical modelling of weld phenomena 3*, eds. H. Cerjak and H. K. D. H. Bhadeshia, Institute of Materials, London (1997) 359, 3. D. J. C. MacKay's website at http://wol.ra.phy.cam.ac.uk/mackay/README.html

6 Input parameters

The input variables are listed in the README file in the corresponding directory. The maximum and minimum values for each variable are given in the file MINMAX.

7 Output parameters

These give the creep life in log h. The output is written in the file result.txt.

Accuracy

A full calculation of the error bar is presented in reference 1.

Program data

See sample file test.dat

Program results

See sample file result.txt

Keywords

Neural networks, creep strength, austenitic stainless steels.

APPENDIX THREE

MAP_DATA_MTDATA_CAPILLARITY

This appendix presents the databases created to include capillarity effects in MT-DATA calculations, as decribed in chapter 5 and associated documentation following the MAP format, http://www.msm.cam.ac.uk/map/mapmain.html.

1 Provenance of Source Code

Thomas Sourmail
Phase Transformations and Complex Properties Group,
Department of Materials Science and Metallurgy,
University of Cambridge,
Cambridge, CB2 3QZ U.K.

The original data were from the SGTE (Scientific Group Thermodata Europe) databases included with MT-DATA,
National Physical Laboratory,
Teddington,
Middlesex,
TW11 0LW, U.K.

Added to MAP: December 2001.

2 Purpose

To allow calculation of capillarity corrected equilibrium with thermodynamic calculation softwares such as MT-DATA.

3 Description

Two types of binary files are provided: *.dbs* and *.inx* files for direct use with MT-DATA. These data are replicated from the original databases, but a pressure dependency term has been added so that the MT-DATA user can increase the Gibbs energy of any of the precipitates by a given amounts.

The user should be aware that this pressure dependency terms are in no way real volumetric data. There only purpose is to allow the addition of 10^{-6} J mol^{-1} per Pascal. When using these database, a conventional calculation can be performed by setting the pressure to 1 Pa. If the Gibbs energy of, say, M23C6 is to be raised by 1000 J mol^{-1}, the pressure should be set to 10^9 Pa.

Once the file map_data_mtdata_capillarity uncompressed, the directory *databases* contains the following files:

README

Contains detailed instructions on how to install the databases and set up MT-DATA to use them.

cementite.dbs and cementite.inx

Binary files (database and index) providing thermodynamic data for cementite.

m23c6.dbs and m23c6.inx

Binary files (database and index) providing thermodynamic data for M23C6.

hcpa3.dbs and hcpa3.inx

Binary files (database and index) providing thermodynamic data for HCP_A3

sub_p.dbs and sub_p.inx

Binary files (database and index) providing thermodynamic data for the following substances: NTi, CTi, NNb, CNb, C0.479Nb, C0.877Nb, C0.98Nb.

SUBDIRECTORY loa_files

Contains the plain text load files corresponding to the above binary files.

Keywords

capillarity, coarsening, MT-DATA

APPENDIX FOUR

MAP_MT-DATA_KINETICS

This appendix presents the model described in chapter 6 and associated documentation following the MAP format, http://www.msm.cam.ac.uk/map/mapmain.html.

1 Provenance of Source Code

Thomas Sourmail and H. K. D. H. Bhadeshia
Phase Transformations and Complex Properties Group,
Department of Materials Science and Metallurgy,
University of Cambridge,
Cambridge, CB2 3QZ U.K.

This program is interfaced with MT-DATA,
National Physical Laboratory,
Teddington,
Middlesex,
TW11 0LW, U.K.

Added to MAP: December 2001.

2 Purpose

A program to estimate the kinetics of diffusion-controlled, multiple precipitation reactions in austenitic stainless steels. This program can also be used for the same purpose in different systems for which the SGTE databases provide thermodynamic data, but the user will be required to input the diffusion coefficients.

3 Specification

Language: FORTRAN
Product Form: Source Code
Operating System: tested on Solaris.

4 Description

MAP_MT-DATA_KINETICS contains the program which enable the user to obtain an estimate of the volume fraction of various precipitates forming in austenitic stainless steels during ageing at elevated temperature, as a function of time.
All thermodynamic calculations are handled internally by MT-DATA, therefore suppressing the need for the user to input driving forces or equilibrium compositions.
The software uses MT-DATA *.mpi* files, from which the user selects required phases. This file has to be created in first place, using the ACCESS module of MT-DATA.
Once uncompressed, MAP_MT-DATA_KINETICS contains:

kinetics.f
The source code for the program.

compile
A unix shell script to compile the program and link it to MT-DATA object files. It needs to be edited to point to the directory where the latter are found.

precipitate_data
A file containing information about a number of precipitates, that is, lattice parameter, number of atoms per unit cell, and parameters for nucleation (nucleation site density and interfacial energy).

spheregrowth.out and planargrowth.out
Contains 500 precalculated points for the solution to the sphere growth and planar growth equations as described in [1].

README
Complete instructions for installation and use.

5 References

1. Thomas Sourmail, *PhD thesis, Chapter 6*, available on http://www.msm.cam.ac.uk/phase-trans/

6 Input parameters

The user is only required to select the phases allowed in the calculation and the elements which are expected to control their growth, for example Cr and C in the case of $M_{23}C_6$. For most other input parameters, such as composition, ageing temperature and solution-treatment temperature, the user has the possibility to create, with the software files which

can be used for faster access in later calculations.

7 Output parameters

The default output is
Time /s — Vf of precipitate 1 — Vf of precipitate 2 — etc
where Vf is the volume fraction.
This can be easily modified by editing the subroutine SNAPSHOT.

Keywords

Simultaneous precipitation reaction kinetics, austenitic stainless steels.

Bibliography

[1] Vanstone R. W. Advanced pulverised fuel power plant. In Strang A., Banks W. M., Conroy McColvin G. M., Neal J. C., and Simpson S., editors, *Advanced Materials for 21st Century Turbines and Power Plant*, pages 91–97. The Institute of Materials, 2000.

[2] Evans R. W. and Wilshire B. *Introduction to Creep.* The Institute of Materials, London, 1993.

[3] MT-DATA. National Physical Laboratory, Teddington, Middlesex, U.K., 1989.

[4] Lacombe P., Baroux B., and Beranger G., editors. *Stainless Steels.* Les Editions de Physiques, Les Ulis, 1993.

[5] Pickering F. B. Physical Metallurgical Development of Stainless Steels. In *Proc. Conf. Stainless Steels 84, Gothenburg, Sept 1984*, pages 2–28, 1984.

[6] Marshall P. *Austenitic Stainless Steels, Microstructure and Mechanical Properties.* Elsevier, London, 1984.

[7] Nippon Steel Corporation. Quality and Properties of NF709 Austenitic Stainless Steel for boiler tubing applications. Technical report, Nippon Steel Corporation, 1996.

[8] Davis J.R., editor. *Metals handbook*, volume 6. ASM International, Materials Park, OH, 10 edition, 1990.

[9] Naylor D. J. and Cook W. T. *Materials Science and Technology*, volume 7. VCH Publishers Inc., 1992.

[10] Gavrilnjuk V. G. and Berns H. *High Nitrogen Steels.* Springer-Verlag, Berlin, 1999.

[11] Masuyama F. New Developments in Steels for Power Generation Boilers. In Viswanathan R. and Nutting R., editors, *Advanced Heat Resistant Steels for Power Generation*, pages 33–47, London, 1998. The Institute of Materials.

[12] Kikuchi M., Sakabibara M., Otoguro Y., Mimura M., Takahashi T., and Fujita T. An Austenitic Heat Resisiting Steel Tube developed for Advanced Fossil Steam Plant. In *International Conference on Creep, Tokyo, April 14–18, 1986*, pages 215–220, 1986.

[13] Rios P. Expression for Solubility Product of Niobium Carbonitride in Austenite. *Mater. Sci. Techn.*, 4:324–327, 1988.

[14] Rios P. Method for Determination of Mole Fraction and Composition of a Multicomponent f.c.c. Carbonitride. *Mater. Sci. Eng.*, 142:87–94, 1991.

[15] Heilong Z. and Kirkaldy J. S. Thermodynamic Calculation and Experimental Verification of the Carbonitride-Austenite Equilibrium in Ti-Nb Microalloyed Steels. *Metal. Trans. A*, 23:651–657, 1992.

[16] Hughes H. Complex Nitride in Cr-Ni-Nb Steels. *J.I.S.I.*, pages 775–778, 1967.

[17] Andrén H. O., Henjered A., and Karlsson L. MX Precipitates in Stabilized Austenitic Stainless Steels. In *Proc. Conf. Stainless Steels 84, Gothenburg, Sept 1984*, pages 91–96, 1984.

[18] Andrén H. O., Henjered A., and Norden H. Composition of MC Precipitates in a Titanium Stabilised Stainless Steel. *J. Mater. Sci.*, 15:2365–2368, 1980.

[19] Wadsworth J., Woodhead J. H., and Keowm S. R. The Influence of Stoichiometry upon Carbide Precipitation. *Metal Sci.*, pages 342–348, 1976.

[20] Keown S. R. and Pickering F. B. Effect of Niobium Carbide on the Creep Rupture Properties of Austenitic Stainless Steels. In *Creep strength in steel and high-temperature alloys*, pages 229–234, London, 1974. The Metals Society.

[21] Adamson J. M. and Martin J. W. Tertiary Creep Processes in 20%Cr, 25%Ni Austenitic Stainless Steels of differing Nb/C Ratios. *J.I.S.I.*, pages 271–275, 1972.

[22] Jack D. H. and Jack K. H. Structure of Z-phase. *J.I.S.I.*, pages 790–792, 1972.

[23] Vodárek V. Morphology and Orientation Relationship of Z-phase in Austenite. *Scripta Metall. Mater.*, 25:549–552, 1991.

[24] Raghavan A., Klein C. F., and Marzinsky C. N. Instabilities in Stabilized Austenitic Stainless Steels. *Metall. Trans. A*, 23:2455–2467, 1992.

[25] Robinson P. W. and Jack D. H. Precipitation of Z-phase in a High-Nitrogen Stainless Steel. In Lula R., editor, *New Developments in Stainless Steel Technology*, pages 71–76, Metals Park, OH, 1985. Amer. Soc. Metals.

[26] Vorádek V. Effect of Niobium on the Microstructure and Creep Properties of AISI 316LN type steels. In Nordberg H. and Björklund J., editors, *Applications of Stainless Steels '92*, volume 1, pages 123–132. Jernkontoret and Avesta Research Foundation and ASM ineternational, 1992.

[27] Thorvaldsson T. and Dunlop G. L. Effect of Stabilizing Additions on Precipitation Reactions in Austenitic Stainless Steel. *Metal Sci.*, 16:184–190, 1982.

[28] Knowles G. The Creep Strength of a 20%Cr-25%Ni-Nb Steel Containing Controlled Particle Dispersions. *Metal Sci.*, pages 117–122, 1977.

[29] Uno H., Kimura A., and Misawa T. Effect of Nb on Intergranular Precipitation Behavior of Cr Carbides in N-bearing Austenitic Stainless Steels. *Corrosion*, 2(6):467–474, 1992.

[30] Beckitt F.R. and Clarck B.R. The Shape and Mechanism of Formation of $M_{23}C_6$ Carbide in Austenite. *Acta Metall.*, 15:113–129, 1967.

[31] Lewis M.H. and Hattersley B. Precipitation of $M_{23}C_6$ in Austenitic Steels. *Acta Metall.*, 13:1159–1168, 1965.

[32] Tanaka H., Murata M., Abe F., and Yagi K. The Effect of Carbide Distributions on long-term Creep Rupture Strength of SUS321H and SUS347H stainless steels. *Mater. Sci. Eng.*, A234:1049–1052, 1997.

[33] Singhal L.K. and Martin J.W. The Growth of $M_{23}C_6$ on Incoherent Twin Boundaries in Austenite. *Acta Metall.*, 15:1603–1610, 1967.

[34] Sasmal B. Formation of lamellar $M_{23}C_6$ on and near Twin Boundaries in Austenitic Stainless Steels. *Bul. Mat. Sci.*, 6:617–623, July 1984.

[35] Sasmal B. Mechanism of the Formation of $M_{23}C_6$ Plates around undissolved NbC Particles in a Stabilized Austenitic Stainless Steel. *J. Mater. Sci.*, 32:5439–5444, 1997.

[36] Ägren J. Computer Simulation of Diffusional Reactions in Complex Steels. *ISIJ International*, 32:291–296, 1992.

[37] Van der Ven A. and Delaey L. Models for the Precipitate Growth during the $\gamma \rightarrow \gamma + \alpha$ Transformation in Fe-C and Fe-Mn-C Alloys. *Progress in Mat. Sci.*, 40:181–264, 1996.

[38] Hättestrand and Andrén H.-O. Boron distribution in 9-12% chromium steels. *Mater. Sci. Eng.*, A270:33–37, 1999.

[39] Lai J. K. L. A Review of Precipitation Behaviour in AISI Type 316 Stainless Steel. *Mater. Sci. Eng.*, 61:101–109, 1983.

[40] Deighton M. Solubility of $M_{23}C_6$ in Type 316 Stainless Steel. *J.I.S.I.*, pages 1012–1014, 1970.

[41] Degalaix S. and Foct J. Nitrogen in Austenitic Stainless Steels(I). *Mém. Rev. Métall.*, pages 645–653, 1987.

[42] Biss V. A. and Sikka V. K. Metallography Study of Type 304 Stainless Steel Long-Term Creep-Rupture Specimen. *Metall. Trans. A*, pages 1360–1362, 1981.

[43] Thier H., Baumel A., and Schmidtmann P. Effect of Nitrogen on the Precipitation Behaviour of the Steel X 5 CrNiMo 17 13. *Arch. Eisenhuettenwesen*, 40:333–339, 1969.

[44] Minami Y., Kimura H., and Ihara Y. Microstructural Changes in Austenitic Stainless Steels during Long-Term Aging. *Mater. Sci. Techn.*, 2:795–806, 1986.

[45] Thorvaldsson T. and Dunlop G. L. Precipitation Reactions in Ti-stabilized Austenitic Stainless Steel. *Metal Sci.*, pages 513–518, 1981.

[46] Thorvaldsson T. and Dunlop G. L. The Influence of Composition on Precipitation in Stabilized Austenitic Stainless Steels. In *Proc. Int. Conf. on The strength of metals and alloys*, pages 755–760, 1979.

[47] Grot A. S. and Spruiell J. E. Microstructural Stability of Titanium-modified Type 316 and Type 317 Stainless Steel. *Metall. Trans. A*, pages 2023–2030, 1975.

[48] Bentley J. and Leitnaker J. M. Stable Phases in aged Type 321 Stainless Steel. In Collings E.W. and King H.W., editors, *The Metal Sience of Stainless Steels*, pages 70–91. The Metallurgical Society of AIME, 1978.

[49] Lai J. K. L. Precipitate Phases in Type 321 Steel. *Mater. Sci. Techn.*, 1:97–100, 1985.

[50] Stadelmaier H.H. Metal-rich metal-metalloid phases. In Plenum Press, editor, *Development in the Structural Chemistry of Alloy Phases*, pages 141–180, 1969.

[51] Weiss B. and Stickler R. Phase Instabilities During High Temperature Exposure of 316 Austenitic Stainless Steel. *Metall. Trans A*, 3:851–866, 1972.

[52] Brun G., Naour J.L., and Vouillon M. Etude de la Microstructure d'un Acier 316 au Titane apres Vieillissement et apres Irradiation aux Neutrons. *J. Nucl. Mater.*, 101:109–123, 1981.

[53] Williams T.M. Precipitation in Neutron-Irradiated Type 316 Austenitic STeel. In Institute of Metals, editor, *Stainless Steels 84*, pages 403–412, 1985.

[54] Titchmarsh J.M. and Williams T.M. Precipitates in Neutron-Irradiated Austenitic Stainless Steel . In Lorimer G.W, Jacobs M.H., and Doig P., editors, *Quantitative Microanalysis with High Spatial Resolution*, pages 223–228, London, 1981. Institute of Metals.

[55] R. F. A. Jargelius-Petterson. Precipitation in Nitrogen-Alloyed Stainless Steel at 850 °C. *Scripta Metall. Mater.*, 28:1399–1403, 1993.

[56] Lai J. K. L and Meshkat M. Kinetics of Precipitation of χ-phase and $M_{23}C_6$ Carbide in a Cast Type 316 Stainless Steel. *Metal Sci.*, pages 415–420, 1978.

[57] Barcik J. The Kinetics of σ-phase Precipitation in AISI 310 and AISI 316 Steels. *Metall Trans. A*, pages 635–641, 1983.

[58] Stoter L. P. Thermal Ageing Effects in AISI Type 316 Stainless Steel. *J.Mater.Sci.*, pages 1039–1051, 1981.

[59] R. F. A. Jargelius-Petterson. Precipitation Trends in Highly Alloyed Austenitic Stainless Steels. *Z. Metallkd.*, pages 177–183, 1998.

[60] Powell D. J, Pilkington R., and Miller D. A. The Precipitation Characteristics of 20%Cr/25%Ni-Nb Stanilised Stainless Steel. *Acta Metall.*, 36(3):713–724, 1988.

[61] Minami Y., Kimura H., and Tanimura M. Creep Rupture Properties of 18%Cr-8%Ni-Ti-Nb and Type 347H Austenitic Stainless Steels. In Lula R., editor, *New Developments in Stainless Steel Technology*, pages 231–242. Amer. Soc. Metals, 1985.

[62] Sumerling R. and Nutting J. Precipitation in a 20%Cr-25%Ni Steel Stabilized with Niobium. *J.I.S.I.*, pages 398–405, 1965.

[63] Ramaswamy V. and West D. R. F. NbC Precipitation in a 20%Cr-25%Ni-1%Nb Austenitic Steel. *J.I.S.I.*, pages 391–394, 1970.

[64] Williams T.M. and Titchmarsh J.M. Silicon rich Phases in Austenitic Alloys. *J. Nucl. Mater.*, 98:223–226, 1981.

[65] Powell D. J., Pilkington R., and Miller D. A. Influence of Thermal Ageing on Creep Properties of a 20/25/Nb-stabilised Steel. In *Proc. Conf. Stainless Steels 84, Gothenburg, Sept 1984*, pages 382–390, 1984.

[66] Ecob R. C., Lobb R. C., and Kohler V. L. The Formation of G-phase in 20/25 Nb Stainless Steel AGR Fuel Cladding Alloy and its Effect on Creep Properties. *J. Mater. Sci.*, 22:2867–2880, 1987.

[67] Barcik J. Mechanism of σ-phase Formation in Cr-Ni Austenitic Steels. *Mat. Sci. Techn.*, 4:5–15, 1988.

[68] Denham A.W. and Silcock J.M. Precipitation of Fe_2Nb in a 16-wt%Ni 16-wt%Cr Steel, and The Effect of Mn and Si Additions. *J.I.S.I.*, pages 585–592, 1969.

[69] Lai J. K. L. A Study of Precipitation in AISI Type 316 Stainless Steel. *Mater. Sci. Eng.*, 58:195–209, 1983.

[70] White W. E. and Le May I. Metallographic Observations on the Formation and Occurence of Ferrite, Sigma Phase, and Carbides in Austenitic Stainless Steels. Part II: Studies of AISI Type 316 Stainless Steel. *Metallography*, 3:51–60, 1970.

[71] Beattie H. J. and Hagel W. C. Intermetallic Compounds in Titanium-Hardened Alloys. *J. Metals*, pages 911–917, 1957.

[72] Dewey M. A. P., Sumner G., and Brammar I. S. Precipitation of Carbides in a Low-Carbon Austenitic Stainless Steel containing 20wt%Cr-25wt%Ni-0.7%Nb. *J.I.S.I.*, pages 938–944, 1965.

[73] Pickering F.B. Some Aspects of the Precipitation of Nickel-Aluminium-Titanium Intermetallic Compounds in Ferrous Materials. In Pickering F.B., editor, *The metallurgical evolution of Stainless Steels*, pages 391–401. The Metals Society, London, 1979.

[74] Satyanarayana D.V.V., Pandey M.C., and Taplin D.M.R. Creep Behaviour of a Precipitation Hardenable Austenitic Stainless Steel. *Trans. Indian Inst. Met.*, 49(4):419–423, 1996.

[75] Dulis E.J. Age-hardening Austenitic Stainless Steels. In Pickering F.B., editor, *The metallurgical evolution of Stainless Steels*, pages 420–441. The Metals Society, London, 1979.

[76] Tohyama A. and Minami Y. Development of the High Temperature Materials for Ultra Super Critical Boilers. In Viswanathan R. and Nutting J., editors, *Advanced Heat Resistant Steels for Power Generation*, pages 494–506. IOM Communications Ltd, IOM Communications Ltd, 1999.

[77] Rowcliffe A.F. and Nicholson R.B. Quenching Defects and Precipitation in a Phophorus-Containing Austenitic Stainless Steel. *Acta Metall.*, 20:143–155, 1972.

[78] Kolmogorov A. N. *Bulletin de l'Académie des Sciences de L'URSS*, 3:355–359, 1937.

[79] Johnson W. A. and Mehl R. F. *Transactions of the American Institute of Mining and Metallurgical Engineers*, 135:416–458, 1939.

[80] Avrami M. *Journal of Chemical Physics*, 7:1103–1112, 1939.

[81] Saunders N. and Miodownik A. P. *Calphad, Calculation of Phase Diagrams, A Comprehensive Guide*. Pergamond Press, Oxford, 1998.

[82] Hack K., editor. *The SGTE Casebook*. The Institute of Materials, London, 1996.

[83] National Physical Laboratory, Teddington, Middlesex, UK. *MT-DATA Handbook, Utility Module*.

[84] Christian J. W. *Theory of Transformation in Metals and Alloys*. Pergamond Press, Oxford, 1975.

[85] Johnson W. C., White C. L., Marth P. E., Ruf P. K., Tuominen S. M., Wade K .D., Russell K. C., and Aaronson H. I. Influence of Crystallography on Aspects of Solid-Solid Nucleation Theory. *Metall. Trans.*, 6:911–919, 1975.

[86] Bhadeshia H. K. D. H. *Bainite in Steels*. The Institute of Materials, London, 1992.

[87] Zener C. *Transactions of the American Institute of Mining and Metallurgical Engineers*, 175:15–51, 1946.

[88] Robson J. D. and Bhadeshia H. K. D. H. Modelling Precipitation Sequences in Power Plant Steels. Part 1 - Kinetic Theory. *Mater.Sci.Techn.*, pages 631–639, 1997.

[89] Coates D. E. Diffusion-Controlled Precipitate Growth in Ternary Systems I. *Metall. Trans.*, pages 1203–1212, 1972.

[90] Coates D. E. Diffusion-Controlled Precipitate Growth in Ternary Systems II. *Metall. Trans. A*, pages 1077–1086, 1973.

[91] Ziebold T. O. and Ogilvie R. E. Ternary Diffusion in Copper-Silver-Gold Alloys. *Trans. Met. Soc. AIME*, 239:942–953, 1967.

[92] Carolan R. A. and Faulkner R. G. Grain Boundary Precipitation of $M_{23}C_6$ in an Austenitic Steel. *Acta Metall.*, pages 257–266, 1988.

[93] Fujita N. and Bhadeshia H. K. D. H. Precipitation of Molybdenum Carbide in Steel: Multicomponent Diffusion and Multicomponent Capillarity Effects. . *Mater.Sci.Techn.*, 15, 1999.

[94] Jönsson B. Assessment of the Mobility of Carbon in fcc C-Cr-Fe-Ni Alloys. *Z. Metallkd.*, 85:502–509, 1994.

[95] Kirkaldy J.S. and Young D.J. *Diffusion in the Condensed State.* Institute of metals, London, 1987.

[96] Andersson J-O. and Ågren John. Models for Numerical Treatment of Multicomponent Diffusion in Simple Phases. *J. Appl. Phys.*, 72(4):1350–1355, 1992.

[97] Záhumenský P., Ševc P., and Janovec J. Kinetics of Growth of $M_{23}C_6$ Intergranular Precipitates in 18Cr-12Ni-2.5Mo Austenitic Stainless Steel. *Kovové Materiály*, 37:108–119, 1999.

[98] Assassa W. and Guiraldenq P. *Met. Corros. Ind.*, 621:170, 1977.

[99] Ågren J. Local Equilibrium and Prediction of Diffusional Transformations.

[100] Boeuf A., Coppola R., Zamboni F., Morlevat J. P., Rustichelli F., and Wenger D. Time Dependence at 600 °C and 650 °C of $M_{23}C_6$ Precipitate Composition in AISI 304 Stainless Steel. *J. Mater. Sci.*, 16:1975–1979, 1981.

[101] Hillerts M. *Phase Equilibria, Phase Diagrams and Phase Transformations, Their Thermodynamic Basis.* Cambridge University Press, Cambridge, 1998.

[102] Faulkner R. G. Discontinuous Precipitation Kinetics in Austenitic Steels. *Mater. Sci. Techn.*, pages 118–124, 1993.

[103] Morral J.E. and Purdy G.R. Particle Coarsening in Binary and Multicomponent Alloys. *Scripta Metall. Mater.*, 30(7):905–908, 1994.

[104] Thorvaldsson T., Rubinsztein-Dunlop H., Andrén H.-O., and Dunlop G.L. Analytical Electron Microscopy of Carbides Precipitates in a Stabilized Austenitic Stainless Steel. In *Quantitative Microanalysis with high spatial resolution*, pages 250–254. The Metals Society, 1981.

[105] Thorvaldsson T. and Dunlop G. L. Precipitation Reactions in Ti-stabilized Austenitic Stainless Steel. *Metal Sci.*, pages 513–518, 1981.

[106] G. F. Vander Voort, editor. *Applied Metallography.* Van Nostrand Reinhold Company, 1986.

[107] Suryanarayana C. and Norton M.G. *X-ray Diffraction, a Practical Approach.* Plenum Press, New York, 1998.

[108] Colombier L. and Hochmann J. *Stainless and Heat Resisting Steels.* Edward Arnold Ltd, 1965.

[109] Jenkins R. and Snyder R. L. *Introduction to X-ray Powder Diffraction.* Wiley-Interscience, New York, 1996.

[110] MacKay D. J. C. Probable networks and plausible predictions - a review of practical bayesian methods for supervised neural networks. *unpublished, can be obtained from http://wol.ra.phy.cam.ac.uk/mackay/BayesNets.html*, 1995.

[111] Mackay D. J. C. A Practical Bayesian Framework for Backpropagation Networks. *Neural Comput.*, 3:448–472, 1992.

[112] The British Steelmakers Creep Committee. BSCC high temperature data. Technical report, The Iron and Steel Institute, 1973.

[113] Jenkinson E. A., Day M. F., Smith A. I., and Hopkin L. M. T. The Long-Term Creep Properties of an 18%Cr-12%Ni-1%Nb Steel Steampipe and Superheater Tube. *J.I.S.I*, pages 1011–1024, 1962.

[114] Morris D. G. Creep Failure in Type 316 Austenitic Steel. *Metal Sci.*, pages 19–29, 1978.

[115] Strutt A. J. and Vecchio K. S. Simultaneous Oxidation and Sigma-phase Formation in a Stainless Steel. *Metal. Trans. A*, 30A:355–362, 1999.

[116] Keown S. R. and Pickering F. B. Effect of Niobium Carbide on the Creep Rupture Properties of Austenitic Stainless Steels. In *Creep strength in steel and high-temperature alloys*, pages 229–234. The Iron and Steel Institute, The Metal Society, 1974.

[117] Irvine K. J., Murray J. D., and Pickering F. B. The effect of Heat-Treatment and Microstructure on the High Temperature Ductility of 18%Cr-12%Ni-1%Nb Steels. *J.I.S.I.*, pages 166–179, 1960.

[118] Gittins A. The Kinetics of Cavity Growth in 20Cr/25Ni Stainless Seel. *J. Mater. Sci.*, 5:223–232, 1970.

[119] Takahashi T., Sakakibara M., Kikuchi M., Araki S., Ogawa T., and Nagao K. Develpment of a High-Strength 25Ni-20Cr Steel for Tubes in Ultra-Supercritical Power Boilers. In Armor A. F., Bartz J. A., Touchton G., and Valverde A. J., editors, *Improved Coal-Fired Power Plants*, volume 1, pages 3–17. Electric Power Research, 1991.

[120] Naoi H., Ohgami M., Araki S., Ogawa T., Fujita T., Mimura H., Sakakibara H., Sogon Y., and Sakurai H. Development of Tubes and Pipes for Ultra-Supercritical Thermal power Plant Boilers. Technical Report 57, Nippon Steel, april 1993.

[121] Araki S., Takahashi T., Sakakibara M., Mimura H., Ishitsuka T., Naoi H., and Fujita T. Behaviors of Microstructures and Precipitates during Creep and Aging of High-Strength 20Cr-25Ni Steel for Tubes in Ultra-Supercritical Power Boilers. In Liaw P. K., Viswanathan R., Murty K. L., Simonen E. P., and Frear D., editors, *Microstructures and Mechanical Properties of Aging Materials*, pages 99–105. TMS, November 1992.

[122] Araki S., Takahashi T., and Sakakibara M. Life Prediction Technique for Stainless Steels in Hot Corrosion Environment of Boilers. In *Life Prediction of Corrodible Structures*, pages 1–15, Hawai, 1991. NACE.

[123] Takahashi T., Kikuchi M., Sakurai H., Nagao K., Sakakibara M., Ogawa M., Araki T., and Yasuda H. Development of High-Strength 20Cr-25Ni (NF709) Steel for USC Boiler Tubes. Technical Report 38, Nippon Steel, july 1988.

[124] Mathew M. D., Sasikala G., Rao K. B. S., and Mannan S. L. Creep Deformation and Fracture Behavior of a Type 316LN Stainless Steel. In Woodford D. A., Townley C. H. A., and Ohnami M., editors, *Fifth International Conference on Creep of Materials*, pages 577–585, Florida, May 1992.

[125] Elliott D. and Tupholme S. M. An Introduction to Steel Selection: Part 2, Stainless Steels. Oxford University Press, 1981.

[126] F. B. Pickering. *Physical Metallurgy and the Design of Steels.* Applied Science Publishers Ltd, London, 1978.

[127] Sourmail T. Precipitation in Creep Resistant Austenitic Stainless Steels. *Mat. Sci. Tech.*, 17:1, 2001.